NUMERICAL SIMULATION OF WAVE PROPAGATION DUE TO CARBON DIOXIDE STORAGE IN ANISOTROPIC POROUS MEDIA

Investigating the Potential of Micro-Seismicity During Geological Carbon Sequestration (GCS)

Written by

NKENG GEORGE ELAMBO

Department of Civil, Environmental, and Architectural Engineering

University of Catania in collaboration with University of Padova

A dissertation submitted for the Degree of Doctor of Philosophy in

Defense against Natural Risks and Ecological Transition of Built Environment

Supervisors:

Professor Giovanna Xotta,

Professor Carmelo Maiorana,

Dr. Nico De Marchi

September, 2025

Acknowledgement

First, I want to begin by expressing my deepest gratitude to my supervisors: Professor Giovanna Xotta, Professor Carmelo Maiorana, and Dr. Nico De Marchi for their continuous guidance, constructive feedback, and support through the course of this doctorate programme. Their expertise has been instrumental in shaping the technical aspects of this dissertation. It has been an honour to be part of this research team.

Special thanks to my colleagues and friends, whose insightful discussions, and camaraderie made research period both productive and enjoyable. I also acknowledge the research funds and resources provided, without which this study would not have been possible.

On a personal note, I thank my family for their unwavering support, and prayers. Their continuous words of encouragement provided the motivation and resilience needed to get to this stage of my Ph.D. program.

Finally, I thank God for wisdom, knowledge, and strength, that permitted me to accomplish this Doctoral program.

Abstract

Geological carbon sequestration (GCS) is central to global decarbonisation strategies, yet its long-term safety is challenged by the potential for injection-induced seismicity. While prior research has addressed pore-pressure build-up and micro-seismic events in porous reservoirs, the crucial stage of how seismic waves propagate through anisotropic, layered depleted reservoirs to produce ground shaking effects, remains unexplored. This gap undermines risk assessments, as ground-motion metrics such as peak ground velocity (PGV) and intensity are directly relevant to GCS design. Addressing this shortcoming, the dissertation develops and applies an integrated two-stage numerical framework that couples hydromechanical processes with full three-dimensional poroelastic wave propagation, thereby linking CO_2 injection dynamics to seismic source generation and surface ground-shaking intensity.

The framework was designed in two stages. Stage one applies a hydromechanical (u-p) formulation using finite-volume multiphase flow (MATLAB Reservoir Simulation Toolbox) coupled with finite-element geomechanics (GeoMatFEM) to quantify pore-pressure evolution, and fault slip, leading to the estimation of seismic source parameters such as: seismic moment (M_o), moment magnitude (M_w), energy magnitude (M_e), and radiated energy (E_r). Stage two transfers these source parameters into a displacement-velocity-pressure (u-v-p) poroelastic model, implemented in GeoMatFEM. This dynamic deformation-diffusion problem is formulated using mixture theory and Biot's principle, and solved with a finite element method that simulates P-wave, S-wave, and Rayleigh wave propagation in three cases: i.e. an isotropic medium, layered-anisotropic reservoirs, and medium where transverse vertical isotropy is imposed in the layers. The formulation employs a fully implicit monolithic solver for coupled multi-field (displacement-velocity-pressure) problem, based on Newton scheme, and combined with Bi-Conjugate Gradient Stabilized iterations, accelerated by a Multi-Physics Reduction (MPR) preconditioner. This two-stage approach allows a rigorous evaluation of both source characteristics and their propagation effects, enabling the estimation of PGV and Modified Mercalli Intensity (MMI) to quantify ground shaking potential.

Numerical results demonstrate that CO_2 injection generates significant pore-pressure build-up in all case studies, with the layered anisotropy and TVI models, amplifying pressure due to the confining effect of low-permeability layers. This amplified pressure translated into larger fault displacements compared with isotropic cases, increasing the likelihood of fault reactivation. Both media produced micro-seismic events of magnitude < 3, but VTI model reservoirs released greater seismic energy. Wave propagation analysis revealed that anisotropy induces directional wave amplification, shear-wave splitting, and altered arrival times, producing higher

displacement and velocity peaks at the surface. Despite these effects, both cases corresponded to weak shaking intensities (PGV = 0.243 in isotropic medium, PGV= 0.362 cm/s in the layered anisotropic medium and PGV = 0.398 cm/s in the TVI model; MMI II–III), with no anticipated surface damage. These findings confirm that anisotropy not only governs fault slip but also strongly influences seismic energy transmission, underscoring its importance in GCS design and reservoir characterization.

This research makes three principal contributions. First, it establishes a novel workflow that couples u-p hydromechanical modelling with a multifield poroelastic wave propagation in anisotropic reservoirs, filling a key methodological gap in GCS risk assessment. Second, it advances seismic source characterisation by integrating energy-based measures (M_e, E_r) alongside conventional magnitudes, thereby providing a richer understanding of event size and radiated energy. Third, it demonstrates how layered anisotropy affects both the onset and amplitude of ground shaking, yielding critical insights for site selection, monitoring, and regulatory frameworks.

This dissertation develops a transferable numerical framework that enhances the ability to predict, quantify, and mitigate injection-induced seismic hazards. By linking injection processes to ground-motion observables, this study strengthens the evidence base for safe, efficient deployment of geological carbon sequestration. The work thus contributes not only to advancing academic knowledge but also to supporting policy and engineering practice in achieving net-zero carbon goals.

List of Acronyms

Acronym/Nomenclature	Definition
GCS	Geological carbon sequestration / Geological carbon storage
TVI	Transverse vertical isotropy
PGV	Peak ground velocity
MMI	Modified Mercalli Intensity
IPCC	Intergovernmental Panel on Climate Change
IEA	International Energy Agency
FEM	Finite Element Method
FVM	Finite Volume Method
CO_2	Carbon dioxide
HM	Hydromechanical
THM	Thermo-hydro-mechanical
THMC	Thermo-hydro-mechanical-chemical
u-p	Displacement-pressure
u-v-p	Displacement-velocity-pressure

Keywords

Geological carbon storage, Anisotropic materials, Wave propagation, Numerical modelling, Micro-seismicity, Fault displacement, Peak ground velocity, Compressional waves (P-waves), Shear waves (S-waves) and Rayleigh waves, ground shaking intensity.

Table of Content

List of Figures

List of Tables

Chapter 1: Introduction

Geological carbon sequestration (GCS) has been considered a viable element of net-zero strategies for emissions-intensive sectors such as: cement, steel, petroleum, refining and chemicals. Several numerical methods have been developed to understand the safe interaction between the injected carbon dioxide, CO_2, and subsurface strata.

Despite the progress in these models, there remains a gap in linking hydromechanical drivers such as: pressure build-up, stress alteration and fault slip, to fully dynamic 3D poroelastic wave propagation and potential ground shaking in anisotropic materials.

This research aims to evaluate a two-stage numerical framework. First, a coupled hydromechanical u–p (displacement–pressure) model, that estimates injection overpressure, fault reactivation, and derives source parameters such as seismic moment (M_0), moment magnitude (M_w), energy magnitude (M_e), and radiated energy (E_r). Second, a fully coupled 3D u–v–p (displacement–velocity–pressure) wave-propagation model, that simulates P, S, and Rayleigh waves and estimates ground-shaking metrics, comparing isotropic and layered-anisotropic media.

This chapter introduces this study, by discussing the background and context, followed by the research problem and knowledge gaps, the research aims, objectives, method overview and limitations; its significance and finally presents the structural outline of the thesis.

1.1 Background and Context

Geological carbon sequestration (GCS) involves capturing CO_2 at point sources and injecting into deep geological formations (e.g. depleted oil and gas reservoirs, saline aquifers) for long-term storage, thereby mitigating greenhouse-gas emissions [1], [2].

It has been suggested by the Intergovernmental Panel on Climate Change (IPCC) and the International Energy Agency (IEA), that GCS must be deployed to achieve a 45% reduction of GHG by 2030, as well as total decarbonisation by 2050 [3], [4]. This technique is considered the only category of technologies, that simultaneously contribute to direct reduction of emissions in key sectors, facilitating the removal of CO_2 to offset emissions; that are inevitable.

The strategic importance of GCS in mitigating emissions is well-established, with its implementation evolving significantly from early pioneering projects. In the early seventies (70s) in the United States and Canada, CO_2 injection was employed by oil-producing companies

for enhanced oil recovery (EOR). Chevron in 1972 initiated the world's pioneer large-scale carbon dioxide enhanced oil recovery (CO_2-EOR) project, known as the Scurry Area Canyon Reef Operating Committee (SACROC), in Texas [5]. This project involved the injection of approximately 175 million tonnes of natural CO_2 spanning from 1972 to 2009 [6].

Although carbon dioxide was extensively used for EOR, Marchetti, was the first scientist to propose its capture, transport, and storage as a means of reducing anthropogenic emissions in the late 1970s [7], [8]. Adams and Caldeira applied mathematical models to demonstrate that the injected CO_2 could be safely sequestrated in underground facilities for centuries [9].

In recent times, the number of GCS large-scale projects have risen significantly. As of 2020, 65 significant GCS projects, were reported by the International Energy Agency & Global CCS Institute to be either operational or in various stages of development (Global CCS Institute, 2020). By 2023, it was reported that this number had risen to 392 (Figure 1.1; [10]).

The Sleipner project, initiated by Statoil off the coast of Norway, was the first industrial-scale CO_2 injection project aimed at GHG emission reduction [11]. Since the inception of this project in 1996, approximately 1 million metric tons of CO_2, has been stored annually into Utsira formation under the North Sea [12].

Other notable large-scale CO_2 storage repositories consist of the In Salah project in Algeria; Snohvit Norwegian North Sea project; Boundary Dam project in Canada; the Kemper, Petro-Nova, and Illinois projects in the United States of America.; and the Gorgon Projects in Australia. Amid these storage projects, Australia's Gorgon Project as of 2019, is considered the largest operation with an injection capacity of 3.4 to 4.0 million metric tons per annum (Mt CO2/yr.) [13].

Figure 1.1: Geologic carbon storage (GCS) projects and reported capacities.

With the increase in the number of GCS projects, safe and efficient techniques must be developed to avoid geomechanical hazards. Studies [14], [15], [16] have shown that the injection of CO_2 alters pressure configurations, causing fault reactivation, and potentially nucleates micro-seismic events within the reservoir (Figure 1.2).

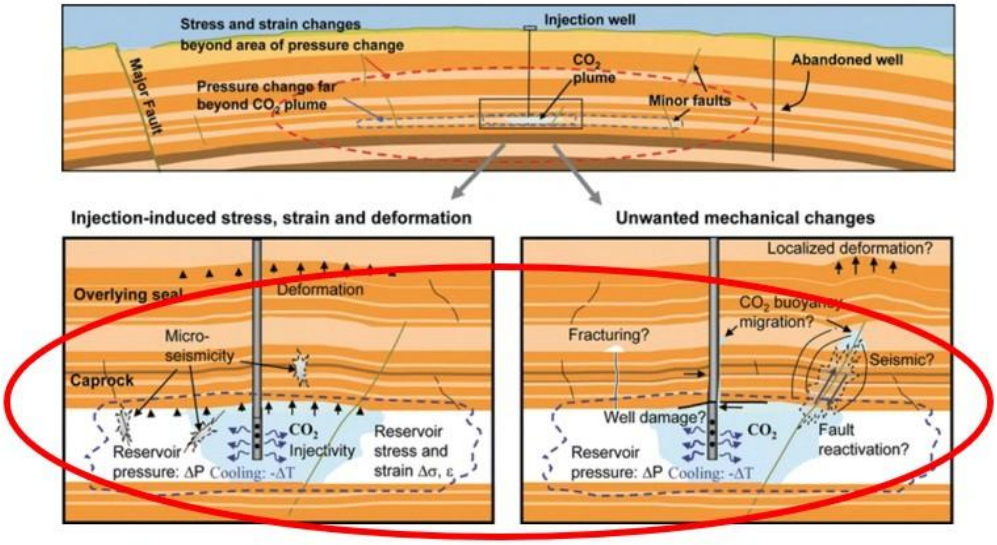

Figure 1.2: Overview of the potential geomechanical risks associated with GCS (modified from [14]

A wide range of multiphysics models based on hydromechanical (HM), thermo-hydro-mechanical (THM), and thermo-hydro-mechanical-chemical (THMC), have been used to predict and reduce GCS risks. These frameworks couple multiphase fluid flow with rock deformation (HM); extend to incorporate heat transport (THM), and further integrate geochemical reactions (THMC), that alter porosity, permeability, and mechanical strength. Using numerical discretization techniques of finite-element, finite volume and/or finite difference formulations, they forecast pore pressure build-up, fault slip tendency, and micro-seismicity.

So far, studies have had as aim, obtaining the overall size of seismic event, by presenting the earthquake with only two seismic sources of seismic moments, M_o and magnitude, M_w. However, the extent to which such micro-seismic events produce perceptible ground shaking depends not only on source moment and energy but also on wave propagation in the reservoir.

The objective of wave propagation analysis is to simulate the seismogram that a set of sensors would register for a prescribed subsurface structure and composition, a capability that is central to seismic interpretation and a key element of seismic inversion. Seismic modelling approaches are typically organized into three classes: direct, integral equation, and ray tracing [17]. In direct methods, the wave equation is solved after representing the geologic model on a numerical mesh, i.e., discretizing it into a finite set of points. These direct methods place no restrictions on material variability and can be highly accurate when the grid is sufficiently refined; moreover, they readily generate snapshots that are valuable for result interpretation. For this

research, the focus is on the direct methods, which is easily described using the Biot's theory of poroelasticity.

Wave propagation in saturated porous media, classically described by Biot poroelasticity [18], has been adopted in studying the coupled reaction between the deformation of the fluid-saturated solid frame. The variables of displacement, relative velocity of solid and fluids, and pressure, provide an insight to three fundamental modes: a fast compressional (P) wave primarily carried by the frame, a shear (S) wave, a slow compressional wave that is diffusive at low frequencies, and Rayleigh waves at surface [19], [20]. In practice, the propagation response is strongly site specific. That is stratification, and anisotropic layering, impart and modify phase and group velocities, amplitudes, attenuation, and polarization. Accounting for these anisotropy-driven path effects in depleted reservoirs, is therefore essential for credible prediction of ground-shaking hazards during fluid-injection operations.

1.2 Problem Statement and Knowledge Gap

Despite the advances in wave propagation modelling in saturated porous media, a systematic, anisotropic application to geological carbon sequestration (GCS), has yet to be explored, leaving the following gaps:

- Literature lacks a workflow that (i) begins with coupled hydro-mechanical (HM) simulations of CO_2 injection to resolve pore-pressure build-up and fault slip; (ii) translate these fields into consistent seismic-source representations (e.g., seismic moment, seismic magnitude, energy magnitude, radiated energy; and (iii) propagates the resulting sources through fully three-dimensional, anisotropic poroelastic media using mixed finite-element (u-v-p) formulations to obtain observable displacement, velocity, pressure and ground shaking metrics.
- In addition, the application of mixed finite element (u-v-p) poroelastic wave-propagation models remain limited, particularly for depleted reservoirs characterized by pronounced layered-anisotropy.
- Although the empirical equations of seismic sources have been used to estimate micro-seismicity during GCS, authors generally neglect evaluating energy release magnitudes and exploiting the use of wave propagation profiles to estimate potential ground shaking effects due to injection-induced activities such as CO_2 storage.

Addressing these gaps, spanning from pressure build-up and fault slip in u-p analysis, through fully coupled wave propagation analysis in anisotropic materials, enables rigorous site

characterization and yields safer, more efficient GCS designs by constraining seismic hazard and mitigating induced seismicity.

1.3 Aim

To develop and apply an extensive integrated numerical framework that links a hydromechanical u-p (displacement–pressure) model to derive seismic source parameters necessary for analysing a 3D wave propagation model in saturated, layered anisotropic reservoirs. This enables us to quantify the potential effects of ground shaking and energy release due to fault reactivation during GCS.

1.4 Objectives of Research

This research is therefore structured around the following objectives:

- Perform a hydromechanical study to quantify pore-pressure build up, fault slip in an isotropic and anisotropic depleted reservoir medium,
- Determine if micro-seismic events are recorded due to GCS injection-induced activities in both reservoir media,
- Quantify the seismic sources of seismic moment, M_o, seismic magnitude, M_w, energy magnitude, M_e, and released seismic energy, E_r, from the micro-seismic event recordings during injection,
- Carryout a wave propagation multifield analysis based off the seismic source results, to determine P-wave, S-wave, and Rayleigh seismic configurations, that are necessary for assessing implications for the ground shaking intensity during a micro-seismic event.

1.5 Method Overview and Limitations

This study focuses on depleted oil and gas reservoirs and early-injection, hydraulically dominated processes. The first part of the analysis deals with a hydromechanical study applied to GCS at early stages of injection. In this section we apply a one-way coupling scheme to quantify the effects of pressure on pre-existing fault configuration. We employ a coupled finite volume – finite element numerical scheme: i.e. MATLAB Reservoir Simulation Toolbox solves the multiphase flow using finite volume, and GeoMatFEM solves the geomechanics using FE approach. The fault configuration is designed using a set of continua elements.

Thereafter, we use seismic source empirical formulations, to evaluate the magnitude of the earthquake, due to potential fault-reactivation during the early stages of injection.

Finally, for the wave propagation u-v-p analysis, we employ an efficient multi–field coupled dynamic model for saturated anisotropic porous materials. The mathematical formulation of the

dynamic deformation–diffusion problem is derived from mixture theory with an appropriate definition of effective stress for anisotropic poroelasticity, explicitly incorporating fluid phase compressibility and anisotropy. The effective stress principle is extended via the Biot tensor to capture the coupling between the shear stress of the solid skeleton and the pore fluid pressure. The coupled problem is discretized using inf-sup stable Finite Element spaces. We employ a fully implicit monolithic solver based on Newton procedure where the system solution is given by the Bi–Conjugate Gradient Stabilized (Bi-CGStab) scheme, enhanced with an ad–hoc Multi–Physics Reduction (MPR) preconditioner. The developments are implemented in the 3D GeoMatFEM research code, and a series of numerical studies are conducted to evaluate 3D wave propagation applications in fully saturated anisotropic media.

However, based on this method approach, we have some limitations. They include the following:

- For simplicity of the hydromechanical u-p model, we neglect the effects of temperature and future chemical reactivity which has proven to greatly affect the outcome of pore pressure build-up and fault reactivation in studies carried out by [15], [21], [22], [23].
- In addition, we undermine the capillarity effects that exists due to multiphase reaction between the fluids and solids within the reservoir. This has shown in previous work to affect the safe storage outcome of CO_2 injection[24].
- For the u-v-p wave propagation model, the absence of boundary absorbers or dampeners could affect the readability of the wave propagation profile. This is because the reflections from the waves, could provide spurious boundary reflections.
- Finally for large reservoirs, our model must be downsized because applying finite elements to these reservoirs would require an extremely fine mesh that would need a terabyte class memory demand.

1.6 Significance and Contribution

This thesis addresses a critical missing link in the GCS literature by establishing a link between hydromechanical u-p analysis and multifield wave propagation analysis. That is, it connects injection-driven hydro-mechanical processes to three-dimensional, anisotropy-resolved poroelastic wave propagation and, ultimately, to ground-motion metrics that matter for GCS operations and design.

In addition to the seismic moment and magnitude used in previous studies, this work systematically incorporates energy-based seismic source measures of energy magnitude and radiated energy. Alongside these parameters wave propagation-based observables such as peak-

ground velocity (PGV), mapped to intensity, are provided, thereby assessing ground shaking perceptibility, during CO_2 injection.

By explicitly treating layered anisotropy in depleted reservoirs, the framework clarifies anisotropic effects wave profile recordings when compared to isotropic case studies or single layer studies. Collectively, the approach enhances site characterisation, reduces uncertainty in hazard screening, and strengthens the technical evidence base for safe, efficient deployment of geological carbon sequestration.

In the method adopted, this thesis develops and applies an integrated approach that begins with a hydro-mechanical simulation of CO_2 injection to resolve pore-pressure evolution, stress redistribution, and fault reactivation, then derives physically consistent seismic sources (scalar moment, M_w, M_e, radiated energy, focal mechanism), and finally propagates those sources through fully three-dimensional, anisotropic poroelastic media using a mixed finite-element three-field formulation.

On the computational side, the dynamic propagation stage employs a fully implicit monolithic solver for the coupled multi-field problem, based on Newton scheme and combined with Bi-Conjugate Gradient Stabilized (Bi-CGStab) iterations enhanced by a tailored Multi-Physics Reduction (MPR) preconditioner, implemented in GeoMatFEM. This yields a stable, scalable workflow for large 3-D poroelastic simulations in saturated isotropic and anisotropic media.

The outputs are translated into, expected arrival wave patterns, shear wave polarization diagnostics, ground shaking evaluation, PGV/MMI maps, which could be important for earthquake early warning (EEW) studies during CO_2 storage operations. Beyond the immediate application, the methodology is transferable to other storage settings and can be extended to richer couplings such as thermo-hydromechanical/chemical (THM/THMC) and advanced boundary treatments (e.g., PML) where warranted. In summary, the thesis establishes a rigorous, anisotropy paradigm for assessing wave propagation and ground shaking due to CO_2 injection, advancing the aim of safe geological carbon sequestration.

1.7 Structural Outline

The other sections of this research are organized as follows:

In Chapter 2, a literature review is presented by providing an overview of the underground facilities and trapping mechanisms compatible with GCS procedure, highlighting the importance of exploring depleted oil and gas reservoirs. Thereafter, we review the governing equations that control multiphase flow through porous media, while explaining the key

geomechanical outcomes related to GCS procedures. Subsequently, we trace the evolution from hydromechanical (HM) models to thermo-hydro-mechanical(-chemical) (THM/THMC) frameworks grounded in Biot poroelasticity. Furthermore, we review the coupling schemes, discretization paradigms, and software used analysing hydromechanical effects due to CO_2 injection . We then evaluate fault-representation strategies and seismic metrics, demonstrating how exclusive reliance on seismic magnitude, M_w, may bias hazard appraisal, whereas energy magnitude, M_e, better captures radiated energy. Finally, we appraise wave-propagation solvers for saturated, anisotropic media, resolving coupled fluid–solid velocities and displacements pertinent to near-field shaking.

In Chapter 3, the methodology to our two-stage numerical framework, that is; (i) a quasi-static poroelastic u–p analysis to estimate the injection-induced seismic source parameters, and (ii) a dynamic u–v–p wave-propagation analysis to model the seismic wavefield and ground-shaking metrics in both isotropic and anisotropic media are discussed.

Subsequently, Chapter 4 presents a unified geological framework for both case studies. Case A assumes isotropy (uniform petrophysical and mechanical properties), whereas Case B introduces anisotropy from stratified layers with contrasting poromechanical behaviour. The section specifies the computational domain and formation properties that are applied to the two-stage numerical framework.

Thereafter, the results and discussions of the numerical model are presented in Chapter 5.

Finally, in Chapter 6, we conclude and provide recommendations for future work, based on the limitations of our current model.

Chapter 2: Literature Review

2.1 Introduction

Understanding the dynamic response of subsurface structures during carbon dioxide (CO_2) injection is essential for ensuring the long-term safety and efficiency of geological carbon sequestration (GCS).

This chapter provides an overview of the existing research relevant to the numerical simulation of wave propagation resulting from carbon dioxide (CO_2) injection in multiphase, anisotropic materials, with focus on the potential for fault-reactivation and injection-induced micro seismicity during GCS. The review is critical in evaluating existing theoretical, numerical, and empirical work, identifying gaps in current knowledge, and positioning the present study within the broader scholarly context.

This literature review synthesizes foundational and recent research on the potential risks associated with geological carbon sequestration, key theories related to multiphase flow in porous media, and numerical modelling approaches adopted for studying wave propagation due to CO_2 injection in saturated anisotropic media.

This section is structured as follows: First, it reviews the underground facilities that are compatible with GCS operations. Subsequently, it focuses on the trapping mechanisms associated with GCS in depleted oil and gas reservoirs.

Thereafter, we examine the theory of multiphase flow dynamics, highlighting the interaction between CO_2, brine, and key petrophysical properties of the rock (such as porosity, permeability, and capillary pressure). We then highlight the governing equations and distinguish between the main reservoir models used in multiphase flow analyses, while pointing out the major risks associated with the GCS process particularly pressure build up, fault instability and micro-seismicity.

The review then transitions to an examination of the main numerical modelling frameworks developed to investigate injection-induced micro-seismicity during geological carbon sequestration. It introduces the progression from hydromechanical (HM) models—which focus on pore pressure alteration, to more advanced thermo-hydro-mechanical (THM) and thermo-hydro-mechanical-chemical (THMC) frameworks that additionally account for temperature and chemical effects. The discussion highlights key theoretical foundations, such as Biot's theory of poroelasticity, and reviews addresses fault reactivation and micro-seismic risk in response to CO_2 injection. This section sets the stage for more detailed analysis of hydromechanical

coupling and its relevance to early-phase seismic risk assessment in geological carbon storage projects.

Thereafter, we discuss the principal coupling schemes developed for integrating hydraulic and geomechanical processes in hydro-mechanical (HM) models. It outlines the progression from explicitly one-way coupled (loose) schemes, which solve hydraulic and mechanical sub-problems independently, to more advanced iteratively coupled and fully coupled approaches that capture complex interactions between fluid flow and rock deformation. The discussion highlights the computational efficiency, stability, and accuracy of each method, examining their respective advantages, limitations, and typical applications in modelling reservoir geomechanics during CO_2 injection.

The next section then reviews the primary numerical discretization approaches used for modelling the coupled hydro-mechanical (HM) processes in geomechanics. It outlines the classification of these methods into continuum, discontinuum, and hybrid frameworks. In addition to this section, reference is made to the simulation software used for HM modelling, clearly highlighting how the choice of discretization influences both the accuracy and computational efficiency of HM analysis in geological carbon sequestration.

Afterwards, it examines the principal modelling techniques used for fault representation and micro-seismicity assessment in the context of geological carbon sequestration. It explores both discontinuity and continuum approaches for fault implementation, emphasizing their roles in simulating fault reactivation under CO_2 injection scenarios. The review then explains how micro-seismic events are typically quantified through the calculation of static seismic moment (M_o) and corresponding moment magnitude (M_w), drawing on empirical relationships widely applied in the literature. However, relying only on these variables leaves an important gap, as these variables potentially underestimate the size of earthquakes and are insensitive to how much energy is radiated as seismic waves, especially at high frequencies. The energy magnitude, M_e, which scales with radiated energy addresses this aspect.

Thereafter, we examine the computational methods used in studying wave propagation due to CO_2 injection, examining their effectiveness in capturing wave propagation, fluid, and solid velocity, and displacement in saturated anisotropic materials. By evaluating these modelling approaches, this review establishes the basis for the numerical framework developed for this thesis.

Finally, this chapter concludes by providing a summary and positioning the study to address limitations identified in the current wave propagation modelling approaches used in predicting

and mitigating the potential hazards associated with GCS. These gaps shape the direction of the research methodology presented in the next section. By doing so, the review will help set the stage for understanding how the proposed approach is intended to address these challenges and contribute to ongoing advancements in the field.

2.2 Underground Storage Formation Types

For the favourable injection of CO_2, the process of choosing geological sites for storage must adhere to three (3) primary criteria: capacity, injectivity and containment. Ensuring the capacity of storage site involves confirming that it possesses sufficient pore volumes to accommodate significant quantities of carbon dioxide. Typical conditions suggest that the site exhibits substantial porosity, covers a large surface area, and guarantees a high reservoir permeability, facilitating the use of lower wellhead pressure to sustain desired injection rates [25], [26].

The potential geological formations discussed in this section include a.) saline aquifers, b.) unminable coal seams, c.) depleted oil and gas formations.

2.2.1 Saline aquifers

These aquifers are made of reservoir rocks that are both permeable and porous, containing saline fluids distributed within the interstitial spaces among the rock grains. Typically, they are found at depths which extend from 800 – 3000 meters below the earth's surface and can span hundreds of kilometres in width [27]. Numerous studies have identified saline aquifers as the most viable geological formations for CO_2 storage [28], [29]. This is because it is considered to have high storage potential, suitable petrophysical properties and well-understood geological principles.

A study in the United States, deduced that the saline aquifers alone could potentially store approximately 12,000 gigatons of CO_2, with a storage efficiency of about 40% [30]. This suggests that for every 100 metric tons of CO_2 injected into an aquifer, approximately 40 metric tons can be effectively retained within the aquifer. Figure 2.1 illustrates the complete mechanism of CO_2 capture, transport, and storage in deep saline formations.

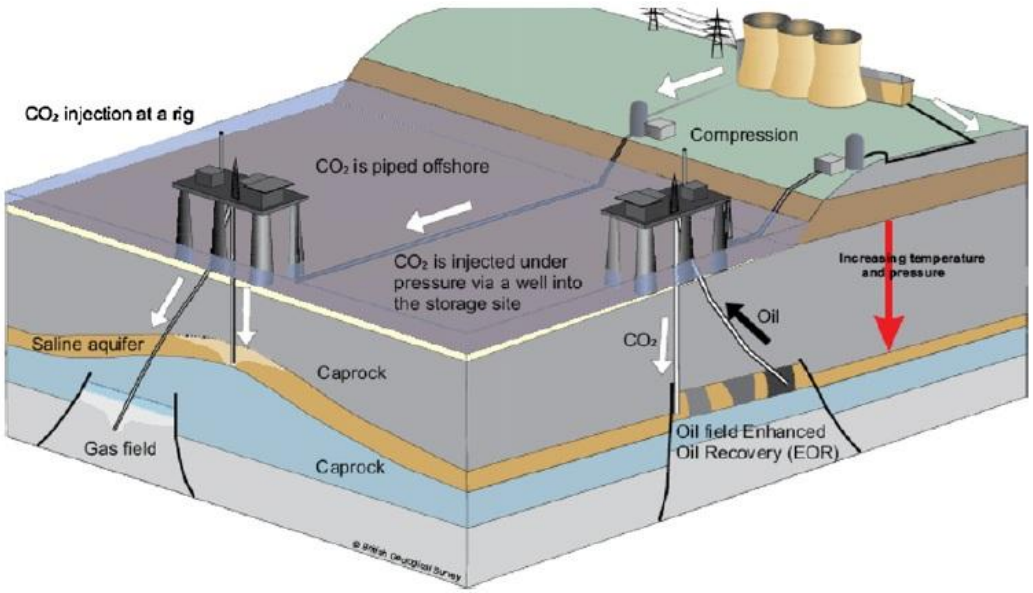

Figure 2.1: CO_2 storage in deep saline aquifers [31]

From a safety perspective, the secure containment within deep saline formations hinges upon the effective immobilization of upward migration of CO_2. These geological formations possess enclosed structures that impede the buoyancy-driven movement characteristics of supercritical CO_2 in reservoirs. Over time, the likelihood of leakage is anticipated to diminish owing to the processes such as dissolution of CO_2 into the brine solution [32], [33].

However, a notable limitation of saline formations is that mineral precipitation can alter rock porosity, potentially reducing its capacity to inject and securely sequester CO_2 over the long term [34].

2.2.2 Unminable coal seams

Coal seams are considered a viable option for storage of CO_2, giving their ability to accommodate large volumes of CO_2 within their coal matrix [35], [36], [37]. The storage potential of coal seams is contingent upon various parameters, including the thickness of the coal seams, coal rank and quality [33].

As per the assessment by the United States Department of Energy, coal seams located at depths exceeding 1500 meters exhibit the potential to store up to ten times more CO_2, compared to shallower coal seams. Research conducted by the University of New South Wales revealed that coal seams exceeding a thickness of 2 meters can store up to quadruple the amount of CO_2 in comparison to thinner seams. For example, a preliminary study showed that the thick and deep coal beds in Alberta, Canada, could potentially store about 20 gigatons of CO_2 [38].

The storage mechanism in coal seams is different from the previously discussed storage facility in that, coal seams inherently harbour methane, which is retained through the adsorption process. The injected CO_2 competes for adsorption sites with the methane. However, owing to CO_2's superior adsorption affinity for coal, it displaces the resident methane, thereby enabling its subsequent capture. This process is termed as CO_2-enhanced coalbed methane production (CO2-ECBM) [35], [39]. Figure 2.2 is an illustration of the mechanism, for CO_2 storage in coal mines.

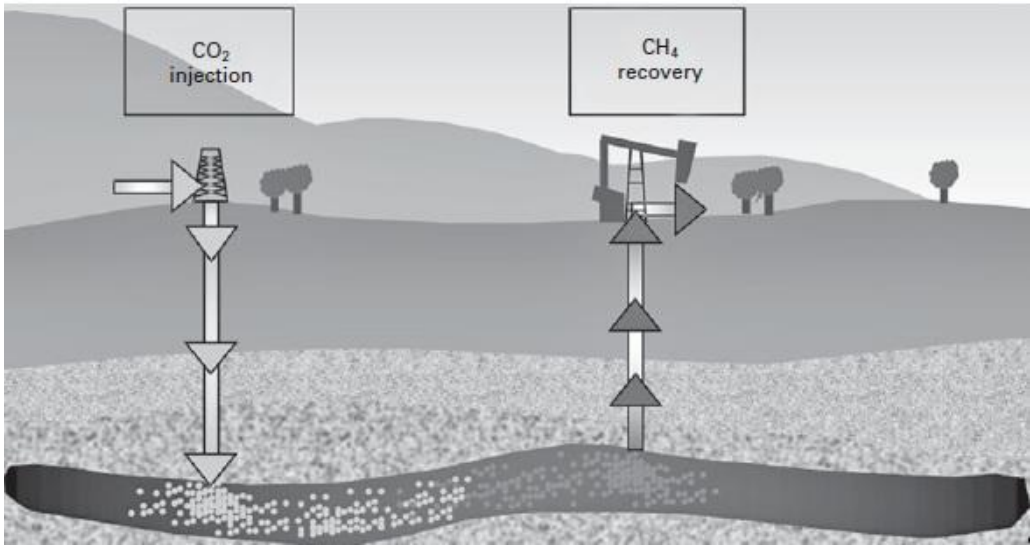

Figure 2.2: Schematic of CO_2 storage in goal mines [40]

2.2.3 Depleted oil and gas reservoirs

These are fields that have undergone full exploration and production and have reached the end of their production life. These fields potentially serve as a good option for CO_2 storage because they are extensively documented, with a variety of data available, including pressure thresholds, seismic readings, and core samples. This information offers a comprehensive understanding of their geological characteristics, such as the rock type, porosity, permeability, and maximum allowable injection pressure. It also includes details of reservoir delineation, cap rock integrity, and major fault or fracture distribution within the formation [41], [42]. Figure 2.3 illustrates the mechanism for CO_2 sequestration in depleted oil and gas reservoirs.

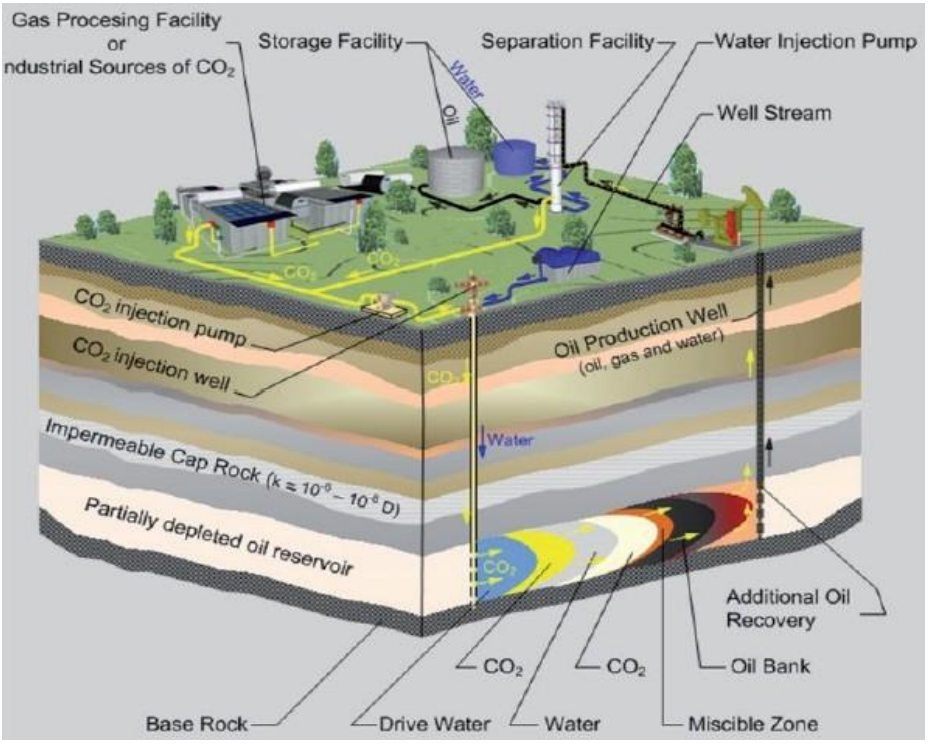

Figure 2.3: CO_2 storage in depleted oil and gas reservoirs. (In this figure the injected CO2 displaces the resident brine) [43]

Despite the potential benefits of GCS in depleted reservoirs, large-scale CO_2 storage projects have yet to be deployed globally. A limited number of CO_2 projects, such as the Otway Project in Australia, have been conducted with ongoing monitoring; however, their storage capacities remain minimal compared to the scale required for industrial-level CO_2 confinement [44].

Authors such as Wei et al. [45], suggested that the limited use of these reservoirs for CO_2 storage is primarily due to geological and engineering challenges. The geological challenges include: 1.) seal or caprock integrity, 2.) unintended migration of the injected CO_2 via faults or fractures, 3.) fault instability, and 4.) salt precipitation. While the engineering risks include: 1.) well integrity failure, 2.) cement failure and 3.) maximum allowable pressure management during injection process.

Given the limited large-scale deployment of GCS in depleted oil and gas reservoirs compared to saline aquifers, this study will lay emphasis on the geomechanical challenges associated with CO_2 storage in these reservoirs.

To fully understand the geomechanical challenges associated with CO_2 storage in depleted reservoirs, it is essential to examine the trapping mechanisms that govern CO_2 containment and their implications for storage security.

2.3 Trapping Mechanisms in Depleted Oil and Gas reservoirs.

The capacity for storage, confinement, and injectivity of carbon dioxide hinges upon the geological and petrophysical attributes of the designated formation. The CO_2, upon injection, is reliably stored underground through two primary trapping mechanisms namely: a.) physical trapping, and b.) geochemical trapping (as seen in Figure 2.4**)**. The efficiency of the storage procedure is determined by the harmonized operation of both trapping mechanisms [25], [46]. In this section, we review each of these entrapment mechanisms.

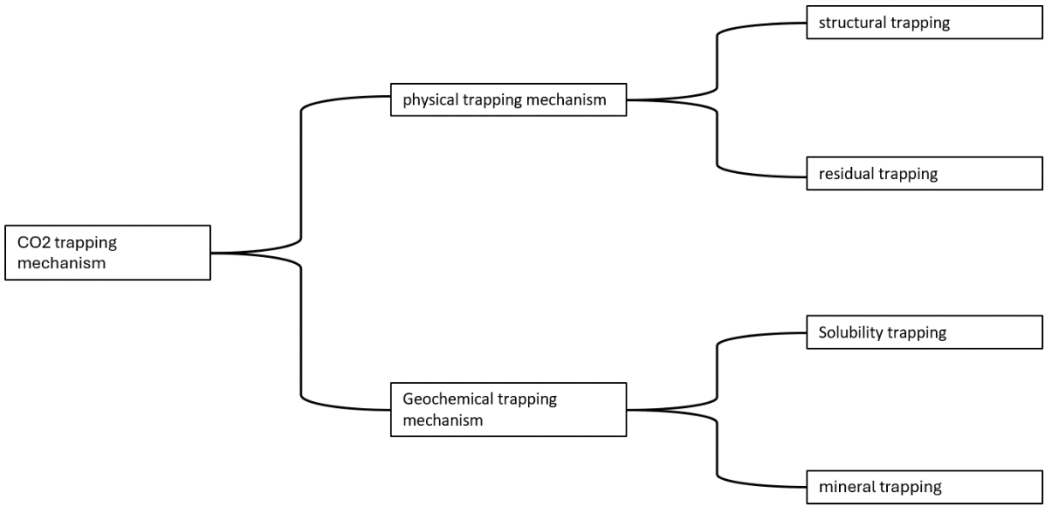

Figure 2.4: Trapping mechanism during GCS (adapted from [26])

2.3.1 Physical trapping

It refers to the retention of CO_2 plume within reservoir physical barriers, such as structural traps and faults, following injection into an aquifer. This process can be delineated into two categories: structural trapping, which pertains to the confinement within geological structures, and residual trapping, which involves the capture of CO2 in pore spaces through capillary forces.

A) Structural trapping: It typically represents the initial phase of trapping encountered in the context of geological carbon sequestration (GCS). At the start of the injection phase within the designated formation, the primary driving forces for the movement of CO_2 are viscous forces. At the end of injection, the gravitational and buoyancy forces dominate due to density difference between CO_2 and resident brine, prompting the upward migration of supercritical CO_2 through the porous and permeable rock [47].

As the CO_2 plume migrates upward, it encounters low-permeability and low-porosity zones, becoming trapped in structural features such as anticlines, faults, sealed discontinuities,

unconformities, and lithological transitions, as well as other geologic traps along its trajectory [48].

B) Residual trapping: The main forces governing the residual trapping mechanism are surface tension and capillary forces existing between the fluids present within the reservoir. After injection, the surface tension existing between the gas and the brine serves to impede the movement of CO_2 [49]. This causes a pressure differential known as capillary pressure at the transition zone where some of the CO_2 residual droplets are left behind in the pore spaces. This transition zone generally known as the capillary fringe could vary from extremely thin to several meters in height, thereby having significant influence on the plume shape and migration speed. Authors such as [50], [51] have considered residual trapping to be the more efficient physical trapping method as it does not have any direct effects on the structural integrity of the formation in short-term.

2.3.2 Geochemical trapping

It involves the transformation of CO_2 through a series of geochemical interactions with reservoir brine and rock, altering its physical and chemical state. As a result, CO_2 transitions from a mobile or immobile phase to a more stable form, enhancing long-term storage efficiency. This mechanism is critical for ensuring secure CO_2 sequestration and is categorized into solubility trapping and mineral trapping.

A) Solubility trapping: During the migration stage, dissolution becomes increasingly evident. As the plume expands and flattens, and a capillary fringe gradually forms, there is a notable increase in the interaction between brine and CO2 leading to the formation of weak carbonic acid which dissociates over time into H^+ ions and HCO_3^- ions [26]. It subsequently reacts with cations in the water, resulting in the formation of insoluble compounds, including $CaHCO_3$, $NAHCO_3$, $Mg(HCO_3)_2$ [8].

The brine saturated with CO_2 exhibits a slightly greater density compared to unsaturated brine. Consequently, gravitational instabilities arise within the vertical brine column, whereby CO_2-enriched brine, denser in nature, settles beneath the CO_2 plume, juxtaposed with a region containing lighter, unsaturated brine. Subsequently, this phenomenon may incite convection currents within the brine phase, characterized by the descent of the heavier, saturated brine and the ascent of unsaturated brine from below [52], [53].

B) Mineral trapping: It is the occurrence of chemical transformations wherein dissolved CO_2 has the potential to precipitate into carbonate minerals. This process is reliant upon various factors such as the chemical composition of pore water and rock, as well as the prevailing

temperature and pressure conditions within the storage aquifer. Such reactions have been observed to significantly impact the permeability and porosity of the rock matrix [54], [55]. This trapping process is perceived to progress at a comparatively gradual pace, as it takes place after or concurrently with solubility trapping. It was regarded as the most permanent method of CO_2 storage [56].

Among the four trapping mechanisms discussed in this section, numerous reports by organizations like the IPCC (Intergovernmental Panel on Climate Change, 2014) highlight mineral trapping as the most secure storage approach, albeit it unfolds over extended periods. In contrast, structural trapping, while short-term, is characterized by heightened susceptibility to geomechanical risks. Figure 2.5 depicts the four trapping mechanisms in order of increasing storage security and time for occurrence.

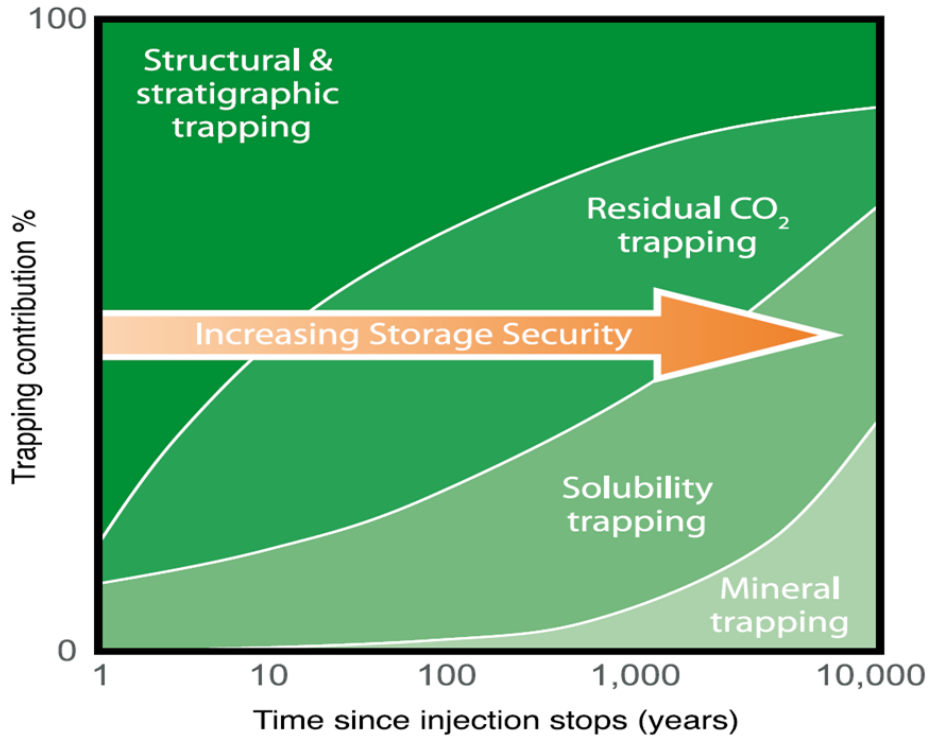

Figure 2.5: Performance of CO_2 trapping mechanisms over time [56].

For the effective trapping of CO_2, it must be injected in a supercritical state. At this state and assuming a hydrostatic pressure distribution within the basin, the gas is compressed to approximately 74 atm and 31.1ºC and subsequently injected at a minimum threshold depth of 800m [8], [34]. Under these conditions, (as illustrated in Figure 2.6**),** CO_2 exhibits characteristics of both a liquid and a gas, enabling it to flow like a gas, while possessing properties like that of a liquid [57], [58].

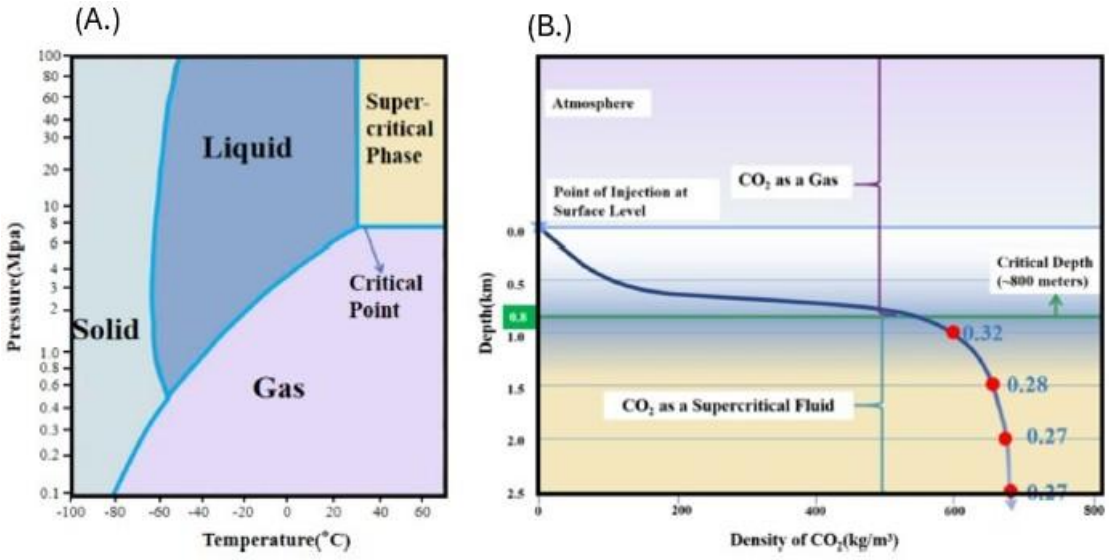

Figure 2.6: (a) Phase diagram and (b) density variation of CO_2 [8], [34]

Figure 2.6(a**)** the phase diagram of CO_2 showing the super-critical phase point at which the gas is injected into reservoir for safe storage [8]**,** Figure2.6(b.) is the variation of density with depth. Super-critical phase of CO2 exists at a minimum depth of 800m (The blue values indicate the relative amount of CO_2 present at various depths, using a surface volume of 100 as a reference point adapted from CO2CRC, [34]).

At the supercritical point, the density of CO_2 increases, but it remains significantly lower than the brine that typically ranges between 1200 – 2000 kgm^{-3} depending on brine salinity [26]. This density disparity initiates fluid interactions between the buoyant CO_2 and the resident brine solution, warranting an understanding of multiphase flow through porous media.

The subsequent section briefly reviews the fundamental theory of multiphase flow in porous media, the key geomechanical challenges associated with CO_2 injection, the theory of poromechanics, and how petrophysical properties of the rock matrix affect storage efficiency.

2.4 Fundamental Theory of Multiphase Flow in Porous Media.

Multiphase flow in porous media is a complex but fundamental aspect in geological carbon sequestration (GCS). When CO_2 is injected into a porous formation, it interacts with the resident brine and the rock through complex physical and chemical processes that significantly affect pore pressure, fluid saturation, and stress conditions [59], [60]. Capturing this behaviour accurately is essential for modelling pressure evolution and fluid saturation, during and after injection. This has been achieved in previous studies through the mathematical formulation of the well-established principles of mass conservation and Darcy's law for multiphase systems [61], [62], [63], [64].

$$\frac{\partial(\phi\rho_\alpha s_\alpha)}{\partial t} + \nabla \cdot (\rho_\alpha v_\alpha) = q_\alpha \tag{2.1}$$

$$v_\alpha = -\mathbf{K}\frac{k_{r\alpha}}{\mu_\alpha}(\nabla p_\alpha - \rho_\alpha \boldsymbol{g}\nabla z) \tag{2.2}$$

In **equation2.1,** α represents the water (w) phase and gaseous phase (g), CO_2, v_α is the Darcy velocity, ϕ is the rock porosity, ρ_α is the density of each phase, S_α is the saturation of the phases, and q_α is the source/sink of each phase.

The Darcy velocities of the phases in **equation 2.1** is obtained using **equation 2.2.** This is typically achieved by extending the Darcy's law to establish a relationship between the phase velocities and their corresponding pressures, by incorporating the relative permeability term. In **equation 2.2**, $k_{r\alpha}$, μ_α, and ∇p_α are the relative permeability, the viscosity, and the pressure gradient of the phases, **K** is considered the absolute permeability, z is the spatial coordinate in vertical direction and **g**, represents the gravitational drawdown term (For full derivation see Eq. (10.5) in [64]).

Although the governing equations and constitutive models describe the relationship between fluid pressure, saturation and permeability, their integration into reservoir simulators require modelling frameworks that take into consideration phase behaviour. The two widely adopted models in multiphase simulation are the black-oil model and the compositional model [61].

The black-oil model stems from the assumption that the chemical component can be aggregated into two pseudo-components (i.e. the water phase and gaseous phase) under surface conditions. The mass balance equation defined in **equation 2.1** is applied separately to each phase, with the saturation of each phase, Sα, and the pressure gradient of each phase, ∇pα, being the primary unknowns [61], [65]. Previous studies have used empirical relationships that link capillary pressure to saturation and relative permeability and saturation such as the Brooks-Corey model and Van Genutchen models proposed [66], [67]

Conversely, with the compositional model, where each component, including H_2S, N_2O, CH_4, CO_2, H_2O, and hydrocarbons, are modelled individually, enabling a more detailed representation of phase behaviour, chemical interactions, and multiphase dynamics within the subsurface. To accurately capture mass transfer between coexisting phases, the governing mass balance equation is reformulated accordingly in **equation 2.3.**

$$\frac{\partial}{\partial t}\left(\phi \sum_\alpha c_\alpha^\ell \rho_\alpha S_\alpha\right) + \nabla \cdot \left(\sum_\alpha c_\alpha^\ell \rho_\alpha \vec{v}_\alpha + \vec{\boldsymbol{J}}_{\boldsymbol{\alpha}}^{\boldsymbol{\ell}}\right) = \sum_\alpha c_\alpha^\ell \rho_\alpha q_\alpha \tag{2.3}$$

Here, c_α^ℓ denotes the mass or mole fraction of component, l in phase, α and $\vec{J}_\alpha^\ell$ represents the diffusive flux of component l in phase α defined by linear Fickian diffusion accounting for Brownian motion and dispersion between the components [61]. The diffusive flux parameter is obtained using **equation 2.4,** where $\mathbf{D}_\alpha^\ell$ denotes the effective diffusion coefficient of component l in phase α. The rest of the variables have been defined in equation 2.1.

$$\vec{J}_\alpha^\ell = -\rho_\alpha S_\alpha \mathbf{D}_\alpha^\ell \nabla c_\alpha^\ell \tag{2.4}$$

Both models have been employed in the simulation of CO_2 injection processes, with each offering distinct advantages and limitations. The black-oil models, as demonstrated by authors such as [15], [62], [68], [69], [70], [71], provide computational efficiency and have been adapted for CO_2 storage by incorporating empirical adjustments to PVT properties, yet they simplify phase behaviour by assuming fixed component distribution, limiting their applicability in systems where solubility, miscibility and compositional changes are significant. In contrast, the compositional model studied by [72], [73], [74], offer a more detailed representation of fluid behaviour, capturing component-specific interactions and phase transitions essential for modelling geochemical trapping mechanisms. However, these models are computationally demanding and require detailed input-data, which may not be readily available for all storage sites [70].

Overall, while compositional models are considered efficient for chemically reactive GCS environments due to their detailed representation of phase-behaviour, the black-oil models offer greater computational efficiency and are appropriate for preliminary screening and large-scale storage scenarios. Their simplified structure makes them advantageous for the evaluation of potential geomechanical effects at the early stages of CO_2 injection. For this reason, a black-oil modelling approach is used in this research.

While the mass balance equation, Darcy's equations, black-oil model, and compositional model form the foundation for reservoir simulators, they assume that the rock matrix is rigid. However, in the context of GCS, injection-induced pressure perturbation triggers rock deformation. This deformation induces a poroelastic response and pose potential geomechanical hazards such as fault re-activation and micro-seismicity [59], [60], [75] as suggested in **Figure 1.2.**

These geomechanical hazards (**figure 1.2**), especially the potential for fault re-activation and injection-induced micro-seismicity, are site specific and necessitates assessment to ascertain methods to mitigate seismic events and, enable the selection of an appropriate injection pressure margin for the secure storage of CO_2 [75], [76].

To address this risk during GCS, numerous studies have developed coupled hydro-mechanical (HM) [14], [62], [77], [78], thermo-hydro-mechanical (THM) [22], [79], or thermo-hydro-mechanical-chemical (THMC) [15], [23] models.

These coupled frameworks solve the fluid flow equation governed by the mass conservation and Darcy's law (**equations 2.1 and 2.2** respectively), mechanical deformation described by linear elastic or elastoplastic constitutive equations, heat transport through Fourier's law and energy conservation, and geochemical processes through advection-diffusion-reaction, capturing feedback among pore pressure, effective stress, temperature gradients and mineral reactions in deformable porous media [80].

The next section examines these coupled frameworks, the constitutive relationships necessary to effectively study fault reactivation and injection-induced seismicity during GCS and coupling schemes necessary to link the various frameworks.

2.5 Modelling Approaches for Injection-Induced Micro-seismicity in GCS: From HM to THMC Frameworks

Injection-induced seismicity during GCS, caused by pressure, stress, thermal and chemical alterations in the subsurface have garnered significant attention in the research community lately. As a result, predictive numerical models in simulating the physical mechanisms leading to fault slip and stress build-up, has evolved and can be grouped into three (3) main categories: 1.) hydromechanical (HM), 2.) thermo-hydro-mechanical (THM), and 3.) thermo-hydro-mechanical-chemical frameworks. Each framework incorporates more coupling, with varying degrees of computational requirements.

2.5.1 Hydromechanical (HM) framework

HM coupling during GCS is observed when injection-induced pore pressure diffusion reduces effective normal stress on pre-existing faults, triggering fault reactivation and potentially micro-seismic events. This occurs as pressure builds up and propagates through the formation, under the assumption of constant fluid density [81].

To understand the two-way coupling scheme that exist between the rock material and the injected fluid, Biot in 1941 [18] proposed the Biot's theory of poroelasticity. This theory builds on the Terzaghi's one-dimensional consolidation theory [82], which initially introduced the concept of effective stress and the role of pore pressure column in saturated soils. The Terzaghi consolidation theory was however limited to one-directional soil columns, assuming deformation in only one direction. Biot reformulated this theory by extending it to a three-

dimensional framework, accounting for volumetric deformation of the pores and flow of fluids according to Darcy's law [18].

The Biot's theory of poroelasticity has facilitated the modelling of complex three-dimensional (3D) geological formations by enabling the formulation of equations that remain valid for arbitrary loads that vary over time.

Building on this theoretical formulation, Biot's theory of poroelasticity is expressed mathematically through a coupled set of partial differential equations that link multiphase fluid flow and mechanical deformation. Assuming a black-oil model, the fluid flow is governed by the mass balance equation and the Darcy flow equation described in **equations (2.1) and (2.2)** respectively. The mechanical deformation of the solid is represented by the linear momentum equation as shown in **equation (2.5).** This equation relates mechanical deformation, stress, strain, external forces acting on the solids, and assumes a quasi-static equilibrium. A full derivation of **equation 2.5** is presented in the foundational paper proposed by [18].

$$\nabla \cdot \boldsymbol{\sigma} + \rho_b \boldsymbol{g} = \mathbf{0} \qquad (\mathbf{2.5})$$

Here, $\boldsymbol{\sigma}$ is the stress tensor, $\nabla\,(\cdot)$ is the divergence of the stress tensor, ρ_b represents the bulk density of the material.

The ability of HM models to simulate injection-induced stress perturbations, fault reactivation and micro-seismic events, is reliant on governing equations presented by **equation (2.1), (2.2), (2.5)** and the constitutive relationship used to describe the stress-strain relationship of the porous material.

A.) Linear elastic constitutive relationship: Several early studies [75], [83], [84], applied a linear poroelastic model to investigate the coupled hydromechanical effects of CO_2 injection on the subsurface stress fields, to the In Salah, Algeria project. In their models, the constitutive relationship used to link stress-strain was defined by the Hooke's law in **equation 2.6.**

$$\boldsymbol{\sigma} = C : \boldsymbol{\epsilon} \qquad (2.6)$$

Here, C is the fourth-order stiffness tensor representing the material properties, $\boldsymbol{\sigma}$ is the stress tensor, and $\boldsymbol{\epsilon}$ is the strain tensor.

By applying this method to the In Salah formation in Algeria, the authors found that after three years of injection, this model captured a pressure driven volumetric strain and geomechanical surface uplift, revealing a significant stress redistribution within the reservoir and the caprock.

Verdon et al. also employed a quasi-static linear elastic analysis [85], [86] in both studies. They provided a correlation between the HM model and observed micro-seismic events recorded at the Krechba field, by integrating seismic data with geomechanical simulations. This approach contributed to the validation of HM model, by allowing a comparison between simulated stress changes and actual micro-seismic observations during CO_2 injection.

These studies collectively highlight the application of quasi-static, linear elastic HM models in accurately predicting micro-seismic responses during CO_2 injection. While they provide information into the stress alteration and potential fault reactivation due to fluid injection, it is important to note that the linear elasticity assumes reversible deformation and may not accurately capture all aspects of fault deformation such as fault slip or plastic deformation. In addition to this, a major gap in these studies is that the authors did not consider the influence of geological layering and mechanical anisotropy, which in respective recent numerical and experimental studies by [87], [88] have shown to significantly influence stress redistribution and seismicity localization.

B.) Elastoplastic constitutive relationship: The elastoplastic constitutive laws are important in simulating mechanical failure and seismicity. These laws allow for the representation of irreversible deformation and provides a failure criterion to study fault slips. During injection of CO_2, once the stress on the faults exceeds the critical yield point, the fault transitions into an irreversible plastic deformation as depicted by Figure 2.7.

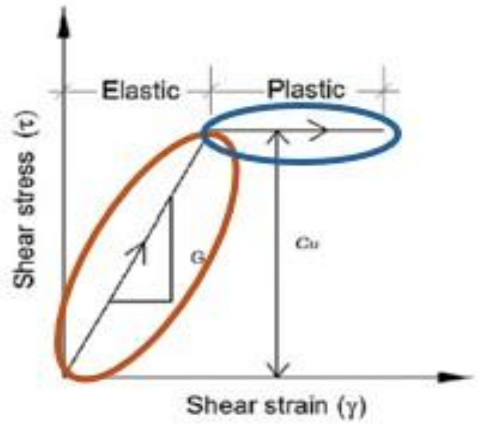

Figure 2.7: Shear stress vs strain curve illustrating elastic (linear) region represented by the orange ellipse, and the plastic deformation region represented by the blue ellipse (modified from [89]

At this point, the total strain, **de**, on the fault is divided into elastic strain, $\delta\mathbf{e}^E$ and plastic strain, $\delta\mathbf{e}^P$ and is presented mathematically by **equation 2.7** [90].

$$d\mathbf{e} = \delta\mathbf{e}^E + \delta\mathbf{e}^P \tag{2.7}$$

The most used elastoplastic laws in the study of GCS are the Mohr-Coulomb failure criterion and the Drucker-Prager.

B1.) Mohr-Coulomb failure criterion: Numerically the Mohr-Coulomb failure criterion has been used by several authors such as [91], [92], [93], [94], [95], [96], [97], [98], [99] in modelling the likelihood of shear failure within the formation and across existing faults, resulting in some micro-seismic activity. In the investigations of these authors, they noticed that for low-permeability and low-porosity rocks, the injection of CO_2 into the subsurface, raises the reservoir pressure thereby reducing the effective stress. The intersection of the Mohr circle as seen in Figure 2.8**,** leaves the storage system prone to brittle failure.

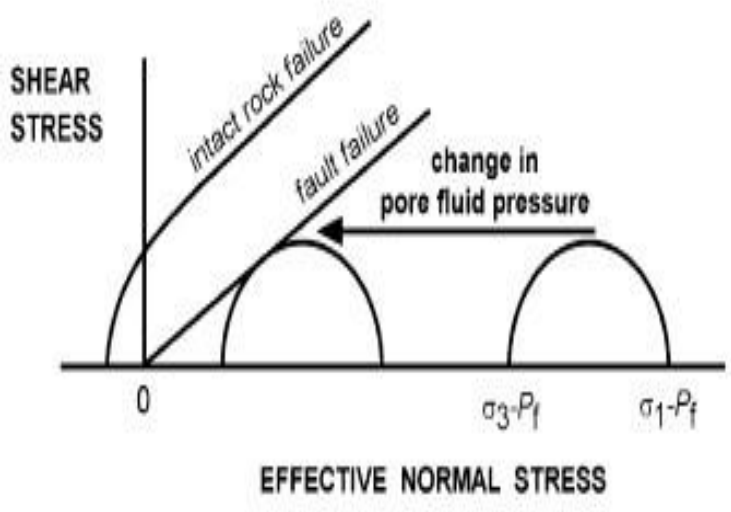

Figure 2.8: Mohr circle figuratively representing the effect of increasing pore fluid pressure on fault stability (adapted from [99])

Cappa and Rutqvist [62] improved on their previous study on linear elasticity on the In Salah, Algeria project by incorporating the Mohr-Coulomb failure criterion into a similar quasi-static HM framework to study a potential fault slip. Using the Mohr-Coulomb mathematical expression defined by **equation 2.8** that relates shear stress to normal stress, and assuming a cohesionless fault (i.e. C = 0), they found that even a small increase in pore pressure could trigger micro-seismicity in critically stressed faults. In this situation, the fault slipped as soon as the ratio of shear stress to effective stress was greater that the coefficient of friction.

$$\tau = c + \sigma_n \tan\phi \tag{2.8}$$

Here, τ represents the shear stress on the fault plane, c is the cohesion describing the shear strength, ϕ is the friction angle and σ_n is the normal stress.

While the Mohr-Coulomb failure criterion has been used a lot in study of fault reactivation and micro-seismicity, it is suitable only for brittle and not ductile materials [98]. One significant disadvantage of using the Mohr-Coulomb failure criterion in geotechnical characterization studies is that it oversimplifies the actual behaviour of soils, particularly under complex loading conditions. The Mohr-Coulomb model assumes a linear relationship between shear strength and normal stress, as **equation (2.8)** suggest. This linear approximation does not accurately reflect the nonlinear and pressure-dependent nature.

B2.) Drucker-Prager criterion: These authors [100], [101], [102] used this criterion in modelling the shear stress in the pre-existing faults during GCS. This model is especially effective for modelling fault reactivation in formations where material strength is sensitive to confining pressure, such as shales and cemented sandstone. The authors adopted the Drucker–Prager yield criterion, f, with a non-associated plastic potential function g, explicitly incorporating the dependency on mean effective stress p', as formulated in **Equation (2.9)** and **(2.10)** respectively.

$$f = q - M_{\phi} p' - c_{\phi} \tag{2.9}$$

$$g = q - M_{\psi} p' \tag{2.10}$$

Here, $M_{\phi} = 6\sin\ \phi/(3 - \sin\ \phi)$, is the term that matches the yield function to Mohr-Coulomb friction angle, q is the deviatoric stress term, $M_{\psi} = 6\sin\ \psi/(3 - \sin\ \psi)$ is a non-associative parameter depending on the dilation angle ψ, and Cϕ matches the yield function to the Mohr Coulomb cohesive strength.

The Drucker–Prager failure surface in Figure 2.9A, is depicted as a cone, reflecting its sensitivity to both shear and mean (hydrostatic) stress.

This failure criterion is preferred in this case because the Drucker-Prager cone-shaped model that approximates the Mohr-Coulomb criterion for shear failure is circumscribed by the Mohr-Coulomb surface, providing a smooth yield surface, and avoiding discontinuity in the yield criterion as shown in Figure 2.9B [102].

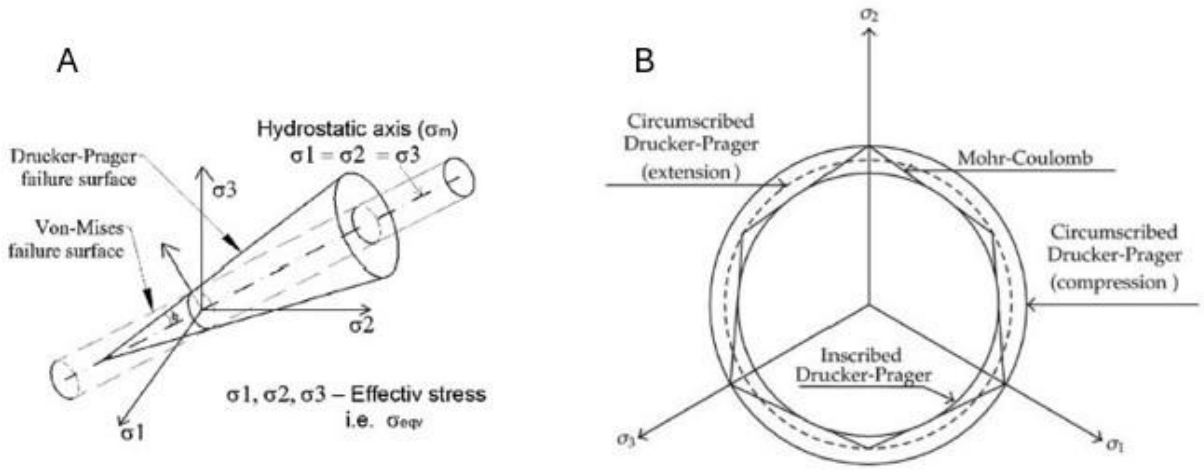

Figure 2.9: a.) Drucker-Prager failure surface model represented as a cone; b.) Drucker-Prager model circumscribed by Mohr-Coulomb surface (adapted from [102], [103])

While both Mohr–Coulomb and Drucker–Prager criteria have effectively been applied in GCS studies to model fault slip and micro-seismicity. The choice between them often depends on the specific geological conditions and the desired balance between model accuracy and computational efficiency. Mohr–Coulomb is advantageous for its simplicity and effectiveness in modelling brittle failure, making it suitable for preliminary assessments. In contrast, Drucker–Prager's smooth failure surface and adaptability to ductile behaviour make it preferable for complex simulations requiring detailed stress analysis. For this research, we adopt the Drucker-Prager failure criterion because we consider our depleted reservoir to contain a considerable amount of shale and cement, and these materials are considered pressure-sensitive.

Although THM and THMC models provide a comprehensive framework for analysing CO_2 injection effects, the HM models have proven to be effective in investigating injection-induced micro-seismicity. This is relevant during the initial stages of injection, where fault reactivation is predominantly driven by pore pressure buildup and effective stress alterations. This is evident in the studies by [15], [22], [23], [62], [102], [104], [105]

HM models offer computational efficiency and sharper resolution of the dominant mechanisms, making them highly suitable for early warning and risk assessment in geological carbon storage applications. This was highlighted in the numerical studies carried out by [106], [107] which modelled the micro-seismic response to CO_2 storage. Their simulations revealed that within three (3) years of injection, a micro-seismic event with magnitude, M_w of 3.4 could be triggered. This value is comparable to the Basel Geothermal Project, where a similar magnitude led to the suspension of operations [108], [109]. These findings clearly highlight the importance of HM

analysis, over THM and THMC models, in the initial stages of simulation. Furthermore, HM models offer advantages in computational efficiency, making it more practical for site-specific risk assessment and micro-seismic monitoring.

2.5.2 Thermo-hydromechanical (THM) framework

The THM models extend the HM framework by incorporating the effects of temperature on injection-induced fault reactivation and micro-seismicity. This model has been studied by authors such as [22], [23], [78], [79], [110], [111] by coupling the heat transport through the energy conservation equations, Fourier's law, expressed mathematically by **equation (2.11 and 2.12)**, respectively, with the mass conservation, Darcy flow and linear momentum equations, previously defined in **equations (2.1, 2.2, 2.5)**

$$\int_{\Omega} \frac{\partial}{\partial t}\left[\phi U_f + (1-\phi)U_s\right] + \beta_s K_s T_0 \frac{\partial(\nabla \cdot \boldsymbol{u})}{\partial t} dx + \int_{\partial\Omega} (\boldsymbol{w} + \boldsymbol{q}) \cdot d\boldsymbol{x} = \int_{\Omega} q_T dx \qquad (2.11)$$

$$\boldsymbol{q} = -\kappa_e \nabla T \qquad (2.12)$$

In **equation 2.11**, the internal energy of the solid phase is expressed as $U_s = \rho_s c_s T$, where c_s denotes the specific heat capacity of the solid matrix, ρ_s is the density of the solid matrix and T represents the temperature term. For the fluid phase, a low-enthalpy approximation is employed, wherein the internal energy is represented as $U_f = \rho_f h_f$, with enthalpy, $h_f = c_f T$, with c_f being the fluid's specific heat capacity. βs represents the volumetric thermal expansion, Ks the bulk modulus of the solid, T_0 the original temperature in the reservoir, $\boldsymbol{u}$ is the displacement term. The model incorporates a thermoelastic dissipation term, which captures the influence of mechanical deformation, specifically the elastic volumetric term on local thermal regime. Importantly, the total heat transfer is represented by both $\boldsymbol{w}$ which is the advective flux term and equation 2.12 which is the diffusive Fourier flux, $\boldsymbol{q}$. κ_e in **equation 2.12** is the effective heat conductivity. For a full derivation of these equations, refer to [111], [112], [113], [114].

Although THM-coupled models offer a more integrated assessment of subsurface stress conditions by accounting for thermal disturbances from cold CO_2 injection, evidence from [21], [62], [115] suggest that the thermal effects typically manifest over extended periods. As a result, their influence on the stress path is delayed, compared to the immediate hydraulic impacts captured by HM models. Additionally, THM simulations demand a broader set of input parameters including thermal and thermoelastic properties, increasing model complexity and reducing computational efficiency. This makes HM frameworks more pragmatic for early-phase

analysis and real-time monitoring where rapid modelling and reservoir characterization decisions are essential.

2.5.3 Thermo-hydro-mechanical-chemical (THMC) framework

Coupled THMC models in GCS, represent the most comprehensive framework for analysing complex environments where chemical reactions and thermal gradients influence the CO_2 storage repositories. These models have been studied by [22], [23] and are advantageous for simulating compositional reservoir systems and evaluating long-term trapping mechanisms such as mineral and solubility trapping mechanisms seen is **Figure 2.5.** Though they are considered the safest trapping mechanisms, it falls outside the scope of our research, as our research focuses on black-oil models, assuming no interaction between the fluids.

Furthermore, the THMC models require an extensive array of input parameters, making it computationally costly. For this reason, HM models are considered more appropriate when studying fault reactivation and potential injection-induced micro-seismicity during the early CO_2 injection phase.

Consequently, the subsequent section reviews the coupling schemes that have been employed in studying the hydromechanical effects due to CO_2 fluid injection into reservoirs, with focus on fault reactivation and micro-seismicity.

2.6 Coupling Schemes for Linking Hydro-Mechanical (HM) Model.

In linking the hydraulic sub-problem and the geomechanical sub-problem, various coupling schemes have been proposed. The most used techniques include a.) explicitly coupled, b.) iteratively coupled scheme, c.) fully coupled scheme [116], [117].

2.6.1 Explicitly coupled scheme.

This scheme (also called loose coupling scheme) applied in foundational studies by [116], [118], is an established approach in solving hydraulic and mechanical problems in reservoir geomechanics. This method decouples the hydraulic and mechanical sub-problems, by solving each independently within discrete time steps. The hydraulic simulator solves the mass balance and Darcy's law equations **(equations (2.1, 2.2)),** generating a pore pressure field that is subsequently passed as a load to the geomechanical solver. This enables the computation of rock displacements and stress distribution at specific time intervals. This considered an appealing aspect due to the significant reduction in computational time which is spent mostly on evaluating the displacements in the mechanical sub-problem. Although this method is good in terms of computational efficiency, it assumes a unidirectional influence, neglecting the

effects geomechanical deformation potentially has on fluid flow. Nonetheless, for early-stage analysis or where deformation-induced permeability changes are minimal, this scheme provides a robust modelling strategy. This is demonstrated in a comparative analysis which evaluated the performance of explicit coupled scheme, iterative and fully coupled schemes. Their analysis showed that, during the initial stages of injection, the pore pressure produced by the explicit approach were quite similar to those of the iterative schemes. This finding underscores the advantage of using explicit coupling scheme for early time analyses, where mechanical deformation has yet to significantly influence fluid flow dynamics.

2.6.2 Iteratively coupled scheme.

For this approach, the multiphase flow set of equations and the geomechanics set of equations are solved sequentially for each time step. The appeal of this methodology is that it allows for the use of separate simulators to address the fluid flow and the geomechanics sub-problem of equations. This approach has been used by researchers such as [15], [96], [119], [120], [121] and found it to be unconditionally stable for fixed-stress analysis only. Authors such as [122] evaluated the stability and convergence for sequential approach by using an implicit approach, whereby the analysis was split into two. That is, the fixed-stress sequential split and fixed-strain sequential split. To evaluate the stability of the fixed-stress and fixed-strain schemes, they employed the Von Neumann method and found that fixed-strain is conditionally stable while the fixed-stress split scheme is unconditionally stable. The authors went further to investigate the convergence rate of the fixed-strain and fixed-stress methods. By applying a matrix-based analysis for the backward Euler method in time, it revealed that the approximate solution of the fixed-strain split is unlikely to converge within a defined number of iterations, unlike, the fixed-stress method which offered a superior accuracy, assuming the equations are well-defined. The results from the sequentially coupled approach when compared to that of the fully implicit method are equivalent if a strict convergence tolerance is applied. The drawback to this method is its slow non-linear convergence rate, particularly under conditions of high-pressure gradients [122], [123]. While this coupling scheme has been effectively applied to flow and geomechanics problems involving fracture propagation in porous media, its use in analysing wave profiles induced by CO_2 injection remains limited. This is primarily due to the extensive data requirements and significant computational cost associated with implementing the iterative coupling framework in displacement-velocity-pressure (u-v-p) analysis.

2.6.3 Fully coupled scheme.

The fully coupled scheme guarantees unconditional stability and is widely regarded as the most appealing coupling scheme when the discretized mathematical sub-problems are well defined

[116], [119]. In this approach, the set of non-linear equations are solved simultaneously, employing the Newton-Raphson scheme. This approach has been used by various authors such as [124], [125], [126], [127], [128]. These authors all found that the fully coupled scheme offers superior accuracy when compared to the other coupling schemes for capturing the interactions between pore pressure and deformation, but it demands extensive code development, and it is considered computationally costly.

Overall, while fully and iteratively coupled schemes provide more accuracy in complex hydro-mechanical (HM) models, loose (explicit) coupling remains an essential approach for early-stage displacement-pressure (u-p) analysis, particularly when geomechanical influences on fluid flow are limited. This is because of its ability to decouple sub-problems and reduce computational time.

The HM analysis depends on robust numerical discretization methods which are essential in solving coupled equations and capturing the effects of CO2 fluid injection on reservoir geomechanics.

2.7 Numerical Discretization Approaches for Coupled HM Processes

Geomechanical challenges that involve fractured rock masses are treated as discrete systems, given the heterogeneity of their geometries. Consequently, numerical methods are considered the appropriate approach for obtaining reliable approximations in geomechanical analysis. These numerical approaches are typically classified into three main categories, namely:

1.) continuum methods, 2.) discontinuum methods, and 3.) hybrid continuum-discontinuum methods [129].

The continuum method consists of the finite volume method (FVM), finite difference method (FDM), finite element method (FEM), boundary element method (BEM), and the new method known as the virtual element method (VEM). For the discontinuum method, it comprises of the discrete element method (DEM), discrete fracture network (DFN), and the discontinuous displacement analysis (DDN). Finally, the hybrid continuum method consists of the hybrid FEM/BEM, hybrid DEM/DEM, and hybrid FEM/DEM [130].

To characterize the geology of a reservoir, models are constructed that aim to represent the large-scale heterogeneity found within the reservoir rock. This is done by assigning macroscopic petrophysical properties derived from the continuum assumption. Thereby making continuum discretization techniques most appropriate for HM analysis [61].

Based on the variety of continuum methods, researchers have either used the FVM, FEM, FDM, VEM or a combination of these methods, in analysing the effects of fluid injection on geomechanics.

2.7.1 Finite difference method (FDM) for coupled HM model.

The FDM is considered one of the oldest and easiest methods used in solving differential equations related to fluid flow and heat transfer. In this method, the conservation equation is discretized to an algebraic form using the Taylor's series expansion. The first derivative is approximated by the forward Euler or backward Euler equations, while higher-order derivatives are approximated by central differences. The system of equation obtained are then solved either iteratively or directly [131]. It is popular because it is considered quite easy to implement on structured grids, however, when irregular shapes or highly variable domains are used especially when applied to fluid flow in complex reservoir geometries, the accuracy of the simulation drops off [132].

2.7.2 Finite volume method (FVM) for coupled HM model.

The FVM is a robust numerical method for obtaining approximate solutions from partial differential equations (PDEs), in computational fluid dynamics (CFD). This done by partitioning the domain into discrete control volumes and applying conservation laws to the centre of each grid point as seen in **Figure 2.10**. This method ensures that the flux of a conserved quantity, is preserved across the boundaries of neighbouring cells by applying various approximations such as two-point flux approximation (TPFA) and multi-point flux approximation (MPFA) [61].

In FVM, the differential equations are converted into algebraic equations and integrated over each control volume. It is particularly useful when using irregular grids and boundary conditions peculiar with real-life geological problems. It is this flexibility and reliability, which makes FVM the most preferred method when analysing data that involves modelling of fluid flow through porous media.

Figure 2.10 illustrates the discretization of a two-dimensional computational domain using the finite volume method (FVM). The grid is divided into small control volumes (highlighted in grey), each centred around a primary grid point (i, j). The variables, ψ, are evaluated at the centre of each control volume. The indices i and j represent the spatial location along the x and y axes, while Δx and Δy denote the spacing between grid points in each direction.

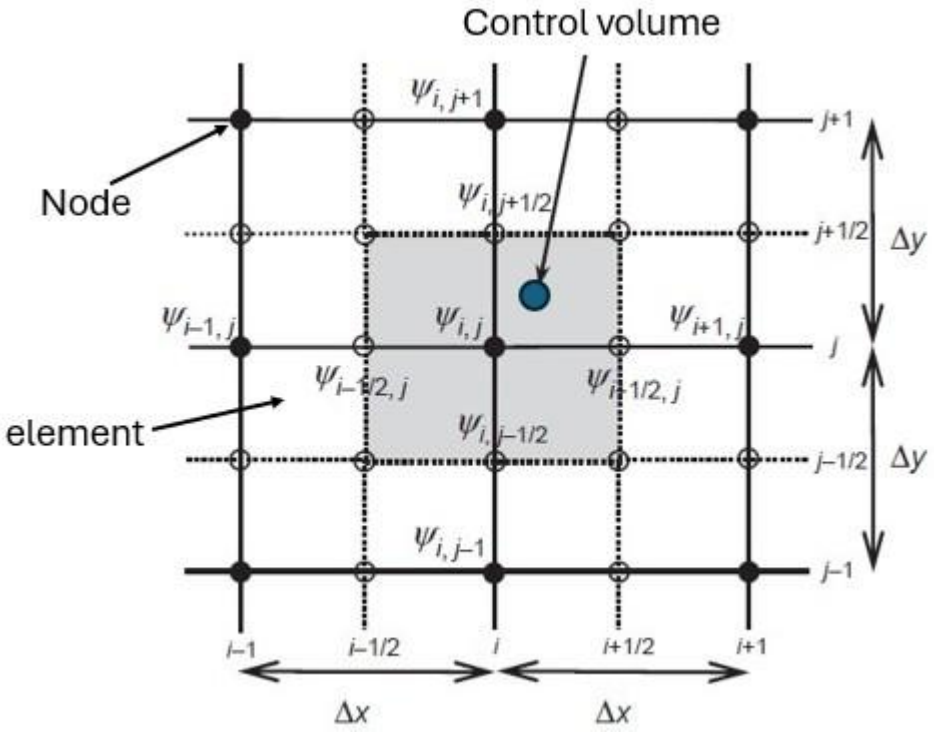

Figure 2.10: Schematic of FVM grid with control volumes.

2.7.3 Finite element method (FEM) for coupled HM model.

The FEM is extensively used in solid mechanics, computational fluid dynamics and related disciplines for resolving partial differential equations that govern phenomena such as earthquake mechanics and fluid flow in porous media. While other methods employ structured grid patterns, FEM partitions the domain into a mesh comprising of elements, which may adopt various geometries such as triangles and quadrilaterals in two dimensions or tetrahedra and hexahedra in three dimensions as seen in Figure 2.11**.**

Within the FEM framework, the governing equations are reformulated into their weak or variational forms, and each individual element is associated with a set of shape functions which helps approximate the solution locally at each node (represented in Figure 2.11 by local numbering). By integrating the variational form of the equations over the elements and assembling the global matrix, along with the relevant boundary conditions, a global system of algebraic equations is constructed. This system is typically solved using robust numerical algorithms, such as the Newton-Raphson method or other iterative solvers, to obtain the field variable distributions throughout the domain (a complete explanation of the FEM could be found in [133]).

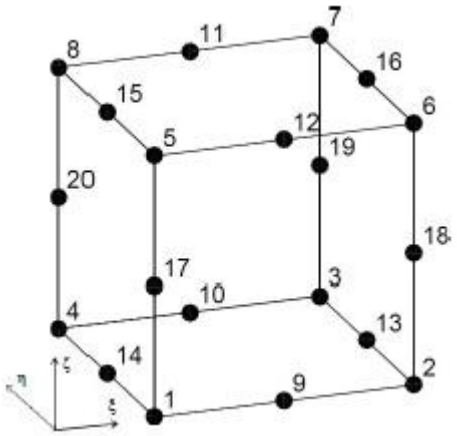

Figure 2.11: Local numbering of finite element nodes for hexahedral 3D domain.

2.7.4 Virtual element method (VEM) for coupled HM model.

The VEM is a significant numerical tool for solving partial differential equations. It emerged in 2012, building on the advances in mimetic finite difference approaches to achieve accuracy for higher-order elements [134]. Research interest grew quickly when it was seen that VEM fits naturally within the established variational framework of finite elements methods (FEM), leveraging similar principles of minimizing over discretized function spaces, allowing for a broader set of basis functions than the traditional piecewise polynomials used in FEM. The advantage of this method is that it offers a great flexibility and precision for higher-order elements, but the mathematical formulation including its ability to map the basis function from a complex function space onto a simpler one is more intricate compared to the FEM, making the FEM suitable for geomechanical analysis [134], [135], [136]. A full overview of this method and its application can be found in [137].

Overall, while these numerical discretization methods form the basis for solving coupled HM models, their implementation is done through software or codes that have proven to solve coupled flow and geomechanical problems related to GCS, with focus on fault reactivation and micro-seismicity. **Table 2.1** provides a comparative overview of some numerical simulators used to model the flow of CO_2 in depleted reservoirs, highlighting the numerical discretization approach incorporated into each software and the coupling technique applied by the various research groups in solving the governing equations.

Table 2.1 Overview of the numerical simulators used for coupled multiphase flow and geomechanics.

Software	Numerical discretization	Coupling technique	Reference
MATLAB Reservoir Simulation Toolbox	FVM-VEM	Fully coupled scheme	[138], [139], [140]
ECLIPSE – PETREL VISAGE	FDM-FEM	Fully coupled scheme	[141], [142]
General Purpose Research Simulator (GPRS) – Pylith	FVM-FEM	Fixed-stress iterative coupling	[119]
Computer Modelling Group Ltd – Geomechanical modelling Software (CMG-GEM)	FDM-FEM	Fixed-stress iterative coupling	[143], [144]
TOUGH -FLAC3D	FVM-FDM	Iterative coupling	[62], [75], [105], [145]
ECLIPSE-VISAGE	FDM-FEM	Explicit coupling	[146]

The simulators listed in **Table 2.1** highlight the range of numerical approaches and coupling strategies that have been used in HM modelling in GCS. Building on this summary, the following section critically reviews the key studies that have used these frameworks in modelling the potential of fault reactivation and micro-seismicity during to CO_2 storage.

2.8 Modelling Techniques for Fault Implementation and Micro-seismicity

Faults play a critical role in controlling the geomechanical response of subsurface formations during CO_2 injection. When fluids are injected into the reservoir, the pressure and stress alterations extend over a radius of more than 100 km, intersecting some major and minor faults and potentially triggering fault reactivation [62]. It is therefore imperative to accurately represent the faults in HM models aimed at evaluating fault reactivation and the potential for injection-induced seismicity [147].

2.8.1 Modelling approach for fault implementation

Given the structural complexity of fault zones, no single modelling approach can capture the full range of fault behaviours. The selection of a fault modelling strategy is influenced by the fault's scale and the specific objectives of the simulation.

A.) Discontinuity fault modelling approach: With this approach, the fault is represented explicitly with lower-dimensional elements than the host computational grid. That is for a two-dimensional (2D) model, a one-dimensional (1D) is used to represent the fault, and for a three-dimensional (3D) model, a two-dimensional (2D) surface is used to represent the fault as seen in Figure 2.12(a & b)**.**

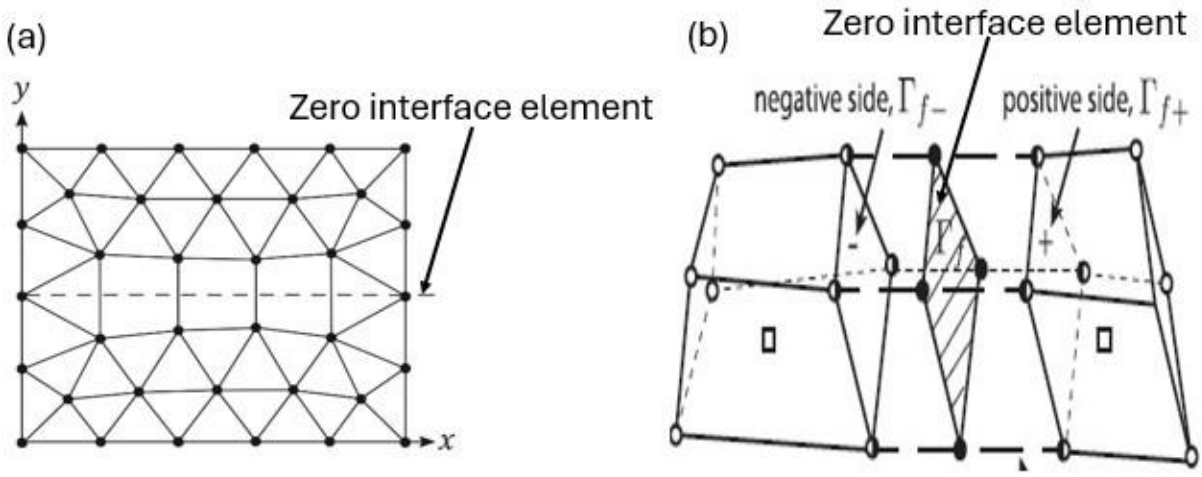

Figure 2.12: (a) 2D Model with fault represented as a line, (b) 3D model with fault as a 2D surface (modified from [119])

The material properties of the fault are set to values equivalent to that of the host rock, if not when the zero-interface element has an extremely high Young's modulus when compared to the surrounding rock, this leads to numerical instability. The implementation of this method has two important aspects: 1.) the finite element grid discretization of the host rock must conform precisely to that of the fault geometry, 2.) the fault zone requires triplicate nodes at the contact plane between the host rock and the fault [119], [148]. That is, Elements that have nodes lying on the fault surface require special treatment. Each node located on the fault is replicated three times: one as a "+" node on the positive side, one as a "–" node on the negative side, and a third as a Lagrange node positioned between them. The nodes on either side record the displacements, u_1 for the positive side and u_2 for the negative side, while the Lagrange node captures both the Lagrange multiplier (l) and the fault slip (d). All three nodes occupy the same

location in the initial mesh, which means that elements representing the fault itself are considered to have zero thickness as seen in Figure 2.12b.

This method has been used by [65], [119], [149], [150], [151], [152] in which they represented the faults as contact elements. These elements transfer both normal and shear stresses and accurately captured fault slip behaviour, which was governed by cohesion and friction angles. Once the local stress state exceeded the failure criterion, relative movement was initiated between the paired nodes across the fault interface [148].

Overall, the explicit representation of faults as discontinuities offers an advantage in capturing localised and sudden displacements occurring during a fault slip. It is also very important when implementing fault reactivation models such as the rate and state dependent model or slip weakening model (which is beyond the scope of this review since we are not implementing a discontinuum modelling approach). However, the fact that this method requires triplicate nodes at the contact plane makes it computationally intensive and can lead to numerical instability particularly when dealing with dynamic fault rupture.

B.) **Continuum fault modelling approach:** In the continuum approach, the fault model is represented implicitly. That is the fault network is modelled as a distinct continuum superimposed on the rock matrix with different material properties as seen in Figure 2.13(a & b) [65], [148].

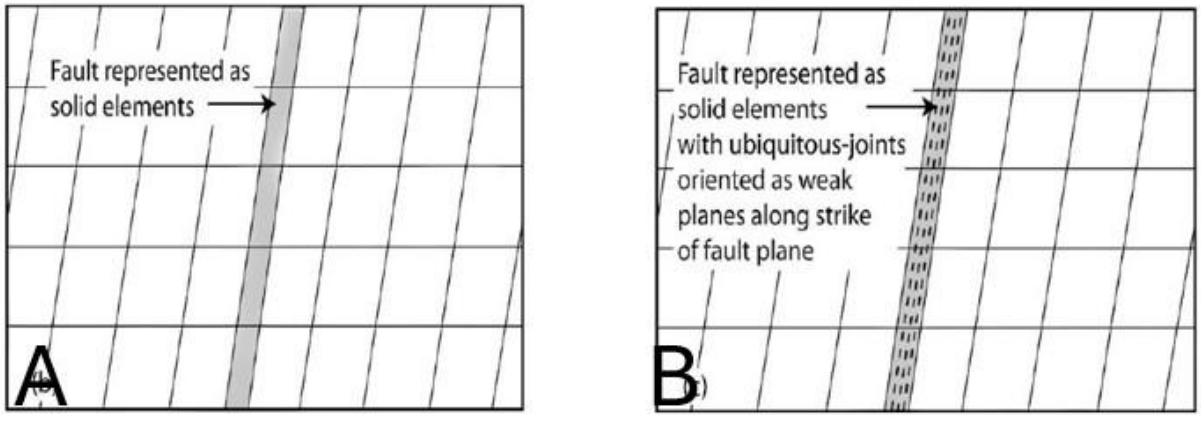

Figure 2.13: a) Fault as a finite-thickness element, b) fault as finite-thickness element with ubiquitous joints represented as weak planes along the strike (modified image from [105])

This method has been used by [62], [65], [96], [105], [148], [153], [154] and unlike the explicit faults which are represented as zero-thickness elements, in the continuum model they use standard solid elements allowing a comprehensive representation of fault mechanics.

An advantage of this approach is that it enables the application of a wide range of constitutive laws from an isotropic linear elasticity [84], [155], [156], [157] to advanced elastoplastic models [62], [158], [159], [160] or viscoelastic formulations [161], depending on the level of mechanical complexity.

Notably, it offers the capability to model fault zones as ubiquitous jointed media, effectively capturing the strongly anisotropic behaviour typical of highly fractured damage zones. These zones, often characterized by intense micro fracturing, vary significantly in thickness and mechanical response based on factors such as lithology, pore pressure, and deformation history.

As a result, modelling faults as a continuum and with volumetric elements offers greater flexibility and lower computational implementation, particularly in scenarios involving stress redistribution and time-dependent deformation during CO_2 injection.

While accurate fault representation is critical for capturing fault slip behaviour, it is equally important for understanding its seismic consequences. Once reactivation occurs, these faults often become sources of micro-seismicity. Therefore, to assess the risks associated with CO_2 storage, it is necessary to examine how fault slip translates into seismic energy release. The subsequent sub-section reviews how micro-seismic responses are modelled, with emphasis on the limitations of current approaches and emphasizing the need for more dynamic analysis.

2.8.2 Modelling approach for micro-seismicity

Injection-induced seismicity occurs when elevated fluid pressures trigger the release of accumulated strain energy within, the subsurface. These events are not confined only to tectonically active regions, but they can also arise in geologically stable intraplate settings where pre-existing faults are critically stressed [162]

Despite improved understanding of the underlying theory, predicting the injection-induced seismic response to subsurface industrial operations remains a significant challenge. [163] therefore proposed a volume-based empirical theory in forecasting seismic moment, M_o, and the seismic magnitude, Mw which are both key parameters in evaluating the impact from earthquakes.

In the empirical theory proposed by [163], [164], the seismic moment, M_0, that typically describes the overall size of the earthquake was evaluated using **equation 2.13**.

$$M_0 = G \cdot A \cdot d \tag{2.13}$$

Where G is the shear modulus of the fault, A is the area of the ruptured surface expressed in square meters (m^2), and d is the slip distance in meters (m) [130].

To scale the seismic moment, M_o, proposed by [163] to a seismic magnitude, M_w, they referred to the work published by [165] who proposed a standard regression relation between body waves, m_B, and surface wave magnitude, M_s, given by **equation (2.14)** and between body waves, m_B, and released seismic energy, E_s, given by **equation (2.15)**

$$m_B = 0.63M_S + 2.5 \tag{2.14}$$

$$\log E_S = 2.4m_B - 1.2 \tag{2.15}$$

However, with a change in the medium period broadband for measuring body-wave magnitudes, m_B, to the use of United States World-Wide Standard Seismograph System (USWWSSN) in the 1960s, Kanamori [166] updated his research to get a direct relationship between released seismic energy, E_s, and surface wave magnitude, M_s, defined by **equation (2.16),** which is sometimes referred to as the "Gutenberg-Richter" energy magnitude relationship

$$\log E_S = 1.5M_S + 4.8 \tag{2.16}$$

However, several authors such as [167], [168] found that **equation (2.16)** is only valid for moderate earthquakes and the surface-wave magnitude M_s, tend to saturate for very large earthquakes, thereby underestimating the real size of the earthquake.

Therefore, to overcome this shortcoming, Kanamori[164] found a relationship between seismic moment, M_o, and seismic energy, E_s, by assuming a complete stress drop, $\Delta\sigma$, across the fault. This relationship was defined by **equation 2.17:**

$$E_S = \frac{\Delta\sigma}{2G} M_0 \tag{2.17}$$

As a result, Kanamori, derived a relationship between seismic energy, E_s, and the non-saturating moment magnitude, M_w, and obtained **equation 2.18:**

$$M_w = \frac{\log M_0 - 4.3 - 4.8}{1.5} = \frac{\log M_0 - 9.1}{1.5} \tag{2.18}$$

This empirical relationship presented in **equation 2.18** has been widely applied by researchers in predicting the moment magnitude resulting from injection-related activities, during CO_2 storage. A summary of its application across various studies is summarized in **table 2.2.**

Table 2.2: Summary of GCS projects that have registered injection-induced seismicity.

Project	Simulated Moment magnitude, M_w range	Important Information	References
Aneth, USA	-1.2 to 3.7	3800 seismic events were recorded within a 4.8km radius along two faults. Also, an earthquake with magnitude 3.7 may have been detected 9.5 km from the Aneth project. However, it was determined that the GCS project may not have been directly responsible for this significant occurrence.	[169], [170], [171]
Weyburn, Canada	-3 to -1	Considered the world's large-scale pioneer GCS project with seismic monitoring tools. Approximately 5.3 million tons of CO2 was injected per annum and recorded about 200 micro-seismic events, owing to stress perturbation rather than pressure induced perturbation.	[34], [86], [169], [172]
Decatur, USA	-2 to -1	Around one million tons of CO2 was injected into a 550 metres thick reservoir between 2011-2014. This project documented more than 10,000 micro-seismic events. Subsequent seismic analysis showed that the undetected small faults were reactivated, due to the stress perturbations induced by the migration of the gas plume away from the injection well.	[169], [171]
In Salah, Algeria	-1 to 3.4	The facility is expected to store at least 17 million tons of CO2 and has observed over 6000 seismic events to date. These occurrences are linked to the project's low porosity and permeability, ranging from 0.13 – 0.2 and 10mD, respectively, leading to pressure buildup during injection and consequent stress redistribution. The injection well penetrates a fault, generating seismic events in the vicinity of both the over-pressure zone near the wellbore and areas distanced from it.	[14], [62], [106], [173], [174], [175]

In the context of GCS, seismic events with a moment magnitude of $M_w < 2$ are classified as micro-seismic, meaning they are not perceptible at the surface and sometimes considered beneficial when limited within the injection zone, as the shear slip along the fault could enhance permeability [15], [176]. Most of the projects reported in **table 2.2** fall within the range, except for the Aneth and In Salah projects.

While these studies have successfully simulated potential seismic events during GCS, they all rely on estimating the static seismic moment, M_o, and its corresponding static seismic magnitude, M_w. Both parameters are convenient in determining the size of the earthquake, and the average tectonic impact of earthquakes triggered by CO_2 injection but does not capture the full energy dynamics released by the seismic waves or their high frequency components which are relevant for engineering applications and the quick evaluation of an earthquake's shaking potential.

To avoid presenting the entire earthquake spectrum with just the static seismic moment, M_o and magnitude, M_w, specialists such as [166], [167], [168], [177], suggested evaluating the energy magnitude, M_e, which quantifies the small fraction of released elastic wave energy, E_s, and captures the key characteristics of the wavefield, by including its dominant frequency content.

Since energy magnitude, M_e and released elastic wave energy, E_s, reflect the actual dynamic energy released from fault rupture, they serve as a crucial input for wave propagation models. This makes them valuable in forward simulations that track how body waves (P-waves and S-waves), and surface waves propagate through the subsurface during CO_2 injection. These models help predict ground motion, wave scattering, seismic wave propagation, and energy dissipation, which are critical for assessing seismic hazard and understanding rupture dynamics in the context of CO_2 injection.

Therefore, the next section presents a focused review of multiphase dynamic modelling approaches for 3D wave propagation in saturated porous media, with emphasis on their relevance to injection-induced seismicity.

2.9 Modelling of 3D Wave Propagation in Saturated Porous Media

Wave propagation analysis is fundamental to understanding the actual dynamic energy magnitude released from a fault during micro-seismic events. Whether the seismic event arose from natural tectonic processes or from anthropogenic activity such as CO_2 injection.

The propagation of compressive/pressure (P) waves, shear (S) waves, and surface waves, their amplitudes, frequency content, wave splitting, arrival times, and wave attenuation, provide key

information about the physical and mechanical state response of the reservoir making it essential for seismology study [178], [179], [180], [181], [182].

The P-waves oscillate parallel to the direction of wave propagation. They are the fastest seismic wave and can travel through both solid and liquid materials. Due to their high velocity, the P-waves are typically the first signals recorded by the seismograph following an earthquake. The S-waves on the other hand shake the ground in a shearing motion that is perpendicular to the direction of wave propagation. They are slower than the P-waves and can travel only through solids [20], [183].

The surface waves travel only through surface media and consists of the Love wave and the Rayleigh wave. They move slower than the body waves, are much larger and are considered more destructive than the P-waves and S-waves. The love waves move the reservoir horizontally, moving it from side to side perpendicular to the direction of motion. The Rayleigh waves on the contrary, have an elliptical motion and are considered the most destructive wave type [20], [184]. Capturing these body and surface wave profiles in three (3D) dimensions, is essential for understanding and mitigating the potential risk of micro-seismicity during GCS. Figure 2.14 is a representation of the P-waves' horizontal motion, S-waves' perpendicular motion and Rayleigh waves' elliptical motion.

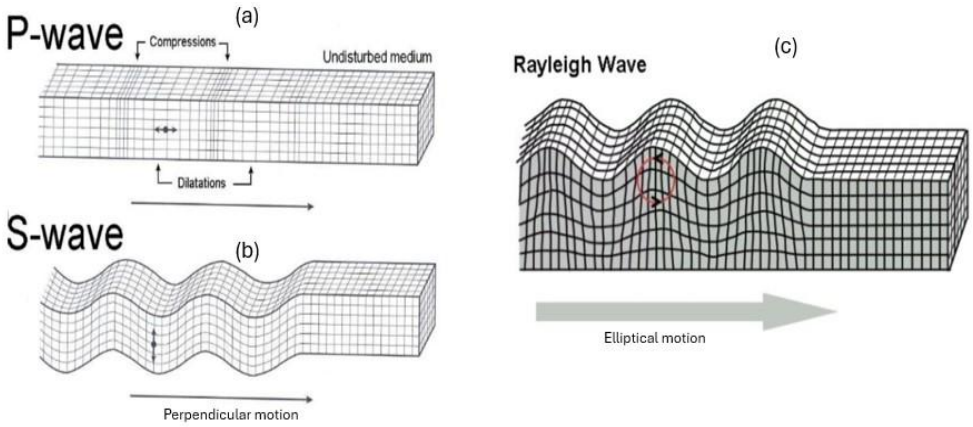

Figure 2.14: Representation of P-waves, S-waves, and Rayleigh waves.

Several models have been developed to analyse the propagation and attenuation of the body and surface waves in saturated porous media. Authors such as [185] regrouped these models into the following: (i) models based on viscoelastic rheology (ii) hydrodynamic models coupled between communicating cavities, and (iii) models based on Biot's theory of poroelasticity.

Models based on viscoelastic rheology, involve modelling the propagation using two moduli, i.e. the unrelaxed high-frequency modulus and the relaxed low-frequency modulus. In the

hydrodynamic model, the pressure relaxation at pores of different sizes, is taken into consideration. This is because authors such as [186] assumed that as fluids flow through the pores, viscous dissipation occurs between two pores of different shapes and orientation. This phenomenon known as squirt flow, makes other models not compatible for describing the wave propagation profile at the pore scale. However, it was argued that squirt-flow wave propagation is solely reliant on aspect-ratio distribution [187]. This led authors such as [188] to propose a model that acknowledged that the pore network has a binary structure, with dominant relatively stiff pores that occupy most of the pore space and a secondary compliant pore section, both responsible for pressure dependence of the elastic moduli. The advantage as suggested by [189] in treating the domain as a binary structure is that, at the micro scale, the material may be modelled as a poroelastic continuum, making it suitable for analysis within Biot's theory of elasticity. In general, using both models to simulate wave propagation and attenuation at the pore scale are suitable as the theoretical models have been tested and validated numerically, at the ultrasonic level [185].

Conversely, the Biot's dynamic poroelasticity supplies the baseline physics for frequency-dependent wave propagation in saturated rocks: it recovers Gassmann's low-frequency limit, predicts fast and slow P modes, and explains how the slow mode becomes a diffusion wave yielding attenuation/dispersion controlled by permeability, viscosity, and heterogeneity scale (with characteristic f_c typically $\sim 10^5$Hz in rocks) [185]. Building on this framework, the review develops models for layered media, and 3D random continua, each providing closed-form asymptotic and characteristic frequencies. The advantage of using the Biot's theory of poroelasticity over the other methods include the following: (i) Biot's-based models are rigorously physics-grounded by measurable rock/fluid properties; (ii) anchored by exact low/high-frequency limits for robustness; (iii) numerically tractable (reflectivity, finite-difference/finite-element), enabling validation and broadband forward simulation; and (iv) useful for fast and slow wave propagation. This research is focused on modelling the wave propagation using the Biot's theory of poroelasticity.

2.9.1 Governing equations for poroelasticity in modelling of wave propagation

Biot's poroelastic theory [178], [179], [180], forms the theoretical framework for modelling wave propagation in fluid saturated porous media. In his initial work, he made the following assumptions: 1.) the host rock is elastic, 2.) the pores within the rock are connected, 3.) the seismic wavelength is larger than the average pore size, 4.) the deformations are quite small, and 5.) the medium was isotropic. This theory was extended by Biot to account for anisotropy within the medium. [190]

It is governed by a coupled system of partial differential equations that describe the mechanical and hydraulic interactions between the solid matrix and the pore fluid. Specifically, Biot's dynamic formulation is based on the principles of linear momentum for solid and liquid phases, coupled with mass balance equation.

The linear momentum equations governing the dynamic regime are formulated for the solid and fluid phases, respectively, as shown in **equations (2.18) and (2.19),** following the formulations by [114], [191], [192]

$$\rho^S \dot{\boldsymbol{v}} = \nabla \cdot \boldsymbol{\sigma}^S + \rho^S \boldsymbol{g} + \boldsymbol{h}^S \tag{2.18}$$

$$\rho^F \dot{\boldsymbol{w}} + \nabla \boldsymbol{w} \cdot \boldsymbol{w_R} = \nabla \cdot \boldsymbol{\sigma}^F + \rho^F \boldsymbol{g} + \boldsymbol{h}^F \tag{2.19}$$

In equations (2.18) and (2.19), ρ^s and ρ^F represent the mass density of the solid (s) and fluid (F) phases, ***v, w*** *and* $\boldsymbol{w_R}$, are the solid, fluid, and relative velocities respectively, $\nabla \cdot \boldsymbol{\sigma}$ is the Cauchy stress tensor, and $\boldsymbol{h^s}$ and $\boldsymbol{h^F}$ denotes the volume specific interaction between both phases.

While the momentum equations govern the mechanical behaviour of each phase, a complete poroelastic formulation also requires the enforcement of mass conservation. This condition ensures continuity of fluid flow and accounts for changes in fluid content due to deformation and pressure gradients. The mass balance equation is therefore essential for capturing the coupled fluid-solid interaction in dynamic loading conditions.:

For displacement-velocity-pressure (u-v-p) based formulation considered in this analysis, the mass conservation equations for the solid and fluid phases can be expressed as [191]

$$\dot{\rho}^S + \rho^S \nabla \cdot \boldsymbol{v} = 0 \tag{2.20}$$

$$\dot{\rho^F} + \rho^F \nabla \cdot \boldsymbol{w} = 0 \tag{2.21}$$

Here, $\dot{\rho}^S$and $\dot{\rho}^F$ denote the material time derivatives of the solid and fluid mass densities, respectively, while $\boldsymbol{v}$ and $\boldsymbol{w}$ represent the velocity vector fields of the solid and fluid phases, respectively. These equations reflect a local balance of mass for each phase, where density changes are directly linked to the divergence of their respective velocities, consistent with the continuum mixture theory framework [191], [192].

It is important to note that, in this formulation, the source terms are deliberately omitted. This simplification is appropriate for the multi-field formulation, where the primary objective is to model mass exchange between the phases and wave propagation governed by mechanical effects. In contrast **equation (2.1),** which describes mass conservation for a fluid phase in porous media, includes a source term to represent external mass input from the injection well;

an approach commonly used in u-p formulations to evaluate the effects of the injected fluid on the solid formation.

By neglecting source terms in the present multifield-based approach, the analysis assumes a closed system, in which no additional fluid enters or exits the porous medium. This assumption aligns with the physical context of high-frequency dynamic loading, where wave-induced deformations dominate and fluid exchange with the surroundings is negligible.

To complete the system, the constitutive relationship for the solid matrix was provided by extending the Terzaghi principle, and Hooke's law as seen in **equation (2.22)** [64], [114], [193]

$$\boldsymbol{\sigma} = \mathbf{C}: \boldsymbol{\epsilon} - bp\mathbf{I} \tag{2.22}$$

where the **C** is the stiffness matrix, **σ** represents the stress tensor, **ϵ** is the strain tensor which is defined as the symmetric gradient of the displacement vector, *b* is the Biot's coefficient, p is the pressure, and **I** is the identity matrix.

The governing equations of poroelasticity **(equations 2.18 – 2.21)**, as described by Biot's theory, form a tightly coupled system of partial differential equations involving mechanical deformation and fluid flow. Due to their complexity, in heterogeneity, anisotropy, or dynamically loaded domains, analytical solutions are often limited to idealized geometries or boundary conditions. Consequently, numerical methods have become indispensable tools for studying wave propagation in saturated porous media. These methods enable the simulation of realistic subsurface conditions, the resolution of multiphase interactions, and the prediction of wavefield characteristics under various loading and material configurations. The following section reviews the primary numerical approaches that have been developed and applied in the literature to solve the poroelastic wave propagation problem.

2.9.2 Numerical model for wave propagation in saturated porous media

Several discretization techniques have been developed to solve wave propagation using Biot-type formulations in time and space, each offering a unique set of advantages and disadvantages in terms of computational cost, accuracy, stability, and geometric flexibility. We refer, for example, to the Finite Difference Method (FDM) [194], [195], [196], [197], the Finite Element Method (FEM) [191], [198], [199], [200], [201], the spectral and pseudo-spectral element method (SEM) [202], [203], and the Lagrange Multipliers method [204], [205], [206]. Most recent advances such as the Virtual Element Method (VEM) have been proposed to handle unstructured and polyhedral meshes [207].

Among these, the FDM, SEM and FEM have emerged as the most widely adopted in practical applications and will be the focus of the review.

A.) FDM for wave propagation in saturated porous media:

The earliest efforts to simulate Biot waves using the grid-based approach emerged in the 1970s. According to available records, [208] were pioneers in this domain, employing a finite difference method (FDM) to calculate one-dimensional Green's functions with artificial damping.

Building on this foundational study, researchers advanced the finite difference method by introducing the staggered-grid formulation to solve the governing equations **(equations 2.18 – 2.21)**. This technique calculates the physical variables like displacement, stress, velocity, and pressure at offset positions (Figure 2.15 a & b), thereby improving accuracy, and numerical stability.

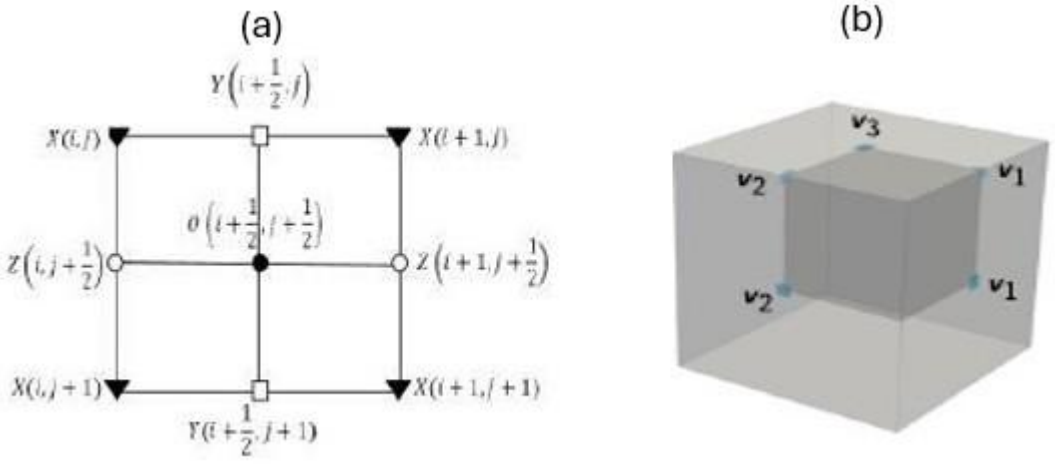

Figure 2.15: (a) 2D Staggered-grid layout and locations of stress, velocity, and pressure components. X is the pressure, Y is horizontal velocities, Z is vertical velocity and O is shear-stress, (b) 3D high order staggered-grid calculating the velocity component [209], [210]

This approach has been applied to two-dimensional (2D) [210], [211], [212], and three-dimensional grids (3D) [213], [214], [215] studies.

Vamaraju and Sen [210] developed a 2D velocity-stress staggered-grid FDM scheme based on Biot's poroelastic theory. With fourth-order spatial and second-order temporal accuracy, the method captures the slow and fast compressional (P-) waves within porous rocks. A linear slip model was employed to simulate the equivalent behaviour of fractures, revealing significant mode conversion effects at fractured interfaces. While this study was effective in understanding complex fracture-pore interactions, it was limited to 2D. In addition, modelling faults as a

discontinuity for the slip analysis, increases the complexity of the numerical implementation and can introduce stability challenges.

While 2D models are valuable for concept testing and computational efficiency**,** 3D models are important for realistic seismic simulation, particularly in fractured, anisotropic, or complex media.

Graves [215] established a 3D velocity-stress staggered grid formulation for elasto-dynamic problems in porous media. The study utilized a half-space model with horizontal length of 10000m, source depth of 2500 m and moment tensor of 10^{16} Nm, varying degrees of inclination of the fault (The fault mechanisms have different orientations as suggested by the article). The domain had a grid spacing of 250 meters and time step of 0.025s. For a P-wave velocity, V_p, 4.0 km/s, a shear wave velocity, V_s, of 2.3 km/s, solid density of 1.8 gm/cm^3 and free surface boundary condition, the time histories of the wave profile were compared with those using a frequency wave number integration technique (which is considered a highly reliable method for ground motion analysis), and found a good correlation in amplitude and wave form between the FDM source and benchmark frequency wave number integration algorithm [215], [216] as seen in Figure 2.16**.**

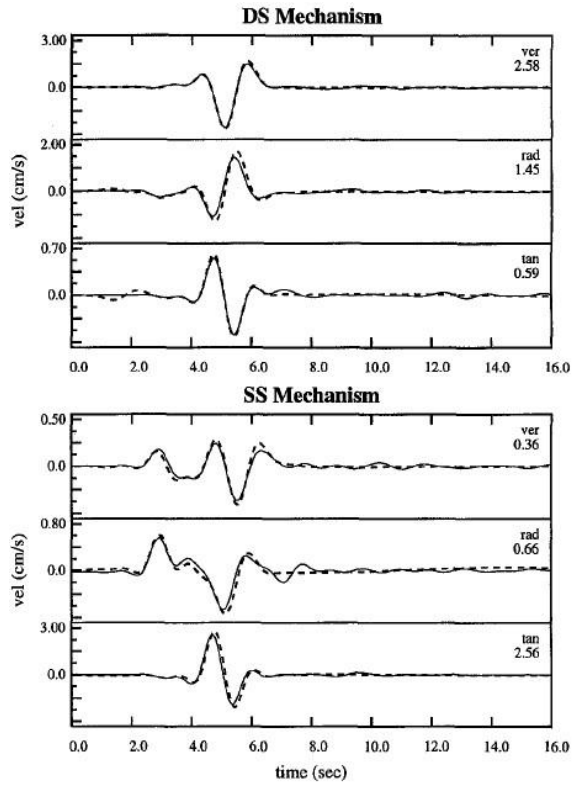

Figure 2.16: Correlation of solid velocity time histories: solid lines (numerical simulation) vs dashed lines (reference) for DS (dip-strike) and SS (strike-slip) mechanism.

While Graves' model was groundbreaking, it was built with older computing technology and does not include modern features like running on multiple processors or using adaptive grids to improve efficiency and accuracy. In addition to this, their model does not explicitly account for the effects of property anisotropy or layered rocks and how they affect seismicity.

Franczyk et al.[213] and O'Reilly et al [214] in their respective studies, introduced a comprehensive assessment of 3D staggered grid FDM applied to elastic and anisotropic media. Their approach integrates non-uniform grid spacing and a free-surface boundary, significantly improving accuracy. The method is especially relevant for near-surface studies and regions with pronounced stress elevation changes. However, due to the increase in the number of degrees of freedom, the implementation is complex requiring numerical optimization.

While these studies collectively demonstrate the strength and adaptability of staggered-grid finite difference methods across a range of seismic modelling challenges, this method presents notable drawbacks.

According to studies carried out by [209], [217] the formulation struggles with stable boundary condition enforcement and accurately modelling complex or discontinuous geometries without advanced techniques like Summation-By-Parts via the Simultaneous-Approximation-Term technique (SBP-SAT). Furthermore, staggered FDM implementations are not naturally compatible with adaptive meshing or irregular grids and may suffer from increased computational time and dispersion errors if the model is not finely discretized, not capturing the effects especially in high-frequency zones. These challenges highlight the method's reliance on structured grids and underscore the trade-offs between accuracy and flexibility.

B.) SEM for wave propagation in saturated porous media:

The spectral element method was initially developed in the 1980s, with foundational work by [218] and later improved by [219]. It was first applied in computational fluid dynamics, and only later attracted attention for use in seismic wave propagation studies in saturated porous media. This method combines the versatility of the FEM method while retaining the accuracy of the SEM. It manages irregular free surfaces with heterogeneous properties, without introducing significant complications into the modelling process.

In the spectral element method, the field variables within each element are interpolated using Lagrange polynomials defined at Gauss-Lobatto-Legendre (GLL) points. This approach ensures high accuracy and efficient handling of element interfaces, since GLL points always include the nodes at the boundaries. This choice ensures spectral accuracy and results in a

diagonal mass matrix, which facilitates explicit time integration and efficient parallel computation. As a heuristic rule, for most wave propagation applications, authors such as [17], [220], [221] suggested high-order polynomials of orders between 4 and 10 to improve accuracy of the simulation.

For SEM mathematical formulation, a cartesian coordinate system (x, y, z) is established, and the physical domain is partitioned into N_e, non-overlapping elements. The integrals appearing in the weak formulation are computed for each element domain, Ωe. For a 3D analysis, hexahedral elements are employed, while in 2D, quadrilateral elements are used. Both models allow a unique mapping from the reference point to each element. The reference point is defined within coordinate ranges $-1 \leq \xi \leq +1$, $-1 \leq \eta \leq +1$, and $-1 \leq \zeta \leq +1$.

The transformation is described using shape functions N_a (ξ, η, ζ) and a corresponding set of nodal points $x_a = x$ (ξ_a, η_a, ζ_a), where a = 1, …., n_a, which collectively define the elements geometry. Each point in the reference element is this associated with a point in the physical domain via the following relationship as defined by [220]:

$$x(\xi,\eta,\zeta) = \sum_{a=1}^{n_a} N_a(\xi,\eta,\zeta)x_a \tag{2.23}$$

$$y(\xi,\eta,\zeta) = \sum_{a=1}^{n_a} N_a(\xi,\eta,\zeta)y_a \tag{2.24}$$

$$z(\xi,\eta,\zeta) = \sum_{a=1}^{n_a} N_a(\xi,\eta,\zeta)z_a \tag{2.25}$$

This mapping establishes the correspondence between the local coordinates of the reference element and the global coordinates of the physical domain.

The SEM has been employed in the time domain and has demonstrated good precision in simulating wave propagation in both 2D models [222] and 3D models [223], [224]. For layered domains with different material properties, SEM has been applied in the frequency domain [225], [226], [227].

Although the spectral methods have been successfully implemented and have shown to reduce computation requirements in these case studies mentioned, some limitations have been identified.

For instance, [228], [229] noted that, the method's reliance on structured hexahedral or quadrilateral meshes complicates its application to domains with complex or highly irregular geometries, often making mesh generation less flexible compared to unstructured finite element approaches. Also, high-order polynomial interpolation, while increasing precision, can lead to ill-conditioned system matrices and greater computational demands, particularly in large-scale three-dimensional simulations. Furthermore, SEM may experience stability issues if not carefully configured, and its extension to highly heterogeneous or porous media is limited by challenges in accurately capturing sharp contrasts material properties. Collectively, these factors can restrict the practical applicability of SEM in certain advanced modelling scenarios, such as those encountered in seismology and subsurface exploration.

C.) FEM for wave propagation in saturated porous media:

The finite element method has proven to be effective in analysing how compressional P-waves and shear S-waves propagate through saturated porous media. It is well suited for solving coupled equations of Biot's poroelastic theory, as it can naturally handle heterogeneous material properties, irregular domains, and a variety of boundary conditions [191], [199], [230].

A key aspect of the FEM is in the appropriate approximation of the unknown variables of displacement, velocity, and pressure (U-V-P) within each element using shape functions. In practice, these variables are expressed as weighted sums of their nodal values and their associated basis functions [133]. The displacement, velocity and pressure variables which are primary unknowns for wave propagation analysis, have been discretised as follows [191], [230], [231], [232], [233]:

$$\mathbf{u}(\mathbf{x},t) \approx \sum_{i=1}^{N_u} N_i^u(\mathbf{x}) U_i(t) \tag{2.26}$$

$$\mathbf{v}(\mathbf{x},t) \approx \sum_{j=1}^{N_v} N_j^v(\mathbf{x}) V_j(t) \tag{2.27}$$

$$\mathrm{p}(\mathbf{x},t) \approx \sum_{i=k}^{N_p} N_k^p(\mathbf{x}) P_k(t) \tag{2.28}$$

Here, N_i^u, N_i^v and N_i^p are the shape functions corresponding to displacement, velocity, and pressure respectively, while U_i, V_j, P_k represent the nodal degrees of freedom.

In UVP wave propagation analyses, the choice of the shape function is crucial, as it determines the accuracy of the FEM solution. For wave dynamics, higher-order polynomial basis functions are frequently employed for displacement and velocity fields, offering better convergence properties, although they require more computational implementation. To ensure numerical stability, an inf-sup stable mixed FEM is popular, whereby a quadratic interpolation is used for displacement and velocity, and a linear interpolation for pressure for Taylor-Hood elements [191], [201]. That is the pressure will be evaluated at all the corner points, while the displacement and velocity variable is evaluated at both corner points and mid-points of the element like **figure 2.12** above. This approach has been applied by [191], [234], [235], [236].

For example, [235] utilized the mixed finite element method to simulate a dynamic, non-isothermal process in porous media. Their approach uses a Taylor-Hood discretization, with quadratic elements for displacement and bilinear elements for both pressure and temperature, enabling simultaneous resolution of thermal, hydraulic, and mechanical effects during wave propagation. The formulation's strength is evident in its rigorous validation against analytical solutions, where it demonstrates higher accuracy and faster convergence for hydraulic permeability, k, of 10^{-2}m/s and less accurate when a low permeability of 10^{-5}m/s is used (as seen in Figure 2.17).

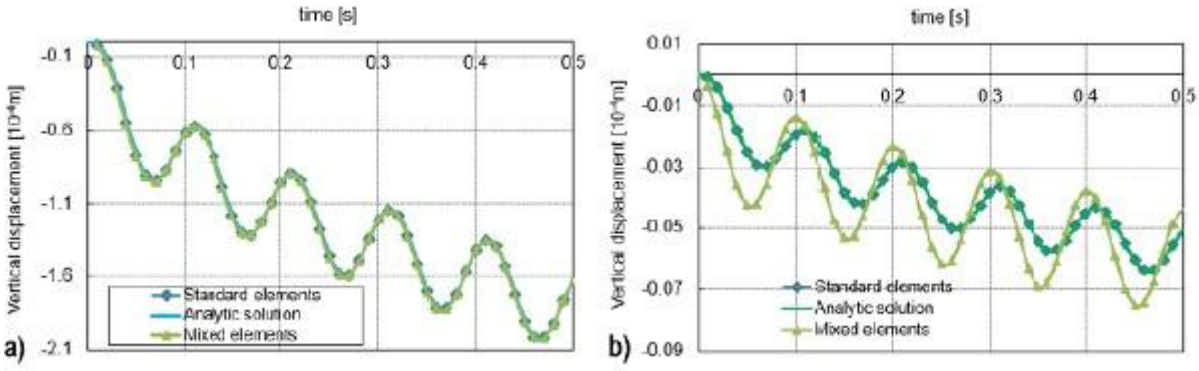

Figure 2.17: Vertical wave solid displacement for (a) k = 10^{-2} m/s and (b) k = 10^{-5} m/s ([235]

While this study captures the rapid transient and complex multiphysics in saturated porous media, the implementation and computational cost increases substantially with each added physical field and the article acknowledges challenges in handling zones with discontinuities and sharp changes in material properties. Furthermore, the match between the numerical results and the analytical solution is much closer in Figure 2.17 (a) than in Figure 2.17 (b). This reduced correlation in (b) is likely related to the lower hydraulic permeability, which makes accurate numerical modelling more challenging. However, the paper does not clearly explain how changes in hydraulic permeability impact the smoothness of the waveforms or the agreement

between methods. This represents a gap in the study, as a more detailed analysis could help clarify the specific effects of hydraulic properties on numerical accuracy.

[191] on the other hand, presents a multi-field finite element framework for modelling 3D wave propagation in saturated, anisotropic porous media. The study is distinguished by its use of a mixed, inf-sup stable finite element scheme, by utilizing a quadratic interpolation for both displacement and velocity, and linear interpolation for pore pressure, following the Taylor-Hood discretization. This choice ensures numerical stability, and accurately captures both P-waves and S-waves in saturated porous media. The computational approach is enhanced by a fully implicit monolithic time integration using the generalized trapezoidal rule, enabling the simultaneous solution of all primary fields without restrictive timesteps conditions. The authors employ a Bi-conjugate stabilization iterative solver, paired with a custom multi-physics reduction preconditioner, to efficiently solve the large, coupled algebraic systems arising in 3D simulations. Their results demonstrate not only high physical fidelity and stability across a range of anisotropic test cases, but also scalability to large and complex models. However, while the methodology achieves robustness and accuracy, the computational expense associated with fully implicit integration and large-scale 3D systems is significant.

While these articles emphasize on the power and flexibility of mixed finite elements methods and the use of Taylor-Hood discretization for modelling wave propagation in saturated porous media with complex multiphysics behaviour, significant gaps remain. First, these tools haven't been employed to GCS repositories, where CO_2, brine and rock interact in complex ways. In addition, we lack studies that show how changes in key petrophysical properties (such as porosity, permeability, and stiffness) affect wave behaviour and ground motion during CO_2 storage, leaving a huge knowledge gap. Moreover, most work stops at earthquake size and magnitude and doesn't utilize wave simulations to find a correlation between peak ground velocity and ground shaking intensity characteristics, which are critical for hazard assessments during GCS activities. Therefore, addressing these gaps is essential for extending the use of FEM approaches to geotechnical and subsurface engineering applications, particularly geological carbon sequestration.

2.10 Summary of Literature Review

This literature review has provided a comprehensive examination of the current state of knowledge and modelling practices relevant to the dynamic response of subsurface formations during geological carbon sequestration (GCS). The chapter covered foundational concepts of GCS, including the principles, history, and status of large-scale projects, and reviewed the

different underground storage formations, emphasizing depleted oil and gas reservoirs and detailing the physical and geochemical trapping mechanisms that ensure storage security.

Thereafter, the discussion extended to the theory of multiphase flow in porous media and highlighted the geomechanical risks associated with CO_2 injection, such as fault reactivation and injection-induced micro-seismicity.

The review systematically evaluated the main numerical frameworks for modelling these risks, tracing the evolution from hydro-mechanical (HM) models to advanced thermo-hydro-mechanical-chemical (THMC) formulations. It examined both explicit and continuum-based approaches for fault representation, reviewed the use of empirical relationships for quantifying micro-seismicity, and assessed state-of-the-art numerical discretization techniques, particularly the adoption of mixed finite element methods (FEM) with Taylor-Hood discretization for modelling wave propagation in complex, anisotropic, and multiphase systems.

Despite significant advances, the review identified key gaps in the literature:

- Existing literature lacks an all-inclusive workflow that (i) begins with coupled hydro-mechanical (HM) simulations of CO_2 injection to resolve pore-pressure build-up and fault slip; and translate these fields into consistent seismic-source representations.
- Prior work focuses on estimating earthquake magnitude using static seismic moment only, without leveraging simulated wave propagation to derive peak ground velocity or ground shaking intensity, that are critical for practical seismic risk assessment and engineering applications.
- There has been limited application of advanced mixed finite element frameworks to the specific context of geological carbon sequestration, especially in depleted oil and gas reservoirs where CO_2, brine, and rock interactions are highly coupled and complex.
- The application of wave propagation analyses to anisotropic saturated porous media in the context of geological carbon sequestration is often underexplored.

These gaps underscore the need for a numerical framework that can model wave propagation and seismic hazards, while explicitly accounting for the effects of layered-anisotropy, the potential for fault-reactivation, and injection-induced micro seismicity during GCS, which would be discussed in the next chapter.

Chapter 3: Methodology

3.1 Introduction

The geomechanical response and seismic risks associated with geological carbon sequestration (GCS) requires an integrated approach that captures both the static and dynamic effects of CO_2 injection in complex, multiphase, anisotropic subsurface depleted reservoirs. In response to the research gaps identified in study, this section presents a two-stage modelling framework designed to:

- Stage 1: Perform a hydro-mechanical (HM) analysis, (displacement-pressure (u-p) formulation) to quantify overpressure, stress variation, and fault slip leading to static seismic moment generation and,
- Stage 2: Dynamic wave propagation analysis (displacement-velocity-pressure (u-v-p) formulation) to evaluate the P-wave, S-wave, Rayleigh wave propagation and ground shaking intensity resulting from injection-induced seismic events.

This methodology allows for a separation between the generation of seismic sources and their subsequent wave propagation, thereby providing a comprehensive modelling framework for this study. The outputs from the first stage, particularly the pressure, stress changes and computed seismic moments, serve as direct input for the dynamic analysis in the second stage.

The methodology section is therefore organized into two (2) sections as follows: Section 3.2 and Section 3.3 present the details of the governing equations, constitutive relationships, and numerical implementation for the u-p analysis, respectively. Subsequently, we describe the model, boundary, and initial conditions in section 3.4. To conclude this section, we evaluate the seismic moment, seismic magnitude, and energy magnitude, and content frequency, f_c necessary for the u-v-p analysis in section 3.5.

The methodology transitions to the second stage of our analysis which commences with the description of the governing equations, constitutive relationship, boundary conditions in section 3.6, and numerical discretization approach for u-v-p wave propagation analysis in section 3.7. Thereafter in section 3.8, we evaluate the potential ground shaking intensity due to CO_2 injection. We conclude this chapter by providing a summary of this chapter in section 3.9.

The computational framework is implemented using two primary research codes: the MATLAB Reservoir Simulation Toolbox (MRST) for the hydraulic analysis, and the GeoMatFEM research code for the mechanical and subsequently the dynamic wave propagation (u-v-p) simulations. A schematic diagram is presented to illustrate the sequence of the modelling stages,

the interaction and transfer of key outputs (such as pressure alterations and seismic moment) from MRST to GeoMatFEM, and the overall structure of data processing and analysis as seen in Figure 3.1

This integrated workflow ensures a robust approach in simulating both static and dynamic responses in geological carbon sequestration scenarios and sets the foundation for the detailed theoretical and numerical implementation discussions in subsequent sections.

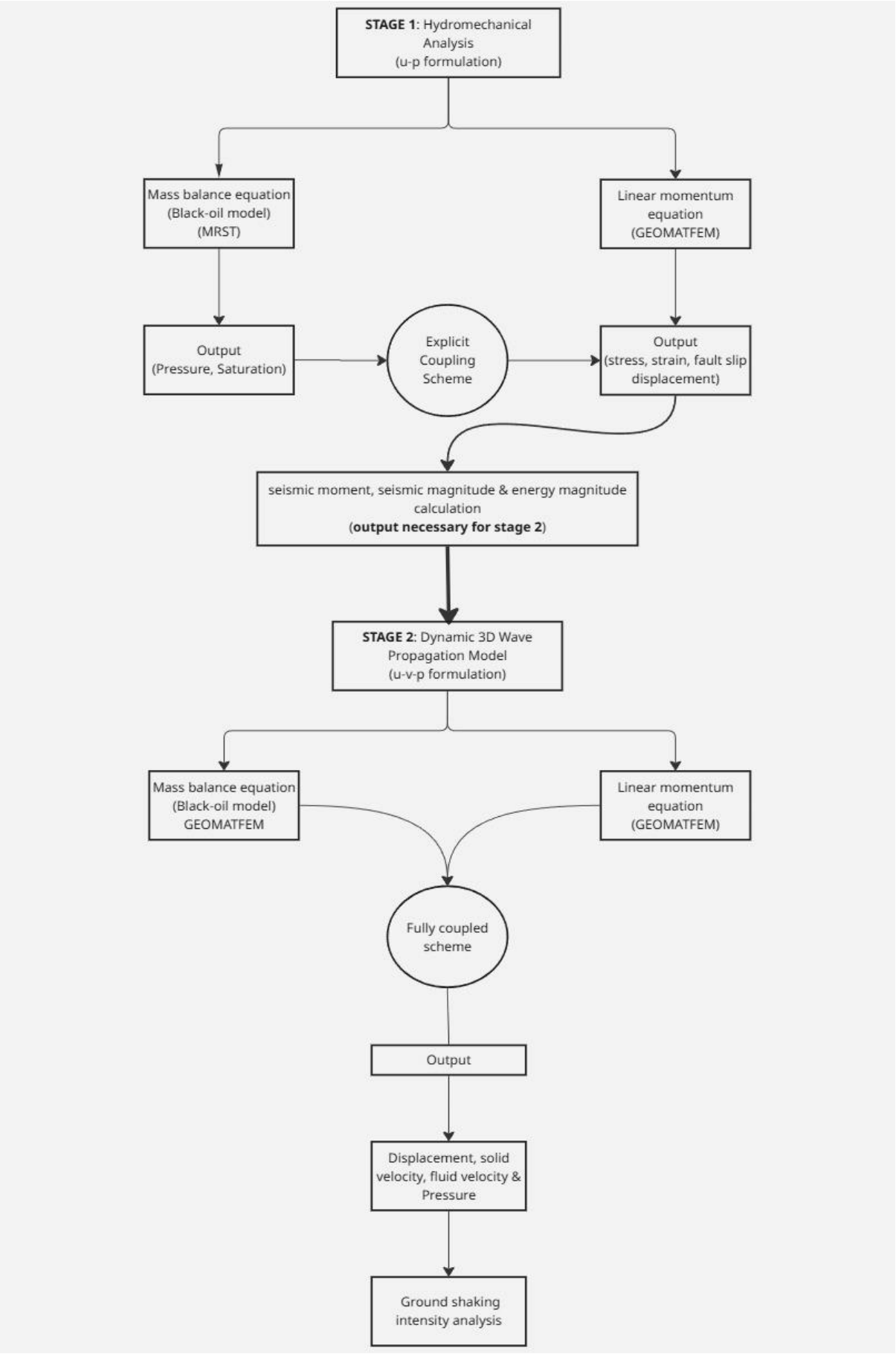

Figure 3.1: Methodology workflow for two-step numerical analysis.

3.2 Governing Equations and Constitutive Relationships for Hydromechanical Analysis

While some of these equations in this section have been previously presented in the literature review section, they are restated here to enhance methodological clarity, and to facilitate a clear understanding of the numerical and analytical approach.

First, the derivation of the mass balance equation for single-phase flow is presented, establishing the foundational conservation principles relevant to porous media. Thereafter, the formulation is extended to the mass balance for multiphase flow, accounting for the presence and interaction of multiple fluid phases within the reservoir.

Next, the linear momentum balance equation is introduced, to describe the mechanical equilibrium in the porous skeleton. We then discuss the basic theory of poromechanics for single-phase systems, illustrating how fluid pressure and mechanical deformation are coupled in classical Biot's framework. Finally, the derivation is generalized to the multiphase poromechanics context, where the presence of several fluid phases necessitates a more comprehensive description of hydro-mechanical coupling.

By following this sequence, we ensured that each conceptual step is understood and that the equations are systematically derived, setting a solid foundation for the subsequent numerical implementation and analysis.

The theories and formulation with respect to the mass balance equations for single and multiphase, linear momentum equation, linear elastic constitutive model, elastoplastic constitutive model and single and multiphase poromechanics is obtained from [18], [47], [61], [64], [103], [114], [119], [178], [237], [238].

3.2.1 Mass balance equation

According to the law of mass conservation, the accumulation of mass within a domain is equal to the net flux over the boundaries given by **equation 3.1:**

$$\frac{\partial}{\partial t}\int_{\Omega}\phi\rho dx + \int_{\partial\Omega}\rho\boldsymbol{v}\cdot\boldsymbol{n}ds = \int_{\Omega}qdx \tag{3.1}$$

where ρ denotes the fluid density, ϕ signifies the porosity of the reservoir rock, $\boldsymbol{v}$ represents the Darcy-scale average fluid velocity, $\boldsymbol{n}$ designates the outward unit normal vector on the computational domain boundary $\partial\Omega$, and q refers to the sources or sinks of the fluid within the system.

By applying the divergence theorem, the mass balance equation is valid through the domain, Ω, and alternatively reformulated as an integral, given by **equation 3.2** (all terms have been previously defined)**:**

$$\int_{\Omega}\left[\frac{\partial}{\partial t}\phi\rho + \nabla\cdot(\rho\boldsymbol{v})\right]dx = \int_{\Omega} q dx \tag{3.2}$$

A.) Single phase equation and constitutive relationship: The integral form in **equation 3.2** is valid for any point within the domain, Ω and for domains that are infinitesimally small. Hence, it is necessary that the macroscopic behaviour of the single-phase fluid satisfies the continuity equation in its differential form, ensuring mass is conserved at every point within the domain, formulated as follows in **equation 3.3** (all terms have been previously defined):

$$\frac{\partial(\phi\rho)}{\partial t} + \nabla\cdot(\rho\boldsymbol{v}) = q \tag{3.3}$$

To obtain a closed system of equations, it was necessary to introduce constitutive relationships, which describe how various systems such as pressure and volumes, are related under different physical conditions. One of such relationships, is the Darcy-scale average fluid velocity, $\boldsymbol{v}$, which describes the relationship between flow velocity, and pressure gradient, as expressed in **equation 3.4:**

$$\boldsymbol{v} = -\frac{\mathbf{K}}{\mu}(\nabla p + \rho\boldsymbol{g}\nabla z) \tag{3.4}$$

where **K** is the permeability tensor of the rock, μ is the viscosity of the fluid, ∇p is the pressure gradient, **g** represents the gravity term and ∇z is the spatial coordinate in the upward vertical direction. It is worth mentioning that for the Darcy velocity, the driving forces include the pressure and gravity [61].

B.) Multiphase equation and constitutive relationship: However, with the injection of CO_2, a two-phase reservoir environment is established. Therefore, we extend the continuity equation and Darcy's law, presented in Equations (3.3) and (3.4), to accommodate this multiphase environment.

To describe our model, we consider a non-reactive medium, meaning the resident brine and injected CO_2 in the porous medium, are immiscible. The core formulation that describes the movement of a multiphase fluid is based on the conservation equations relevant to each individual phase, as here defined by **equation 3.5:**

$$\frac{\partial}{\partial t}(\phi \rho_\alpha S_\alpha) + \nabla \cdot (\rho_\alpha \boldsymbol{v}_\alpha) = q_\alpha \tag{3.5}$$

where α represents the phases involved in our analysis: water (w) and gaseous phase (g), CO_2, $\boldsymbol{v}_\alpha$ is the Darcy velocity, ρ_α is the density, S_α is the saturation of each phase, and q_α is the source/sink of each phase.

Analogous to the single-phase flow, it was essential to model the Darcy velocities of the phases. This was achieved by extending **equation (3.4)** to establish a relationship between the phase velocities and their corresponding pressures, by incorporating the relative permeability term as illustrated in **equation (3.6)**:

$$\boldsymbol{v_\alpha} = -\mathbf{K}\frac{k_{r\alpha}}{\mu_\alpha}(\nabla p_\alpha - \rho_\alpha \boldsymbol{g} \nabla z) \tag{3.6}$$

where α represents the phases involved in our analysis: water (w) and gaseous phase (g), CO_2, **K** is the is the permeability tensor of the rock, μ is the viscosity of the fluid, k_r is the relative permeability, ∇p is the pressure gradient, **g** represents the gravity term and ∇z is the spatial coordinate in the upward vertical direction.

For simplicity of the multiphase fluid flow model, the following assumptions were made to ensure simplicity:

- A black oil model, that is the chemical component can be aggregated into only two pseudo-components (i.e. the water phase and gaseous phase) under surface conditions,
- These pseudo-components present in the reservoir are immiscible and no mass transfer between the co-existing phases,
- The pores within the reservoir are interconnected, sufficiently large that the surface tension effects are minor,
- The capillary pressure effects within the reservoir are negligible,
- A pressure equilibrium exists between the phases (i.e. $P_w = P_{CO2} = P$),
- Temperature effects are constant throughout, thereby assuming isothermal conditions and,
- The sum of all the phases in the pores of reservoir are equal to 100% (i.e. $\sum_\alpha S_\alpha = 1$).

These simplifications have been widely applied in the literature to numerical modelling of large-scale multiphase reservoir systems by authors such as [62], [84], [96], [157]. The evaluation of the primary unknowns, which are the saturation of each phase, S_α, and the pressure gradient, ∇pα, will be discussed in section 3.4.

3.2.2 Linear momentum equation

The mechanical deformation of the reservoir is governed by the linear momentum equation (**equation 3.7**) and their associated constitutive relationships, which describe the interaction between mechanical stress, strain and external forces acting on the reservoir. To evaluate these variables for the first stage of the analysis, the following assumptions were adopted:

- A quasistatic equilibrium condition (i.e. the process occurs slowly enough that inertial effects are negligible, and mechanical equilibrium is always maintained),
- Small deformations (i.e. the process occurs slowly enough that inertial effects are negligible, and mechanical equilibrium is always maintained),
- Isothermal conditions and,
- Closed boundary for a domain, Ω

$$\nabla \cdot \boldsymbol{\sigma} + \rho_b \boldsymbol{g} = \mathbf{0} \tag{3.7}$$

In equation **3.7**, $\boldsymbol{g}$ represents the gravity term, $\nabla \cdot \boldsymbol{\sigma}$ represents the divergence of the stress tensor and $\rho_b = \phi \sum_{\alpha}^{n_{\text{phase}}} \rho_\alpha S_\alpha + (1-\phi)\rho_s$ is the bulk density of the material, ρ_α and S_α are the density and saturation of fluid phase α, ρ_s is the density of the solid phase, ϕ is the true porosity, and n_{phase} is the number of fluid phases.

In the initial stages of CO_2 storage, the deformation of the formation can be assumed to be linearly proportional to the applied stress, consistent with linear elastic behaviour. However, as injection progresses and higher stress levels are encountered, the formation may undergo plastic deformations once a critical stress threshold is exceeded (as seen in Figure 2.7). To accurately capture both the initial elastic response and the potential for permanent deformation in depleted reservoirs, both (a) linear elastic and (b) elastoplastic constitutive models were necessary.

A.) Linear elastic constitutive relationship: To characterize the stress-strain behaviour of the porous medium, the Hooke's law (Equation 3.8) was applied to define the constitutive relationship, that links mechanical stress and strain through the material's elastic properties.

$$\boldsymbol{\sigma} = \boldsymbol{C} : \boldsymbol{\epsilon} \tag{3.8}$$

where **C** is the fourth-order stiffness tensor representing the material properties, **ϵ** is the strain tensor representing the deformation of the material and **σ** is the stress tensor.

B.) Elastoplastic constitutive relationship: The elastoplastic constitutive model was used to potentially capture the non-linear deformation of the rock when subject to stresses exceeding a defined yield criterion. Several elastoplastic constitutive relationships exist, and the interested

reader could refer to articles such as [102], [239], [240], [241]. Mathematically, these constitutive models are defined using four appropriate functions, specifically: the elastic laws, yield functions, plastic potential function, and hardening law.

For our analysis, the Drucker-Prager yield criterion was employed (to check we get to the inelastic regime), as the formation is assumed to contain a significant proportion of shale and/or cemented sandstone, which are expected to exhibit ductile behaviour in certain zones. Furthermore, it was selected due to its smooth yield surface (as seen in Figure 2.9b), which facilitates numerical modelling by eliminating discontinuities in the derivates of the yield function.

The yield function, F, of the Drucker-Prager criterion is defined as follows in equation (3.9), where P is the effective mean stress defined in equation (3.10) and J_2 is the second invariant of the deviatoric stress expressed in equation (3.11). The parameter η relates the yield function to Mohr-Coulomb friction angle, $\boldsymbol{\theta}$, while ξ matches the yield function to the Mohr-Coulomb cohesive strength as detailed in equation (3.12). The implementation of this failure criterion using GeoMatFEM is discussed in section 3.4.

$$F = \sqrt{J_2} + \eta P - \xi c \tag{3.9}$$

$$P = -\frac{1}{3}(\boldsymbol{\sigma_1} + \boldsymbol{\sigma_2} + \boldsymbol{\sigma_3}) \tag{3.10}$$

$$J_2 = \frac{1}{3}\left[\boldsymbol{\sigma_1^2} + \boldsymbol{\sigma_2^2} - \boldsymbol{\sigma_2\sigma_3} + \boldsymbol{\sigma_3^2} - \boldsymbol{\sigma_1}(\boldsymbol{\sigma_2} + \boldsymbol{\sigma_3})\right] \tag{3.11}$$

$$\begin{aligned} \eta &= \frac{6\sin\theta}{\sqrt{3}(3 - \sin\theta)} \\ \xi &= \frac{6\cos\phi}{\sqrt{3}(3 - \sin\theta)} \end{aligned} \tag{3.12}$$

With the governing equations and constitutive framework established, it is essential to incorporate the effects of pore fluids, as pore pressure changes from CO_2 injection directly influence both effective stress and reservoir deformation in GCS applications. The Biot's theory of poromechanics offers a robust framework for capturing these fluid-solid interactions under single and multiphase flow. The following sub-section outlines this theory and coupling mechanisms for single-phase systems and extend this approach to address the multiphase fluid flow.

3.2.3 Single-phase poromechanics

For an isothermal single-phase flow involving an incompressible fluid within a poroelastic material, the theory of poroelasticity introduced by [18] establishes a relationship between variations in total stress and fluid pressure, as well as their effects on strain and fluid content. Expanding on the linear stress-strain relationship defined in Equation (3.8), Coussy [64], [119] presents the governing equations of poroelasticity in incremental form as follows:

$$\delta\boldsymbol{\sigma} = \mathbf{C}\colon \delta\boldsymbol{\epsilon} - b\delta p\mathbf{I} \tag{3.13}$$

where **C** is the stiffness matrix, δ**σ** represents the stress tensor, **ϵ** is the strain tensor which is defined as the symmetric gradient of the displacement vector, **u**, as follows $\boldsymbol{\epsilon} = \frac{1}{2}(\nabla u + (\nabla u)^T)$, b is the Biot's coefficient, δp is the change in pressure and **I** is the rank-2 identity tensor.

It was important for the derivation of the theory of poroelasticity to define the fluid mass content variation, ζ.

$$\zeta = \frac{\delta(\phi\rho_f)}{\rho_{f,0}} \tag{3.14}$$

Here ϕ is the porosity term, and $\rho_{f,0}$ is the reference fluid density. Equation (3.14), when differentiated, leads to an alternative that depicts the changes in volumetric strain, $\boldsymbol{\epsilon}_v$, and the bulk modulus of the fluid, M, through Equation (3.15):

$$\zeta = b\boldsymbol{\epsilon}_v + \frac{1}{M}\delta p \tag{3.15}$$

Considering equations (3.13) and (3.14), we define the effective stress, **δσ′**, for single-phase poroelasticity in incremental form as follows:

$$\boldsymbol{\delta\sigma}' = \delta\boldsymbol{\sigma} + b\delta p\mathbf{I} \tag{3.16}$$

Substituting equation (3.15) into equation (3.3) for a slightly compressible fluid, we obtain the incremental form of the fluid mass balance equation in terms of the pressure and the volumetric strain:

$$\frac{1}{M}\frac{\partial p}{\partial t} + b\frac{\partial \boldsymbol{\epsilon}_v}{\partial t} + \nabla\cdot(\boldsymbol{v}) = q \tag{3.17}$$

The linearized correlation between volumetric stress and volumetric strain, measured relative to the reference configuration, may be expressed as follows:

$$\boldsymbol{\sigma_v} - \boldsymbol{\sigma_{v,0}} = K_{dr}\boldsymbol{\epsilon_v} - b(p - p_0) \tag{3.18}$$

Using equation (3.18) we reformulated equation (3.17) in terms of the pressure and the volumetric total stress as follows:

$$\left(\frac{b^2}{K_{\mathrm{dr}}} + \frac{1}{M}\right)\frac{\partial p}{\partial t} + \frac{b}{K_{\mathrm{dr}}}\frac{\partial \boldsymbol{\sigma_v}}{\partial t} + \nabla \cdot (\boldsymbol{v}) = q \tag{3.19}$$

Equation (3.17) and (3.19) have two coupling terms: the Biot's Modulus, *M*, and the Biot's coefficient, *b*. These terms incorporate the rock and fluid properties as given by equation (3.20) [64]:

$$\frac{1}{M} = \frac{\phi_0}{K_f} + \frac{b - \phi_0}{K_s};\ b = 1 - \frac{K_{\mathrm{dr}}}{K_s} \tag{3.20}$$

In equation (3.18) and (3.20), K_f is the bulk modulus of the fluid (inverse of the fluid compressibility, C_f), K_s is the bulk modulus of the solid grain, and K_{dr} is the drained bulk modulus of the porous medium.

The formulation explicitly illustrates the hydromechanical coupling inherent in poromechanical systems, as the evolution of pore pressure, $\frac{\partial \mathrm{p}}{\partial \mathrm{t}}$, is expressed as a function of volumetric strain, $\boldsymbol{\partial \epsilon_v}$, and as a function of volumetric stress, $\boldsymbol{\partial \sigma_v}$, in equation (3.17) and equation (3.19), respectively.

3.2.4 Multiphase poromechanics

In deriving the multiphase poromechanics equation, we adopted the incremental approach recommended by [64], [114]. This method allows for the evolution of total stress to be captured at the Eulerian frame, without presuming a linear relationship at the Lagrangian frame as was done in equation (3.18).

The non-linear formulation is essential when dealing with fluids, like gases, as fluid phase saturations can vary continuously between zero and one, and capillary pressure introduces additional non-linearities. For a comprehensive discussion of the incremental approach in such contexts, refer to section 10.5.2 of [64].

In the incremental framework, under isotropic and isothermal conditions, the relationship between changes in pore pressure and corresponding increments in fluid mass is governed by the non-linear constitutive relationship presented as equation (3.21):

$$dp_\beta = \sum_\beta M_{\alpha\beta}\left(-b_\alpha d\boldsymbol{\epsilon_v} + \left(\frac{d\phi\rho}{\rho}\right)_\alpha\right) \tag{3.21}$$

Here $\mathbf{M} = M_{\alpha\beta} = M_{\beta\boldsymbol{\alpha}}$ denotes the Biot modulus, which, in the context of multiphase systems, is characterized as a symmetric and positive-definite tensor. The Biot coefficient, b, is represented as a vector in this formulation. For each fluid phase, the phase-specific Biot coefficient b_β is related to the overall Biot coefficient by $b = \sum_\beta b_\beta$. A common convention is to express the Biot coefficient for an individual phase as $b_\beta = S_\beta b$ [119], [238], [242]. In equation (3.21) it highlights how changes in pore pressure are influenced by both variations in volumetric strain, $\boldsymbol{d\epsilon_v}$, and changes in the fluid content variation, $\mathrm{d}\boldsymbol{\zeta_\alpha}$.

However, to derive the mass balance equation for a multiphase poroelastic medium, Equation (3.21) was first reformulated to express the fluid mass in terms of fluid pressure and volumetric strain as follows:

$$\left(\frac{d\phi\rho}{\rho}\right)_\alpha = b_\alpha d\boldsymbol{\epsilon}_v + \sum_\beta N_{\alpha\beta} dp_\beta \tag{3.22}$$

Where $\mathrm{N} = M^{-1} = \mathrm{N}_{\boldsymbol{\alpha\beta}} = \mathrm{N}_{\boldsymbol{\beta\alpha}}$ is the inverse of the Biot's modulus.

To formulate the relationship between deformation, total stress, and pore pressure in a multiphase porous medium, the effective stress principle was adopted, consistent with standard practice for single-phase systems. While capillary pressure in multiphase flow would require the introduction of an equivalent pressure to define effective stress within the linear poroelasticity framework as was done in the research by [114], [119], [243], this study neglects capillary effects. Consequently, the effective stress equation takes the following simplified form as defined by [64]:

$$\delta\boldsymbol{\sigma} = \delta\boldsymbol{\sigma}' - b\delta p\mathbf{1}, \qquad \delta\boldsymbol{\sigma} = \boldsymbol{C}:\delta\boldsymbol{\epsilon} \tag{3.23}$$

In equation (3.23), δp is the pressure of the fluid, $\delta\boldsymbol{\sigma}$ is the total stress and $\boldsymbol{\delta\sigma'}$ is the effective stress component. This formulation is used because a pressure equilibrium exists between the phases (i.e. $P_w = P_{CO2} = P$) and capillary pressure effects within the reservoir are negligible.

By combining the effective stress relationship given in equation (3.22) with equation (3.23), the resulting expression for the increment in fluid mass, ζ, was formulated as follows:

$$d\zeta_\alpha = \rho_\alpha b_\alpha \frac{1}{K_{dr}}\left(d\sigma_v + \sum_\beta b_\beta dp\right) + \rho_\alpha \sum_\beta N_{\alpha\beta} dp \tag{3.24}$$

Finally, by incorporating equation (3.24) into equation (3.5), we obtained the comprehensive fluid mass balance equation, governing multiphase poroelastic systems defined in equation (3.25):

$$\frac{\partial}{\partial t}\left(\rho_\alpha \sum_\beta \left(N_{\alpha\beta} + \frac{b_\alpha b_\beta}{K_{dr}}\right)p\right) + \frac{1}{K_{dr}}\frac{\partial}{\partial t}(\rho_\alpha b_\alpha \sigma_v) + \nabla \cdot \boldsymbol{w}_\alpha = q_\alpha \tag{3.25}$$

Except for the coupling coefficient, $N_{\alpha\beta}$, for the water-gas system under the assumption of negligible capillary pressure, all terms in equation (3.25) have been introduced earlier. The definition of $N_{\alpha\beta}$ under these conditions is provided in the equations below [119];

$$N_{gg} = \phi_0 S_g c_g + S_g^2 N \tag{3.25a}$$

$$N_{gw} = N_{wg} = S_g S_w N \tag{3.25b}$$

$$N_{ww} = \phi_0 S_w c_w + S_w^2 N \tag{3.26c}$$

In this context N is given by $N = (b - \phi)(1 - b)/K_{dr}$. Here the indices w and g refer to water and gas phases, respectively. Φ_0 represents the reference porosity, while Φ denotes the porosity in the current state, which is approximated by $\phi \approx \phi_0$. S_w, S_g, c_w, c_g, are the saturations of water phase, gas phase, compressibility of the water phase and compressibility of the gas phase, respectively.

3.3 Numerical Implementation of Hydromechanical (u-p) Analysis

We propose the details of the numerical implementation of the coupled hydromechanical (u-p) analysis, by highlighting the integration of two computational tools. The hydraulic processes which provide a platform for modelling multiphase fluid flow and pressure evolution are implemented within the MRST repository. Concurrently, the geomechanical effects of displacement, strain and stress evolution are modelled using finite element methods within GeoMatFEM research code. By coupling these tools explicitly, a comprehensive (u-p) formulation is achieved, enabling a detailed assessment of the interactions between pore pressure and mechanical deformation. Here we describe the discretization techniques, the temporal discretization, the numerical scheme used to solve the set of discrete equations.

3.3.1 Implementation of flow and mass balance equations in MRST

The equations reported in this section have been obtained from the following references [61], [237], [244].

For a structured grid we considered two immiscible and incompressible fluids, typically water (w) and CO_2 (g), flowing through a rigid, homogeneous porous medium. The main assumptions adopted here are consistent with those outlined in section 3.2.1B and include:

- The pores within the reservoir are interconnected, sufficiently large that the surface tension effects are minor,
- The capillary pressure effects within the reservoir are negligible,
- A pressure equilibrium exists between the phases (i.e. $P_w = P_{CO2} = P$),
- Temperature effects are constant throughout, thereby assuming isothermal conditions and,
- The sum of all the phases in the pores of reservoir are equal to 100% (i.e. $\sum_\alpha S_\alpha = 1$).

With these assumptions, the physical domain was discretized using the finite volume method.

A.) Control volume discretization: As seen in Figure 3.2 (used for illustration), the domain was subdivided into a structured set of control volumes ($\boldsymbol{\Omega}$i & $\boldsymbol{\Omega}$k), with each finite volume characterized by a unique set of rock and fluid properties. Fluid transfer occurs between adjacent control volumes.

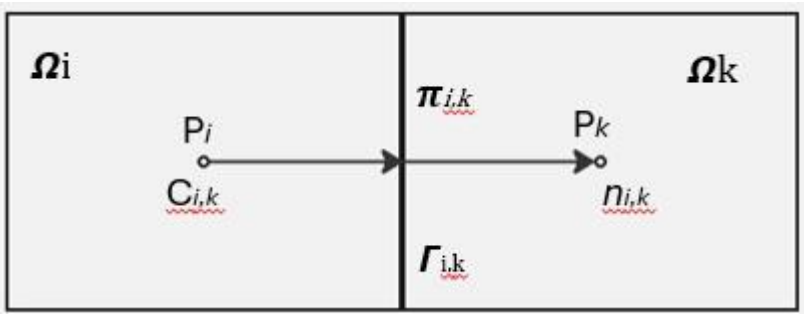

Figure 3.2: Control volume for FVM discretization.

Integrating the mass balance equation (Equation 3.5) over each cell yields equation 3.27:

$$\frac{\partial}{\partial t}\left(\phi_i S_{\alpha,i} V_i\right) + \sum_{f \in \partial i} \boldsymbol{v}_{\alpha,f} = q_{\alpha,i} V_i \tag{3.27}$$

Here, ϕ_i denotes the porosity of cell i, $S_{\alpha,\,i}$ is the phase saturation, V_i, is the cell volume, $\boldsymbol{v}_{\alpha,f}$, represents the Darcy velocity through face, f, and $q_{\alpha,i}$ is the rate at which the fluid phase α is injected into the control volume per unit time.

B.) Evaluation of the phase flux: To determine the flux across each half face, $\boldsymbol{\Gamma}_{i,k}$, we employ the two-point flux approximation method. In this approach, an essential step in evaluating the flux between two neighbouring cell volumes, $\boldsymbol{\Omega}_{i,k}$ is the determination of the transmissibility

that links these grids. For a conforming grid, every half-face, $\boldsymbol{\Gamma}_{i,,k,}$ is matched by a neighbouring half-face, $\boldsymbol{\Gamma}_{k,I}$. These paired faces have equal areas but have opposite normal vector (as illustrated in Figure 3.2). Specifically,

$$A_{i,k} = A_{k,i}, \mathbf{n}_{k,i} = -\mathbf{n}_{i,k} \tag{3.28}$$

where $A_{i,\,k}$ is the area of the interface and $\mathbf{n}_{i,\,k}$ is the outward normal vector at the face between cells *i* and *k*. The flux across each face is then determined using the following equation:

$$v_{i,k} \approx A_{i,k}\boldsymbol{v}(x_{i,k}) \cdot n_{i,k} = -A_{i,k}\left(\mathbf{K}\frac{k_{r\alpha}}{\mu_\alpha}(\nabla p_\alpha - \rho_\alpha \boldsymbol{g}\nabla z)\right)(\mathrm{x}_{i,k}) \cdot \boldsymbol{n}_{i,k} \tag{3.29}$$

here $A_{i,\,k}$ is the interface area, $n_{i,\,k}$ is the outward normal vector at the face, and $x_{i,\,k}$ is the spatial coordinates of the interface between grid cells *i* and *k*, while all other variables have been previously defined**.**

The product of interface area and permeability, projected along the normal direction and normalized by the distance between the grid cell centroids, defines the transmissibility for the cell pair. The upwind phase mobility, $\lambda_{\boldsymbol{\alpha},\,\mathrm{f}}$ is used at the interface. This the transmissibility, T_{ik} and mobility, $\lambda_{\alpha,\,\mathrm{f}}$ is given by:

$$T_{ik} = \frac{\boldsymbol{K}_{ik}A_{i,k}}{C_{ik}} \tag{3.30}$$

$$\lambda_{\alpha,f} = \frac{k_{r\alpha,f}}{\mu_\alpha} \tag{3.31}$$

where $\boldsymbol{K}_{ik}$ is the harmonic average permeability between cells, and $C_{i,\,k}$ the distance between cell centres. Using these definitions, equation (3.29) can be reformulated as follows (all variables have been previously defined):

$$\boldsymbol{v}_{\alpha,ik} = -T_{ik}\lambda_{\alpha,f}[p_i - p_k - \rho_\alpha \boldsymbol{g}(z_i - z_k)] \tag{3.32}$$

where p_i and p_k are the pressures, and z_i and z_k are the elevations at the centres of the cell volume *i* and *k*, respectively.

C.) Temporal discretization: The multiphase mass balance equation contains a time derivative only in the accumulation term and is therefore discretized using a finite difference scheme as follows:

$$\frac{\partial m_{\alpha,i}}{\partial t} \approx \frac{m_{\alpha,i}^{n+1} - m_{\alpha,i}^{n}}{\Delta t} = \frac{\phi_i S_{\alpha,i}^{n+1}\rho_{\alpha,i}^{n+1} - \phi_i S_{\alpha,i}^{n}\rho_{\alpha,i}^{n}}{\Delta t} \tag{3.33}$$

Here, the superscript n indicates the current time step, while Δt represents the time step increment.

D.) Fully discrete system and solution strategy:

By combining the spatial discretization, the phase flux and temporal discretization under the assumption that the fluids are immiscible at each control volume, a fully implicit backward Euler approach is adopted to ensure stability and accuracy:

$$\phi_i \rho_\alpha V_i \frac{S_{\alpha,i}^{n+1} - S_{\alpha,i}^{n}}{\Delta t} + \sum_{k \in N(i)} \left[-T_{ik} \lambda_{\alpha,ik}^{n+1} \left(p_i^{n+1} - p_k^{n+1} - \bar{\rho}_\alpha^{n+1} \boldsymbol{g}(z_i - z_k) \right) \right] = q_{\alpha,i}^{n+1} V_i \quad (3.34)$$

Equation (3.34) is non-linear and requires an iterative approach to obtain the primary unknowns of pressure and saturation. The automatic differentiation framework within MRST repository was utilized. This method applies the Newton-Raphson method to efficiently resolve the resulting set of linear equations (see chapter 12 of [61]).

These primary unknowns of pressure and saturation are computed at the centroids of each hexahedral control volume within the structured grid. Each cell is represented as a hexahedron with eight corner nodes, numbered from 1 to 8 (as depicted in Figure 3.3), ensuring an efficient mapping and assembly from local to global system matrices.

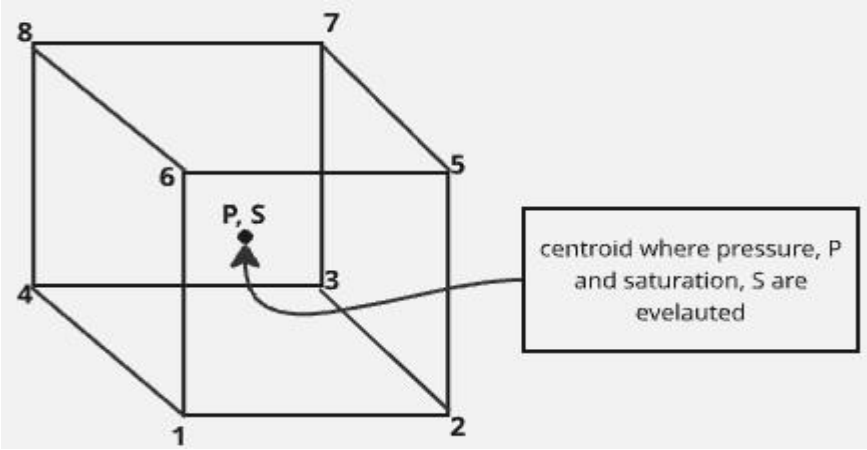

Figure 3.3: Hexahedral element with cell-centred unknowns (8-corner nodes shown)

To ensure integration into the mechanics simulator, which is based on the finite element method (FEM) and requires nodal input, a linear interpolation procedure is employed to transfer the cell-centred pressure values to the nodal points in equation (3.35)

$$P_n = \frac{1}{N_n} \sum_{i \in \mathcal{N}_n} p_i \quad (3.35)$$

Here, P_i is the pressure at the centroid of the grid cell, i, N_n, number of cells sharing node, n and P_n is the interpolated pressure at node, n.

This nodal pressure distribution is supplied to the GeoMatFEM research code, which employs the finite element method (FEM) to solve the quasistatic linear momentum equation, governing reservoir geomechanics. By incorporating the interpolated pore pressures as a load in the FEM framework, the model captures the effect of fluid pressure on the rock matrix, allowing for an evaluation of deformation and stress redistribution within the reservoir.

3.3.2 Implementation of U-P analysis using GeoMatFEM

We let $\Omega \subset \mathbb{R}^d$, be the solid domain with boundary $\Gamma = \Gamma_u \cup \Gamma_t$. Within MRST, each grid cell consists of 8 corner nodes, however, to improve the accuracy of our solution, the elements within the GeoMatFEM repository are extended to a 20-node serendipity domain. The 20-node hexahedral elements comprise of eight corner nodes (nodes 1 to 8) and twelve mid-side nodes (nodes 9 to 20), (refer to figure 2.11)**.**

For a one-way coupling scheme adopted for our analysis, the primary unknown within GeoMatFEM is the displacement, $\boldsymbol{u}(\boldsymbol{x}, t)$. That is, we evaluate the effects of pressure on displacement field.

The pore pressure obtained from the MRST repository is mapped on to the 8 corner nodes of each element of the FE mesh via a consistent projection. The solid skeleton is modelled as a linear elastic with stiffness tensor, **C;** with anisotropy captured by assigning different petrophysical and stiffness properties to each layer of the rock unit. Coupling to pore pressure is represented through the Biot's coefficient, b; and body forces are $\rho_b \boldsymbol{g}$**.**

A.) Weak form or variational form of linear momentum equation:

By combining equations (3.7 and 3.13) and applying the divergence theorem, we obtain the variational form of the linear momentum equation, defined as follows:

$$\int_\Omega \boldsymbol{\epsilon}(\delta \boldsymbol{u}) : \mathbf{C} : \boldsymbol{\epsilon}(\boldsymbol{u}) d\Omega - \int_\Omega b p_{\mathrm{MRST}} \nabla \cdot \delta \boldsymbol{u} d\Omega = \int_\Omega \rho \boldsymbol{g} \cdot \delta \boldsymbol{u} d\Omega + \int_{\Gamma_t} \bar{\boldsymbol{t}} \cdot \delta \boldsymbol{u} d\Gamma \qquad (3.36)$$

Here the variables not previously defined, include:

- $\boldsymbol{\epsilon}(\cdot)$ is the small-strain operator, where $\boldsymbol{\epsilon}(\boldsymbol{u}) = \frac{1}{2}(\nabla u + (\nabla u)^T)$,
- p_{MRST} prescribed pore-pressure field imported from MRST and projected onto the corner nodes of FE mesh and,
- $\bar{\boldsymbol{t}}$, the prescribed traction.

B.) Spatial discretization:

We discretize, Ω, with a conforming FE mesh of 3-D hexahedral isoparametric elements. The displacement field is interpolated with standard vector shape functions, and the small-strain operator is formed from their spatial gradient's equations (3.37-3.38):

$$\boldsymbol{u}(\boldsymbol{x}) \approx \mathbf{N}_i(\xi, \eta, \zeta)\hat{\boldsymbol{u}}_i \tag{3.37}$$

$$\boldsymbol{\epsilon}(\boldsymbol{u}) = \mathbf{B}(\xi, \eta, \zeta)\hat{\boldsymbol{u}}_i \tag{3.38}$$

where $\mathbf{N}_i$ collects the 20 shape functions of each cell, *i*, and **B** is the symmetric strain–displacement matrix.

Having introduced the displacement interpolation and the small-strain operator, we evaluate the derivatives of the shape function $\boldsymbol{N_i}$, for 8/12/16/20 nodes using a sequential approach (adopted by [245]) through the following relationship:

- For 8-corner node elements the shape function is derived:

$$N_i = \frac{1}{8}(1 + \xi_0)(1 + \eta_0)(1 + \zeta_0), \qquad i = 1,2, \dots ,8 \tag{3.39a}$$

- For 12-node elements the shape function is obtained by:

$$\begin{aligned} &\xi_i = 0, \eta_i = \pm 1, \zeta_i = \pm 1, \\ &N_i = \frac{1}{4}(1 - \xi_0^2)(1 + \eta_0)(1 + \zeta_0), \qquad i = 9, \dots ,12 \end{aligned} \tag{3.39b}$$

The derivatives at the vertices are calculated by updating those of previous elements as follows:

$$\begin{aligned} N_1 &= N_1 - \tfrac{1}{2}N_9, \quad & N_2 &= N_2 - \tfrac{1}{2}N_9 \\ N_3 &= N_3 - \tfrac{1}{2}N_{10}, \quad & N_4 &= N_4 - \tfrac{1}{2}N_{10} \\ N_5 &= N_5 - \tfrac{1}{2}N_{12}, \quad & N_6 &= N_6 - \tfrac{1}{2}N_{12} \\ N_7 &= N_7 - \tfrac{1}{2}N_{11}, \quad & N_8 &= N_8 - \tfrac{1}{2}N_{11} \end{aligned} \tag{3.39c}$$

- For 16-node elements the shape function is obtained as follows:

$$\begin{aligned} &\xi_i = \pm 1, \eta_i = 0, \zeta_i = \pm 1, \\ &N_i = \frac{1}{4}(1 - \xi_0^2)(1 + \eta_0)(1 + \zeta_0), i = 13, \dots ,16 \end{aligned} \tag{3.39d}$$

The derivatives at the vertices are calculated by updating those of previous elements as follows:

$$
\begin{aligned}
N_1 &= N_1 - \frac{1}{2}N_{14}, \quad N_2 = N_2 - \frac{1}{2}N_{13} \\
N_3 &= N_3 - \frac{1}{2}N_{13}, \quad N_4 = N_4 - \frac{1}{2}N_{14} \\
N_5 &= N_5 - \frac{1}{2}N_{15}, \quad N_6 = N_6 - \frac{1}{2}N_{16} \\
N_7 &= N_7 - \frac{1}{2}N_{16}, \quad N_8 = N_8 - \frac{1}{2}N_{15}
\end{aligned} \tag{3.39e}
$$

- For 20-node element, the shape function derived by:

$$
\begin{aligned}
&\xi_i = \pm 1, \eta_i = \pm 1, \zeta_i = 0 \\
&N_i = \frac{1}{4}(1 - \xi_0^2)(1 + \eta_0)(1 + \zeta_0), i = 17, \dots, 20
\end{aligned} \tag{3.39f}
$$

$$
\begin{aligned}
N_1 &= N_1 - \frac{1}{2}N_{17}, \quad N_2 = N_2 - \frac{1}{2}N_{18} \\
N_3 &= N_3 - \frac{1}{2}N_{19}, \quad N_4 = N_4 - \frac{1}{2}N_{20} \\
N_5 &= N_5 - \frac{1}{2}N_{17}, \quad N_6 = N_6 - \frac{1}{2}N_{18} \\
N_7 &= N_7 - \frac{1}{2}N_{19}, \quad N_8 = N_8 - \frac{1}{2}N_{20}
\end{aligned} \tag{3.39g}
$$

Collecting these scalars into a vector interpolation yield:

$$
\mathbf{N}_i(\xi, \eta, \zeta) = [N_1\mathbf{I}_3 \quad N_2\mathbf{I}_3 \cdots N_{20}\mathbf{I}_3], \boldsymbol{u} = \mathbf{N}_i\widehat{\boldsymbol{u}}_i, \widehat{\boldsymbol{u}}_i \in \mathbb{R}^{60} \tag{3.40}
$$

and, with the interpolation fixed, we map derivatives to physical space to obtain gradients and the **B**-matrix used in all element integrals. Specifically, the isoparametric geometry map is:

$$
x(\xi, \eta, \zeta) = \sum_{i=1}^{20} N_i(\xi, \eta, \zeta)x_i \tag{3.41}
$$

with $x_i = (x_i, y_i, z_i)$ the nodal coordinates. The Jacobian and its determinant follow as:

$$
\mathrm{J} = \frac{\partial x}{\partial(\xi, \eta, \zeta)} = \begin{bmatrix}
\sum_{i=1}^{20} \frac{\partial N_i}{\partial \xi} x_i & \sum_{i=1}^{20} \frac{\partial N_i}{\partial \eta} x_i & \sum_{i=1}^{20} \frac{\partial N_i}{\partial \zeta} x_i \\
\sum_{i=1}^{20} \frac{\partial N_i}{\partial \xi} y_i & \sum_{i=1}^{20} \frac{\partial N_i}{\partial \eta} y_i & \sum_{i=1}^{20} \frac{\partial N_i}{\partial \zeta} y_i \\
\sum_{i=1}^{20} \frac{\partial N_i}{\partial \xi} z_i & \sum_{i=1}^{20} \frac{\partial N_i}{\partial \eta} z_i & \sum_{i=1}^{20} \frac{\partial N_i}{\partial \zeta} z_i
\end{bmatrix} \tag{3.42a}
$$

and the chain rule gives spatial gradients via:

$$\begin{bmatrix} \frac{\partial N_i}{\partial x} \\ \frac{\partial N_i}{\partial y} \\ \frac{\partial N_i}{\partial z} \end{bmatrix} = \mathrm{J}^{-1} \begin{bmatrix} \frac{\partial N_i}{\partial \xi} \\ \frac{\partial N_i}{\partial \eta} \\ \frac{\partial N_i}{\partial \zeta} \end{bmatrix} \tag{3.42b}$$

These gradients assemble pointwise into the Voigt-ordered strain–displacement blocks:

$$\mathrm{B}_i = \begin{bmatrix} \frac{\partial N_i}{\partial x} & 0 & 0 \\ 0 & \frac{\partial N_i}{\partial y} & 0 \\ 0 & 0 & \frac{\partial N_i}{\partial z} \\ \frac{\partial N_i}{\partial y} & \frac{\partial N_i}{\partial x} & 0 \\ 0 & \frac{\partial N_i}{\partial z} & \frac{\partial N_i}{\partial y} \\ \frac{\partial N_i}{\partial z} & 0 & \frac{\partial N_i}{\partial x} \end{bmatrix}, \qquad \mathrm{B} = [\mathrm{B}_1\ \mathrm{B}_2 \cdots \mathrm{B}_{20}] \tag{3.43}$$

So that, $\boldsymbol{\epsilon}(\boldsymbol{u}) = \mathbf{B}\hat{\boldsymbol{u}}_i$. The volumetric strain is $\boldsymbol{\epsilon}_v = \nabla \cdot \boldsymbol{u} = \mathbf{m}^\top \mathbf{B}\hat{\boldsymbol{u}}_e$ with $\mathbf{m} = [1,1,1,0,0,0]^\top$.

With the interpolation Jacobian, and **B**-matrix defined, the numerical integration of these element matrices and load vectors are needed. We start by evaluating the volume (and face) integrals in the parent domain using a tensor-product Gauss–Legendre rule. For 20-node, a 3×3×3 scheme—three points in each of ξ, η, ζ is standard because it exactly integrates polynomials up to fifth order in each direction and provides reliable accuracy for elasticity terms. Accordingly, the element integral is approximated as:

$$\int_{\Omega_e} f(\boldsymbol{x}) d\Omega \approx \sum_{i=1}^{n_\xi} \sum_{j=1}^{n_\eta} \sum_{k=1}^{n_\zeta} f(\xi_i, \eta_j, \zeta_k) \det\mathbf{J}(\xi_i, \eta_j, \zeta_k) w_i w_j w_k \tag{3.44}$$

with $n_\xi = n_\eta = n_\zeta = 3$ and the abscissae and weights (Table 3.1)

Table 3.1 Coordinates and weights for Gauss quadrature.

nip	ξ_i	ω_i	$p = 2nip - 1$
1	0	2, 0	1
2	$\pm\frac{1}{\sqrt{3}}$	1, 0	3
3	0	8/9	5
	$\pm\sqrt{\frac{3}{5}}$	5/9	

With this derivation, at each Gaussian point, g, and material stiffness, **C,** we form the global elastic stiffness matrix as follows:

$$\mathbf{K}_e = \int_{\Omega_e} \mathbf{B}^\top \mathbf{C}\mathbf{B} d\Omega \approx \sum_g \mathbf{B}_g^\top \mathrm{C}_g \mathbf{B}_g \det\mathbf{J}_g w_g \tag{3.45}$$

where **B** is the strain-displacement matrix, **C** is the fourth order tensor, and $\det\mathbf{J}_g w_g$ is the from the Gauss quadrature.

The pressure-displacement coupling term is derived using the following relationship:

$$\mathbf{Q}_e = \int_{\Omega_e} b\mathbf{B}^\top \mathbf{m}\mathbf{N}_p d\Omega \approx \sum_g b\mathbf{B}_g^\top \mathbf{m}\mathbf{N}_{p,g} \det\mathbf{J}_g w_g \tag{3.46}$$

With the mapped pressure dofs $\hat{\boldsymbol{p}}_{\mathrm{FE}}$ known, the global system quasi-static mechanics with prescribed pressure on the nodes is given as:

$$\mathbf{K}\hat{\boldsymbol{u}} = \boldsymbol{f}_u + \mathbf{Q}\hat{\boldsymbol{p}}_{\mathrm{FE}} \tag{3.47}$$

3.4 Boundary Conditions for GeoMatFEM

Within the GeoMatFEM repository, we partition the boundary into Dirichlet and Neumann sections, $\Gamma = \Gamma_u \cup \Gamma_t$, with $\Gamma_u \cap \Gamma_t = \emptyset$. For our analysis, the mechanical problem is solved by imposing Neumann boundary condition on the top of the domain and Dirichlet displacement boundary conditions on all other sections of the reservoir.

For Dirichlet displacement boundary condition, Γ_u, the domain is partitioned into bottom, Γ_b, roller, Γ_r, and top segments, Γ_{top} as follows:

$$\Gamma = \Gamma_b \cup \Gamma_r \cup \Gamma_{top}, \Gamma_b \cap \Gamma_r = \Gamma_r \cap \Gamma_{top} = \Gamma_b \cap \Gamma_{top} = \emptyset \quad (3.48)$$

Table 3.2: Boundary conditions for mechanical domain.

Bottom domain Γ_b (fixed):	$u_x(x,y,0,t) = 0, u_y(x,y,0,t) = 0, u_z(x,y,0,t) = 0 (3.48a)$
X-axis side boundary Γ_r (Roller constraints):	$u_y(x,0,z,t) = 0, u_y(x,L_y,z,t) = 0 \quad (3.48b)$
Y-axis side boundary Γ_r (Roller constraints):	$u_x(0,y,z,t) = 0, u_x(L_x,y,z,t) = 0 \quad (3.48c)$
Top domain, Γ_{top}, (no displacement):	no displacement constraint and left free in XYZ-direction

3.5 Evaluating the seismic moment, M_o, seismic magnitude, M_w, energy magnitude, M_e, and radiated seismic energy, E_r.

Using the pressure, and displacement profiles obtained from solving the coupled equations outlined above, we evaluate the seismic moment M_0, seismic magnitude M_w, and energy magnitude M_e of the domain. This evaluation enables us to assess the size of the earthquake and the energy released because of the seismic activity.

3.5.1 Evaluation of seismic moment, M_o, and seismic magnitude, M_w

In evaluating the maximum induced earthquake magnitude, we used the model proposed by [163]. This was done by evaluating the seismic moment, M_o, that describes the overall size of the earthquake, where the rupture induced by fault reactivation across the fault boundary was evaluated using equation (**3.49**), where G is the shear modulus of the fault, A is the area of the rupture surface expressed in meters (m^2), and d is the slip distance in meters (m) [130].

$$M_0 = G \cdot A \cdot d \quad (3.49)$$

To scale the seismic moment, M_0, to a seismic magnitude, M_w, we referred to the work published by [165] who proposed a standard regression relation between body-wave magnitudes, m_B, and surface-waves magnitudes, M_s, given by equation (3.50) and between body-waves, m_B, and released seismic energy, E_r, given by equation (3.51)

$$m_B = 0.63M_S + 2.5 \quad (3.50)$$

$$\log E_r = 2.4m_B - 1.2 \quad (3.51)$$

However, with the change in the medium-period broadband for measuring body-wave magnitudes, m_B, changing to the use of the US World-Wide Standard Seismograph System (WWSSN) in the 1960s, who followed the suggestions by Gutenberg and Richter and inserted equation (3.50) into equation (3.51):

$$\log E_r = 1.5M_S + 4.8 \tag{3.52}$$

Equation (3.52) is often referred to as the "Gutenberg-Richter" energy magnitude relationship. However, several authors such as [167], [168] found that $\log E_s \propto 1.5M_s$ was mostly valid for moderate earthquakes and the surface-wave magnitudes, M_s, tend to surface for very large earthquakes, thereby underestimating the real size of the earthquake.

To account for this shortcoming, we adopted the work by [164] who started by finding a relationship between seismic moment, M_0, and the seismic energy, E_r, (assuming complete stress drop, $\Delta\boldsymbol{\sigma}$) given by equation (3.53):

$$E_r = \frac{\Delta\sigma}{2G} M_0 \tag{3.53}$$

As a result, it was replaced by M_S in the $\log E_r - M_S$ relationship derived in equation (3.52) with M_w, representing the intended non-saturating moment (or "work") magnitude. By applying these relationships with international standard units, equation (3.54) was obtained:

$$\log E_r = \log M_0 - 4.3 = 1.5M_w + 4.8 \tag{3.54}$$

By resolving equation (3.54) for M_w, the following relationship was obtained:

$$M_w = \frac{\log M_0 - 4.3 - 4.8}{1.5} = \frac{\log M_0 - 9.1}{1.5} \tag{3.55}$$

This is considered an oversimplified concept of seismic scaling therefore to avoid presenting the entire earthquake source spectrum with just a single parameter which is Mw, specialists such as [166], [167], [168], [177], the energy magnitude, M_e, which largely incorporates the small fraction of released elastic wave energy, E_r, and its dominant frequency content.

3.5.2 Evaluation of energy magnitude, M_e

To get the relationship between the energy magnitude, M_e, seismic magnitude, M_w, seismic moment, M_0, released seismic energy, E_r, is given by equation 3.56 as suggested by [167]:

$$M_e = M_w + \frac{4.3 + 4.7}{1.5} = M_w + \frac{\log\left(\frac{E_S}{M_0}\right) + 4.7}{1.5} \tag{3.56}$$

With equation (3.56), the amplitudes over the radiated energy release, for wave propagation and source radiation pattern effects are determined.

By utilizing the seismic moment (M_0), energy magnitude, (M_e) we can determine the corner frequency, which provides a compatible reference point for our analysis. This relationship is effectively illustrated in the seismic moment graph versus frequency content (see Appendix A [246]), allowing us to ensure that the selected frequency range is consistent with the dynamic characteristics of the reservoir and the relevant seismic events.

3.5.3 Evaluation of radiated seismic energy, E_r.

Following [167], [247], under the assumption of complete stress drop, where the fault slip releases all its elastic strain energy accumulated prior to rupture, the radiated energy, E_r is evaluated as follows:

$$\log_{10} E_r = \frac{3}{2}(M_e + 2.9) \tag{3.57}$$

3.6 Governing Equations, Constitutive Relationship, Boundary Conditions, and Numerical discretization for Multi-field Wave Propagation Analysis

After the determination of the seismic moment in Stage 1, the GeoMatFEM research code is employed to conduct the numerical simulation of wave propagation. To show how the results are obtained, the governing equations necessary for u-v-p formulation are first outlined, providing a clear foundation for how the seismic response is captured and interpreted within the simulator.

For the coupled solid-fluid system, the governing conservation laws are derived based on the Mixture Theory principle [192], which provide a rigorous framework for modelling multiphase interactions. The theory and formulation with respect to the governing equations, constitutive relationships, numerical discretization, and numerical implementations, are obtained from [191], [192].

The dynamic behaviour of the model is described by the mass balance (equation 3.58 & 3.59) and linear momentum (equation 3.60 & 3.61) equations for both phases, **α**, denoted as S for solid, and F for the fluid phase given by the following equations:

$$\dot{\rho}^S + \rho^S \nabla \cdot \boldsymbol{v} = 0 \tag{3.58}$$

$$\dot{\rho}^F + \rho^F \nabla \cdot \boldsymbol{w} = 0 \tag{3.59}$$

$$\rho^S \dot{\boldsymbol{v}} = \nabla \cdot \boldsymbol{\sigma}^S + \rho^S \boldsymbol{g} + \boldsymbol{h}^S \tag{3.60}$$

$$\rho^F \dot{\boldsymbol{w}} + \nabla \boldsymbol{w} \cdot \boldsymbol{w_R} = \nabla \cdot \boldsymbol{\sigma}^F + \rho^F \boldsymbol{g} + \boldsymbol{h}^F \tag{3.61}$$

Here, ρ^F and ρ^s represent the partial mass densities of the fluid and solid phases respectively. These are defined as $\rho^F = \varphi\rho_F$ and $\rho^S = (1-\varphi)\rho_S$, where φ is the porosity of the medium. Each is calculated by multiplying the porosity with its intrinsic density of the corresponding material. The velocity vectors of the solid, fluid, and relative fluid are denoted by $\boldsymbol{v}$, $\boldsymbol{w}$, $\boldsymbol{w_R}$. The variable **g** is the acceleration due to gravity term, $\boldsymbol{\sigma}^S$ and $\boldsymbol{\sigma}^F$ are the Cauchy stress tensors of the solid and fluid phases respectively. The volume specific local interaction between forces defined by variable, $\mathbf{h}^{\boldsymbol{\alpha}}$, has the following relationship $\sum_{\alpha=S,F} \boldsymbol{h}^{\alpha} = 0$. In addition, the time derivative, spatial gradient field, scalar product, and divergence operators are denoted as $(*)$, $\nabla(*)$, "$\cdot$", $\nabla\cdot$, respectively.

It is worth mentioning that the mass balance and linear momentum equations utilized in the u-v-p analysis takes into consideration the dynamic momentum balance for the fluid and solid phases, accounting for inertial effects, fluid acceleration, and phase interaction forces within a two-phase mixture framework unlike the quasi-static condition stated in equation (3.7) that describes the stress variation due to fluid injection. This dynamic formulation captures the dynamic behaviour of pore fluids, making it essential for simulating seismic wave propagation, and high-frequency oscillations within the domain.

Based on the assumption of homogeneity, linear elasticity and anisotropy in the layered domain, the following constitutive relationships and boundary conditions for the fluid and solids are provided:

A.) Darcy law: For steady, laminar flow with a low Reynolds number, the constitutive relationship between flow rate and pore pressure gradient is given by equation (3.62):

$$\varphi \boldsymbol{w}_R = \left(-\frac{\boldsymbol{k}^F}{\gamma_F}\right) \nabla p \tag{3.62}$$

Here, $\boldsymbol{k}^F$ is the second order hydraulic conductivity tensor, $\varphi \boldsymbol{w}_R$ represents the Darcy velocity. The intrinsic fluid weight, γ_F, is given by $\gamma_F = \rho_F g$, where g is the acceleration due to gravity and ρ_F the density of the fluid.

B.) Volume specific local interaction for fluid: The constitutive relationship that describes how the resident CO_2 fluid interacts with the surrounding solid structure, contributing to the net force balance in the fluid's momentum is given by equation (3.63):

$$\boldsymbol{h}^F = -\varphi^2 \gamma_F \boldsymbol{k}^{F,-1} \boldsymbol{w}_R + p\nabla\varphi \tag{3.63}$$

C.) Biot's effective stress principle and Hooke's law: For the solid domain, the effective stress principle and the Hooke's law are adopted as the constitutive equations. By combining these equations, we obtain the following relationship:

$$\boldsymbol{\sigma}'^S = \boldsymbol{\sigma} + \boldsymbol{b}p = \mathbf{C}:\frac{1}{2}(\nabla\boldsymbol{u} + \nabla^T\boldsymbol{u}) = \mathbf{C}:\nabla^s\boldsymbol{u} \tag{3.64}$$

$$\boldsymbol{b} = (\mathbf{1} - \mathbf{C}\mathbf{S}_S):\mathbf{1} \tag{3.65}$$

Here, $\boldsymbol{\sigma}'^S$ denotes the second order effective stress tensor, while $\boldsymbol{\sigma}$ is the total stress tensor accounting for both solid and the fluid contributions. The term p refers to the pore pressure, and $\boldsymbol{b}$ is not a scalar quantity but a second order Biot effective stress coefficient tensor [248]. The symmetric gradient operator is denoted by, ∇^s, and $\boldsymbol{u}$ denotes the solid displacement vector. Additionally, $\mathbf{S}_s$ is the compliance tensor and $\mathbf{C}$ is the fourth order stiffness matrix.

In this work, anisotropy is introduced through a stratified domain composed of multiple layers, each characterized by distinct material properties. While the overall domain exhibits anisotropic behaviour, each individual layer is assumed to have an isotropic linear elastic medium. Consequently, the mechanical response within each layer is governed by an isotropic stiffness matrix, using Lamé parameters, where λ is the first Lame parameter and μ is the shear modulus. This approach simplifies the constitutive modelling while preserving the physical relevance of the domain's layered heterogeneity. The fourth-order stiffness tensor **C,** is defined for each layer as follows:

$$\mathbf{C} = \begin{bmatrix} \lambda+2\mu & \lambda & \lambda & 0 & 0 & 0 \\ \lambda & \lambda+2\mu & \lambda & 0 & 0 & 0 \\ \lambda & \lambda & \lambda+2\mu & 0 & 0 & 0 \\ 0 & 0 & 0 & \mu & 0 & 0 \\ 0 & 0 & 0 & 0 & \mu & 0 \\ 0 & 0 & 0 & 0 & 0 & \mu \end{bmatrix} \tag{3.66}$$

With the governing laws (equation 3.58 - 3.61) and the constitutive relationships (equation 3.62 & 3.64) we obtain the following strong forms of the partial differential equations (PDEs):

$$\rho^S \dot{\boldsymbol{v}} = \nabla \cdot [\boldsymbol{\sigma}'^S - (\boldsymbol{b} - \varphi \mathbf{1})p] + \rho^S \boldsymbol{g} + \varphi^2 \gamma_F \boldsymbol{k}^{F,-1} \boldsymbol{w}_R - p \nabla \varphi \tag{3.67}$$

$$\rho^F \dot{\boldsymbol{w}} + \rho_F \nabla \boldsymbol{w} \cdot \boldsymbol{w}_R = -\varphi \nabla p + \rho^F \boldsymbol{g} - \varphi^2 \gamma_F \boldsymbol{k}^{F,-1} \boldsymbol{w}_R \tag{3.68}$$

$$\Lambda \dot{p} + \boldsymbol{b} : \nabla^s \boldsymbol{v} + \frac{1}{\rho_F} \nabla \cdot (\rho^F \boldsymbol{w}_R) = 0 \tag{3.69}$$

Equation (3.67 & 3.68) represent the linear momentum of the solid and fluid phases, while equation (3.69) is the mass balance for both phases. This was obtained following the procedure presented by [238]. The compressibility modulus, Λ, is a scalar quantity defined as follows [248]:

$$\Lambda = \frac{(1-\varphi)}{\mathrm{K}_S} + \frac{\varphi}{\mathrm{K}_F} - \boldsymbol{b} : \mathbf{S} : \boldsymbol{b} = \frac{(1-\varphi)}{\mathrm{K}_S} + \frac{\varphi}{\mathrm{K}_F} - \mathbf{1} : \mathbf{S}_S \mathbf{C} \mathbf{S}_S : \mathbf{1} \tag{3.70}$$

Under the assumption of infinitesimal deformations, the systems of equations (3.67 – 3.69) reduces to a linear form. Furthermore, assuming $\varphi \approx \varphi_0$, both the convection variable, $\nabla \boldsymbol{w} \cdot \boldsymbol{w}_R \approx \mathbf{0}$ and spatial gradient of the fluid density, $\nabla \rho^F \approx 0$ can be neglected.

D.) Initial-boundary value problem (IBVP) and boundary condition: The initial–boundary value problem was obtained by summing the solid-phase momentum equation (3.67) with the fluid-phase momentum equation (3.68) and the mass conservation equation (3.69), thereby reformulating the system to enhance numerical stability for a fully coupled dynamic poroelastic model as proposed in [249]:

$$\dot{\boldsymbol{u}} - \boldsymbol{v} = \mathbf{0}, \text{ in } \Omega \times \Gamma \tag{3.71}$$

$$(1-\varphi)\rho_S \dot{\boldsymbol{v}} + \varphi \rho_F \dot{\boldsymbol{w}} - \nabla \cdot (\mathbf{C} : \nabla^s \boldsymbol{u} - \boldsymbol{b} p) = \rho \boldsymbol{g}, \text{ in } \Omega \times \Gamma \tag{3.72}$$

$$\rho_F \dot{\boldsymbol{w}} - \varphi \gamma_F \boldsymbol{k}^{F,-1} \boldsymbol{v} + \varphi \gamma_F \boldsymbol{k}^{F,-1} \boldsymbol{w} + \nabla p = \rho_F \boldsymbol{g}, \text{ in } \Omega \times \Gamma \tag{3.73}$$

$$-\nabla \cdot \left(\frac{\boldsymbol{k}^F}{g} \dot{\boldsymbol{w}} \right) + \Lambda \dot{p} + \boldsymbol{b} : \nabla^s \boldsymbol{v} - \nabla \cdot \left(\frac{\boldsymbol{k}^F}{\gamma_F} \nabla p \right) = -\nabla \cdot \left(\frac{\boldsymbol{k}^F}{g} \boldsymbol{g} \right), \text{ in } \Omega \times \Gamma \tag{3.74}$$

In equation (3.72-3.74), Ω, describes the porous medium of the domain given by $\Omega \subset \mathbb{R}^d$ (where d is the dimension of the model), while the boundary is denoted by Γ.

In addition, we denote time by t, which ranges over the open interval, $\mathcal{I} =]0, T[$. For any regions $\Omega \subset \mathbb{R}^d$, the union between the domain, Ω, and its boundary, $\boldsymbol{\Gamma}$, is written as $\overline{\Omega} = \Omega \cup \Gamma$. This boundary, Γ**,** is partitioned into the following subsets of boundary conditions:

$$\Gamma = \overline{\Gamma_u \cup \Gamma_\sigma}, \quad \Gamma_u \cap \Gamma_\sigma = \emptyset \tag{3.75}$$

$$\Gamma = \overline{\Gamma_p \cup \Gamma_q}, \quad \Gamma_p \cap \Gamma_q = \emptyset \tag{3.76}$$

To solve the equation (3.71-3.74), with primary unknowns of $\boldsymbol{u}: \bar{\Omega} \times [0,T] \to \mathbb{R}^d$ (displacement), $\boldsymbol{v}: \bar{\Omega} \times [0,T] \to \mathbb{R}^d$ (solid velocity), $\boldsymbol{w}: \bar{\Omega} \times [0,T] \to \mathbb{R}^d$ (fluid velocity) and $p: \bar{\Omega} \times [0,T] \to \mathbb{R}$ (pressure) we adopted the following boundary (3.77(a) - (d)) and initial conditions (3.77(e) - (g)):

$$\boldsymbol{u} = \overline{\boldsymbol{u}}, \text{ on } \Gamma_u \times \mathcal{I} \tag{3.77a}$$

$$(\mathbf{C}: \nabla^s \boldsymbol{u} - \boldsymbol{b}p) \cdot \boldsymbol{n} = \overline{\boldsymbol{t}}, \text{ on } \Gamma_\sigma \times \mathcal{I} \tag{3.77b}$$

$$\left(\frac{\boldsymbol{k}^F}{\gamma_F} \nabla p\right) \cdot \boldsymbol{n} = \bar{q}, \text{ on } \Gamma_q \times \mathcal{I} \tag{3.77c}$$

$$p = \bar{p}, \text{ on } \Gamma_p \times \mathcal{I} \tag{3.77d}$$

$$\boldsymbol{u}(x,0) = \boldsymbol{u}_0, x \in \bar{\Omega} \tag{3.77e}$$

$$\boldsymbol{v}(x,0) = \boldsymbol{v}_0, x \in \bar{\Omega} \tag{3.77f}$$

$$p(x,0) = p_0, x \in \bar{\Omega} \tag{3.77g}$$

Here $\boldsymbol{u}_0$, $\boldsymbol{v}_0$, p_0, represent the initial displacement, solid velocity, and excess pore pressure while $\overline{\boldsymbol{u}}$, $\overline{\boldsymbol{t}}$, $\bar{q}$, and $\bar{p}$, denote the displacement, traction, flux, and excess pore pressure prescribed on the boundary. The solid velocity and Darcy velocity at the boundary, Γ, together with its initial conditions are described as:

$$\boldsymbol{v} = \dot{\boldsymbol{u}}, \text{ on } \Gamma \times \mathcal{I}, \tag{3.78a}$$

$$\boldsymbol{w} = -\frac{\boldsymbol{k}^F}{\varphi \gamma_F} \nabla p + \boldsymbol{v}, \text{ on } \Gamma \times \mathcal{I}, \tag{3.78b}$$

$$\boldsymbol{w}(\boldsymbol{x},0) = -\frac{\boldsymbol{k}^F}{\varphi \gamma_F} \nabla p_0 + \boldsymbol{v}_0, x \in \bar{\Omega} \tag{3.78c}$$

Following standard notations, we define the types of functions adopted for our mathematical model as follows:

- The spaces $H^1(\Omega)$ and $\mathbf{H^1}(\Omega)$ are the Sobolev spaces that consist of scalar and vector functions, respectively, defined over the domain, Ω, for which the functions and their first derivates are square-integrable,

- $\mathbf{H^1}(\text{div}; \Omega)$ denotes the Sobolev space for vector fields whose divergence are square-integrable,
- The spaces $H^1(\Omega)$, $\mathbf{H^1}(\Omega)$, and $\mathbf{H^1}(\text{div}; \Omega)$ denote the respective Sobolev spaces of the functions whose traces vanish at the boundary, Γ, thereby incorporating the Dirichlet boundary condition and,
- $\boldsymbol{H}^{1/2}(\Gamma)$ the space of square-integrable traces on boundary, Γ, of vector functions in $\mathbf{H^1}(\Omega)$

With these notations, the function spaces used in our formulation are specified in equations (3.79a – 3.79d):

$$\boldsymbol{U} = \left\{ \boldsymbol{u} \in \boldsymbol{H}^1(\Omega) | \quad \boldsymbol{u}|_{\Gamma_u} = \overline{\boldsymbol{u}} \in \boldsymbol{H}^{\frac{1}{2}}(\Gamma) \right\} \tag{3.79a}$$

$$\boldsymbol{\mathcal{V}} = \left\{ \boldsymbol{v} \in \boldsymbol{H}^1(\Omega) | \quad \boldsymbol{v}|_{\Gamma} = \dot{\boldsymbol{u}} \in \boldsymbol{H}^{\frac{1}{2}}(\Gamma) \right\} \tag{3.79b}$$

$$\boldsymbol{\mathcal{W}} = \left\{ \boldsymbol{w} \in \boldsymbol{H}(\text{div}; \Omega) | \quad \boldsymbol{w}|_{\Gamma} = -\frac{\boldsymbol{k}^F}{\varphi \gamma_F} \nabla p + \boldsymbol{v} \right\} \tag{3.79c}$$

$$\mathcal{P} = \{ p \in H_0^1(\Omega) \} \tag{3.79d}$$

3.7 Numerical Model

3.7.1 Weak or variational formulation

The variational formulation for the initial value boundary problem described in equations (3.80 (a) – (d)) is expressed as follows: for each time step, $t \in \mathcal{I}$, we obtain the unknowns of $\{\boldsymbol{u}, \boldsymbol{v}, \boldsymbol{w}, p\} \in \boldsymbol{U} \times \boldsymbol{\mathcal{V}} \times \boldsymbol{\mathcal{W}} \times \mathcal{P}$ that satisfy the following conditions:

$$a(\boldsymbol{\psi}, \boldsymbol{u}, \boldsymbol{v}) = 0, \qquad \forall \boldsymbol{\psi} \in \boldsymbol{H}_0^1(\Omega) \tag{3.80a}$$

$$b(\boldsymbol{\Psi}, \boldsymbol{u}, \boldsymbol{v}, \boldsymbol{w}, p = (\boldsymbol{\Psi}, \rho \boldsymbol{g})_{\Omega} + (\boldsymbol{\Psi}, \overline{\boldsymbol{t}})_{\Gamma_\sigma}, \qquad \forall \boldsymbol{\psi} \in \boldsymbol{H}_0^1(\Omega) \tag{3.80b}$$

$$c(\boldsymbol{\phi}, \boldsymbol{v}, \boldsymbol{w}, p) = (\boldsymbol{\phi}, \rho_F \boldsymbol{g})_{\Omega} - (\boldsymbol{\phi} \cdot \boldsymbol{n}, \bar{p})_{\Gamma_p}, \qquad \forall \boldsymbol{\phi} \in \boldsymbol{H}_0^1(\text{div}, \Omega) \tag{3.80c}$$

$$d(\eta, \boldsymbol{v}, \boldsymbol{w}, p) = \left(\eta, \text{div} \frac{\boldsymbol{k}^F}{g} \boldsymbol{g}\right)_{\Omega} + (\eta, \bar{q})_{\Gamma_q}, \qquad \forall \eta \in H_0^1(\Omega) \tag{3.80d}$$

Here the operators $a(\cdot)$, $b(\cdot)$, $c(\cdot)$, and $d(\cdot)$ denote bilinear mappings that characterize the interactions between pairs of functions in the variational formulation as such:

$$a(\boldsymbol{\psi}, \boldsymbol{u}, \boldsymbol{v}) = (\boldsymbol{\psi}, \dot{\boldsymbol{u}})_\Omega - (\boldsymbol{\psi}, \boldsymbol{v})_\Omega, \tag{3.81a}$$

$$b(\boldsymbol{\psi}, \boldsymbol{u}, \boldsymbol{v}, \boldsymbol{w}, p) = (\boldsymbol{\psi}, \rho^S \dot{\boldsymbol{v}})_\Omega + (\boldsymbol{\psi}, \rho^F \dot{\boldsymbol{w}})_\Omega + (\nabla^s \boldsymbol{\psi}, \mathbf{C}\colon \nabla^s \boldsymbol{u})_\Omega - (\nabla^s \boldsymbol{\psi}, \boldsymbol{b}p)_\Omega \tag{3.81b}$$

$$c(\boldsymbol{\phi}, \boldsymbol{v}, \boldsymbol{w}, p) = (\boldsymbol{\phi}, \rho_F \dot{\boldsymbol{w}})_\Omega - (\boldsymbol{\phi}, \varphi \gamma_F \boldsymbol{k}^{F,-1} \boldsymbol{v})_\Omega + (\boldsymbol{\phi}, \varphi \gamma_F \boldsymbol{k}^{F,-1} \boldsymbol{w})_\Omega - (\mathrm{div}\boldsymbol{\phi}, p)_\Omega \tag{3.81c}$$

$$d(\eta, \boldsymbol{v}, \boldsymbol{w}, p) = \left(\eta, \mathrm{div}\frac{\boldsymbol{k}^F}{\gamma_F}\dot{\boldsymbol{w}}\right)_\Omega + (\eta, \Lambda \dot{p})_\Omega + (\eta, \boldsymbol{b}\colon \nabla^s \boldsymbol{v})_\Omega + \left(\nabla\eta, \frac{\boldsymbol{k}^F}{\gamma_F}\nabla p\right)_\Omega \tag{3.81d}$$

The notation $(\cdot, \cdot)_\Omega$ represents the inner product taken over the domain, Ω, and is applied to scalar, vector, or second-order tensor functions. Similarly, $(\cdot, \cdot)_{\Gamma *}$ denotes the corresponding inner product defined on the boundary segment, $\Gamma *$, for either scalar or vector functions.

3.7.2 Numerical approach

A finite element approach was adopted to numerically approximate the variational formulation of the coupled dynamic system for a fully saturated porous medium. The continuous solution fields are substituted with their discrete components, $\boldsymbol{u}^h$, $\boldsymbol{v}^h$, $\boldsymbol{w}^h$, p^h representing the finite-dimensional approximations as follows:

$$\boldsymbol{u}^h = \sum_{i=1}^{n_u} \boldsymbol{\psi}_i(\boldsymbol{x}) u_i(t) \tag{3.82a}$$

$$\boldsymbol{v}^h = \sum_{i=1}^{n_v} \boldsymbol{\psi}_i(\boldsymbol{x}) v_i(t) \tag{3.82b}$$

$$\boldsymbol{w}^h = \sum_{j=1}^{n_w} \boldsymbol{\phi}_j(\boldsymbol{x}) w_j(t) \tag{3.82c}$$

$$p^h = \sum_{i=k}^{n_p} \eta_k(\boldsymbol{x}) p_k(t) \tag{3.82d}$$

Here, n_u, n_v, n_w, n_p represents the degrees of freedom associated with the displacement field, solid velocity, fluid velocity and pressure, respectively. These variables are organized into vectors $\mathbf{u} \in \mathbb{R}^{n_u}, \mathbf{v} \in \mathbb{R}^{n_v}, \mathbf{w} \in \mathbb{R}^{n_w}$, and $\mathbf{p} \in \mathbb{R}^{n_p}$. The functions $\boldsymbol{\psi}_i$, $\boldsymbol{\phi}_j$, η_k, represent the finite element basis functions that correspond to the approximation spaces for the fields. A stable

discretization satisfying the inf-sup condition is achieved by using $\mathbb{Q}_2 - \mathbb{Q}_1$ Taylor-Hood elements [250], [251]. Given our hexahedral mesh, $\mathcal{T}^h$, composed of non-overlapping elements, Ω^e, covering the domain, Ω, the basis functions were constructed accordingly:

$$\boldsymbol{\psi}_i \in S^h_{u,v}(\Omega) = \{\boldsymbol{\psi} \in \boldsymbol{H}^1(\Omega), \boldsymbol{\psi}|_{\Omega^e} \in [\mathbb{Q}_2(\Omega^e)]^d \forall \Omega^e \in \mathcal{T}^h\}, \qquad i = 1, \dots, n_v \quad (3.83a)$$

$$\boldsymbol{\phi}_j \in \mathcal{S}^h_w(\Omega) = \{\boldsymbol{\phi} \in \boldsymbol{H}(\mathrm{div}; \Omega), \boldsymbol{\phi}|_{\Omega^e} \in [\mathbb{Q}_1(\Omega^e)]^d \forall \Omega^e \in \mathcal{T}^h\}, \qquad j = 1, \dots, n_w \quad (3.83b)$$

$$\eta_k \in S^h_p(\Omega) = \{\eta \in H^1(\Omega), \eta|_{\Omega^e} \in \mathbb{Q}_1(\Omega^e) \forall \Omega^e \in \mathcal{T}^h\}, \qquad k = 1, \dots, n_p \quad (3.83c)$$

Here, $\mathbb{Q}_1(\Omega^e)$ and $\mathbb{Q}_2(\Omega^e)$ are the finite element spaces consisting of tensor polynomials of degree one and two, respectively, in each spatial direction over the element, Ω^e. The number of degrees of freedom for displacement and solid velocity fields are equal (i.e. $n_u = n_v$), while the degrees of freedom for solid velocity exceeds the fluid velocity field (i.e. $n_v > n_w$). Finally, the number of pressure degree of freedom is less than that of the fluid velocity, given by $n_p < n_w$.

Hence, by combining the discrete terms from equation (3.82 (a) - (d)) with the variational approach outlined in equation (3.80 (a) – (d)), and by replacing the function spaces specified in equation (3.83 (a) – (c)), we arrive at a set of time-dependent first-order differential equation:

$$\mathbf{M\dot{z}} + \mathbf{Kz} + \mathbf{f} = \mathbf{0} \quad (3.84)$$

Here, **M, K, and f** are the global mass matrix, stiffness matrix, and the vector that gathers the source terms and natural boundary conditions, respectively. The vector of discrete $n_u + n_v + n_w + n_p$ unknowns is represented by **z**, where $\mathbf{z} = [\mathbf{u}; \mathbf{v}; \mathbf{w}; \mathbf{p}]^T$. To provide clarity and implementation, the general equation above can be expressed in matrix format as follows:

$$\begin{bmatrix} \boldsymbol{I_u} & 0 & 0 & 0 \\ 0 & \boldsymbol{M_{vv}} & \boldsymbol{M_{vw}} & 0 \\ 0 & 0 & \boldsymbol{M_{ww}} & 0 \\ 0 & 0 & \boldsymbol{M_{pw}} & \boldsymbol{M_{pp}} \end{bmatrix} \begin{bmatrix} \dot{\boldsymbol{u}} \\ \dot{\boldsymbol{v}} \\ \dot{\boldsymbol{w}} \\ \dot{\boldsymbol{p}} \end{bmatrix} + \begin{bmatrix} 0 & -\boldsymbol{I_u} & 0 & 0 \\ \boldsymbol{K_{vu}} & 0 & 0 & \boldsymbol{K_{vp}} \\ 0 & \boldsymbol{K_{wv}} & \boldsymbol{K_{ww}} & \boldsymbol{K_{wp}} \\ 0 & \boldsymbol{K_{pv}} & 0 & \boldsymbol{K_{pp}} \end{bmatrix} \begin{bmatrix} \boldsymbol{u} \\ \boldsymbol{v} \\ \boldsymbol{w} \\ \boldsymbol{p} \end{bmatrix} + \begin{bmatrix} 0 \\ \boldsymbol{f_v} \\ \boldsymbol{f_w} \\ \boldsymbol{f_p} \end{bmatrix} = 0 \quad (3.85)$$

Each block entry in these matrices corresponds to a specific coupling between the solid and fluid variables as follows:

$$[\boldsymbol{M_{vv}}]_{ij} = \left(\boldsymbol{\psi}_i, \rho^S \boldsymbol{\psi}_j\right)_\Omega, \qquad i = 1, \dots, n_v, j = 1, \dots, n_v \quad (3.86a)$$

$$[\boldsymbol{M_{vw}}]_{ij} = \left(\boldsymbol{\psi}_i, \rho^F \boldsymbol{\phi}_j\right)_\Omega, \qquad i = 1, \dots, n_v, j = 1, \dots, n_w \quad (3.86b)$$

$$[\boldsymbol{M_{ww}}]_{ij} = \left(\boldsymbol{\phi}_i, \rho_F \boldsymbol{\phi}_j\right)_\Omega, \qquad i = 1, \dots, n_w, j = 1, \dots, n_w \quad (3.86c)$$

$$\left[\boldsymbol{M_{pw}}\right]_{ij} = \left(\eta_i, \operatorname{div}\frac{\boldsymbol{k}^F}{g}\boldsymbol{\phi}_j\right)_\Omega, \qquad i = 1, \dots, n_p, j = 1, \dots, n_w \tag{3.86d}$$

$$\left[\boldsymbol{M_{pp}}\right]_{ij} = \left(\eta_i, \Lambda\eta_j\right)_\Omega, \qquad i = 1, \dots, n_p, j = 1, \dots, n_p \tag{3.86e}$$

And,

$$[\boldsymbol{K_{vu}}]_{ij} = \left(\nabla^s\boldsymbol{\Psi}_i, \mathbf{C}\colon\nabla^s\boldsymbol{\Psi}_j\right)_\Omega, \qquad i = 1, \dots, n_v, j = 1, \dots, n_u \tag{3.87a}$$

$$\left[\boldsymbol{K_{vp}}\right]_{ij} = -\left(\nabla^s\boldsymbol{\psi}_i, \boldsymbol{b}\eta_j\right)_\Omega, \qquad i = 1, \dots, n_v, j = 1, \dots, n_p \tag{3.87b}$$

$$[\boldsymbol{K_{wv}}]_{ij} = -\left(\boldsymbol{\phi}_i, \varphi\gamma_F\boldsymbol{k}^{F,-1}\boldsymbol{\psi}_j\right)_\Omega, \qquad i = 1, \dots, n_w, j = 1, \dots, n_v \tag{3.87c}$$

$$[\boldsymbol{K_{ww}}]_{ij} = \left(\boldsymbol{\phi}_i, \varphi\gamma_F\boldsymbol{k}^{F,-1}\boldsymbol{\phi}_j\right)_\Omega, \qquad i = 1, \dots, n_w, j = 1, \dots, n_w \tag{3.87d}$$

$$\left[\boldsymbol{K_{wp}}\right]_{ij} = -\left(\operatorname{div}\boldsymbol{\phi}_i, \eta_j\right)_\Omega, \qquad i = 1, \dots, n_w, j = 1, \dots, n_p \tag{3.87e}$$

$$\left[\boldsymbol{K_{pv}}\right]_{ij} = \left(\eta_i, \boldsymbol{b}\colon\nabla^s\boldsymbol{\psi}_j\right)_\Omega, \qquad i = 1, \dots, n_p, j = 1, \dots, n_v \tag{3.87f}$$

$$\left[\boldsymbol{K_{pp}}\right]_{ij} = \left(\nabla\eta_i, \frac{\boldsymbol{k}^F}{\gamma_F}\nabla\eta_j\right)_\Omega, \qquad i = 1, \dots, n_p, j = 1, \dots, n_p \tag{3.87g}$$

To solve equation (3.84) in time we used the standard trapezoidal $\boldsymbol{\theta}$-method which contains time derivate, $\dot{\mathbf{z}}$. At discrete time steps, we use the finite difference approximation from which we obtain:

$$\dot{\boldsymbol{Z}}_{n+1} \approx \frac{\boldsymbol{Z}_{n+1} - \boldsymbol{Z_n}}{\Delta t} \tag{3.88}$$

Both the stiffness matrix, **K,** and forcing vector, **f,** are evaluated at the current time step, as a weighted average between t_n, and t_{n+1}:

$$t^* = \vartheta t_{n+1} + (1-\vartheta)t_n$$

Given that the primary unknown is $\mathbf{z} = [\mathbf{u}; \mathbf{v}; \mathbf{w}; \mathbf{p}]^T$, its value at this intermediate time is likewise computed as with:

$$Z_{t^*} = \vartheta Z_{n+1} + (1-\vartheta)Z_n, \quad \vartheta \in [0,1] \tag{3.89}$$

By replacing equation (3.88) and (3.86) into equation (3.84) and regrouping like terms we obtain an expression of the residual, **R**:

$$\overline{\mathbf{R}} = \left[\vartheta\mathbf{K}_{t^*} + \frac{\mathbf{M}_{t^*}}{\Delta t_n}\right]\mathbf{z}_{n+1} - \left[\frac{\mathbf{M}_{t^*}}{\Delta t_n} - (1-\vartheta)\mathbf{K}_{t^*}\right]\mathbf{z}_n + \vartheta\mathbf{f}_{n+1} + (1-\vartheta)\mathbf{f}_n = 0 \tag{3.90}$$

Equation (3.90) exhibits non-linearity due to the phase compressibility variable. Therefore, a Newton-Raphson iterative algorithm was employed. The iterative process continues until the residual norm, $\overline{\mathbf{R}}$, converges (i.e. it is less than a specified tolerance, t). If this criterion is not met, further refinement of the solution vector is required. At each iteration, ***k,*** the solution is updated by adding the current estimate with an incremental correction, $\delta\mathbf{z}^{k+1}$:

$$\mathbf{z}^{k+1} = \mathbf{z}^{k} + \delta\mathbf{z}^{k+1}$$

The increment, $\delta\mathbf{z}^{k+1}$ is determined by solving a corresponding linear system of equations:

$$\overline{\mathbf{A}}d\mathbf{z} = \overline{\mathbf{R}}^{k} \tag{3.91}$$

where, $\overline{\mathbf{R}}^{k}$, is the residual evaluated corrected solution vector $\mathbf{z}_{n+1}^{k}$, $d\mathbf{z} = [d\mathbf{u}; d\mathbf{v}; d\mathbf{w}; d\mathbf{p}]^{T}$ and $\overline{\mathbf{A}}$ is the system matrix obtained by assembling the global matrix, **M** and stiffness matrix, **K:**

$$\overline{\mathbf{A}} = \begin{bmatrix} \dfrac{\boldsymbol{I_u}}{\Delta t_n} & -\vartheta I_u & 0 & 0 \\ \vartheta \boldsymbol{K_{vu}} & \dfrac{\boldsymbol{M_{vv}}}{\Delta t_n} & \dfrac{\boldsymbol{M_{vw}}}{\Delta t_n} & \vartheta \boldsymbol{K_{vp}} \\ 0 & \vartheta \boldsymbol{K_{wv}} & \vartheta \boldsymbol{K_{ww}} + \dfrac{\boldsymbol{M_{ww}}}{\Delta t_n} & \vartheta \boldsymbol{K_{wp}} \\ 0 & \vartheta \boldsymbol{K_{pv}} & \dfrac{\boldsymbol{M_{pw}}}{\Delta t_n} & \vartheta K_{pp} + \dfrac{\boldsymbol{M_{pp}}}{\Delta t_n} \end{bmatrix} \tag{3.92}$$

To lower the dimensionality of equation (3.91), we explicitly derive the displacement increment, $d\mathbf{u}$***:***

$$d\mathbf{u} = \vartheta\Delta t_n d\mathbf{v} + \mathbf{u}_{n+1}^{i} - \vartheta\Delta t_n \mathbf{v}_{n+1}^{i} - \mathbf{u}_n - (1-\vartheta)\Delta t_n \mathbf{v}_n \tag{3.93}$$

When substituted into the second, third, and fourth equations of our system matrix, we obtain the following residuals, $\mathbf{R} = \left[\mathbf{R}_v; \mathbf{R}_w; \mathbf{R}_p\right]^{T}$ for the solid velocity, fluid velocity, and pressure, respectively:

$$\begin{aligned} \boldsymbol{R}_v = {} & [M_{vv}/\Delta t_n + \vartheta^2 \Delta t_n K_{vu}]\mathbf{v}_{n+1}^{i} + M_{vw}/\Delta t_n \mathbf{w}_{n+1}^{i} + \vartheta K_{vp}\mathbf{p}_{n+1}^{i} \\ & + K_{vu}\mathbf{u}_n - [M_{vv}/\Delta t_n - \vartheta(1-\vartheta)\Delta t_n K_{vu}]\mathbf{v}_n - M_{vw}/\Delta t_n \mathbf{w}_n + (1-\vartheta)K_{vp}\mathbf{p} \\ & + \vartheta \mathbf{f}_{n+1}^{(v)} + (1-\vartheta)\mathbf{f}_n^{(v)}, \end{aligned} \tag{3.94a}$$

$$\boldsymbol{R}_w = \vartheta K_{wv}\mathbf{v}_{n+1}^i + [M_{ww}/\Delta t_n + \vartheta K_{ww}]\mathbf{w}_{n+1}^i + \vartheta K_{wp}\mathbf{p}_{n+1}^i + (1-\vartheta)K_{wv}\mathbf{v}_n - [M_{ww}/\Delta t_n - (1-\vartheta)K_{ww}]\mathbf{w}_n + (1-\vartheta)K_{wp}\mathbf{p}_n + \vartheta\mathbf{f}_{n+1}^{(w)} + (1-\vartheta)\mathbf{f}_n^{(w)}, \quad (3.94b)$$

$$\mathbf{R}_{\boldsymbol{p}} = \vartheta K_{pv}\mathbf{v}_{n+1}^i + M_{pw}/\Delta t_n\mathbf{w}_{n+1}^i + \left[M_{pp}/\Delta t_n + \vartheta K_{pp}\right]\mathbf{p}_{n+1}^i + (1-\vartheta)K_{pv}\mathbf{v}_n - \frac{M_{pw}}{\Delta t_n\mathbf{w}_n} - \left[\frac{M_{pp}}{\Delta t_n} - (1-\vartheta)K_{pp}\right]\mathbf{p}_n + \vartheta\mathbf{f}_{n+1}^{(p)} + (1-\vartheta)\mathbf{f}_n^{(p)} \quad (3.94c)$$

The reduced form of the system matrix, $\overline{\mathbf{A}}$, after explicitly representing the displacement increment, $d\mathbf{u}$ and obtaining the residuals, $\mathbf{R} = \left[\mathbf{R}_v; \mathbf{R}_w; \mathbf{R}_p\right]^T$ is given by:

$$\mathbf{A} = \begin{bmatrix} \vartheta^2\Delta t_n K_{vu} + \frac{M_{vv}}{\Delta t_n} & \frac{M_{vw}}{\Delta t_n} & \vartheta K_{vp} \\ \vartheta K_{wv} & \vartheta K_{ww} + \frac{M_{ww}}{\Delta t_n} & \vartheta K_{wp} \\ \vartheta K_{pv} & \frac{M_{pw}}{\Delta t_n} & \vartheta K_{pp} + \frac{M_{pp}}{\Delta t_n} \end{bmatrix} = \begin{bmatrix} \boldsymbol{A_{vv}} & \boldsymbol{A_{vw}} & \boldsymbol{A_{vp}} \\ \boldsymbol{A_{wv}} & \boldsymbol{A_{ww}} & \boldsymbol{A_{wp}} \\ \boldsymbol{A_{pv}} & \boldsymbol{A_{pw}} & \boldsymbol{A_{pp}} \end{bmatrix} \quad (3.95)$$

The resulting equation after linearization using the Newton-Raphson iteration, takes the linear algebraic form:

$$\boldsymbol{A}x = \boldsymbol{R} \quad (3.96)$$

Where $\mathbf{A}$ is the reduced system matrix in equation (D88), $\mathbf{x} = [d\mathbf{v}; d\mathbf{w}; d\mathbf{p}]^T$ is the solution increment, and R, the residual vector variable derived from equation (3.94(a) - 3.94(c). Efficiently solving the three-field dynamic poroelastic model remains a critical challenge when applying it to wave propagation analysis.

3.7.3 Linear solver

By examination of the system matrix, $\mathbf{A}$, it reveals that the diagonal blocks namely, $\boldsymbol{A_{vv}}$, $\boldsymbol{A_{ww}}$ and $\boldsymbol{A_{pp}}$, are symmetric and positive definite. Nevertheless, the off-diagonal components are not symmetric; for emphasis, $\boldsymbol{A_{vw}} \neq \boldsymbol{A_{wv}^T}$, $A_{vp} \neq \boldsymbol{A_{pv}^T}$, and $\boldsymbol{A_{wp}} \neq \boldsymbol{A_{pw}^T}$. Consequently, the global system matrix is non-symmetric.

Accordingly, a fully implicit monolithic solver employing a Krylov subspace algorithm, specifically the Bi-conjugate Gradient Stabilized (Bi-CGStab) method [252] is used.

To speed up the convergence of the linear solver, a Multi-Physics Reduction strategy was adopted, wherein the coupled system is systematically reduced to a single physics formulation

before being extended back into the fully coupled problem (i.e. a natural sequence that proceeds from most extensive matrix block to the least extensive block, specifically progressing through solid velocity, fluid velocity, and finally pressure) as seen in Figure 3.4 [19], [191]. For a full algorithm of the Multi-Physics Reduction process, refer to Appendix D.

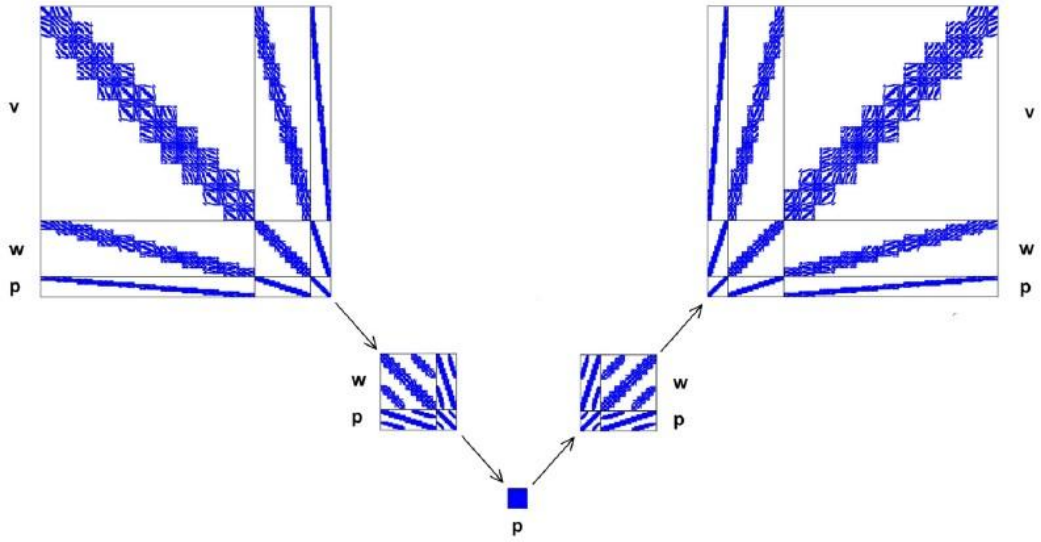

Figure 3.4: Sketch of multi-physics reduction process (MPR) [191]

3.8 Potential Ground Shaking Intensity

For the potential ground shaking intensity from the simulated wave propagation, we evaluate *i*.) the amount of the incident wave either reflected or transmitted due to the configuration of our layered rock and choice of boundary conditions and *ii*.) use the MMI-PGV relationship to analyse the perceptibility of the seismic event.

3.8.1 Reflectivity of the wave due to layered anisotropy

Given the presence of layered geological media and the imposed boundary conditions, we assess the reflectivity and transmissibility across each interface exhibiting significant material stiffness contrasts. This evaluation is conducted using the analytical expressions presented below [253], which account for wave interactions at discontinuities in mechanical properties:

$$R_{pp}^{u} = \frac{D_2^u - D_1^u}{D_1^u + D_2^u} \tag{3.97a}$$

$$R_{ss}^{u} = \frac{D_2^u - D_1^u - 2\rho_1\rho_2(a_2b_1 - a_1b_2)}{D_1^u + D_2^u} \tag{3.97b}$$

$$R_{ps}^{u} = \frac{2ua_2}{D_1^u + D_2^u}\{(cu^2 - \rho_1 + \rho_2)(cu^2 - \rho_1) + c(cu^2 + \rho_2)a_1b_1\} \tag{3.97c}$$

$$R_{sp}^{u} = -\frac{2ub_2}{D_1^u + D_2^u}\{(cu^2 - \rho_1 + \rho_2)(cu^2 - \rho_1) + c(cu^2 + \rho_2)a_1 b_1\} \quad (3.97d)$$

The variables used in the wave reflection coefficient equations represent physical properties and geometrical relationships governing how seismic waves behave at material interfaces. Here, ρ_1 and ρ_2 denote the mass densities of the first and second medium, respectively. The terms a_1 , a_2 and b_1, b_2 refer to the vertical slowness components (i.e., inverses of wave speeds) for P-waves, P, and S-waves, S in each medium. The parameter u represents the horizontal slowness, which is related to the angle of incidence and wave type. D_1^d and D_2^d are generalized impedance quantities that account for the interaction of wave modes, including directionality and stiffness contrasts. Finally, c may appear as a coupling constant or scaling factor in shear-modulated terms. These variables together capture the anisotropic and heterogeneous effects at interfaces, allowing for accurate estimation of how much energy is reflected or transmitted as different wave types. (Review Appendix C for solution to anisotropic case study).

3.8.2 Modified Mercalli intensity (MMI) vs peak ground velocity (PGV) correlation evaluation for ground shaking intensity evaluation

The solid velocity output was used to compute the Peak Ground Velocity (PGV). This value is then correlated with the Modified Mercalli Intensity (MMI) using the established empirical relationships suggested by [253], [254] to evaluate the ground shaking intensity:

$$MMI = 2.10 \log(PGV) + 3.40 \quad (3.98)$$

The computed MMI value are benchmarked against findings from prior studies, specifically the comparative analysis of MMI-PGV relationships conducted across regions in China and California (see Appendix B [255]).

3.9 Summary of Methodology

A concise summary of the methodology has been organized into two tables. It outlines the complete workflow of this study. These tables contain the key modelling steps, the necessary equations, the numerical methods implemented, and the outputs that link the two stages of this analysis .

- Stage 1: Hydromechanical (u-p) analysis (Table 3.3): This tables presents the steps required to simulate multiphase flow, poromechanics and seismic source evaluation.
- Stage 2: Dynamic wave propagation (u-v-p) analysis (Table 3.4): Presents the steps for P-wave, S-wave, and Rayleigh wave analysis. Followed by reflectivity and ground shaking analysis.

Table 3.3: Summary of Hydromechanical (u-p) methodology.

Stage 1 – Hydromechanical (u–p analysis)			
Stage / Step	**What is done**	**Methods / Equations**	**Outputs (and role for next stage)**
S1.1 Multiphase analysis	Multiphase flow analysis.	Finite volume method implemented in MRST. (Equations 3.1 – 3.6)	Pressure and saturation → with pressure variation necessary for geomechanics
S1.2 Geomechanics analysis	Pressure from (S1.1) interpolated to nodes for poromechanics analysis.	Finite element method implemented in GeoMatFEM. (Equations 3.7- 3.26 One-way coupling scheme applied Solution performed in linear regime, however code checks if at any time step, we get into the elastoplastic regime, assuming Drucker-Prager constitutive model and using algorithm from the article by [256]	Stress, strain and nodal displacement → with nodal displacement important for obtaining fault slip history and seismic source evaluation
S1.3 Seismic source evaluation	Fault slip history from (S1.2) used to quantify static seismic source parameters	Seismic scaling laws (Equations 3.49 – 3.57).	Seismic moment (M_o), seismic magnitude (M_w), energy magnitude (M_e), released energy magnitude, Er, corner frequency (f_c) → with Mo and fc being inputs for Stage 2.

Table 3.4: Summary of wave propagation (u-v-p) analysis

Stage 2 – Dynamic wave propagation (u–v–p analysis)			
Stage / Step	**What is done**	**Methods / Equations**	**Outputs (and role for next stage)**
S2.1 Wave propagation modelling	Propagate induced P, S, and Rayleigh waves through isotropic and anisotropic layered reservoir	Mixed finite element approach based on mixture theory principle. Equations (3.58 – 3.74). Finite element discretization approach Equations (3.80 – 3.85) Fully coupled implicit scheme See Appendix D for full algorithm.	Full wavefield of displacement, velocity, and pressure of the wave → important for ground shaking analysis
S2.2 Reflectivity analysis	Assess mode conversions and spurious reflections at interfaces.	Reflection coefficients Rpp, Rps, Rss, Rsp (Eqs. 3.97a–3.97d, [253]	Reflection coefficients → validate boundary design and confirm minimal artifacts.
S2.3 Ground shaking intensity	Estimate perceptibility of induced events at the surface.	Evaluate the velocity magnitude of XYZ, Obtain the peak from velocity vs time graph and use PGV–MMI correlation (Equation. 3.98).	Peak Ground Velocity (PGV), Modified Mercalli Intensity (MMI) → final indicator of seismic risk.

Chapter 4: Geological Model Grid and Petrophysical Properties

In this thesis, three case studies are analysed. Across these case studies, a common geological framework is used. Case A: assumes isotropy, where all petrophysical and mechanical properties are similar throughout the domain. Case B: represents anisotropy arising from stratification, i.e. the layers of the domain have contrasting poromechanical properties. Case C: represents transverse vertical anisotropy in the stratified geological domain.

This section describes the computational domain, the relevant petrophysical and mechanical properties of the geological formation, for the two stages of the study:

- the quasi-static poroelastic U-P analysis to estimate the seismic source (seismic moment) associated with the CO_2 injection, and
- the dynamic U-V-P wave propagation analysis to model seismic wavefield and ground shaping metrics in isotropic and anisotropic media.

For the quasi-static poroelastic U-P analysis, the geological formation is designed to capture pressure and stress redistribution during the geological carbon sequestration (GCS) period. However, for the multifield wave propagation analysis, we downsize the geological domain used in the U-P analysis. This is because, wave propagation modelling with finite element method (FEM) requires a mesh fine enough to resolve the shortest wavelengths, typically a minimum of 10 nodes per wavelength as suggested by [257]. In addition, the grid size depends on the P-wave velocity, S-wave velocity, and the content frequency, which was set as 100Hz in this study. Therefore, without a downsized domain, using a very fine mesh would drive the cell sizes to single-digit metre scale, yielding a 3D system with $O(10^9)$ unknowns and a terabyte-class memory demand. Such discretization is not computationally feasible on the workstation specified in Table 4.1.

Table 4.1: Windows specification for workstation

Edition	Windows 11 Pro
Processor	13th Gen Intel ® Core ™ i9-13900 (2.00GHz)
Installed RAM	64.0 GB
System Type	64-bit operating system, x64-based processor

The boundary conditions are chosen to (i) capture the pressure variation induced by CO_2 injection in the multiphase fluid flow model, (ii) impose far-field stress and pore-pressure states

for the quasi-static u-p model, and iii.) represent the wave profile from the seismic source, by minimizing the reflections from the layered domain and outer boundary.

In this chapter, we first specify the modelling domain and its discretization, which are common to all case studies as follows: First, the geological domain (geometry, stratigraphic layering) for the multiphase-flow configuration used to simulate CO_2 injection. Subsequently, the quasi-static u-p configuration for the geological framework, detailing the poromechanical constraints that align with producing the unknowns of displacement, stress and strain variations. Thereafter, the subdomain and its respective mechanical constraints required to model, potential seismic activity and ground motion for the u-v-p wave propagation analysis. Finally, we introduce the case-specific material properties (Cases A-C) at the end of the chapter, with all deviations from the common baseline explicitly identified.

4.1 Geological Geometry and Stratigraphy for Multiphase-Flow Simulation

The conceptual model spans 30 km x 20 km x 5 km in the x-y-z directions, enclosing the reservoir interval, as seen in **Figure 4.1**. The volume serves as the domain from which the subsequent u-p and u-v-p models are analysed.

All coordinates are expressed in a metric Coordinate Reference System (CRS) as described by [258]. The depths are reported as True Vertical Depths Subsea (TVDSS). In numerical implementation, the global axes are taken as X, Y (which are the horizontal axes) and Z (which is the vertical axis). All quantities are reported in SI units unless stated otherwise.

The geological domain consists predominantly of sandstone, with some amount of shale present at certain sections of the domain. The domain is therefore stratified as follows:

Table 4.2: Stratigraphic sequence of geological formations.

Section of domain	Formation characteristics	Depth interval (m)
Overlying Caprock	Predominantly sandstone (expected to act as perfect seal, preventing fluids from migrating out of target storage zone)	0 – 1000 m
Target reservoir	Sandstone with some amounts of mudstone and shale (expected to safely store 90% of the injected CO_2	1000 – 4500 m
Underlying Caprock	Consist of sandstone and some amount of limestone	4500 – 5000 m

A major fault, discretized with a set of continuum elements (as described in section 2.7.1B), intersects the reservoir domain between x = 29.5 km and x = 30 km (Figure 4.1)

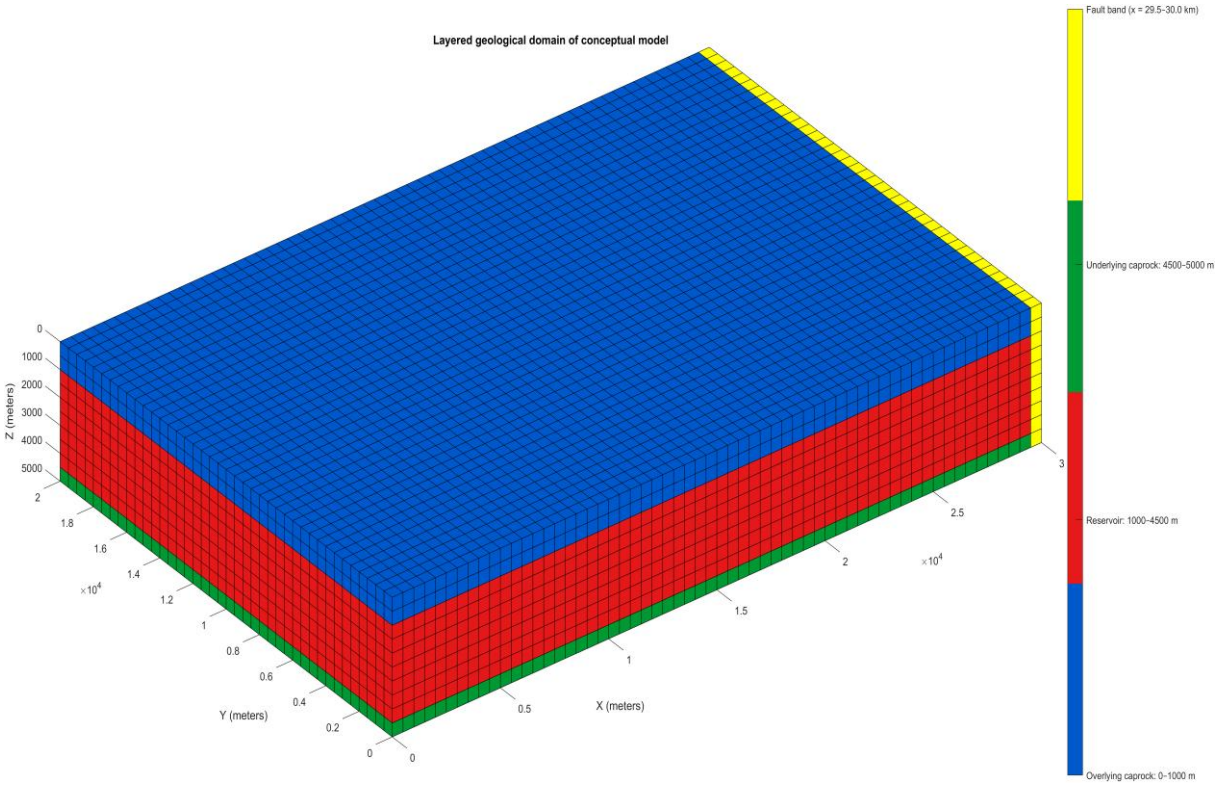

Figure 4.1: Layered geological domain, modelled in MRST.

4.1.1 Domain discretization and grid resolution for multiphase model

The modelling volume in **Figure 4.1** is discretized using a structured cartesian grid of hexahedral cells with uniform $\Delta x = \Delta y = \Delta z = 500\text{m}$. Based on the domain dimensions in **Figure 4.1**, the cell counts in the x, y, z directions, together with the total number of discrete volumes for the multiphase-flow domain are summarized below:

Table 4.3: Number of finite volume blocks after discretization of domain.

Coordinate direction	Number of discretized finite volume grids
X-direction	60
Y-direction	40
Z-direction	10
Total number of finite volumes in domain	24000

Each discrete volume within the domain is an 8-corner node hexahedron cell (as illustrated in Figure 3.3). Accounting for node sharing among adjacent cells, the resulting mesh comprises of 27,511 unique nodes. For this analysis, a simple, structured, and regular cartesian grid is utilised to represent the geological domain.

4.1.2 Initial and boundary conditions for multiphase model

A.) Initial conditions: For clarity, these conditions are distinguished into saturation, pressure, and temperature initial conditions.

- **Saturation:** The initial state of the domain is brine saturated (i.e. 100% filled with brine: $S_w = 1 - S_{g,\,\text{res}}, S_g = S_{g,\,\text{res}} \approx 0$). Here, S_w is the saturation of brine, $S_{g,\,\text{res}}$ is the gas saturation in the reservoir. Capillary pressure is negligible.
- **Pressure:** Consistent with the assumption in Section 3.2.1B, the model is initialized as brine-saturated (i.e. 100% filled with brine). The initial pressure is prescribed as hydrostatic:

$$p_0(z) = p_{\text{ref}} + \rho_w g(z_{\text{ref}} - z) \tag{4.1}$$

where p_{ref} is the reference pressure, ρ_w is the density of brine, z_{ref} is the reference depth and z is the TVDSS.

- **Temperature and salt concentration:** An isothermal assumption is adopted at T = 50°C with brine salinity of 3.5 wt.%, taken at 0.997 kg/L, implying the salt concentration is low.

B.) Boundary conditions: Within MRST repository and for this analysis, the boundary conditions prescribed are both Dirichlet and Neumann conditions.

- **Neumann boundary conditions:** Consistent with our aim of safely storing carbon dioxide (CO_2) in our domain, sections of the domain in Figure 4.1 (top, lateral, back of domain and bottom boundaries) are considered closed (i.e. no flow and sealed in all directions).

$$\mathbf{q}_w \cdot \mathbf{n} = 0, \mathbf{q}_g \cdot \mathbf{n} = 0 \tag{4.2}$$

where, $\mathbf{q_w}$ and $\mathbf{q_g}$ are the fluxes of both brine and gases, and **n,** is the outward normal.

- **Dirichlet boundary conditions:** For illustration, as seen in Figure 4.2, the front boundary, Γ_{front}, (highlighted in blue) of the model (Figure 4.1) is connected to a hydrostatic far field via a Dirichlet condition. On the front of the domain, the water-phase pressure is prescribed to the reference hydrostatic profile. This Dirichlet condition renders the boundary open: the boundary pressure is maintained by the far-field hydrostatic column:

$$p_w(x, y, z)|_{\Gamma_{front}} = p_\infty(z) \tag{4.3}$$

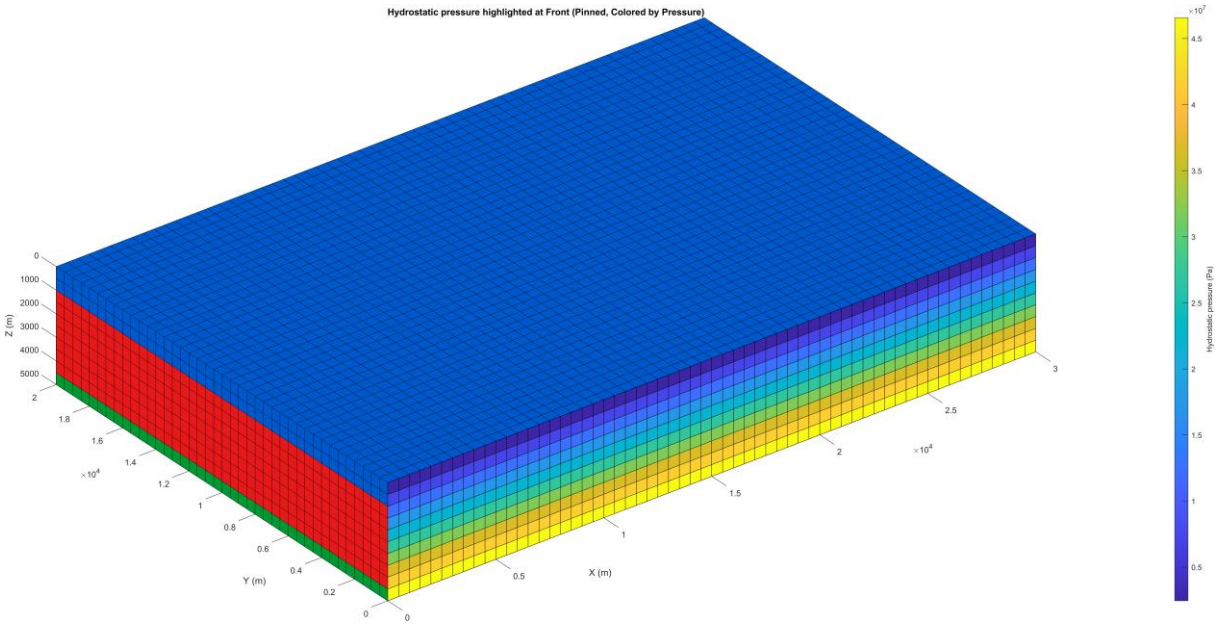

Figure 4.2: Front of the domain connected to active aquifer, (lighter patch)

- **Internal boundary conditions:** Conceptually, wells are sources of fluid, yet they are distinguished by a constitutive model that ties the injected volumetric rate to the pressure contrast between the wellbore and the surrounding cell. The injection well in this analysis is set at coordinates (0, 15000, 3500) which is at cell number 15541 (Figure

4.3). In this thesis, we avoid a conservative rate control. That is the well is operated in rate-controlled mode set at an injection rate of 1.6168 m^3/s for a mass rate of 40 Mt/yr., thereby permitting a pressure buildup that is necessary for coupled poromechanical analysis.

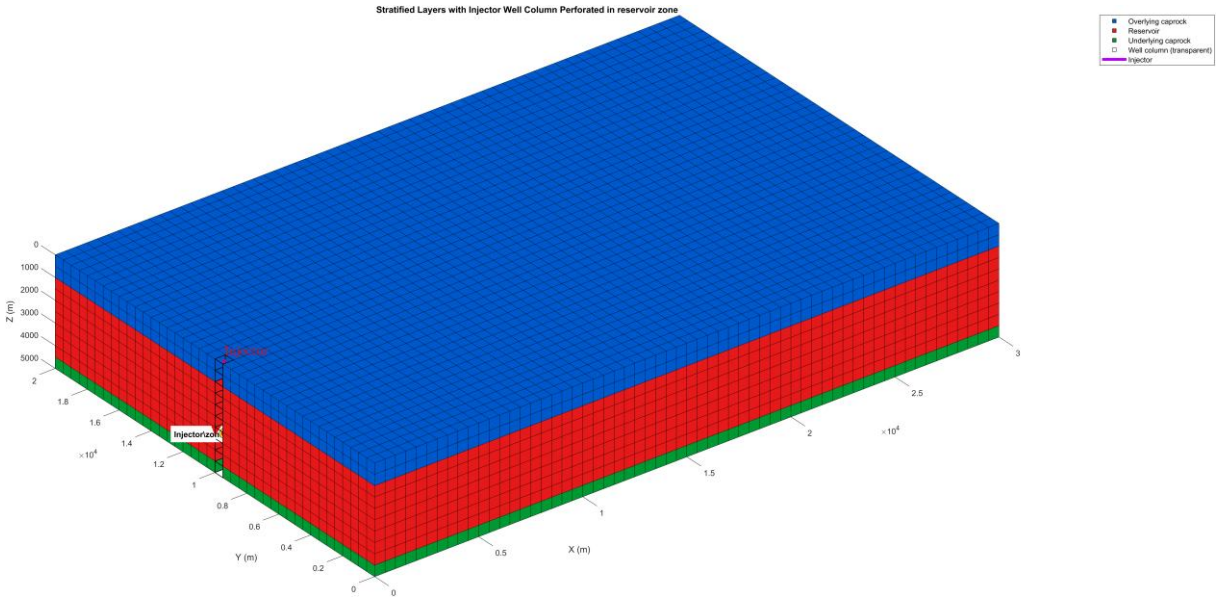

Figure 4.3: CO_2 injector well perforated at coordinates (0, 10000, 3500)m.

4.2 Mechanical Model, Initial and Boundary Conditions for Hydromechanical Analysis

Having established the hydraulic model and its initial (section 4.1.2 A) and boundary conditions (section 4.1.2B), we describe the mechanical model, initial and boundary conditions on the same geological framework. The finite volume, cell-centred pore pressure field is projected to nodal values on the mechanical (FEM) mesh via the consistent interpolation (**equation 3.35**), and these nodal pressures influence the mechanical domain.

4.2.1 Description of the mechanical domain for u-p analysis

The mechanical model is posed on the same geological volume (Figure 4.1– 4.3). The only change is the finite-element discretization. To improve the displacement, stress/strain accuracy without excessive mesh refinement for the U-P analysis, each 8-corner node finite element is subdivided to a 20-node serendipity hexahedron by adding mid-edge nodes (Figure 4.4**),** within Strauss7 software**.** The resulting input file is then exported into the GeoMatFEM research code for analysis.

This increases the number of mesh degrees of freedom while maintaining the element count aligned with the hydraulic model (**table 4.4**). The reason for increasing the number of nodes to a quadratic interpolation is to reduce the numerical dispersion and improve the representation

of the stress gradients across the layered domain, which is critical for poromechanical response and for deriving source terms for the wave propagation analysis.

Table 4.4: System parameters of mechanical domain designed in Strauss 7 and analysed in GeoMatFEM.

Total number of cells	24000 cells (i.e. 60 cells in x-axis, 40 cells in y-axis & 10 cells in z-axis)
Number of nodes	106421 nodes
Total number of pressure degrees of freedom (ndop)	27511 pressure nodes
Total number of displacement (u_x, u_y, u_z) degrees of freedom (ndof)	3*106421= 319263 displacement nodes

4.2.2 Boundary conditions for mechanical model for u-p analysis

On the mechanical domain (Figure 4.4), we denote the top, lateral, and basal boundaries by Γ_T, Γ_r, and Γ_b, respectively; **n** is the outward unit normal and **t,** the prescribed traction vector. The adopted boundary conditions for each face, together with any case-specific variants, are summarized in **Table 3.3.**

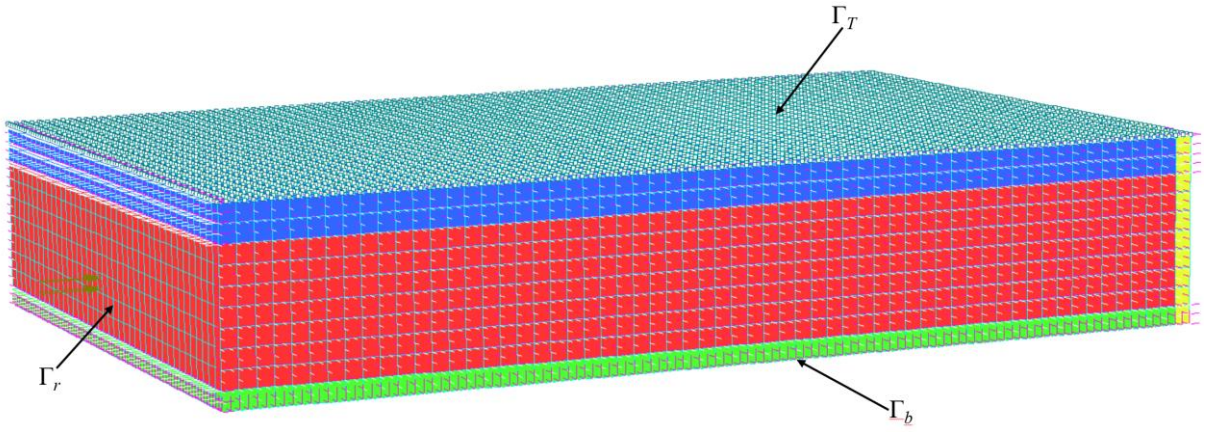

Figure 4.4: Representation of mechanical domain with case-specific boundary conditions.

4.3 Domain and Boundary conditions for Wave Propagation Analysis for u-v-p analysis

To remain numerically and computationally tractable, the UVP model employs a downsized domain to the source region and receivers, reducing each dimension by approximately a 10^3 reduction in volume. This preserves the physics of interest ensuring that the wave-induced

propagation due to the impulse, is captured throughout the simulation (i.e. the near-field generation and field propagation meets the wavelength and stability-based resolution criteria.

The domain in Figure 4.4, is downsized to 0.03 x 0.02 x 0.005 km (approximately 30 x 20 x 5m domain). To maintain the same number of cells and nodes in Table 4.4, the grid resolution is set at 0.5m for each cell in the XYZ-direction.

For the multifield initial and boundary conditions, the top boundary is assigned a pressure condition, the lateral boundaries carry displacement and velocity constraints, and the base is fully fixed in displacement and velocity, as detailed in Section 3.6D

4.4 Case Definitions, Petrophysical and Material Properties

The two (2) case studies are then presented to analyse wave propagation induced by CO_2 storage in a reservoir system. All cases share the geological domain, grid, and boundary conditions described above; only the petrophysical and mechanical properties differ. This helps us evaluate the observed differences in simulated wavefields and ground motions due to material property contrast of the medium, rather than changes in geometry of the domain.

4.4.1 Case A: Isotropic case (baseline scenario)

In this case, all the petrophysical and mechanical properties are similar through all the layers of the domain (i.e. the overlying caprock, reservoir, underlying caprock and fault). **Table 4.5** provides a list of petrophysical and mechanical properties in the isotropic case.

Table 4.5: Material properties for the isotropic case scenario.

Material Properties	**Overlying caprock**	**Reservoir**	**Underlying caprock**	**Fault**
Porosity, $\boldsymbol{\varphi}$	0.38	0.38	0.38	0.38
Permeability, **K**	1 x 10^{-13} m^2	1 x 10^{-13} m^2	1 x 10^{-13} m^2	1 x 10^{-13} m^2
Density, ρ	2600 kgm^{-3}	2600 kgm^{-3}	2600 kgm^{-3}	2600 kgm^{-3}
Young's Modulus, E	3.0GPa	3.0GPa	3.0GPa	3.0GPa
Poisson's ratio, v	0.3	0.3	0.3	0.3
P-wave velocity, V_p	1246.3 ms^{-1}	1246.3 ms^{-1}	1246.3 ms^{-1}	1246.3 ms^{-1}
S-wave velocity, V_s	666.2 ms^{-1}	666.2 ms^{-1}	666.2 ms^{-1}	666.2 ms^{-1}

4.4.2 Case B: Anisotropic case (layered anisotropic scenario)

In this scenario, anisotropy arises from stratification, i.e. the layers of the domain have contrasting material properties. **Table 4.6** provides the list of petrophysical and mechanical properties, specific to each layer.

Table 4.6: Material properties for the anisotropic case (layered anisotropic scenario).

Material Properties	**Overlying caprock**	**Reservoir**	**Underlying caprock**	**Fault**
Porosity, $\boldsymbol{\varphi}$	0.25	0.38	0.25	0.25
Permeability, **K**	1 x 10^{-20} m^2	1 x 10^{-13} m^2	1 x 10^{-20} m^2	1 x 10^{-20} m^2
Density, ρ	2600 kgm^{-3}	2600 kgm^{-3}	2600 kgm^{-3}	2500 kgm^{-3}
Young's Modulus, E	3.0GPa	2.09GPa	3.0GPa	2.04 Pa
Poisson's ratio, v	0.3	0.3	0.3	0.25
P-wave velocity, V_P	1246.3 ms^{-1}	1040 ms^{-1}	1246.3 ms^{-1}	990 ms^{-1}
S-wave velocity, V_s	666.2 ms^{-1}	556 ms^{-1}	666.2 ms^{-1}	571 ms^{-1}

4.4.3 Case C: Transverse vertical isotropy condition

For Case C, anisotropy condition arises due to the material properties being isotropic in the plane direction but shows variability when measured in the vertical direction. **Table 4.7** provides the list of petrophysical and mechanical properties, specific to each section of the geological domain.

Table 4.7: Material properties for the anisotropic case (transverse vertical anisotropic scenario).

Material Properties	**Overlying caprock**	**Reservoir**	**Underlying caprock**	**Fault**
Porosity, $\boldsymbol{\varphi}$	0.25	0.38	0.25	0.25
Permeability, **K**	1 x 10^{-20} m^2	1 x 10^{-13} m^2	1 x 10^{-20} m^2	1 x 10^{-20} m^2
Density, ρ	2600 kgm^{-3}	2600 kgm^{-3}	2600 kgm^{-3}	2500 kgm^{-3}
Young's Modulus, $E_x = E_y$	2.5GPa	2.09GPa	3.0GPa	2.04GPa
Young's Modulus, E_z	2.0GPa	1.8GPa	2.5GPa	1.7GPa
Poisson's ratio, $v_x = v_y$	0.12	0.20	0.12	0.20
Poisson's ratio, v_z	0.15	0.3	0.15	0.25
Shear Modulus, G_{xy}	1.12GPa	0.75GPa	1.34GPa	0.708GPa
Shear Modulus, $G_{xz} = G_{yz}$	0.67GPa	0.45GPa	0.803GPa	0.425GPa
P-wave velocity, V_P	1006.4 ms^{-1}	938.7 ms^{-1}	1101.6 ms^{-1}	910.6 ms^{-1}
S-wave velocity, V_s	655.2 ms^{-1}	537.1 ms^{-1}	717.7 ms^{-1}	532.3 ms^{-1}

The fluid properties of the resident brine and CO_2 are identical for Cases A-C and are highlighted in **Table 4.7.**

Table 4.8: Fluid properties of resident brine and CO_2.

Fluid Properties	**Density, $\rho_{w,CO2}$ (kgm^{-3})**	**Viscosity, $\mu_{w,CO2}$ (Pa.s)**	**Compressibility, $c_{w,CO2}$ (MPa^{-1})**
Resident brine, (w)	997	$5.5 * 10^{-4}$	$4.19 * 10^{-4}$
Carbon dioxide, (CO_2)	784	$6.9 * 10^{-5}$	$1.66 * 10^{-2}$

4.5 Summary

In this chapter we defined a unified modelling framework for three CO_2–reservoir case studies: an isotropic baseline (Case A), a layer-induced anisotropic model (Case B), and a transverse vertical anisotropic model in all sections of the stratified domain (Case C).

We specified a 30 × 20 × 5 km geological domain (500 m grid resolution; 24,000 cells, 27,511 nodes) and formulated the multiphase flow problem with brine-saturated, hydrostatic initial conditions and mixed Dirichlet/Neumann boundaries, including a hydrostatic far-field.

The quasi-static u–p model was posed on the same volume, upgrading each eight-node brick to a 20-node serendipity finite element (106,421 nodes) to improve displacement and stress/strain accuracy; cell-centred pressures from flow were consistently projected to nodal values.

For the multifield analysis, we adopted a downsized subdomain to meet wavelength and stability criteria at the 100 Hz target without exceeding workstation resources; velocity-based spacing were verified, with details provided in the Appendix E. Fluid properties for brine and CO_2 are held common across all cases. Case-specific parameters are reported in **tables (4.5 - 4.7**), ensuring that differences in wavefields and ground-motion reflect material contrasts rather than geometry.

In the next chapter, we present and discuss the findings of our analysis for multiphase flow, hydromechanical u-p and u-v-p wave propagation analysis.

Chapter 5: Results and Discussion

Here, we present the results and discussion of the numerical simulation of wave propagation associated with geological CO_2 sequestration, with emphasis on how the anisotropy in the layered reservoir affects pressure evolution, fault reactivation and ground shaking motion. The analysis is organized into the following categories: i.) a quasi-static u-p hydromechanical analysis to quantify injection-induced pore pressure changes on critically stressed faults within a reservoir and ii.) a dynamic u-v-p analysis to resolve dynamic wave fields radiated by fault reactivation. The results are reported for three case studies: i.) a homogeneous isotropic baseline medium, (labelled CASE A), where all petrophysical and mechanical properties of the reservoir are equal as shown (refer to **Table 4.5**) and ii.) an layered-anisotropic medium, (labelled CASE B), where anisotropy is due to the difference in material and petrophysical properties in each layer of the reservoir (refer to **Table 4.6**), and a stratified anisotropic medium, (labelled C), where transverse vertical isotropy is imposed in each section of the domain. The results for pressure evolution of Cases B and C, are presented with a single discussion of the hydraulic evolution, since the petrophysical properties are similar and thus lead to similar outcomes. However, the geomechanical response of Case C is examined separately, as the transverse vertical isotropy introduces differences relative to the other Case studies.

Contrasting these cases allows us to isolate the role of anisotropy in governing both pressure build-up, the characteristics of induced micro-seismicity and wave propagation during GCS activities.

This section would address the research questions stated above of 1.) Does a measurable pressure build-up occur during injection of CO_2 into the reservoir, and could anisotropy in the layers significantly affect the pressure build-up? 2.) Does the pressure build-up lead to fault reactivation due to pressure alteration throughout the reservoir ? 3) if fault reactivation occurs, what is the dynamic response, i.e. how is the energy released partitioned into radiated seismic waves, and to what extent could the associated seismic wave help in the prediction of potential ground shaking intensity ?

5.1 Results of Hydromechanical U-P Analysis

This subsection presents the U-P (displacement-pore pressure) results that quantify how CO_2 injection drives reservoir pressurization and redistribute effective stress under quasi-static conditions. We first tract the evolution of overpressure during constant injection rate of 16.168 m^3/s and compare the isotropic case to the anisotropic case, highlighting differences in the pressure build-up. With the pressure build-up, we evaluate the effects on fault reactivation

through the displacement of the fault and finally quantify the seismic moment, Mo, seismic magnitude, Mw, energy magnitude, Me and radiated seismic energy, Er for both case studies.

5.1.1 Pressure evolution in the isotropic baseline scenario (CASE A)

The isotropic, homogeneous reservoir pressure response serves as the reference case for this analysis. In this scenario, the rock and fluid properties (listed in Table 4.5) are spatially uniform with permeability being equal in all directions (i.e. K_x=K_y=K_z).

Consistent with the assumptions detailed in Section 3.2.1B, a single well (Figure 4.3) was used to inject 40 Mt/yr. at a constant rate of 1.6168 m^3/s over a three-year period.

With the system initialized by a hydrostatic pressure gradient (Figure 5.1a), a near-well overpressure lobe was registered within the first three years of CO_2 injection (Figure 5.1 b-d), with the absolute pressure ranging from ~5 MPa to ~50 MPa. This pressure distribution reflects the isotropic character of the domain as permeability is similar in all directions, so no preferential flow channel is favoured and the overpressure spreads uniformly and radially from the injector, with the injected CO_2 getting into the underlying caprock zone, an outcome inconsistent with safe CO_2 storage guidelines.

To analyse the near-well overpressure over time, we interpret the time series in Figure 5.1e, as pressure changes relative to the initial state, i.e. $\Delta P(t) = P(t) - P_{\text{hydrostatic}}\,(t = 0)$. The injection well (volume 15541 of the domain) exhibits a distinct early spike after approximately 6 months, reaching $\Delta P \approx 8.6$ MPa. This is because the depleted reservoir is assumed to be initially 100 % saturated with brine, so this pressure difference is necessary to displace the brine, pushing the brine into a smaller preferentially water-wet pore. This is evidenced in the injection/pressure build-up tests carried out by [143], [259], [260]. As the CO2 saturation builds around the well, the relative permeability evolution sharply increases total mobility as the injected CO2 has a lower viscosity than brine. This explains why after one year of injection, the observed pressure difference relaxes to $\Delta P \approx 7.2$ MPa, ~5.6 MPa after 2 years of injection, and ~5.0 MPa at the third year. The mean pressure throughout the domain increases by about 0.8 MPa (Figure 5.1e).

(a) t = 0-yr (reference state)

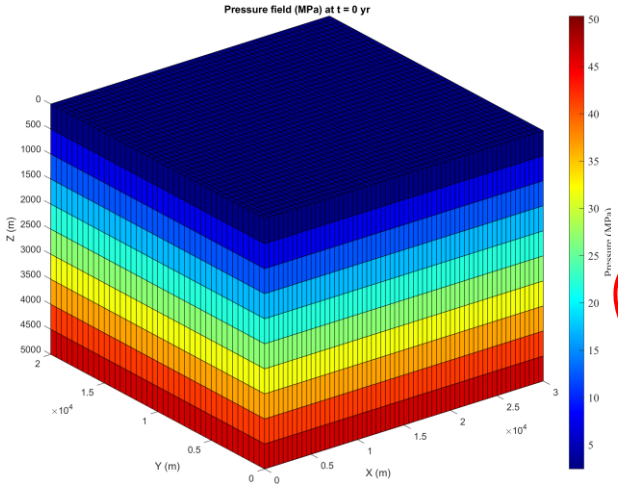

(b) t = 1-year

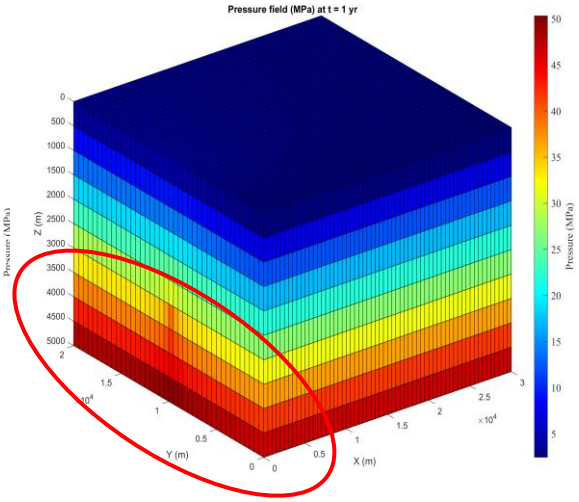

(c) t = 2-years

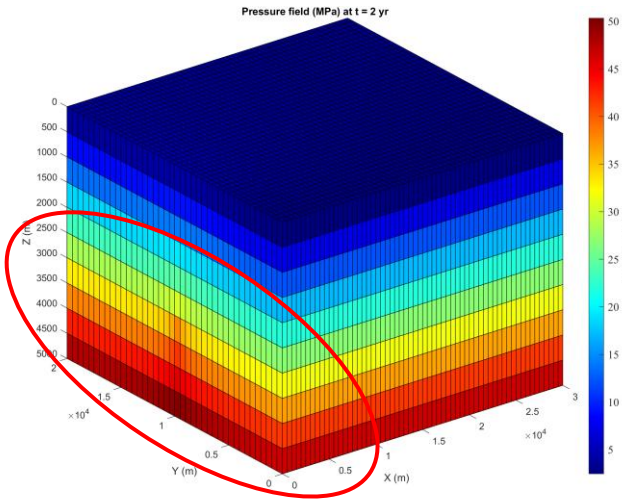

(d) t = 3-years

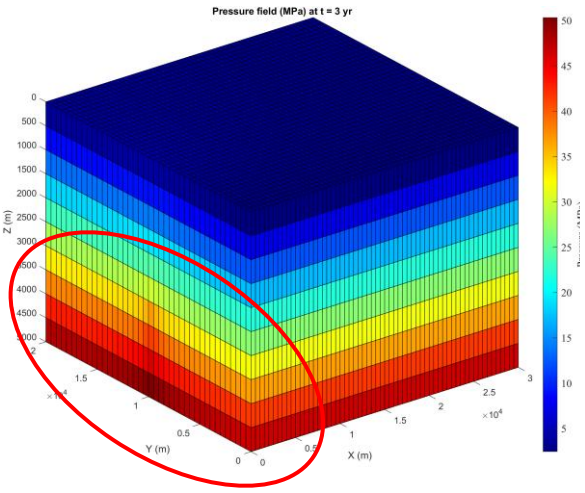

(e) change in pressure time series in injector cell vs whole domain

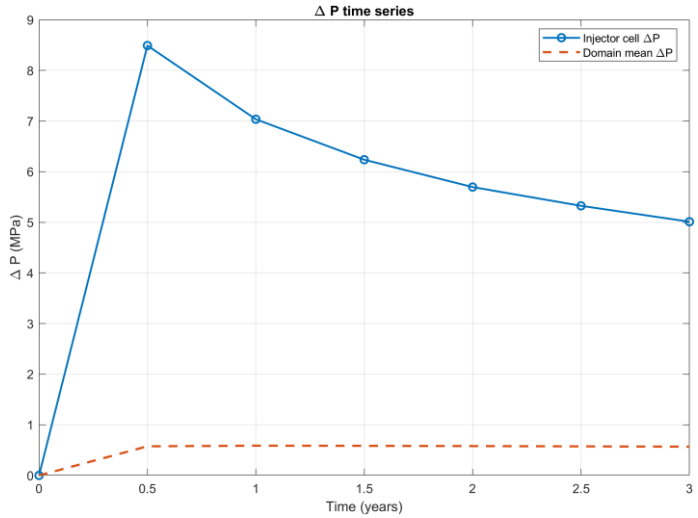

Figure 5.1: Pressure evolution over time, t (isotropic case): (a) t=reference state, (b) t=1- year; (c) 2-years, (d) t = 3-years; (e) pressure variation at injector well over time.

5.1.2 Pressure evolution in the anisotropic scenarios (CASES B & C)

For these scenarios, anisotropy arises from stratification (Case B), i.e. each layer of the domain (Figure 4.1) has contrasting material and petrophysical properties (listed in **Table 4.6)** and transverse vertical anisotropy in mechanical properties (Case C)**, (**(listed in **Table 4.7**). However, since the petrophysical properties in both Cases B and C are the same, the pressure evolution is identical in both scenarios and therefore presented together.

Similarly to the isotropic case, the assumptions detailed in Section 3.2.1B, and a single well (Figure 4.3**)** are maintained to inject 40 Mt/yr., at a constant rate of 1.6168 m^3/s over a three-year period.

The system initialized by a hydrostatic pressure gradient (Figure 5.2a), witnessed a near-well overpressure lobe within the first three years of CO_2 injection (Figure 5.2 b-d), with the absolute pressure ranging from ∼10 MPa to ∼70 MPa.

It is worth mentioning that, unlike the isotropic case (i.e. CASE A), the anisotropic simulation (i.e. CASE B & C) shows the pressure alteration confined to the reservoir interval only (Figure 5.2 b-d). This confinement arises because the overlying and underlying caprocks, serve as seals with an extremely low permeability, acting as effective barriers to vertical flow, preventing the injected CO_2 from migrating into units above or below the reservoir, an outcome that favours the long-term and safe CO_2 storage guidelines.

Likewise, for CASE B & C, the near-well overpressure over time, is interpreted using the time series in Figure 5.2e, as pressure changes relative to the initial state, i.e. $\Delta P(t) = P(t) - P_{\text{hydrostatic}}\ (t = 0)$. The injection well (cell volume 15541 of the domain) exhibits an early spike after 6 months, reaching ΔP ≈ 40 MPa. Critically, this overpressure is confined to the reservoir interval, with no transmission into the overlying caprock or underlying seal, preventing vertical transmissibility. The pressure difference displaces the resident brine laterally within the reservoir because the vertical seals inhibit upward or downward migration and curtails avenues for pressure relaxation; as a result , the injected volume is accommodated in the reservoir zone. With continued injection, the injection-cell pressure relaxes from ΔP ≈ 34 MPa after the first year of injection to ΔP ≈ 30 MPa after 2 years and ΔP ≈ 28 MPa by the third year of injection. For the anisotropic case study, the mean pressure throughout the domain increases by 4.8 MPa (Figure 5.2e).

(a) t = 0-yr (reference state)

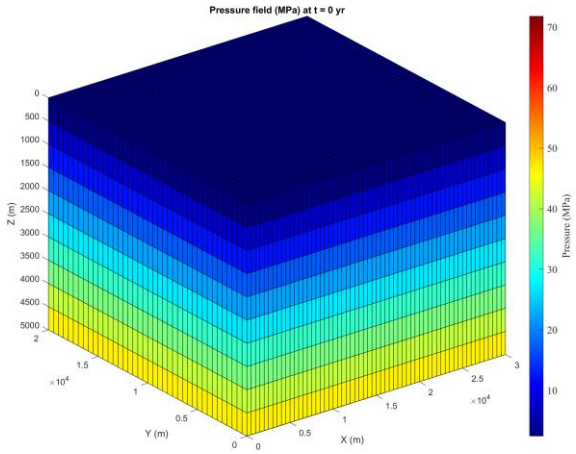

(b) t = 1-year

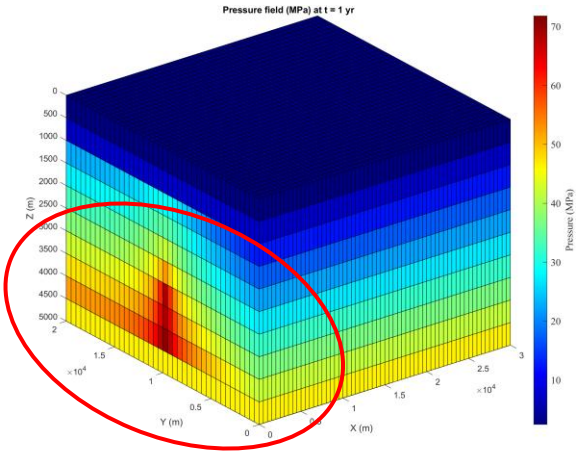

(c) t = 2-years

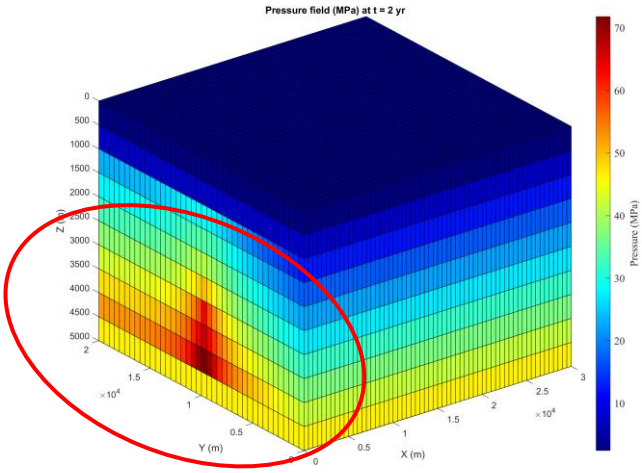

(d) t = 3-years

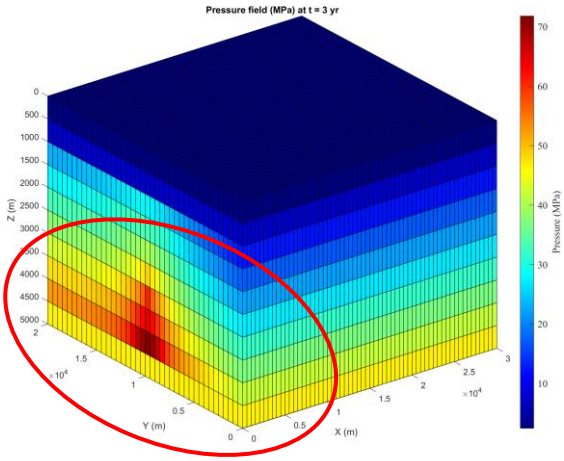

(e) change in pressure time series in injector cell vs whole domain

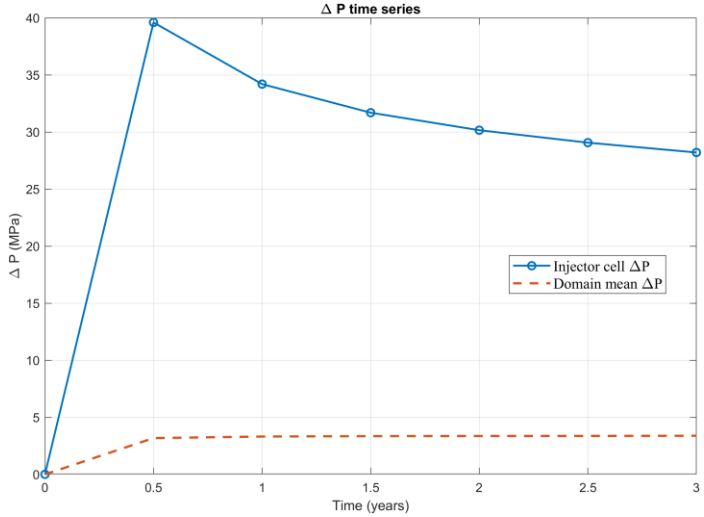

Figure 5.2: Pressure evolution over time, t (anisotropic case): (a) t=reference state, (b) t=1-year; (c) t=2-years, (d) t = 3-years; (e) pressure variation at injector well over time.

Across CASE A (isotropic) and CASE B & C (anisotropic), it becomes apparent from Figure 5.1 and 5.2, that the spike in pressure is localised only around the injection well. However, as injection continues over time, the pressure build-up is ultimately affected by the size of domain and its outer boundary.

As the pressure front expands with time, it encounters a critically stressed fault positioned at the boundary of the domain (Figure 4.1). In case A, this fault has the same permeability as the rest of the domain, hence it permits the flow of the injected CO_2. On the other hand, in CASE B & C, the fault acts as a no flow boundary with low permeability, preventing the fluid from moving out of the reservoir zone. Studies carried out by [143] established that reservoir model size has a pronounced effect on pressure build-up. Larger domains exhibit a lower build-up than compact models because their outer boundaries are set further away from the injection well. Nevertheless, it remains essential to evaluate pressure at the far end of the domain, because modest far-field pressure changes, ΔP, can accumulate over vast areas, an influence the geomechanics of critically stressed faults. Given the large domain and critically stressed fault, we evaluate the pressure evolution at far end of domain for CASES A, B, and C.

5.1.3 Pressure evolution at far end of domain (close to fault)

The results here focus on the second layer, which is the designated CO_2 storage reservoir, and we interpret the curves as a per-cell pressure change relative to the initial state. The fault is positioned towards the outer boundary (Figure 4.1) in both simulations, so it controls how the reservoir pressure front interacts with the far-field.

In CASE A (isotropic), the fault has the same permeability as the rest of the domain (**Table 4.5**) and behaves as a conductive pathway. Within a year, the near fault cells ($r > 5$km) levels off at $\approx$ 1.5 MPa and remains close to that value through the 3 years (Figure 5.3). This modest reservoir pressure response arises because the over- and underlying layers are permeable, acting as pressure sinks that prevent significant overpressure from developing in the storage zone.

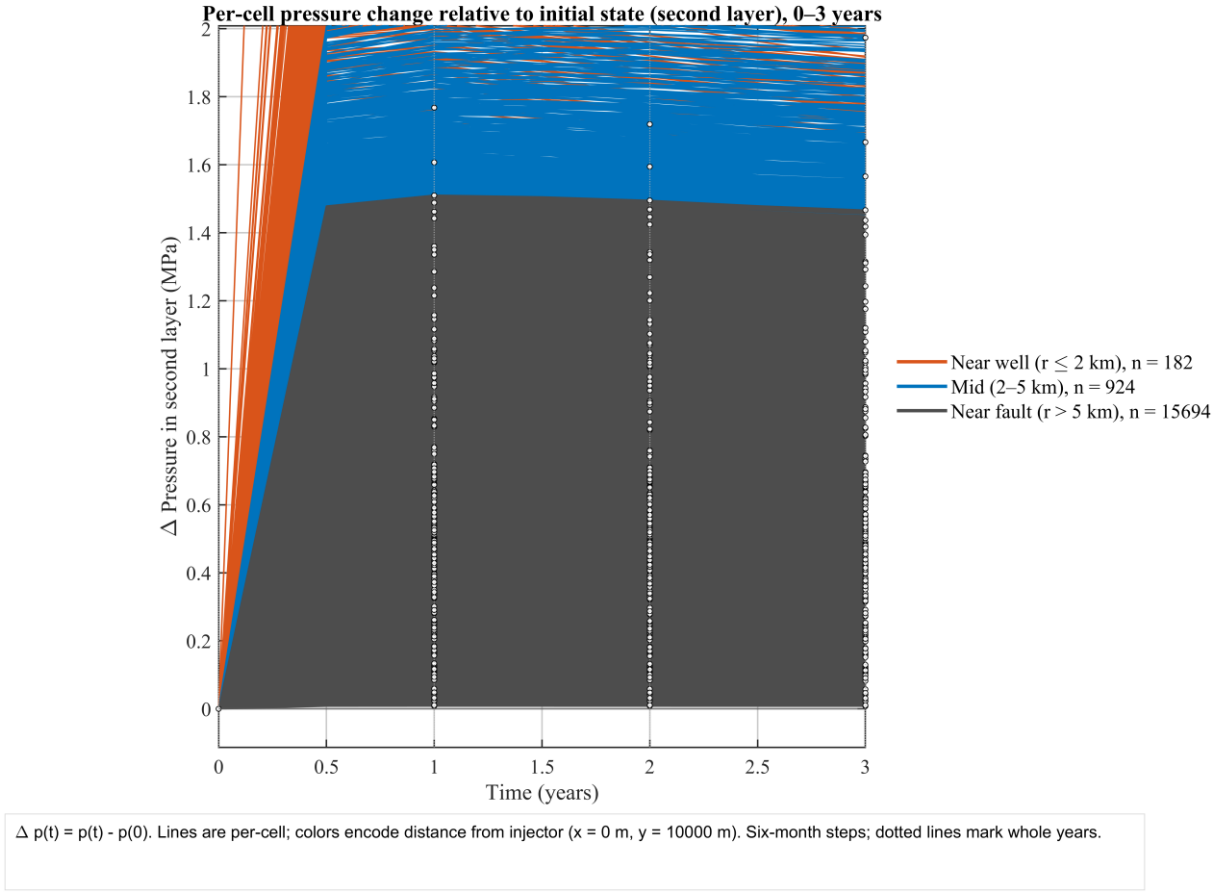

Figure 5.3: Reservoir layer per-cell pressure change at different locations of the domain (isotropic case).

Conversely, in CASE B & C (anisotropic), the fault is assigned low permeability (**Table 4.6 and Table 4.7**) and functions as an effective seal. The near fault cells in this case have a much higher pressure , building to ≈ 12.5 MPa within a year and stays elevated within the three (3) years of injection with minimal decay (Figure 5.4).

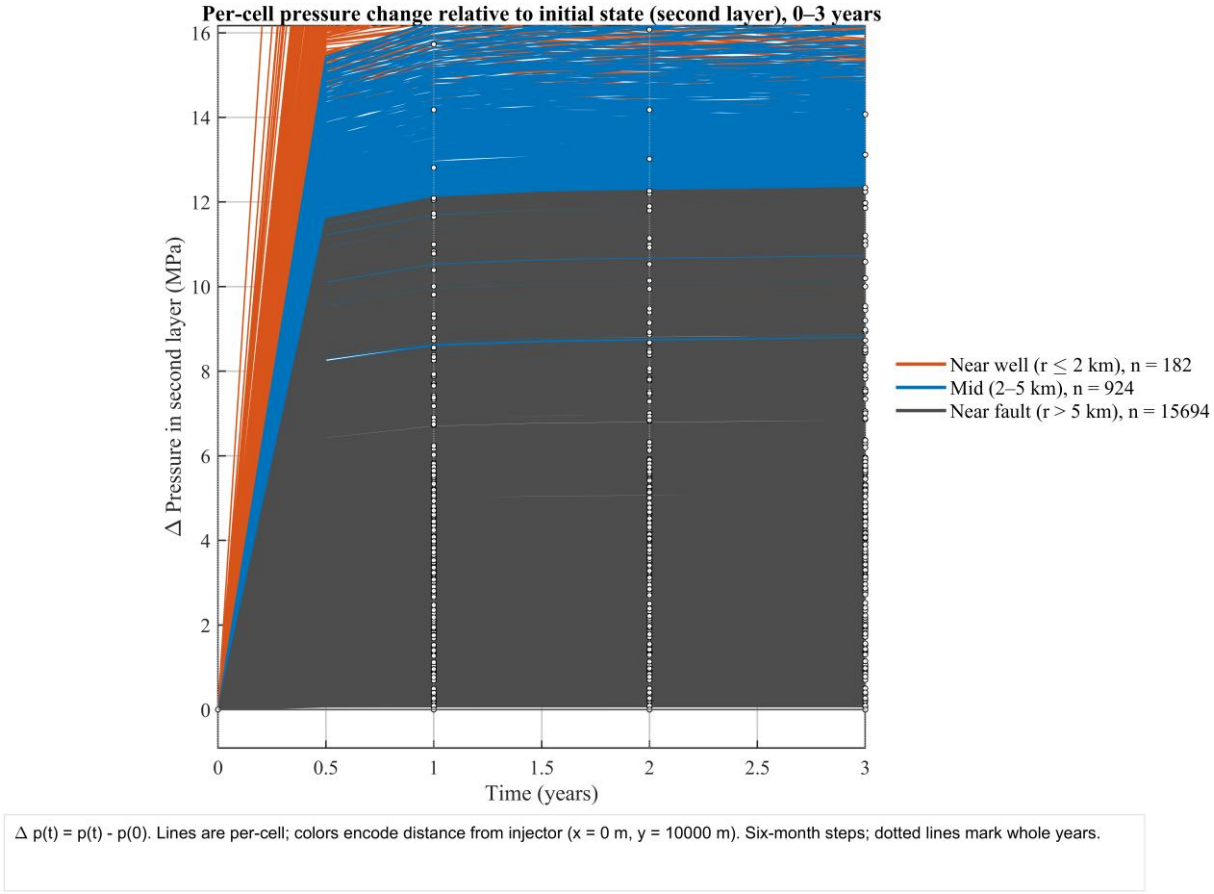

Figure 5.4: Reservoir layer per-cell pressure change at different locations of the domain (anisotropic case studies (B&C))

These reservoir layer results show distinct regimes. With a conductive fault (CASE A), the pressure dissipates laterally into the far field, keeping far-end changes in pressure, ΔP small while with the sealing fault (CASE B), the pressure front impinges on the boundary, producing boundary-controlled build-up that persists at the far end of the storage. Although both scenarios, registered distinct pressure changes at close to the fault, research has shown that minimal alterations in the pressure/stress field could potentially reactivate the critically stressed fault. This was evident in the study carried out by [162], [259] were approximately, a 7.5 MPa spike in pressure was enough to cause a fault slip at the far-end of their domain. Therefore, all categories, i.e. CASE A (isotropic), CASE B (anisotropic), and CASE C (transverse vertical isotropy) could register micro-seismic events during GCS operations. For this reason, we evaluate the geomechanical response in terms of displacement of the fault (fault reactivation) due to pressure alteration in both scenarios.

5.1.4 Geomechanical response due to pressure evolution in CASE A (isotropic)

After three (3) years, the displacement field reflects the poroelastic response to injection-induced overpressure, with magnitudes and spatial patterns tracking how pressure diffuses and

is confined within the domain. The displacement pattern is smooth and radially symmetric around the injection well, consistent with isotropic pressure diffusion. The uplift in the domain due to injection is modest, ranging between 3-5 mm across the whole domain. Although the fault is far away from the injector well, the injection-induced pressure is felt at the fault nodes registering a fault displacement of approximately 3.5 mm in the vertical direction (u_z) (Figure 5.5a). The horizontal displacement (u_x, u_y) on the contrary, is quite low, recording less than 1 mm throughout the domain (Figure 5.5b). This low displacement arises because with all formations being equal in permeability, the injected fluid migrates into the over- and underlying formations, acting as sinks limiting significant reservoir overpressure. Near the fault, the displacement field remains non-zero in the horizontal direction, indicating negligible far-end deformation in the isotropic case.

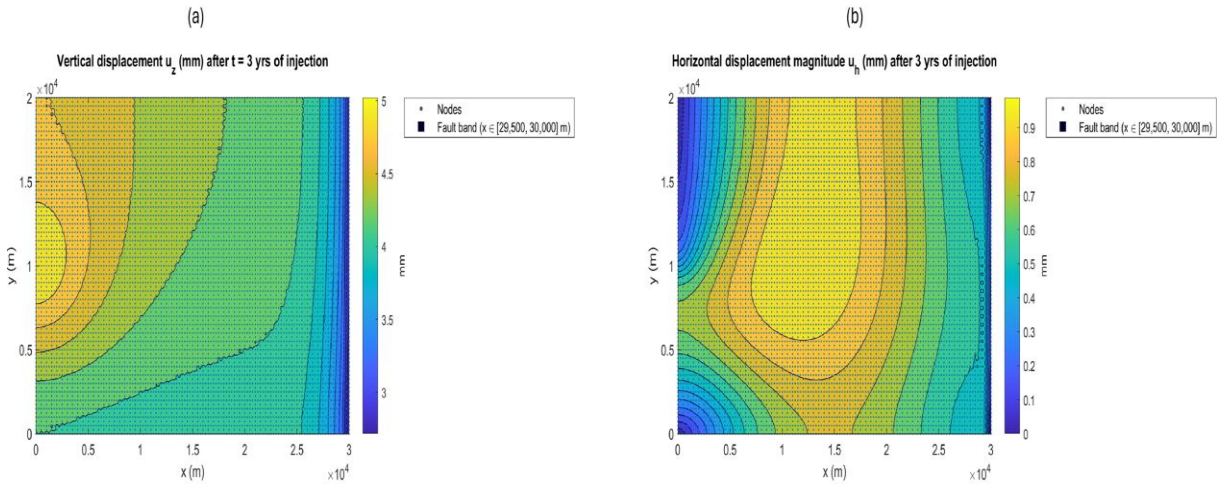

Figure 5.5: Fault displacement evaluation (isotropic case) (a) vertical direction, (b) horizontal direction.

5.1.5 Geomechanical response due to pressure evolution in CASE B (layered anisotropy)

In case B (anisotropic, stratified with sealing caprock and base) the same injection procedure, instigates a much stronger and more extensive deformation in both the vertical and horizontal directions. The caprocks confine the pressure within the reservoir, so the effective stress reduction is much larger and more persistent. Consequently, the vertical displacement (u_z) increases to approximately 5-17 mm, while the horizontal displacement (u_x, u_y) reaches about 10 mm (Figure 5.6 a & b). The lobes of these figures in the anisotropic case are mildly elongated when compared to the isotropic case due to anisotropic transmissibility, and stiffness between the layers of the domain.

In addition, the deformation within the domain does not dissipate before the boundary. That is, within the fault band , the nodes register a measurable horizontal and vertical displacement of 5 mm and 8 mm respectively. This indicates that the confined over pressure has propagated sufficient poroelastic effects at the far-end of the domain, causing fault displacement (fault reactivation).

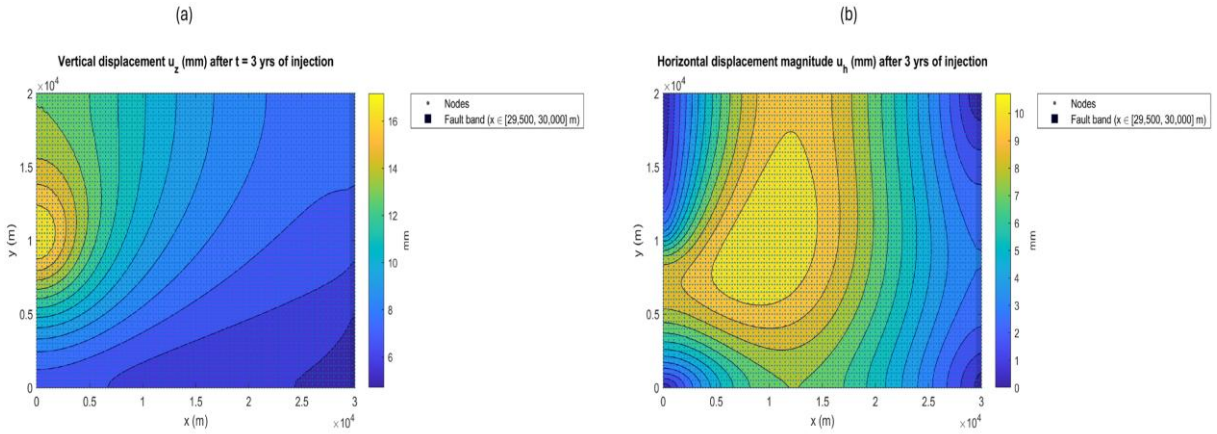

Figure 5.6: Fault displacement evaluation (anisotropic case) (a) vertical direction, (b) horizontal direction.

5.1.6 Geomechanical response due to pressure evolution in CASE C (transverse vertical isotropy imposed in all sections of the domain

For case C (stratigraphy, with transverse vertical isotropy imposed in each layer of the reservoir), under similar injection procedure as Case B, an even more pronounced deformation is registered in both the vertical and horizontal displacements. The presence of the impermeable caprock, similarly restricts pressure within the reservoir as observed in Case B; however, the imposed transverse vertical isotropy (VTI), leads to a greater and more sustained reduction in effective stress. The vertical displacement (u_z) ranges from approximately 5-25 mm, while the horizontal displacement (u_x, u_y) reaches about 16 mm (Figure 5.7 a & b)

The simulations shows that injection-driven pressure redistribution produces fault displacement (reactivation) in all scenarios, with a strongest response in CASE C. The anisotropic sealed architecture in cases B & C, confines overpressure within the storage interval, increasing ΔP and poroelastic strain and thereby amplifying both horizontal and vertical displacements transmitted to the fault band. CASE A, the isotropic, baseline scenario exhibits a more negligible far-field response because pressure can leak off into adjacent permeable units, limiting stress perturbations at the fault.

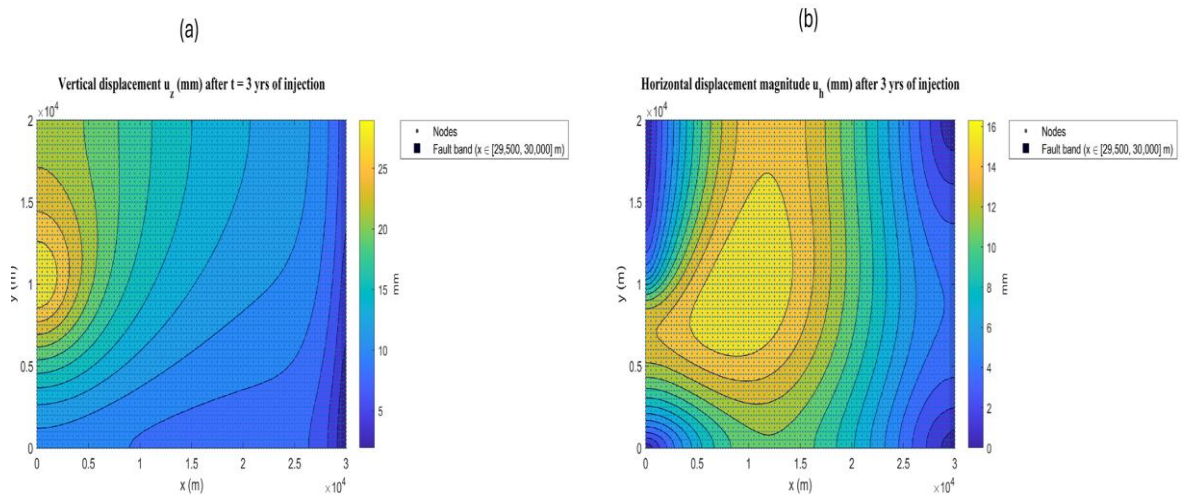

Figure 5.7: Fault displacement evaluation (transverse vertical isotropy case) (a) vertical direction, (b) horizontal direction.

These findings are consistent with field-scale geomechanical interpretations at In Salah (Krechba), where the authors [260] coupled CO_2 injection to fracture/fault-zone reactivation inferred from ground deformation. In their study a ~2 cm uplift signal after ~2 years of injection was registered. This was largely attributed to the proximity of the reactivated fracture zone to the injection well (KB-502), concentrating pressure and deformation locally. In contrast, our modelled fault lies far from the injector, yet reactivation still occurs because even modest, far-end changes in pressure can alter effective stress sufficiently on a critically stressed structure. Together, these results motivate explicit evaluation of far-end pressure and displacement effects in GCS projects: the isotropic case provides a conservative baseline, while the anisotropic, pressure-confined case indicates a higher reactivation potential despite the position of the well.

With the fault slip registered, it is essential to quantify the source metrics that govern seismic hazard and monitoring: i.e. the seismic moment, M_o, seismic magnitude, M_w, energy magnitude, M_e, and radiated seismic energy, E_r.

5.1.7 Seismic source characterization (Mo. Mw) for Case A (isotropic)

We quantify the seismic source variables using seismic moment, M_o, and seismic magnitude, M_w, computed from the modelled fault displacements via equations (3.49 & 3.55). The analysis is restricted to the reservoir interval segment, a 3500 m long section represented by the red slab (Figure 5.8a). Events are restricted to the fault region (x = 29.5 – 30 km). Each nodal displacement along the fault is used to evaluate the seismic moment range within the reservoir zone. The resulting cloud cluster along the fault surface (Figure 5.8a), suggests that the micro-seismic moment, M_o range spans from 10^{10} Nm to about 10^{12} Nm.

Following the spatial characterization, panel (Figure 5.8b) condenses the events into an occurrence histogram of $\log_{10}(M_0)$ within the region of interest (ROI). The distribution proves to unimodal and tightly clustered with more than 90 events registered near the magnitude of $\log_{10}(M_0) \approx 11 = M_0 \sim 10^{11}$Nm. The vertical reference at 10^{15}Nm (red line) emphasizes that all modelled events are orders of magnitude lower than seismic moments registered by larger earthquakes.

Figure 5.8c translates the fault-plane seismic moments, M_o, to frequency distribution of seismic magnitude, M_w. The distribution is concentrated with an event range of Mw ≈ 0.7-1.9. CASE A, therefore, registers a low magnitude indicating that fault reactivation remains micro-seismic under the modelled pressure loads, consistent with the fault-slip inferred from poroelastic displacement field.

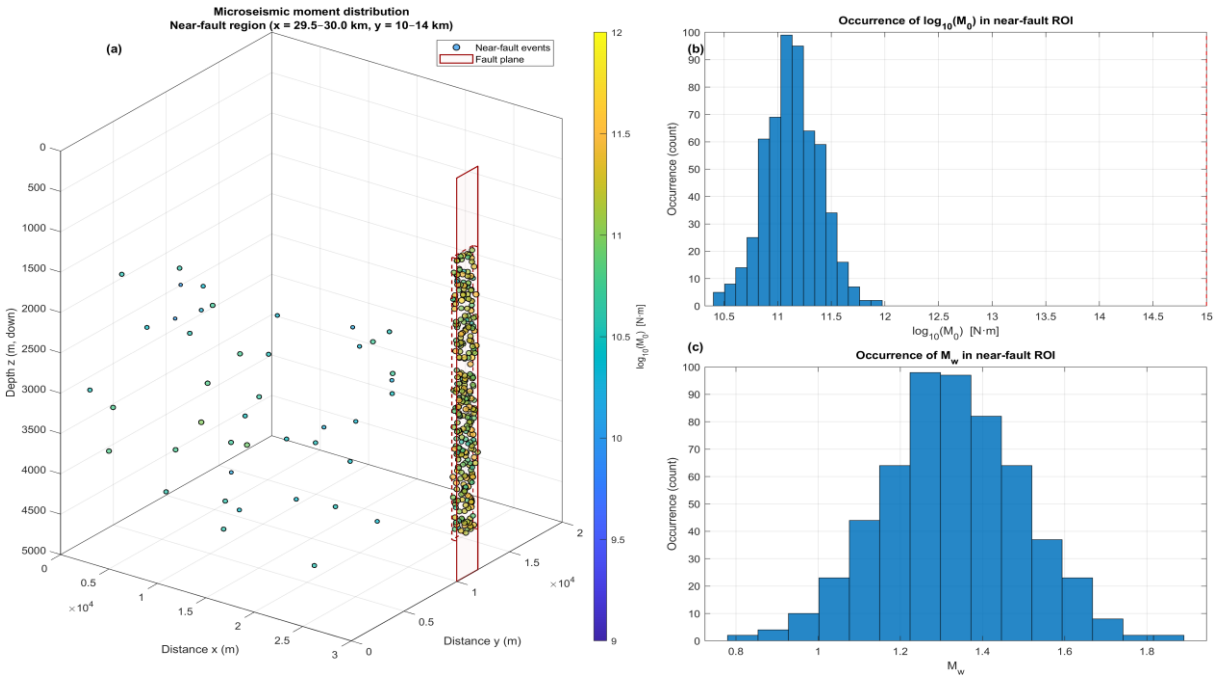

Figure 5.8: (a) Seismic moment (M_0) variation across the fault; (b) along-fault occurrence of M_0 within the region of interest (ROI); (c) along-fault occurrence of moment magnitude (Mw) within the ROI. (isotropic case)

5.1.8 Seismic source characterization (M_o, M_w) for Case B (layered anisotropy)

In CASE B (layered anisotropy), we quantify the seismic moment, M_o, and seismic magnitude, M_w, under conditions of higher-pressure build-up arising from the impermeable overlying and underlying caprocks, confining CO_2 storage within the storage reservoir (Figure 5.2 b - d).

The resulting cloud cluster along the fault plane surface (Figure 5.9a), suggests that the micro-seismic moment, M_o, ranges from 10^{11} Nm to about 10^{13} Nm for the confined higher-pressure

scenario. This accounts for about 150 seismic events recorded within three (3) years of CO_2 injection, with magnitudes between of $\log_{10}(M_0) \approx 12 = M_0 \sim 10^{12}$Nm and $\log_{10}(M_0) \approx 13 = M_0 \sim 10^{13}$Nm (Figure 5.9b). The frequency distribution in CASE B is concentrated, with an event range of Mw ≈ 1.6 – 2.8 (Figure 5.9c).

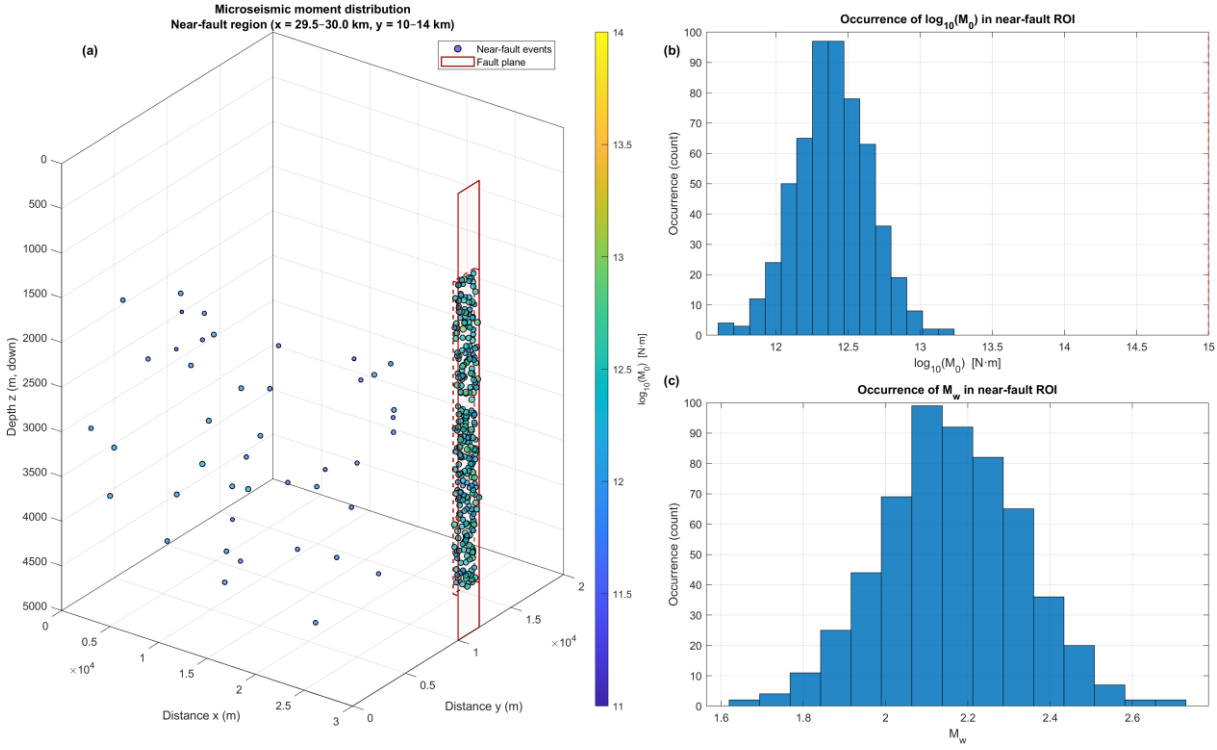

Figure 5.9: (a) Seismic moment (M_0) variation across the fault; (b) along-fault occurrence of M_0 within the region of interest (ROI); (c) along-fault occurrence of moment magnitude (Mw) within the ROI. (layered anisotropy case)

5.1.9 Seismic source characterization (M_o, M_w) for Case C (layered anisotropy, with transverse vertical isotropy imposed)

With transverse vertical isotropy imposed in each section of the domain, we quantify the seismic moment, M_o, and seismic magnitude, M_w, under similar conditions of high-pressure build-up, with the injected fluid injected within the storage reservoir (Figure 5.2 b – d) analogous to Case B.

The cloud cluster along the fault plane surface (Figure 5.10a), suggests that the micro-seismic moment, M_o, ranges from 10^{11} Nm to about $10^{13.5}$ Nm for the confined higher-pressure scenario. This accounts for about 170 seismic events recorded within three (3) years of CO_2 injection, with magnitudes between of $\log_{10}(M_0) \approx 12 = M_0 \sim 10^{12}$Nm and $\log_{10}(M_0) \approx 13.5 = M_0 \sim 10^{13.5}$Nm (Figure 5.10b). The frequency distribution in CASE B is concentrated, with an event range of Mw ≈ 1.7 – 2.9 (Figure 5.10c).

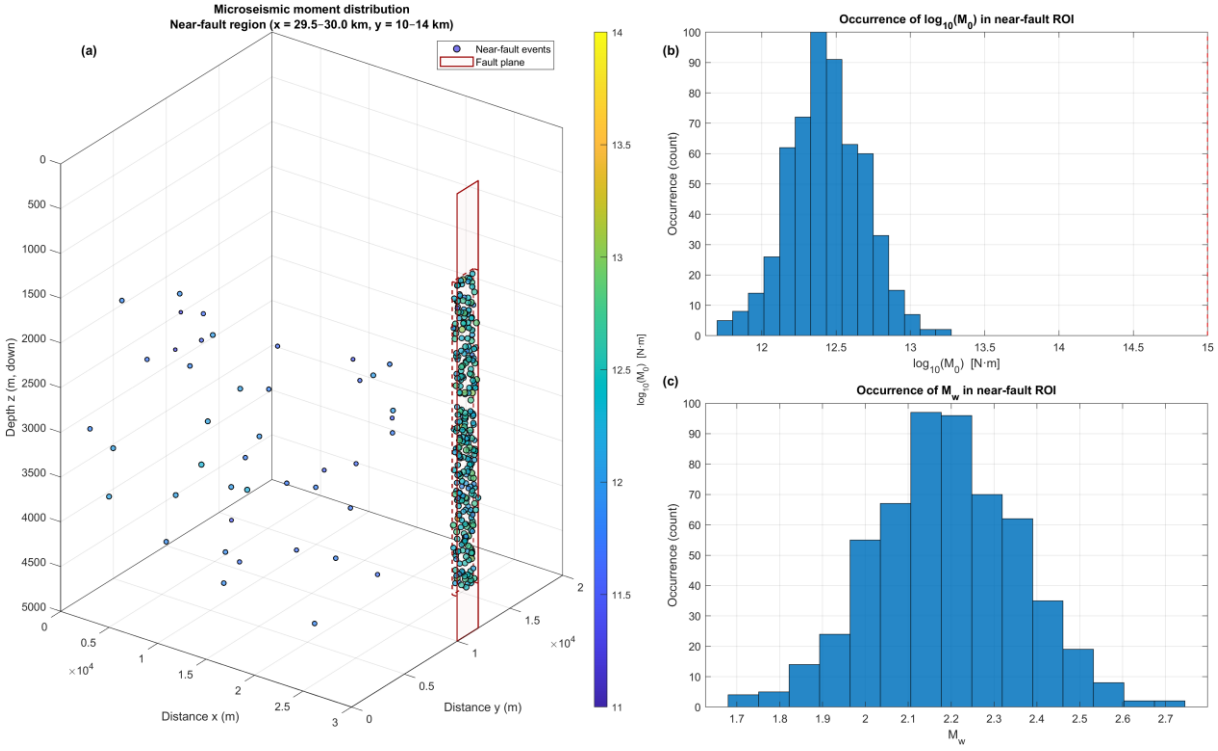

Figure 5.10: (a) Seismic moment (M_0) variation across the fault; (b) along-fault occurrence of M_0 within the region of interest (ROI); (c) along-fault occurrence of moment magnitude (Mw) within the ROI. (Transverse Vertical Isotropy imposed)

In summary, the isotropic (CASE A), layered anisotropy (CASE B) and the transverse vertical isotropy (CASE C) simulations, yield source sizes that are micro-seismic with moments below the order of 10^{15}Nm as seen in **Table 5.1.** These values are analogous to those registered in some fields stated in Table 2.2 such as the In Salah field studied by [106] and Aneth project researched by [169]. For context, the standard magnitude classified from "light" to "great" are listed below in (**Table 5.2**), showing that our modelled moments lie beneath those ranges.

Table 5.1: Summary of seismic source range for M_o and M_w.

Seismic source	**Case A (Isotropic)**	**Case B (layered anisotropy)**	**Case C (TVI)**
Seismic moment, M_o (Nm)	$10^{10} < M_o < 10^{12}$	$10^{11} < M_o < 10^{13}$	$10^{12} < M_o < 10^{13.5}$
Seismic magnitude, M_w	$0.8 < M_w < 1.9$	$1.6 < M_w < 2.8$	$1.7 < M_w < 2.9$

Table 5.2: Seismic moment ranges for earthquakes [261]

Earthquake size	Seismic Moment, M_o (Nm)
Light earthquake	$10^{15} – 10^{16}$
Moderate earthquake	$10^{16} – 10^{17}$
Strong earthquake	$10^{18} – 10^{19}$
Major earthquake	$10^{19} – 10^{20}$
Great earthquake	$> 10^{21}$

While the seismic magnitude, M_w, and seismic moment, M_o, are both convenient when estimating earthquake size, they do not offer a direct insight into the energy released by seismic waves, which are more relevant for engineering applications and quick evaluation of an earthquake's shaking potential. To avoid presenting the entire earthquake spectra with these two variables, specialists such as [166], [167], [168], [177], suggested evaluating the energy magnitude, M_e and radiated seismic energy, E_r. These added variables offer a deeper insight into evaluating seismic risk, and how the seismic P-waves and S-waves propagate once the energy is released during GCS.

5.1.10 Seismic source characterization (M_e, E_r) to evaluate the energy radiated for Cases A, B and C

Using equation (3.56) and equation (3.57), the radiated energies, are computed from the reported seismic moment and magnitude. The results in Figure 5.11 & Figure 5.12 of $\log_{10} E_r$ vs. M_e shows a linear trend consistent with the theoretical scaling factor defined by [163], [164], [166], [167].

For CASE A (Figure 5.11Figure 5.11), the near fault (blue) and near well (orange) estimates for M_e fall on a range from 1.2 – 2.8, corresponding to a released seismic energy of $10^{2.5}$J – $10^{4.7}$J. For CASE B (Figure 5.12), the estimates of Me ranges from 2.4 – 3.8 for an energy seismic release of 10^4J – 10^6J. Conversely, the near fault (blue) and near well (orange) estimates for M_e fall on a range from 2.2 – 3.7, corresponding to a released seismic energy of $10^{7.5}$J – $10^{8.8}$J. These analyses show that the energy released after fault reactivation in the transverse vertical isotropic (TVI) scenario registered the most released energy when compared to the isotropic (CASE A) and stratified anisotropy (CASE B) scenarios. In addition, the estimated energy magnitudes for both scenarios fall within the range of micro-seismic radiated energies observed in a study, performed in the northeastern Alps [262].

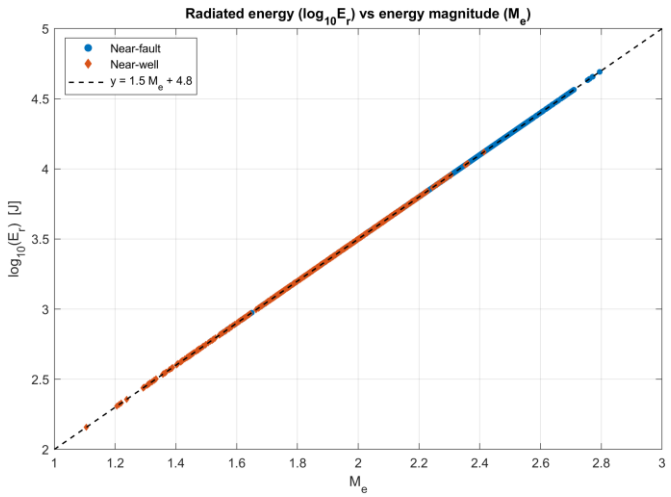

Figure 5.11: Energy released, Er, near-well vs near fault (isotropic case)

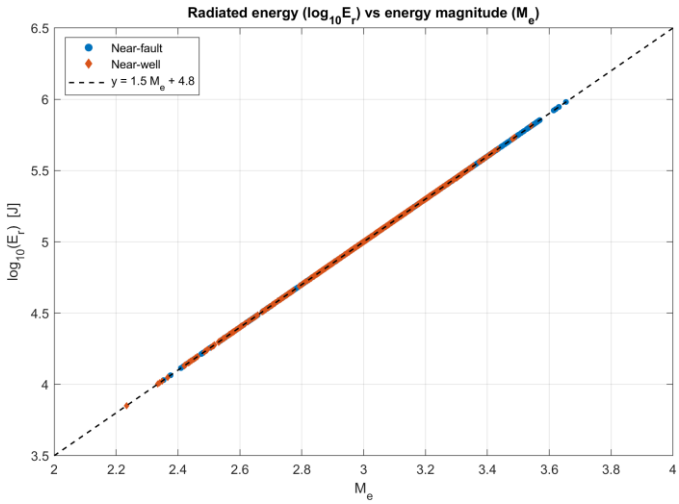

Figure 5.12: Energy released, Er, near-well vs near fault (layered anisotropic case)

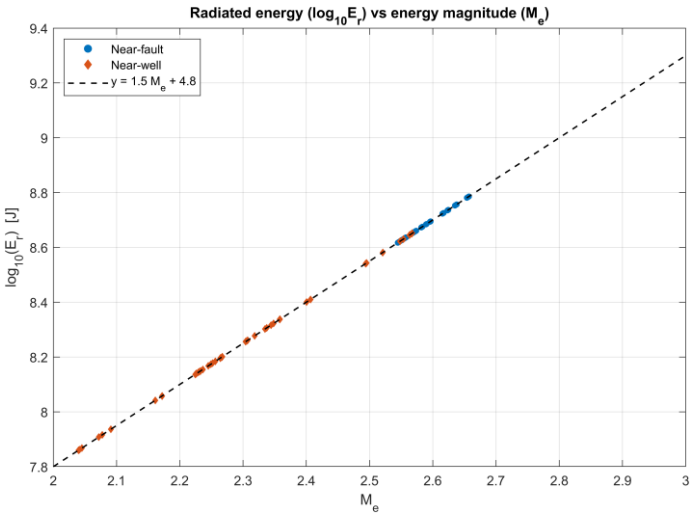

Figure 5.13: Energy released, Er, near-well vs near fault (transverse vertical isotropy case)

5.1.11 Summary of Hydromechanical Analysis

In summary, under constant injection (1.6168 m^3s^{-1}; 40 Mt $yr.^{-1}$), the hydromechanical study through the u-p analysis shows that the pressure build-up in the transverse vertical isotropic scenario was much stronger than that of the isotropic and stratified anisotropic case studies. Despite the large model domain, injection-driven overpressure propagated to the fault boundary, and produced measurable fault displacement in both case studies. Expressed as seismic source parameters of seismic moment, M_o, seismic magnitude, M_w, energy magnitude, M_e, and released seismic energy, E_r, these fault displacements fall within the micro-seismic range, but they reveal clear contrasts: the stratified anisotropic and the transverse vertical isotropic, sealed configurations (i.e. CASES B & C, respectively) confines overpressure within the storage interval and therefore generates larger seismic moments and higher radiated energy than the isotropic baseline (CASE A). Collectively, these results indicate that, reservoir anisotropy govern the amplitude and persistence of far-field stress perturbations and in turn the magnitude and energy of the resulting micro-seismicity.

Having established these source parameters for CASE A, B, and C, we assess if the radiated energy released, causes a potential ground shaking effect. This is done via a wave-propagation analysis, from which we compute the displacement, velocity, and pressure (u-v-p) of the wave front. The subsequent section presents the wave propagation results and their implications for monitoring.

5.2 Results of Hydromechanical Wave Propagation U-V-P Analysis

This section presents the numerical simulations that examine wave propagation and shear wave splitting initiated by an impulsive source in the reduced three-dimensional domain. The source is derived from the fault-slip event, with the recorded seismic moments (**Table 5.1**) set as the impulsive strength. In the isotropic scenario, a seismic moment of 10^{11}Nm is used, based on occurrence rate in Figure 5.8Figure 5.8b, while a seismic moment of 10^{12}Nm is adopted for the stratified anisotropic (CASE B) and the transverse vertical isotropic (CASE C) scenarios based on occurrence rates registered in Figure 5.9b & Figure 5.10b, respectively. The system frequency for all scenarios is set at 100 Hz, i.e. above this frequency, the wave component is highly attenuated. The time of the simulation of the wave motion is set at time, t = 0.0425s for CASE A, time, t = 0.054s for CASE B and time, t = 0.058s for CASE C (review appendix E for derivation). The boundary and initial conditions for all scenarios follow those stipulated in section 3.6D.

This section is presented into three parts. First the isotropic case, detailing the ground motion results, the arrival times of the body and surface waves, and the corresponding wave velocities. Thereafter, we review the anisotropic case and transverse vertical isotropy configuration, where we review the same diagnostics and highlight the differences relative to the baseline. In these analyses, the points of interest are the nodes on the fault element. That is, point A (i.e. the fault zone where the reservoir section intersects the overlying caprock layer), and point B (i.e. node of fault that intersects the underlying seal), and impulse at position of injection well. These points were selected based on findings from previous studies [62], [107], [259], [263], which identified these zones as the most heavily impacted during geological carbon storage (GCS) activities. For illustrative purposes, we present the domain indicating the coordinates of interest, and the reduced domain (Figure 5.14).

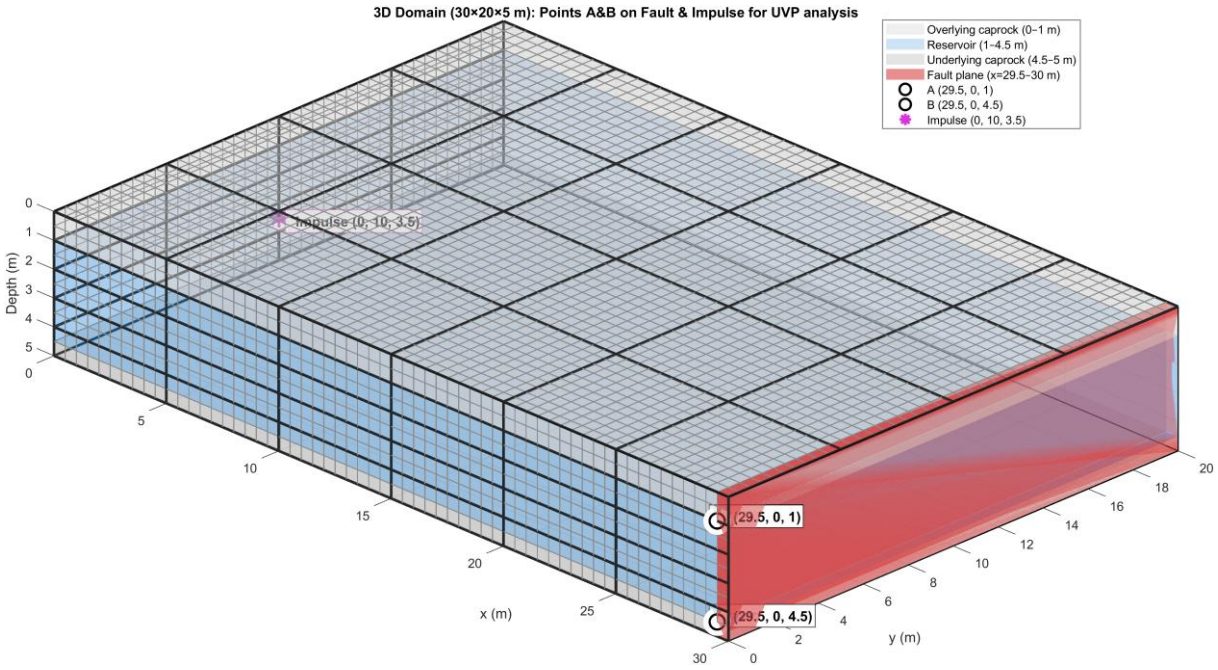

Figure 5.14: Domain layout and points of interest (A, B, and Impulse) for UVP analysis.

5.2.1 Wave propagation results in CASE A (isotropic)

The load history shown (Figure 5.15) is the source function used for the isotropic case. A smooth half-sine pulse of $f(t) = 10^{11}\sin(100\pi \mathrm{T})[1 - H(t - \mathrm{T})]$, with period, T ≈ 10 ms and peak amplitude, of 10^{10} at time, t = T/2. After the period, T, of the impulse, the amplitude goes to zero thereafter. This compact pulse minimizes spurious high-frequency content at onset and at end of pulse, while providing a sufficient bandwidth for travel time analysis. The spectrum is dominated by a frequency order of 100 Hz. Practically, the short, bandwidth impulse, yields

sharp P, S, and Rayleigh waves, facilitating ground motion analysis, peak ground velocity estimation in the isotropic medium.

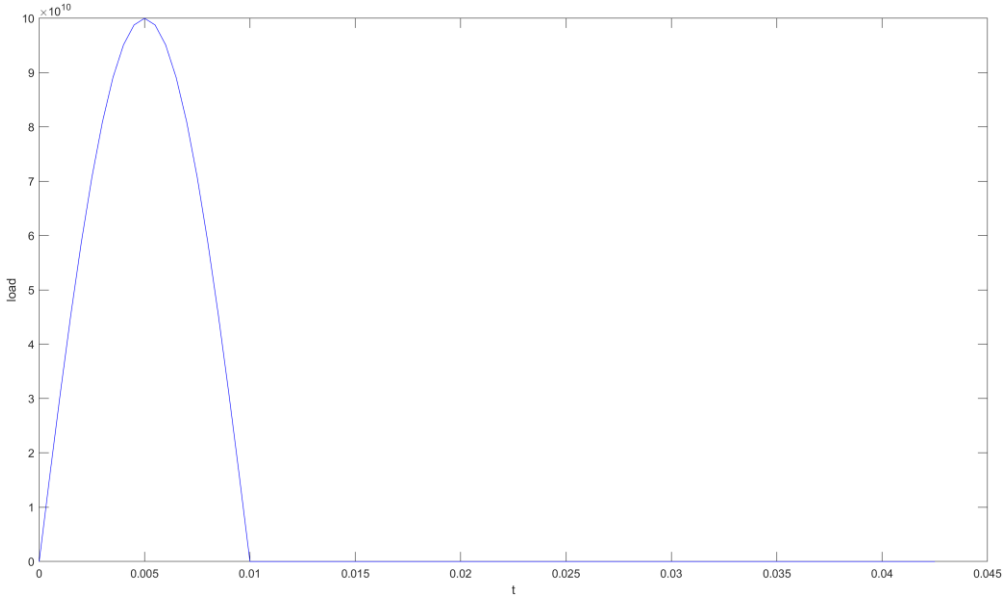

Figure 5.15: Impulsive load (isotropic scenario)

As a prerequisite for the wave-profile analysis, performed calculations detailed in Appendix E and summarized in **Table 5.3.**

Table 5.3: Derived metrics supporting the "CASE-A" wave propagation analysis.

Parameter	**Value**
Period of impulse, T	10 milliseconds (ms)
Time step of simulation, Δt	500 microseconds (μs)
Travel time for P-wave	24 milliseconds (ms)
Travel time for S-wave	45 milliseconds (ms)
Number of time steps required for simulation of P-wave	≈ 48-time steps
Number of time steps required for simulation of S-wave	≈ 86-time steps

Subsequently, we examine the ground motion and particle velocity derived from the wave analysis at the two nodes of interest depicted in (Figure 5.14). For each node we present the results in the horizontal and vertical direction.

A.) Node A (interface between reservoir and overlying caprock: (coordinates 29.5; 0; 1)):

Figures 5.16 (a) and 5.16(b) present the time evolution of nodal displacement, with horizontal and vertical components, respectively. The corresponding solid velocity responses are displayed in Figures 5.16(c) and 5.16(d).

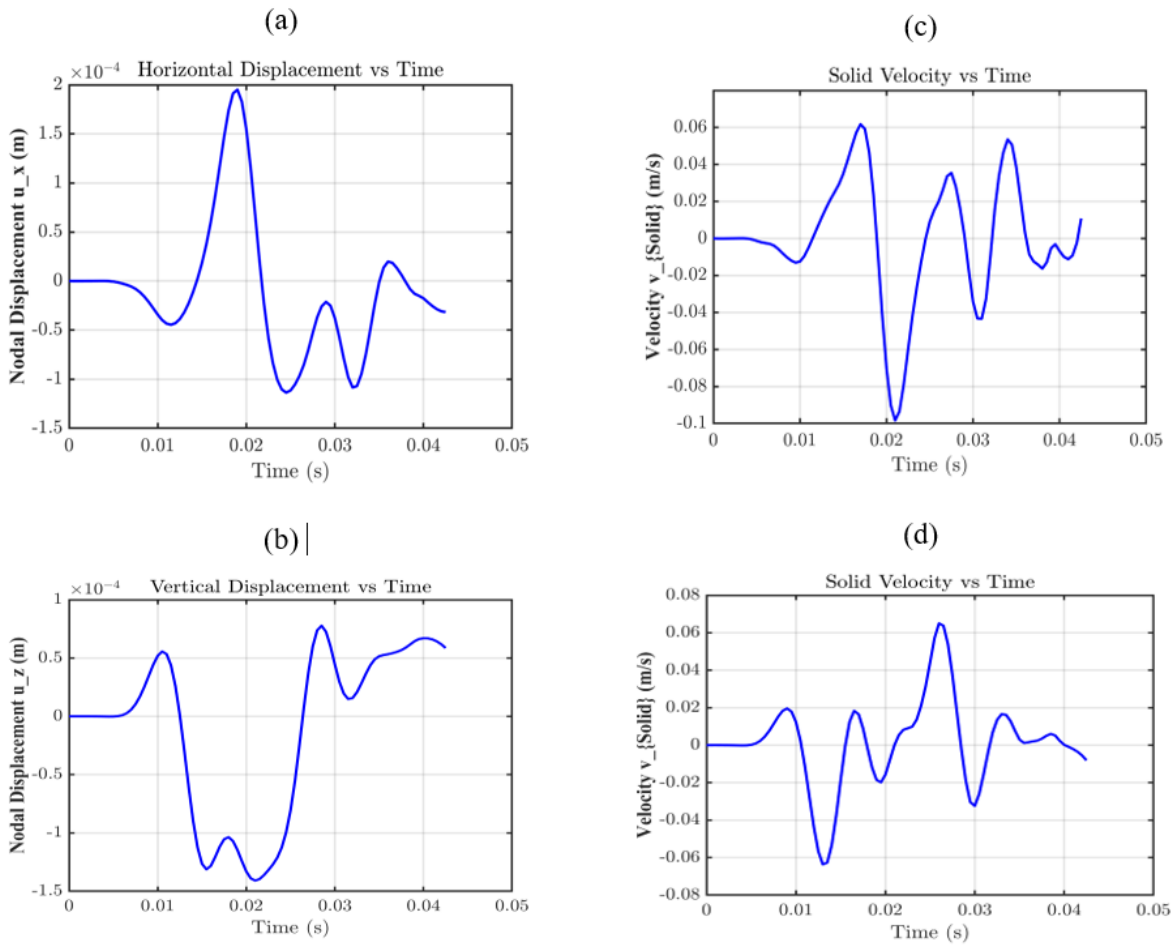

Figure 5.16: Node A; Isotropic case: seismic wave time histories (a) horizontal displacement, (b) vertical displacement, (c) horizontal solid velocity, (d) vertical solid velocity.

From the horizontal displacement plot (Figure 5.16a), the excitation impulse applied to the domain as shown in Figure 5.15 dominates the early motion, producing a slight displacement of the nodes at approximately 0.01s. Following the decay of the applied impulse at the injector well, a displacement peak (~2×10^{-4} m) is recorded at approximately 0.02s. This peak provides evidence of the P-wave, which subsequently decays at 0.024s, consistent with the predicted arrival time reported in **Table 5.3.**

Conversely, the vertical displacement response (Figure 5.16b) shows a less pronounced response during the impulse period. However, at approximately 0.025s, the P-wave mode is converted to S-wave, and the shear wave produces a strong ground motion (perpendicular to

the direction of propagation of the wave). This initially results to a small displacement at approximately -1.3×10⁻⁴ m, followed by a large rebound of about 0.8×10⁻⁴ m. This alternating displacement cycles, indicate shear wave oscillations. The slower arrival of the shear wave is consistent with our prediction, as the S-wave starts its decay at about 0.043s.

With a comparison of the solid velocity plots, it is observed that, the S-wave has a higher velocity of 0.075m/s recorded in the vertical direction, at time, 0.025s in Figure 5.16 (d) compared to 0.6m/s recorded in the horizontal direction, at time 0.019s in Figure 5.16(c).

This is compatible with peak ground velocity studies (PGV) that suggest that on a seismograph, the S-waves travels slower than the P-wave, but it produces a larger PGV amplitude because of stronger ground motion [264].

This analysis shows that at the interface between the reservoir and the overlying caprock, there is a significant ground motion and velocity recorded in the vertical and horizontal directions due to fault slip.

B.) Node B (interface between reservoir and underlying caprock (coordinates 29.5; 0; 4.5)):

The displacement and velocity responses presented in Figure 5.17(a-d), exhibit wave propagation characteristics consistent with the previously analysed case (Node A), with evidence of P- and S- wave arrivals.

In the horizontal displacement profile (Figure 5.17(a)), the largest positive peak reaches approximately 2.1×10⁻⁴ m at 0.019 s, which is slightly higher than the ~2.0×10⁻⁴ m observed in the earlier node. The corresponding horizontal velocity profile (Figure 5.17(c)) records a maximum of about 0.058 m/s at 0.002s followed by a strong decay to nearly -0.095 m/s at 0.024s, highlighting the conversion from P-wave to S-wave.

For the vertical direction, the displacement record (Figure 5.17(b)) shows a significant negative trough of around –1.8×10⁻⁴ m at 0.025s, with the arrival of the P-wave at the boundary. It is then followed by a rebound to approximately 0.45×10⁻⁴ m at approximately 0.028 s and keeps growing to about 0.06 m/s at 0.04. These features are indicative of the delayed S-wave motion. The corresponding velocity profile (Figure 5.17 (d)) captures a strong negative excursion of –0.076 m/s at 0.019 s, balanced by a subsequent positive peak of roughly 0.046 m/s at 0.028 s, indicative of S-wave dominance.

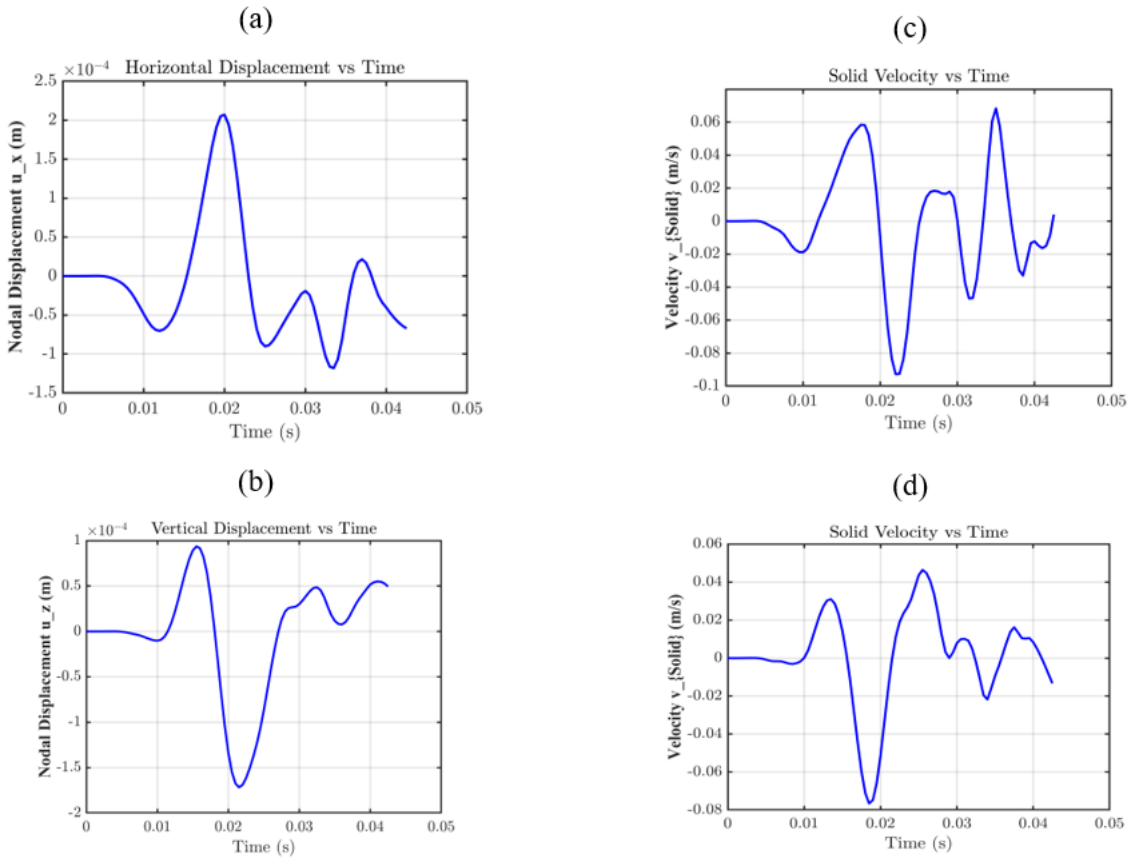

Figure 5.17: Node B Isotropic case: seismic wave time histories (a) horizontal displacement, (b) vertical displacement, (c) horizontal solid velocity, (d) vertical solid velocity.

C.) Comparison of pressure wave energy at Nodes A & B

The results presented in Figure 5.18 compare the pressure waveforms at both locations to assess the relative energy transported by the propagating phases.

As expected, the P-wave exhibits stronger pressure fluctuations, indicating that it carries a greater proportion of the total seismic energy than the S-wave. This observation is consistent with the theoretical understanding that compressional waves transport energy more efficiently through the medium.

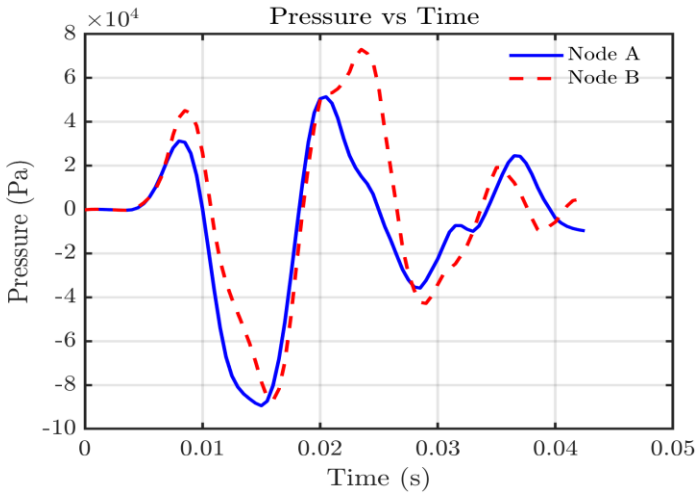

Figure 5.18: Node A vs Node B Isotropic case: seismic wave pressure vs time history.

As expected, the P-wave (which travels till 24ms) exhibits stronger pressure fluctuations, indicating that it carries a greater proportion of the total seismic energy than the S-wave (that travels from 24ms to 45ms). For Node A, the recorded peak pressure is approximately 5×10^4 Pa, whereas Node B reaches about 7×10^4 Pa at 24 milliseconds (ms). This difference in pressure amplitude explains the minor variation in observed displacement and velocity observed at Node B compared to Node A.

When both P-waves are compared to that of the S-waves, their amplitudes are considerably higher. This observation is consistent with the theoretical understanding that compressional waves travel faster and transport more energy through the porous medium [265].

D.) Plane motion comparison at Nodes A and B

The looping path registered at both nodes (Figure 5.19 (a) & (b)) indicate that the domain does not just move vertically and horizontally but follows an elliptical trajectory. This observation is consistent with studies carried out by [20], [184] that found Rayleigh waves to move in an elliptical path and are the most destructive.

The trajectory in Node A (Figure 5.19 **(**a)) and Node B (Figure 5.19(b)), confirms the presence of a Rayleigh wave motion with an elongated path in the horizontal direction. Node B, however, shows a indicates some amount of interference between the P-waves and S-waves.

In ideal conditions and depending on the material properties, this loop is fully circular, but in most real materials (such as subsurface structures), it becomes an ellipse. In the baseline (isotropic) scenario, minor reflections from the model's boundary, prevent the trajectory from closing into a full circle, resulting in the observed elliptical motion. The prediction of the

particle motion illustrates how Rayleigh waves transport seismic energy along the surface and why they are often the most destructive component of earthquakes.

(a) (b)

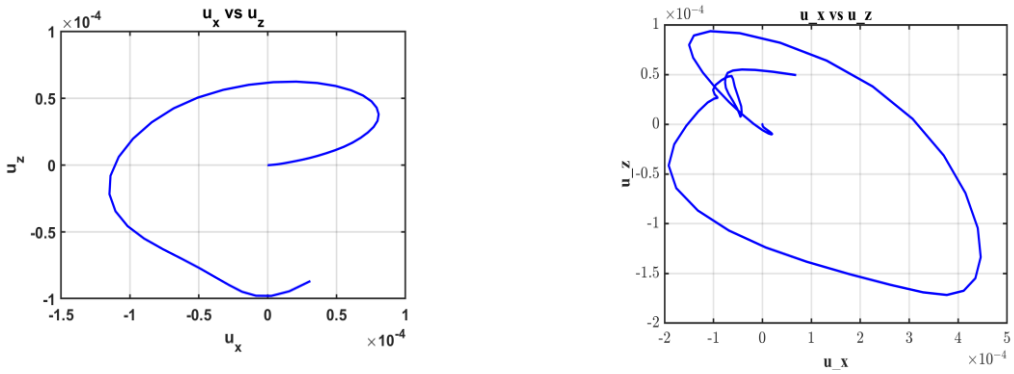

Figure 5.19: Rayleigh wave polarization at: (a) Node A; (b) Node B (Isotropic case)

E.) Three-Dimensional representation of nodal Displacement

To provide an overview of the displacement throughout the domain, a three-dimensional plot confirming displacements are presented from which we observe that the horizontal displacement in Figure 5.20(a) is more pronounced than the vertical displacement in Figure 5.20(b) (N.B: both displacement figures are amplified by scale factor of 1000). The impulse is initiated in the x-direction, suggesting P-waves would be stronger in the direction of propagation, while S-wave would be felt perpendicular to the angle of impulse initiation.

(a)

Horizontal nodal displacement

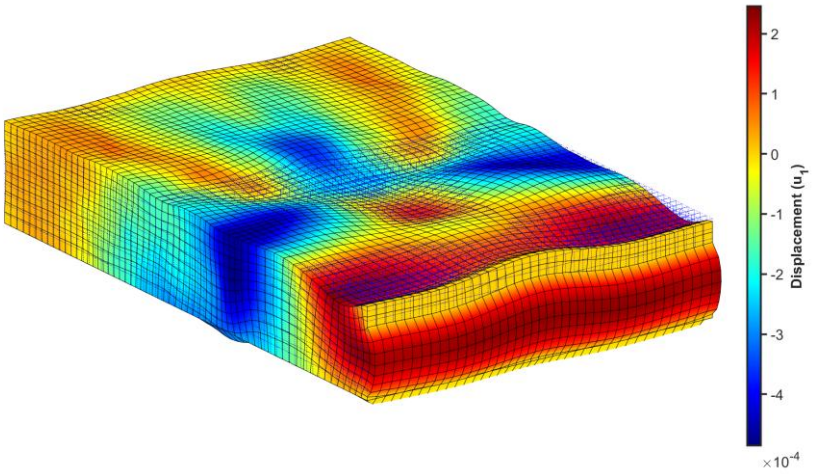

(b)

Vertical nodal displacement

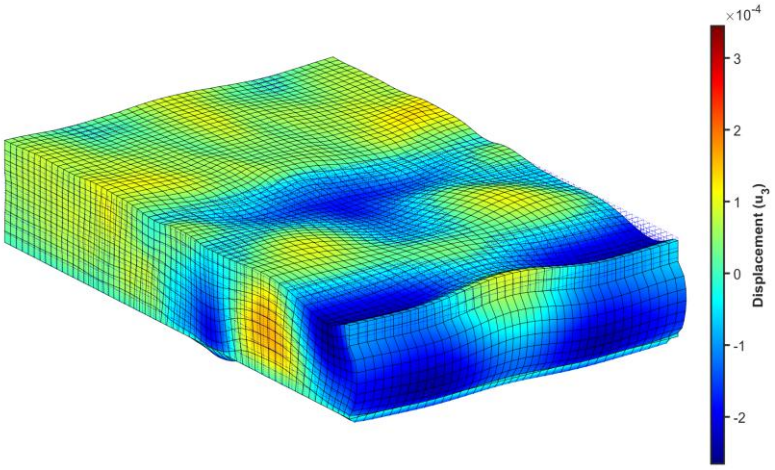

Figure 5.20: Overall nodal deformation of geological formation: (a) Horizontal domain; (b) Vertical domain. (Isotropic case)

F.) Three-Dimensional representation of wave propagation

The preliminary calculations provided in Table 5.3, together with the two-dimensional plots illustrated in Figure 5.16 (a–d) and Figure 5.17(a–d), serve as the foundation for the subsequent three-dimensional wave propagation analysis. This extended analysis corroborates the earlier findings and is presented in two stages: initially, the propagation profile dominated by P-waves (Figure 5.21), followed by the propagation profile governed by S-waves (Figure 5.22) at selected time steps.

(a) t=0 (1st time step)

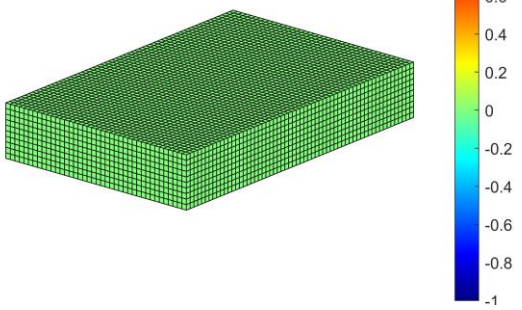

(b) t=0.005s (10th time step)

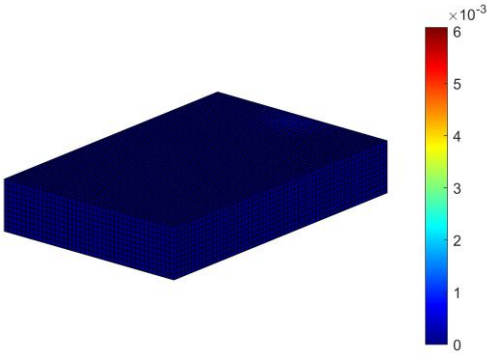

(c) t=0.01s (20th time step)

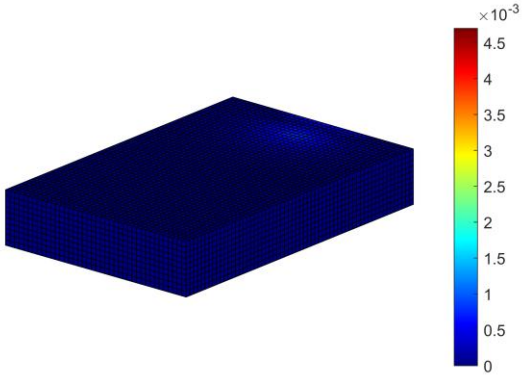

(d) t=0.013s (26th time step)

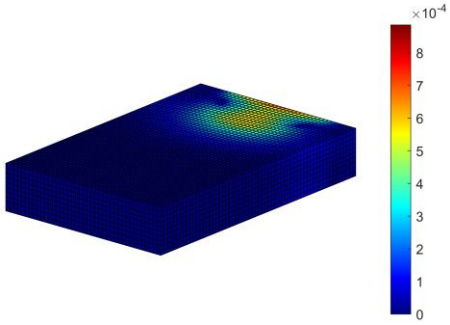

(e) t=0.02s (40th time step)

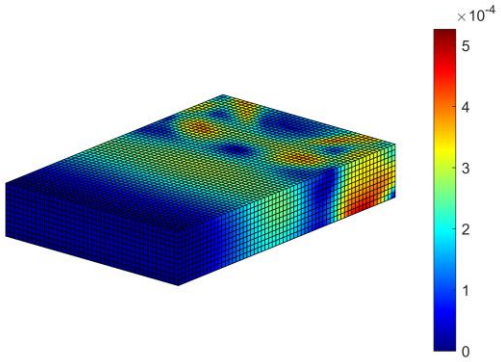

(f) t=0.024s (48th time step)

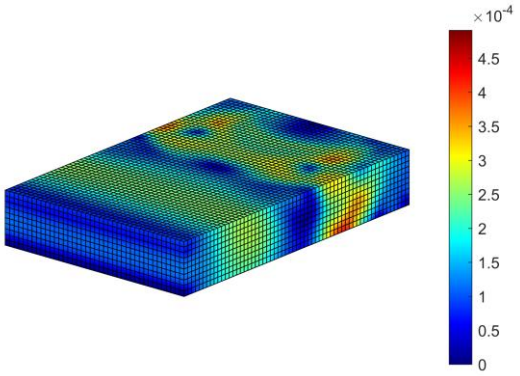

Figure 5.21: P-wave dominated propagation in isotropic study.

At the initial time steps (t = 0 & t = 0.0005s), the P-wave is not yet clearly developed. By t = 0.01s, the onset of the P-wave propagation becomes evident, and its amplitude continues to increase noticeably around t=0.013s. At t=0.02s, the P-wave is clearly the dominant feature of the wavefront, and by t = 0.024s, there are clear indications of its arrival at the model boundary (Figure 5.21 (a) – (f)).

Conversely, the S-wave propagation becomes dominant from t = 0.025s evident by the trailing wave profile (encircled in red). Its amplitude increases over time until it is captured at the boundary at t = 0.043s (Figure 5.22(a) – (f)).

(a) t=0.025s (50th time step)

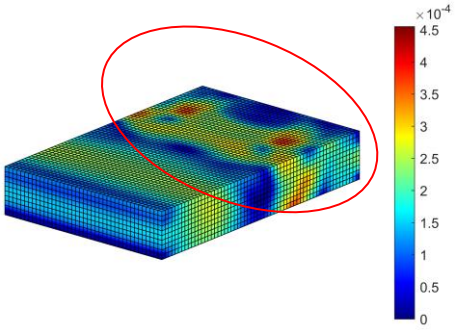

(b) t=0.03s (60th time step)

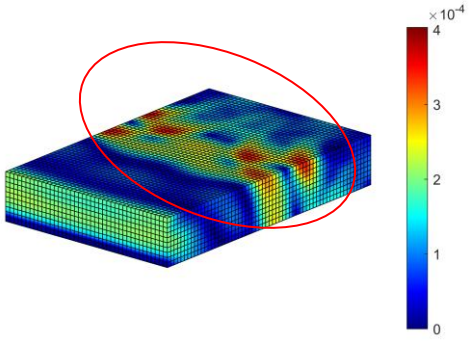

(c) t=0.031s (62nd time step)

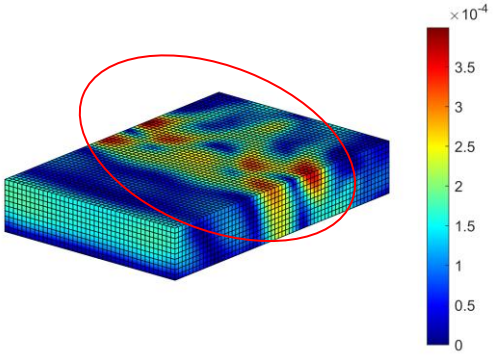

(d) t=0.034s (68th time step)

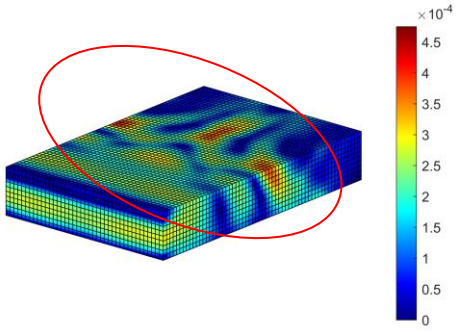

(e) t=0.04s (80th time step)

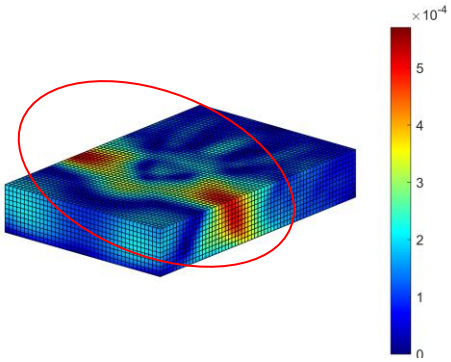

(f) t=0.043s (86th time step)

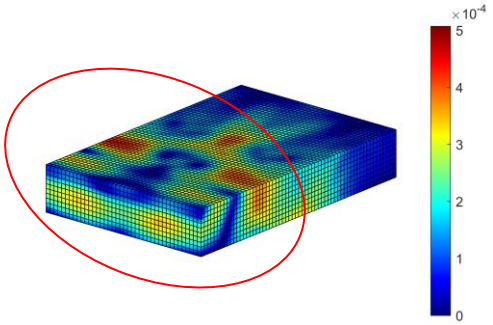

Figure 5.22: S-wave dominated propagation in isotropic study.

In summary, the isotropic case has provided a benchmark for wave propagation in a homogeneous medium, illustrating the expected dominance of P-waves in energy distribution and the delayed but more destructive ground motions associated with the shear and Rayleigh waves. The observed displacement velocity and pressure distribution at those nodal points clearly show that the pre-existing fault is reactivated, with the nodes at the intersection between the caprocks being the most affected. While these results validate the baseline isotropic

response, anisotropy alters both the travel time and energy partitioning, leading to more complex propagation phenomena such as shear-wave splitting. The following section extends this analysis to the anisotropic case , where deviations from the baseline reveal a more intricate representation of dynamic wave propagation in depleted reservoirs.

5.2.2 Wave propagation results in CASE-B (layered anisotropy)

The load history shown (Figure 5.23) is the source function used for the anisotropic case. A smooth half-sine pulse of $f(t) = 10^{12}\sin(100\pi \mathrm{T})[1 - H(t - \mathrm{T})]$, with period, T ≈ 10 ms and peak amplitude, of 10^{11} at time, t = T/2. Thereafter, the period, T, of the impulse, the amplitude decays to zero. The spectrum is dominated by a frequency order of 100 Hz. This yields sharp P, S, and Rayleigh waves, facilitating ground motion analysis, peak ground velocity estimation in the anisotropic medium.

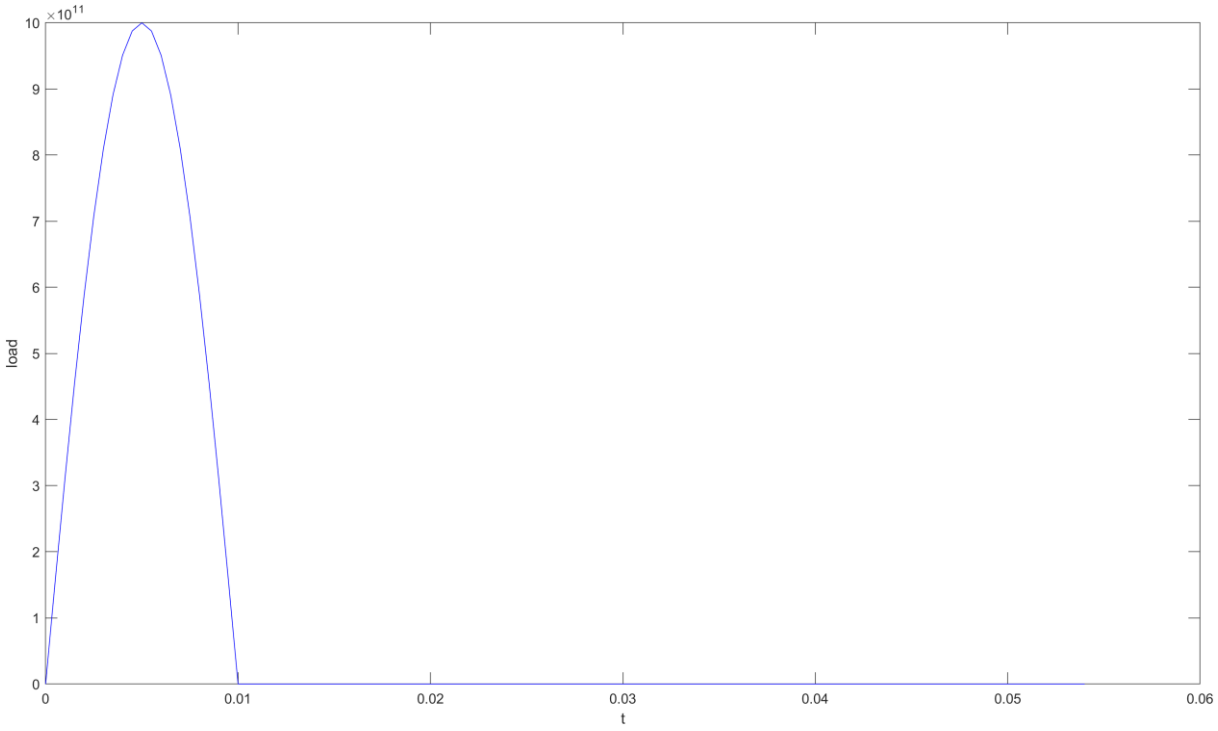

Figure 5.23: Impulsive load (layered anisotropic scenario)

Analogous to the isotropic case, a prerequisite for the wave-profile analysis is calculated in Appendix E and summarized in **Table 5.4.**

Table 5.4: Derived metrics supporting the "CASE-B" wave propagation analysis.

Parameter	Value
Period of impulse, T	10 milliseconds (ms)
Time step of simulation, Δt	500 microseconds (μs)
Travel time for P-wave	28 milliseconds (ms)
Travel time for S-wave	54 milliseconds (ms)
Number of time steps required for simulation of P-wave	≈ 58-time steps
Number of time steps required for simulation of S-wave	≈ 108-time steps

The wave-propagation metrics for the anisotropic model (Table 5.4), diverges from the isotropic benchmark in that despite the larger impulse amplitude (Figure 5.23), the body waves travel times are longer for the same domain configuration, indicating reduced effective velocities due to stratified anisotropy.

Using Figure 5.14 as reference, the ground motion and velocity at the selected nodes on the computational grid, are presented.

A.) Node A (interface between reservoir and overlying caprock: (coordinates 29.5; 0; 1)):

Figure 5.24(a) and (b) present the time evolution of nodal displacement, with horizontal and vertical components, respectively. The corresponding solid velocity responses are displayed in Figure 5.24 (c) and (d)**,** respectively.

In the horizontal displacement window (Figure 5.24 (a)) the largest peak is captured at about 3.2×10^{-4} m at 0.024s. This peak immediately decays at time, t = 0.028s as expected. The displacement amplitude in the anisotropic case study is close to 40 % higher than the benchmark scenario (Figure 5.24 (a) & (b)). The corresponding velocity in the horizontal direction (Figure 5.24(c)) indicates the existence of two prominent wavefronts, suggesting the existence of shear wave splitting due to anisotropy. The first S-wave peaks at approximately, 0.031 – 0.033s and the second around 0.04 s, before its eventual decay at the 0.054s.

When examined in the vertical direction, (Figure 5.24(b)) shows that the displacement recorded at the node (i.e. approximately 1.0×10^{-4}m), doubles that registered in the benchmark. This is then followed by a steep increase to 1.2×10^{-4}m, indicating the dominance of the S-wave at this point. When cross-referenced with the solid velocity plot in the vertical direction (Figure

5.24(d)), we observe two distinct shear waves, corresponding to a fast S-wave peak at 0.038s and the slow S-wave at about 0.048s.

This initial analysis establishes the influence of anisotropy through variations in body-wave arrival times and amplitude differences observed in both displacement and velocity records at the fault boundary.

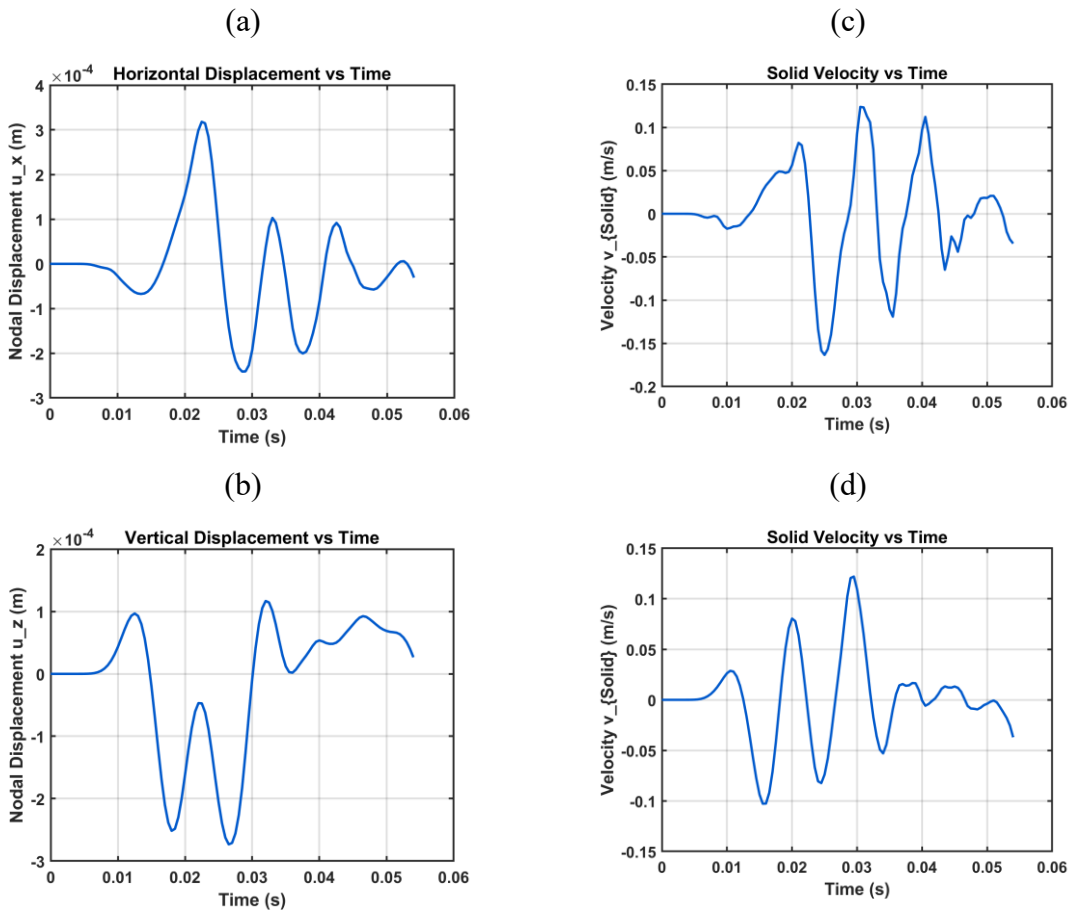

Figure 5.24: Node A; Layered anisotropy configuration: seismic wave time histories (a) horizontal displacement, (b) vertical displacement, (c) horizontal solid velocity, (d) vertical solid velocity.

B.) Node B (interface between reservoir and underlying caprock: (coordinates 29.5; 0; 4.5)):

The P-wave registers a strong pulse at ~0.025s (Figure 5.25(a)), unlike the isotropic case where the impulse decays at this interval. This delayed response in the P-wave velocity, V_p, indicates that the layered-anisotropy affects the propagation of the wave. The corresponding velocity in the horizontal direction, (Figure 5.25 (c)) indicates the existence of two prominent fast S-wave crest at 0.032s and 0.045, followed by a slow S-wave at 0.053s.

Conversely, the records show two distinct S-wave phases: an earlier fast S-wave at ~0.031–0.033s and a slow S-wave at ~0.039–0.041s, indicating clear shear-wave splitting on vertical displacement profile ((Figure 5.25 (b)). Unlike the isotropic case, the anisotropic medium redistributes energy across both vertical displacement and velocity, reflecting rotated particle motions and cross-component coupling. This confirms anisotropy-induced polarization changes and direction-dependent shear velocities.

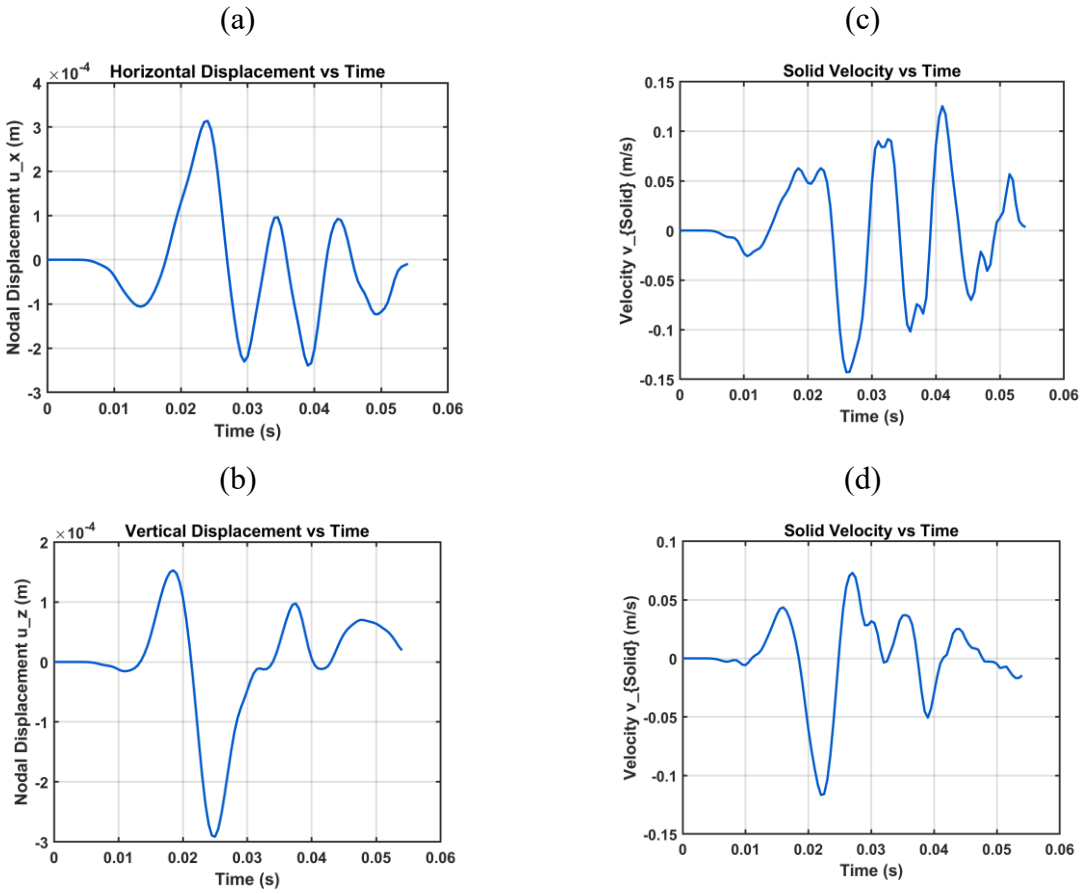

Figure 5.25: Node B; Layered anisotropy case: seismic wave time histories (a) horizontal displacement, (b) vertical displacement, (c) horizontal solid velocity, (d) vertical solid velocity.

C.) Comparison of pressure wave energy at Nodes A & B

Based on the results presented in Figure 5.24 & Figure 5.25, the amplitudes at node B are observed to be slightly greater than those of node A. To validate this observation, the analysis is extended by comparing the pressure wavefronts at both locations (Figure 5.26), thereby enabling an assessment of the relative energy carried by the propagating phases.

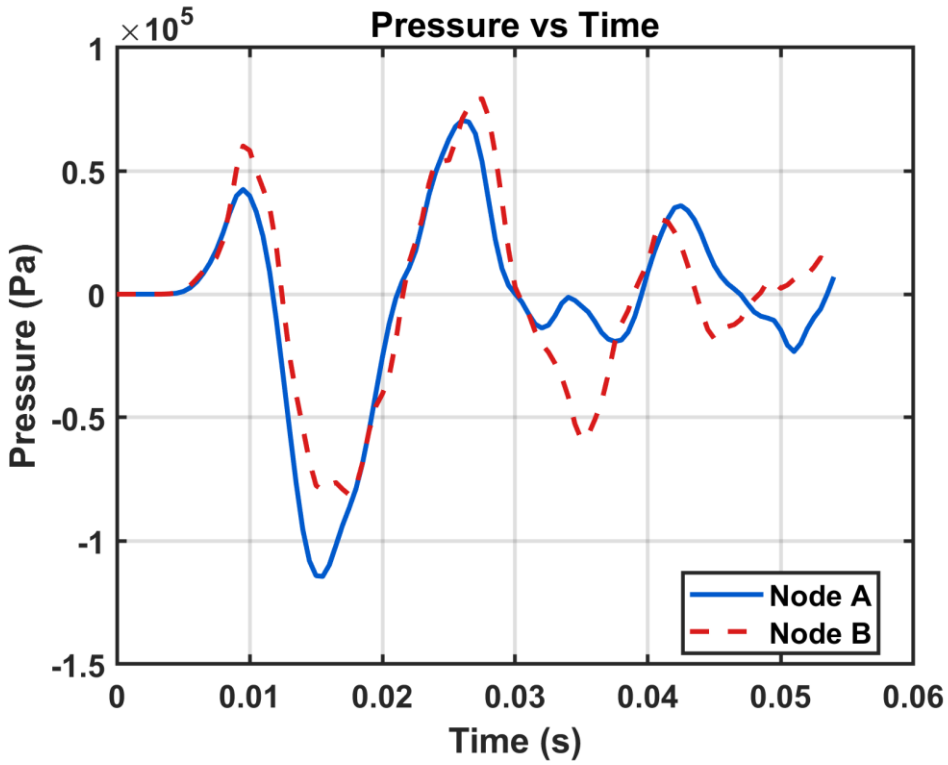

Figure 5.26: Node A vs Node B Layered-anisotropic case seismic wave pressure vs time history.

The P-wave (travels until 28ms) exhibits a more pronounced pressure amplification, indicating that it transports a larger fraction of the total seismic energy compared to the S-wave (travels from 28ms to 54ms). At Node A, the wave crest is recorded at approximately 0.8×10^5Pa, while Node B reaches about 0.9×10^5Pa at 27ms. Notably, these amplitudes are greater than those obtained under isotropic conditions, where the corresponding values were 0.5×10^5Pa and 0.7×10^5Pa at 24ms for Nodes A and B, respectively.

D.) Plane motion comparison at Nodes A and B

The looping path registered at both nodes (Figure 5.27(a) & (b)) indicate that the domain does not just move vertically and horizontally but follows an elliptical trajectory, characteristic of a Rayleigh wave.

Node A (Figure 5.27**(**a)) exhibits the characteristic elliptical polarization of Rayleigh waves, with coupled horizontal and vertical displacements forming elongated loops that confirm retrograde particle motion. The asymmetry of the ellipse reflects the influence of anisotropy, where velocity contrasts and layering distort the ideal polarization pattern. This retrograde Rayleigh mode, although slower than body waves, is well known to be the most destructive due to its large amplitude and long duration at the surface [266]. Node B ((Figure 5.27(b)) similarly

registers an elongated retrograde ellipse, but with the horizontal component exceeding the vertical, indicating that the surface wavefield at this location is dominated by strong horizontal displacements. This horizontal amplification highlights site-specific anisotropic effects that can further intensify ground motion demands.

(a) (b)

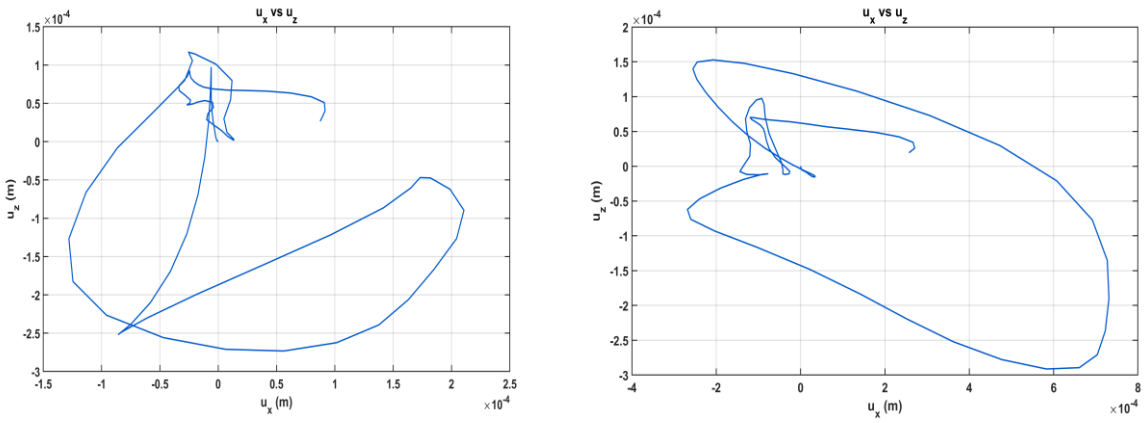

Figure 5.27: Plane wave motion at: (a) Node A; (b) Node B (layered-anisotropic case).

E.) Three-Dimensional representation of nodal Displacement

To provide an overview of the nodal displacement, a deformed three-dimensional plot is presented from which we observe that the horizontal displacement in Figure 5.28(a) is more pronounced than the vertical displacement in Figure 5.28(b) (N.B: both displacement figures are amplified by scale factor of 1000). In addition, the mesh exhibits a larger magnitude of deformation, thereby enhancing the effects of difference in material properties between the layers.

(a)

Horizontal nodal displacement

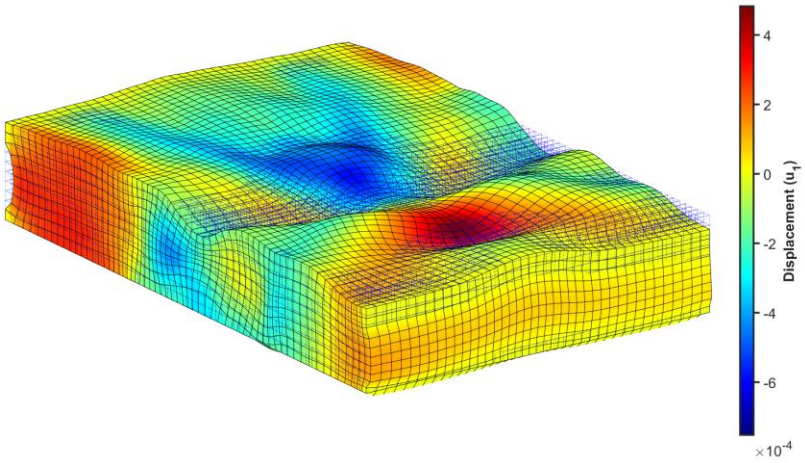

(b)

Vertical nodal displacement

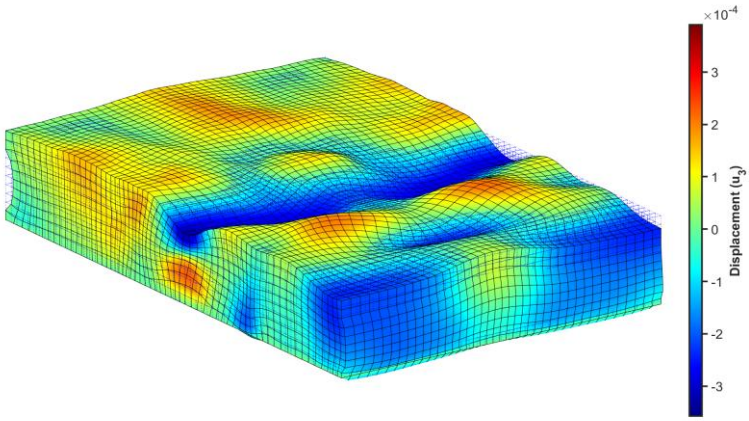

Figure 5.28: Overall nodal deformation of geological formation: (a) Horizontal deformation; (b) Vertical deformation. (Layered anisotropy case).

F.) Three-Dimensional representation of wave propagation

The initial estimates summarized in Table 5.4, together with the two-dimensional representations shown in Figure 5.24 (a-d) and Figure 5.25 (a-d), provide the basis for extending the investigation to three-dimensional wave propagation. The subsequent analysis validates the preliminary observations and is structured in three phases: first, the examination of propagation dominated by P-wave dynamics (Figure 5.29); second, the assessment of fast S-wave controlled propagation patterns (Figure 5.30); and third the assessment of the slow S-wave (Figure 5.31), at selected time intervals.

The P-wave–dominated fields are similar, up to about the 20th time step (Figure 5.29 **(**a)–(c)). Divergence from isotropic case study, emerges at t = 0.013 s (Figure 5.29(d)), where the peak amplitude reaches ≈ 9×10^{-4}**,** compared with ≈ 6×10^{-4} (Figure 5.21(d)**)** for the isotropic case; an increase of ~34%. Thereafter, the amplitudes in the P-wave dominated model (Figure 5.29(e-h)), remains higher than in the isotropic model.

A second notable difference is the arrival time at the model boundary. In the P-wave dominated case the first clear boundary capture occurs at time, t = 28ms (time step 56) (Figure 5.29h), whereas the isotropic model reaches the boundary at t = 24ms (time step 48). Assuming identical Δt, this corresponds to approximately a 15% longer travel time along the modelled path for the P-wave dominated configuration. Taken together, the results indicate enhanced amplitude and reduced propagation speed relative to the isotropic medium, thereby enhancing the effects of layered anisotropy to the wave profile.

(a) t=0 (1st time step)

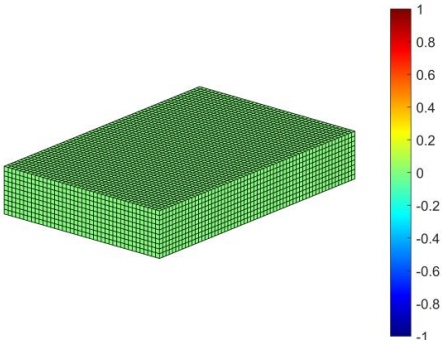

(b) t=0.005s (10th time step)

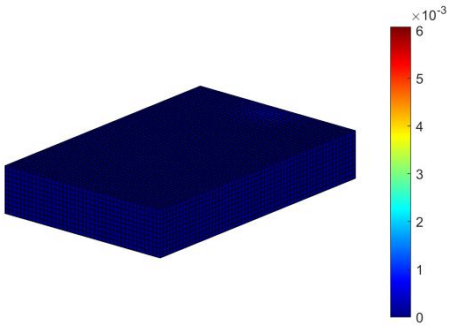

(c) t=0.01s (20th time step)

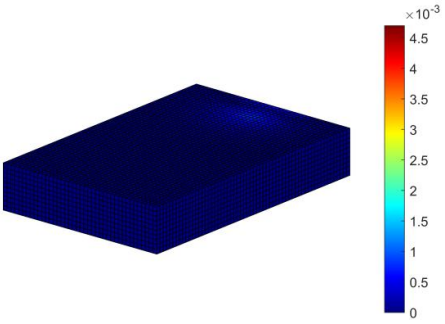

(d) t=0.013s (26th time step)

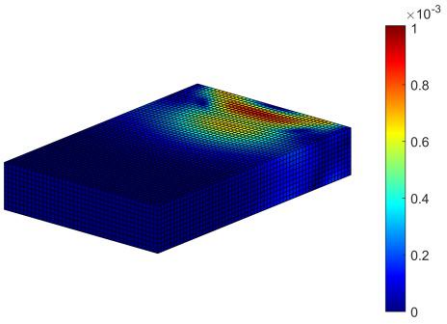

(e) t=0.02s (40th time step)

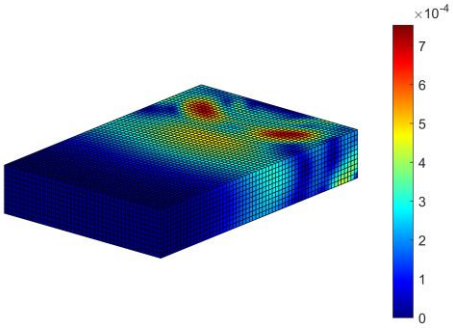

(f) t=0.024s (48th time step)

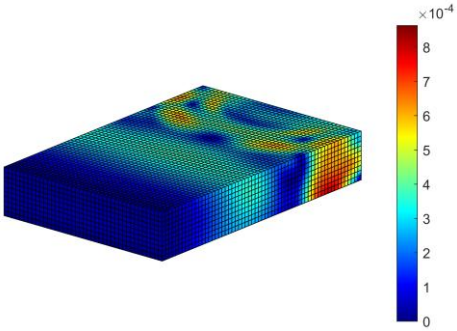

(g) t=0.025s (50th time step)

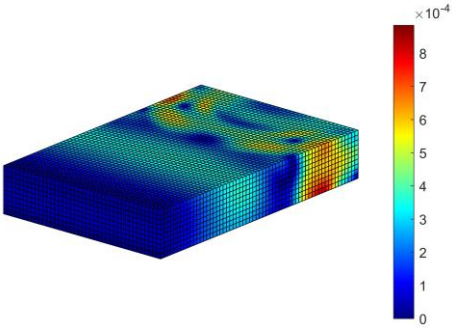

(h) t=0.028s (56th time step)

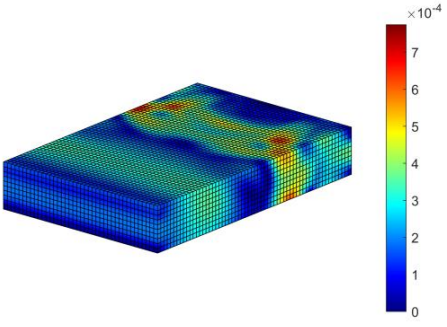

Figure 5.29: P-wave dominated propagation in layered anisotropic case study.

Conversely, the fast S-wave propagation only becomes dominant at time, t = 0.029s evident by the trailing wave profile with two lobes (encircled in red). Its amplitude increases over time until it is captured at the boundary at time, t = 0.04s (Figure 5.30a) – (d)).

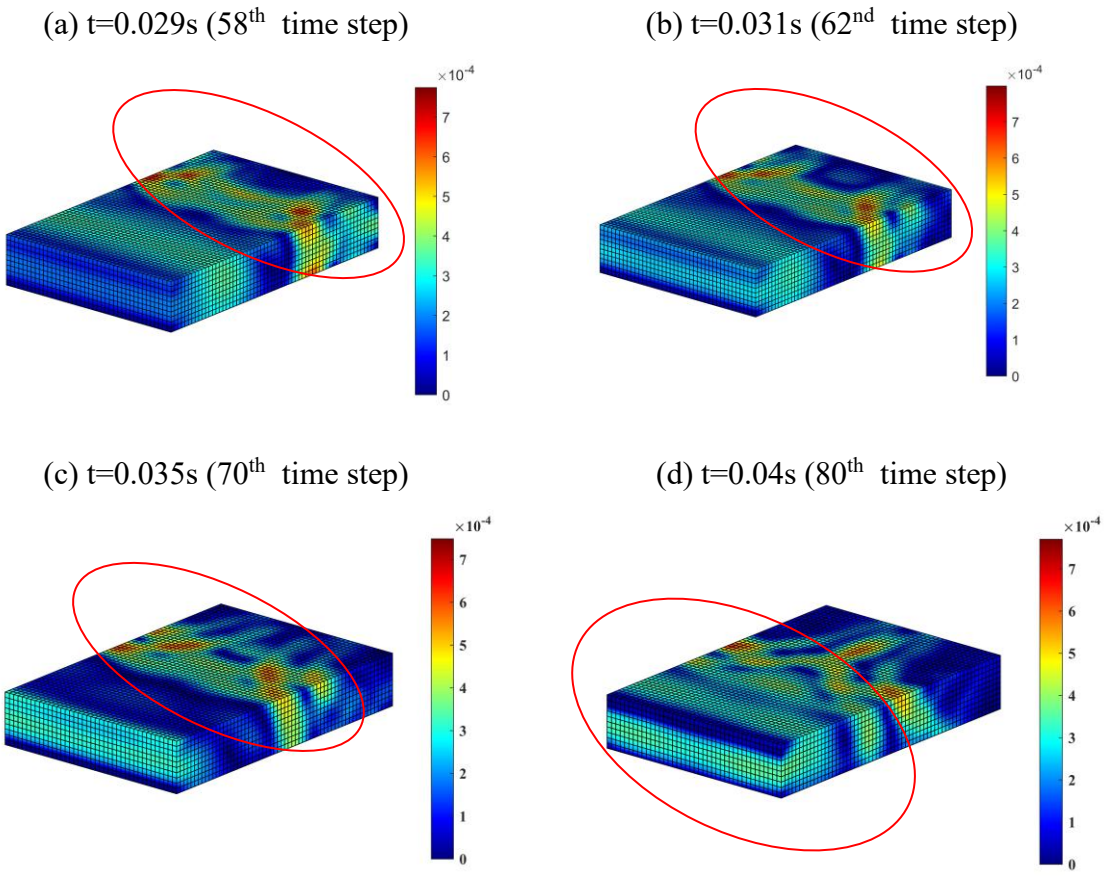

Figure 5.30: Fast S-wave propagation over time in layered anisotropic case study.

Subsequently, a second S-wave packet emerges at t = 0.045, displaying loop-like lobes across the domain (highlighted in green). Consistent with the fast S-wave, its amplitude increases and then attenuates upon reaching the boundary at t = 0.053s (Figure 5.31(a–d)).

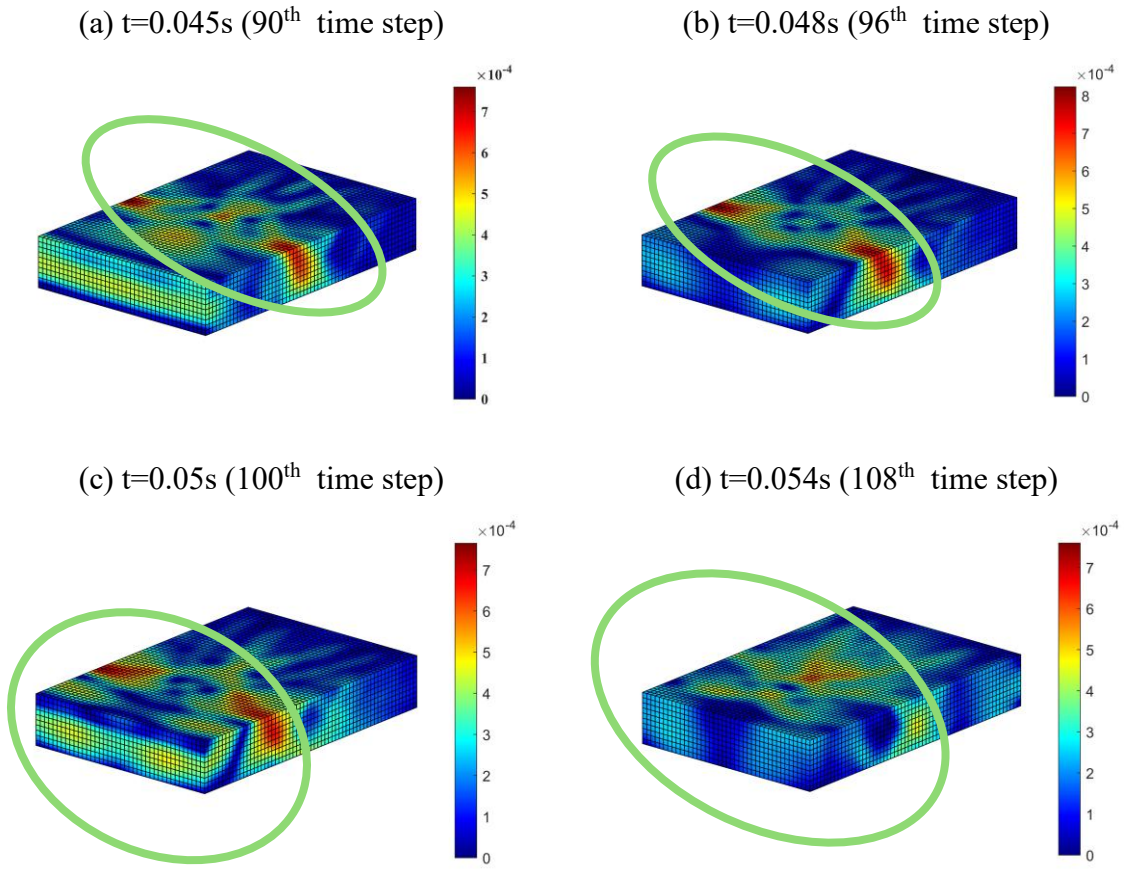

Figure 5.31: Slow S-wave Propagation over time in layered anisotropic study.

5.2.3 Wave propagation results in CASE C (transverse vertical isotropy)

The load history illustrated in Figure 5.32 serves as the source function for the anisotropic study where, transverse vertical isotropy of the mechanical properties (see Table 4.7) is imposed in each layer of the geological domain. It consists of a half-sine pulse defined as $f(t) = 10^{12}\sin(100\pi \mathrm{T})[1 - H(t - \mathrm{T})]$, with a period approximately T ≈ 10 ms and a peak amplitude of 10^{11} at time, t = T/2. Beyond this point, the impulse amplitude decays to zero. It is worth noting that this configuration is quite similar to Case-B; however, the added variability in mechanical properties results in a longer decay after initiation of the pulse, recorded at about 0.056s compared to 0.053s in Case-B.

The spectrum is dominated by frequencies on the order of 100 Hz, producing distinct P, S, and Rayleigh waves that support the analysis of ground motion and the estimation of peak ground velocity in the anisotropic medium where transverse vertical isotropy condition is imposed.

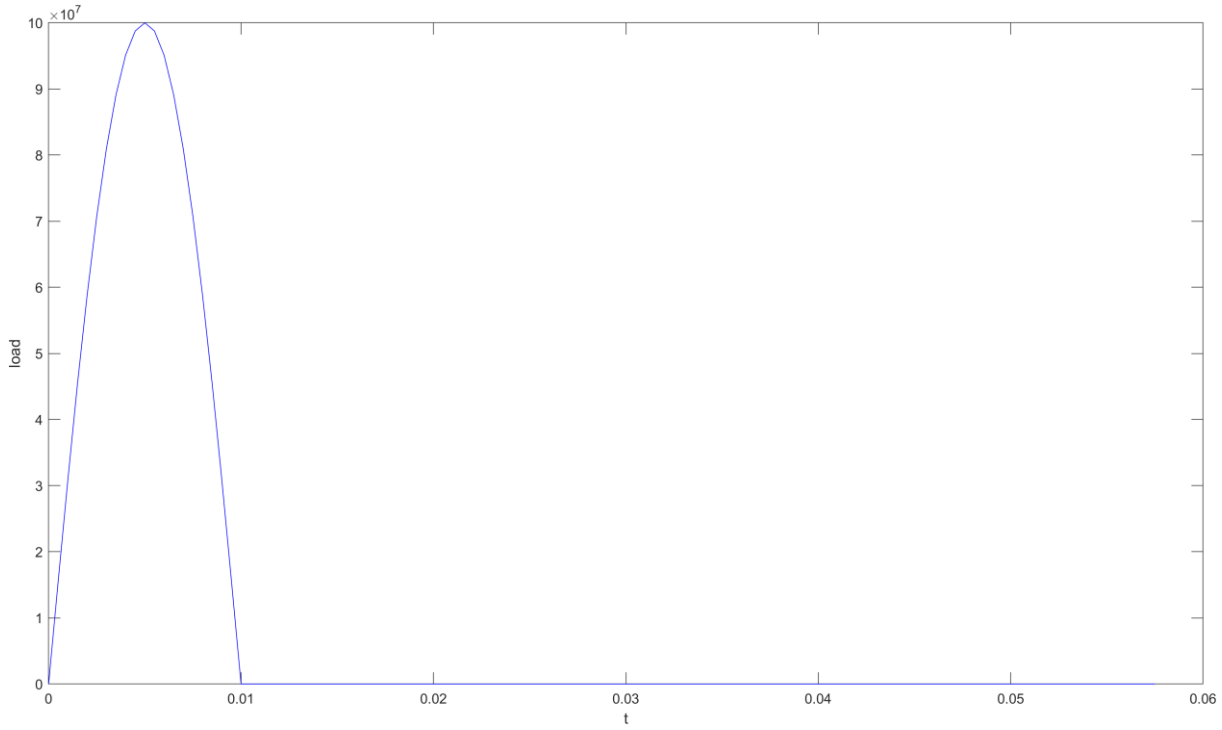

Figure 5.32: Impulsive load (transverse vertical isotropy scenario)

The preliminary calculations required for the wave profile analysis are provided in Appendix E, and the results summarized in Table 5.5.

Table 5.5: Derived metrics supporting the "CASE-C" wave propagation analysis.

Parameter	**Value**
Period of impulse, T	10 milliseconds (ms)
Time step of simulation, Δt	500 microseconds (μs)
Travel time for P-wave	32 milliseconds (ms)
Travel time for S-wave	56 milliseconds (ms)
Number of time steps required for simulation of P-wave	≈ 64-time steps
Number of time steps required for simulation of S-wave	≈ 112-time steps

In Case C, the wave propagation metrics (Table 5.5) demand longer simulation times to fully capture the propagation of the body and surface waves. The variability in mechanical properties increases the computational requirements to accurately represent the full wavelengths within the domain and to accurately predict the arrival times of each wave within the domain.

Using Figure 5.14 as reference, the ground motion and velocity at the selected nodes on the computational grid, are presented.

A.) Node A (interface between reservoir and overlying caprock: (coordinates 29.5; 0; 1)):

Figure 5.33 (a) and (b) present the time evolution of nodal displacement, with horizontal and its vertical components, respectively. The corresponding solid velocity responses are displayed in Figure 5.24 (c) and (d)**,** respectively.

For the VTI model, the horizontal displacement window (Figure 5.33(a)) registers an amplitude of 2.5×10^{-4} m at about 0.028s, due to reduced vertical stiffness across the layers of the domain (Table 4.7) . This peak immediately decays as predicted at 0.032s, where it gets in contact with the domain boundary. A pronounced negative trough of nearly -4.5×10^{-4} m occurs at about 0.039s suggesting the interference between and SV and SH wave. The corresponding velocity in the horizontal direction (Figure 5.33 (c)) confirms the existence of two prominent wavefronts, suggesting the existence of shear wave splitting into and SV and SH wave due to transverse vertical isotropy. The first S-wave peaks at approximately, 0.042 – 0.045s and the second around 0.053 s, before its eventual decay at the 0.056s.

A delayed response is observed in the vertical direction (Figure 5.33(b)), where the amplitude of nodal displacement of 1.0×10^{-4}m is registered at around 0.02s. This contrast with the layered anisotropy (Case-B) where a comparable peak is captured at around 0.12s. This indicates that the reduced vertical stiffness in the VTI model slows the propagation of the P-wave. Furthermore, as illustrated in Figure 5.33 (b) and (d), two distinct shear waves are observed at approximately 0.033s and 0.04s. The amplitude of the S-wave reaches about $1.5\times10-4$ m (Figure 5.33(b)) which is notably higher that that recorded in the layered-anisotropic case-B Figure 5.24 (b).

This analysis establishes the influence of transverse vertical isotropy as the in body-wave arrival times are delayed and amplitude differences observed in both displacement and velocity records at the fault boundary.

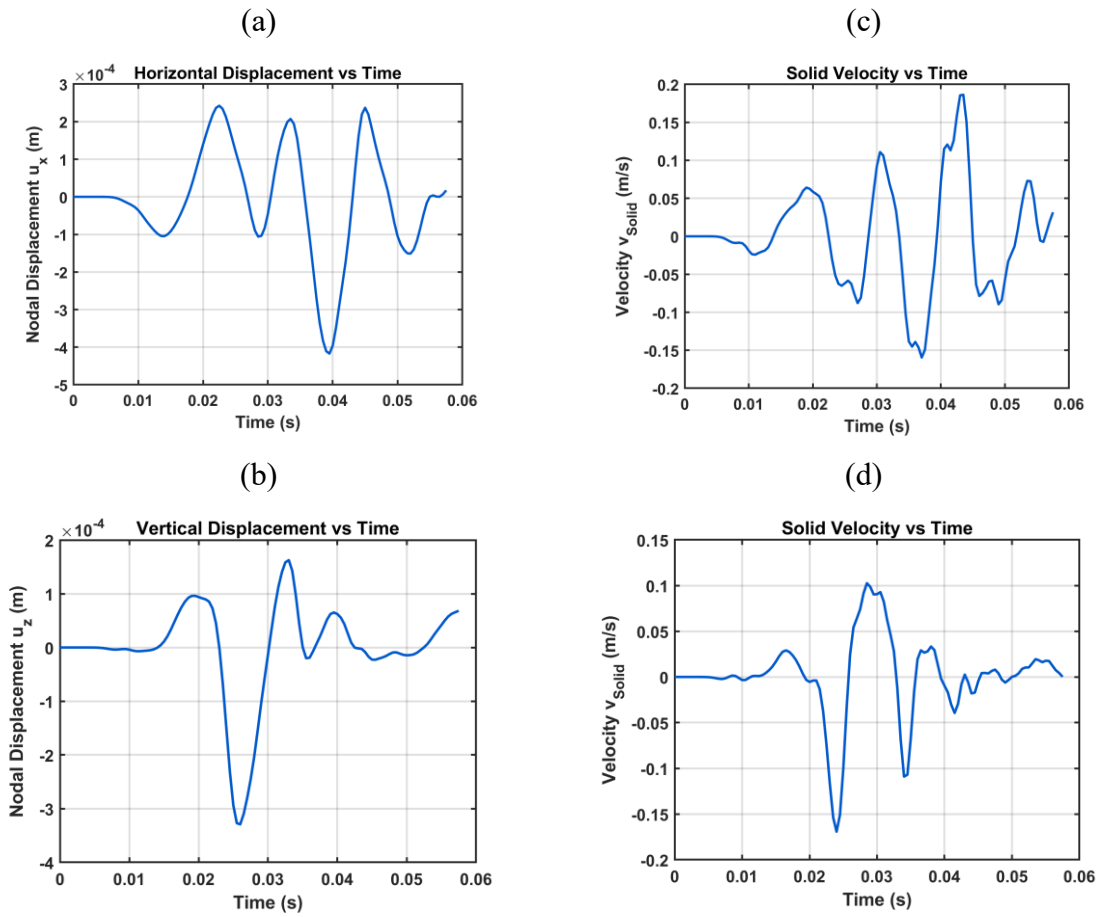

Figure 5.33: Node-A transverse vertical isotropy (TVI) case: seismic wave time histories (a) horizontal displacement, (b) vertical displacement, (c) horizontal solid velocity, (d) vertical solid velocity.

B.) Node B (interface between reservoir and underlying caprock: (coordinates 29.5; 0; 4.5)):

The P-wave detects a weaker pulse at ~0.025s (Figure 5.34(a)), when compared to the Case-B (stratified anisotropy) Figure 5.25(a). This analysis shows the reduced stiffness in the mechanical properties in vertical direction (Table 4.7), influences the amplitude of displacement of the P-wave. The corresponding velocity Figure 5.34(c) registers two distinct S-waves at 0.035s and 0.055s before it eventually decays. It is observed that due to VTI, the P-waves and S-waves are delayed and captured much later when compared to the layered-anisotropic case study. This shows evidence that VTI, heavily affects the wave propagation profile and aits arrival times.

The VTI results in Figure 5.34 (b) and (d) reveal stronger amplitudes (up to -4.5×10^{-4} m), more oscillatory S-wave behaviour, and late arrivals, all of which indicate transverse vertical

effects such as shear-wave splitting, enhanced mode conversions when compared to the previous case studies.

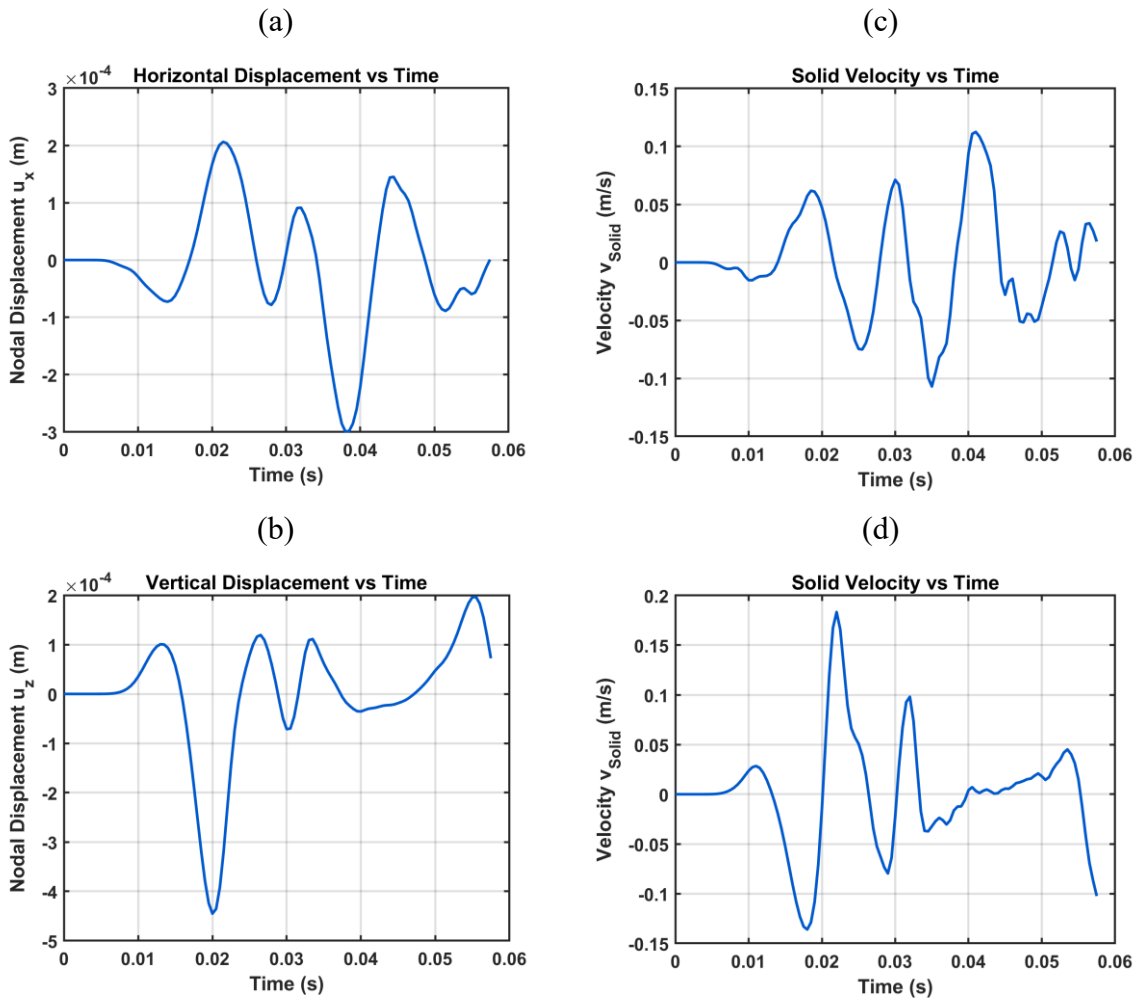

Figure 5.34: Node-B transverse vertical isotropy (TVI) case: seismic wave time histories (a) horizontal displacement, (b) vertical displacement, (c) horizontal solid velocity, (d) vertical solid velocity.

C.) Comparison of pressure wave energy at Nodes A & B

As shown in Figure 5.33and 5.34, the pressure amplitudes at node B are comparable to those at node A, with two notable exceptions: at time, t = 0.01s, node A exhibits a slightly higher response, whereas during the S-wave decay phase at time, t = 0.056s, node B records a greater amplitude than node A. This discrepancy arises from the imposed transverse vertical isotropy (VTI), where the horizontal and vertical stiffnesses differ due to variations in elastic moduli and Poisson's ratios. As a result, the redistribution of deformation between nodes reflects the material's directional dependence.

Overall, the P-wave (travels until 32ms) shows a pronounced pressure amplification, indicating that most of the energy is transported during this phase. At Nodes A and B, the crest

(corresponding to the P-wave) is evaluated at about 1.2×10^5Pa, which is greater than that register in Case-A (isotropic scenario) (Figure 5.18) and Case-B (layered anisotropy) (Figure 5.26).

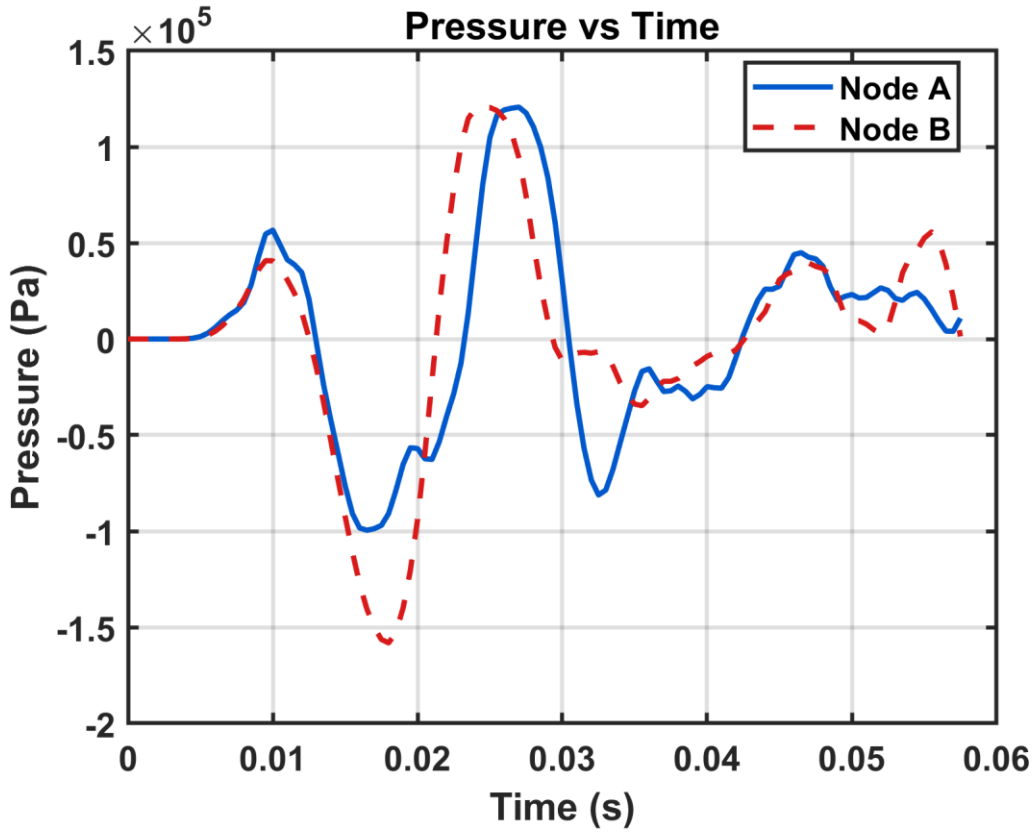

Figure 5.35: Node A vs Node B transverse vertical isotropy (VTI) case seismic wave pressure vs time history.

D.) Plane motion comparison at Nodes A and B

At Node A (Figure 5.36 (a)), the path is a tilted, retrograde ellipse that is dominated in the horizontal direction. From the analysis the magnitude of horizontal displacement, $|u_x|_{max} \approx 9\times10^{-4}$ m and vertical displacement of $|u_z|_{max} \approx 3.3\times10^{-4}$ m, giving a ratio of $u_x/u_z \approx 2.7$. The inner loops indicate wave mode conversion as the wave propagates through the medium. At Node B (Figure 5.36(b)), the motion is more vertically dominated, with the magnitude of horizontal displacement registered at $|u_x|_{max} \approx 2.3\times10^{-4}$ m and magnitude of displacement in the vertical direction at $|u_z|_{max} \approx 5.4\times10^{-4}$ m, corresponding to a ratio of $u_x/u_z \approx 0.43$. This indicates that the motion changes from being horizontally dominated in Node A to it being vertically dominated at Node B. This transition is evidence if the effects of transverse vertical isotropy as the stronger vertical stiffness component, heavily influences the propagation of the

wave. Unlike Case-B (layered anisotropy scenario), where the ratio of u_x/u_z is registered at 0.8 at Node A (Figure 5.27(a)) and 2.5 at Node B (Figure 5.27(b)), respectively.

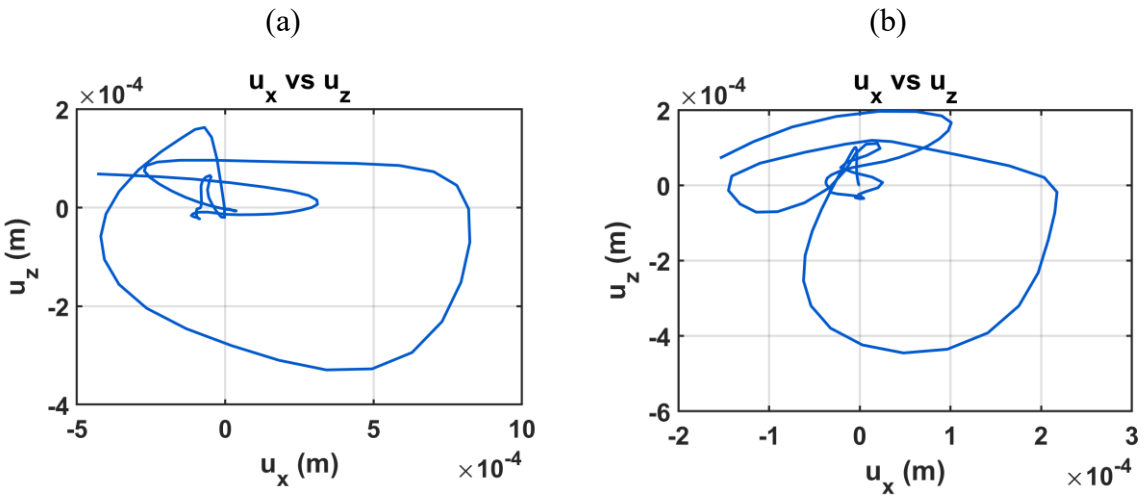

Figure 5.36: Plane wave motion at: (a) Node A; (b) Node B transverse vertical isotropy (TVI case).

E.) Three-Dimensional representation of nodal Displacement

To provide an overview of the nodal displacement, a deformed three-dimensional plot is presented from which we observe that the horizontal displacement in Figure 5.37(a) is less pronounced than the vertical displacement in Figure 5.37(b) (N.B: both displacement figures are amplified by scale factor of 1000). It becomes evident that TVI imposed condition exerts a stronger influence on the deformation in the vertical direction, whereas the Cases (A & B) demonstrate a more pronounced amplification of motion in the horizontal direction, Figure 5.20 and Figure 5.28, respectively. This overview nodal displacement in Figure 5.37, highlights the importance of taking into consideration of the material variability in all directions.

(a)

Horizontal nodal displacement

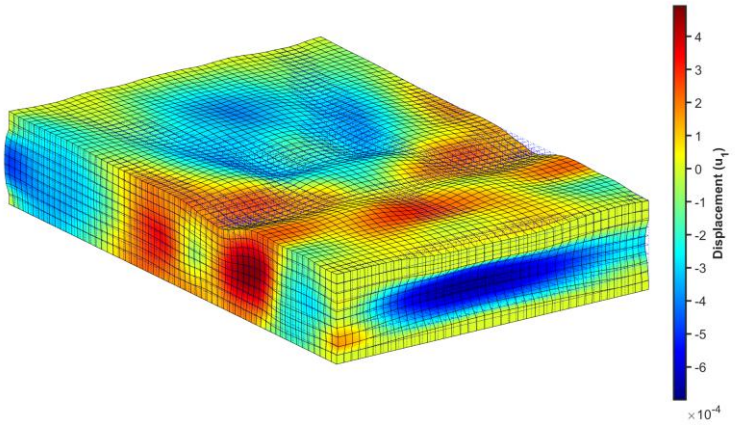

(b)

Vertical nodal displacement

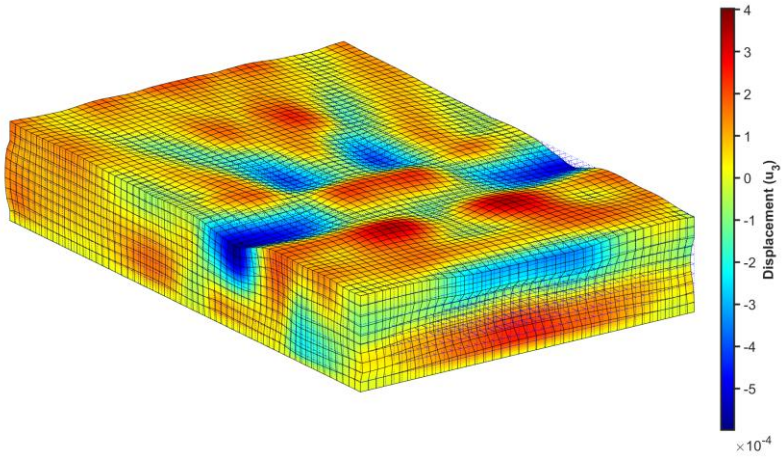

Figure 5.37: Overall nodal deformation of geological formation: (a) Horizontal deformation; (b) Vertical deformation. (transverse vertical isotropy (VTI) case).

F.) Three-Dimensional representation of wave propagation

The preliminary results outlined in Table 5.5, together with the two-dimensional visualizations in Figure 5.33 (a–d) and 5.34 (a–d), serve as the foundation for extending the study into three-dimensional wave propagation. The follow-up analysis, designed to confirm these initial findings, is carried out in three stages: first , by presenting the propagation primarily governed by P-wave dynamics (Figure 5.38); second, by analysing the patterns influenced by the fast S-wave (Figure 5.39); and third, by examining the behaviour of the slow S-wave (Figure 5.40) at selected time intervals.

At time, t = 0 (Figure 5.38(a)), the model is at rest. By time, t = 0.005 (Figure 5.38(b)), only a very small perturbation is visible, consistent with the rapid but localised onset of the P-wave front. At time, t = 0.01s, (Figure 5.38(c)), the disturbance begins to spread uniformly, reflecting the high propagation velocity of P-waves in this model. In Figure 5.38 (d-f), the P-wave spreads further, however, the nearly spherical front appears with a slight elongation due to vertical anisotropy. This elongation is because the wavefront is heavily influenced by the mechanical variability in both the vertical and horizontal directions. At time, t = 0.03s and 0.032s (Figure 5.38 (g-h)), the P-wave has propagated across a significant portion of the medium at it is being captured at the boundary.

(a) t=0 (1st time step)

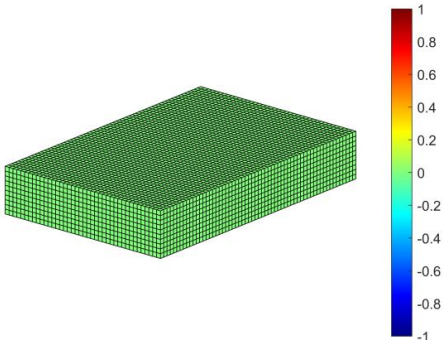

(b) t=0.005s (10th time step)

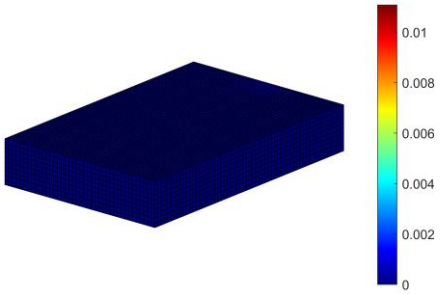

(c) t=0.01s (20th time step)

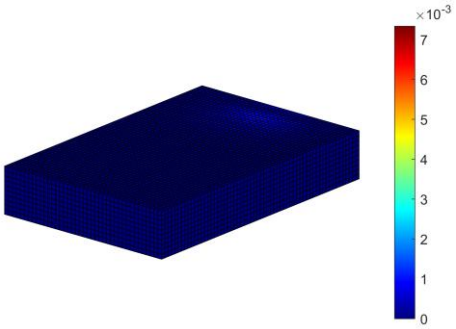

(d) t=0.013s (26th time step)

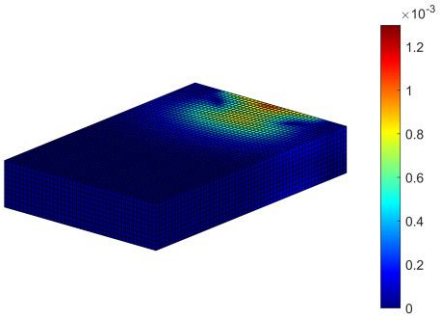

(e) t=0.02s (40th time step)

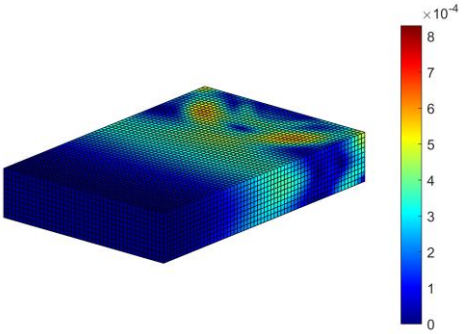

(f) t=0.024s (48th time step)

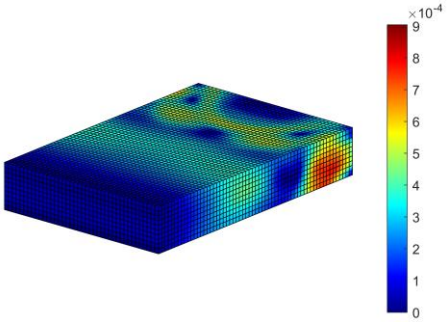

(g) t=0.03s (60th time step)

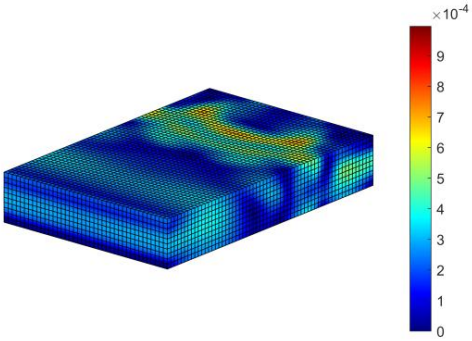

(h) t=0.032s (64th time step)

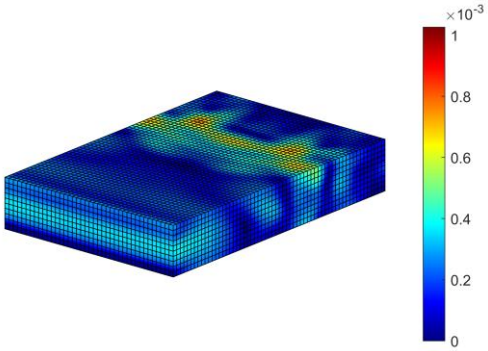

Figure 5.38: P-wave dominated propagation in transverse vertical isotropy (TVI) case study.

The snapshots Figure 5.39 (a–d) show the evolution of fast S-wave propagation in the TVI medium. At t=0.03s Figure 5.39 (a) the shear front (highlighted in red) is clearly identifiable, with peak amplitudes reaching about 9×10^{-4}. By t=0.035s (Figure 5.39 (b)), the fast S-wave front has advanced further across the model while retaining high amplitude $\sim8.5\times10^{-4}$. At t=0.038s (Figure 5.39(c)), the front continues to spread laterally with amplitudes reduced to $\sim7\times10^{-4}$, indicating that the energy carried by the fast S-wave decreases as it propagates through the domain. Finally, at t=0.041s (Figure 5.39 (d)), two features are evident: the fast S-wave front, still carrying amplitudes of $\sim6.5\times10^{-4}$ (captured at the boundary), and a secondary trailing disturbance that follows behind. This latter feature corresponds to the slow S-wave mode, lagging the primary shear front due to its lower velocity. Thus, the sequence captures not only the dominance of the fast S-wave but also the emergence of the trailing slow shear contribution, consistent with TVI anisotropy where shear modes split and propagate with distinct velocities.

(a) t=0.03s (60^{th} time step)

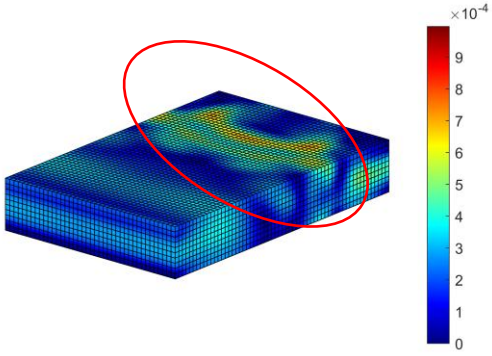

(b) t=0.035s (70^{th} time step)

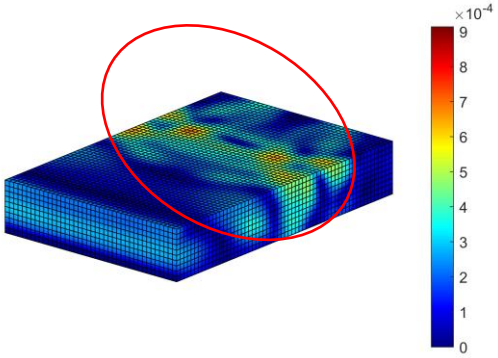

(c) t=0.038s (76^{th} time step)

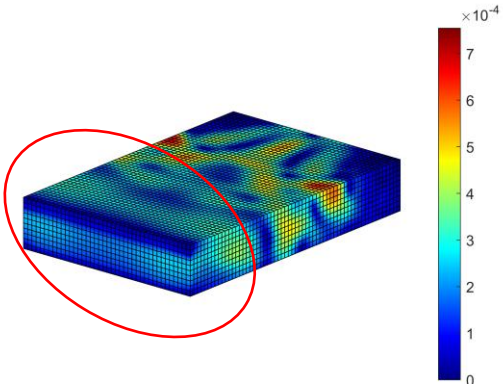

(d) t=0.041s (82^{nd} time step)

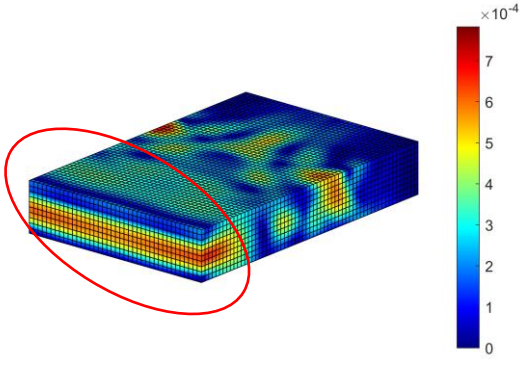

Figure 5.39: Fast S-wave propagation over time in transverse vertical isotropy (TVI) case study.

The sequence Figure 5.40 (a–d) captures the evolution of the slow S-wave in the TVI medium. At t = 0.041s Figure 5.40 (a), the slower shear front emerges with amplitudes that vary between 5-7×10^{-4}. The wave propagates but maintains a lower velocity when compared to the fast S-wave. At t = 0.053s, the S-waves shows clear two distinct amplitudes as the wave gets to the boundary and later dissociates as seen in Figure 5.40(d), where the slow S-wave energy partitions into two preferential propagation directions. This lobe splitting effect is direct evidence of TVI control on the shear wave propagation profile.

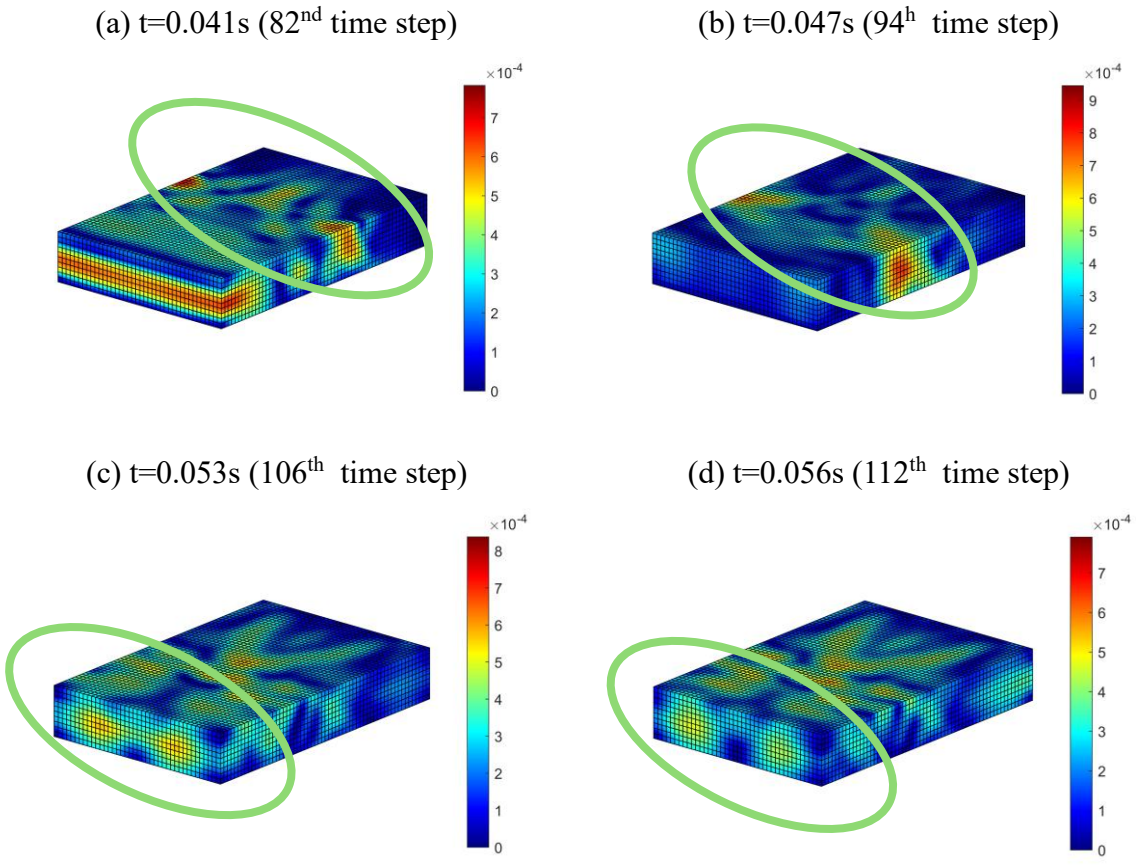

Figure 5.40: : Slow S-wave propagation over time in transverse vertical isotropy (TVI) case study.

5.2.4 Summary of hydromechanical (HM) wave propagation analysis

While the wave profiles obtained for all case studies (CASE A, B and C) demonstrate nodal displacements within the fault region, the anisotropic case (CASE C) produces a wavefield that is stronger, and slower than in the isotropic case (CASE A) and layered anisotropy (CASE B).

After an initial period where the two responses are analogous, the anisotropic model departs clearly at t = 0.013 s, reaching a higher P-wave peak (~9×10^{-4} vs ~6×10^{-4}) and maintaining

systematically larger amplitudes thereafter. At the same time, propagation is slower. That is the first boundary capture, occurs at ~28 ms in the anisotropic medium versus ~24 ms in the isotropic case.

Nodal records reveal shear-wave splitting not captured in the isotropic case. In addition, the pressure fields show greater P-energy (i.e.., ~0.8–0.9×10^5 Pa in anisotropy vs ~0.5–0.7×10^5 Pa in isotropy). Surface motions trace elongated, retrograde Rayleigh ellipses with enhanced horizontal amplitudes, especially at Node B, and 3-D deformation snapshots emphasize larger, more horizontally inclined displacements.

In the case of transverse vertical isotropy (CASE C), these effects are further accentuated: body-wave arrival times are more delayed (P-wave ~32 ms vs 24 ms in CASE A and 28 ms in CASE B), pressure amplitudes are amplified to ~1.2×10^5 Pa at both Nodes A and B, and shear-wave splitting is clearly evident with distinct SV and SH arrivals (first peak ~0.042–0.045 s and second ~0.053s). Plane motion records confirm a transition from horizontally dominated ellipses at Node A ($u_x/u_z \approx 2.7$) to vertically dominated motion at Node B ($u_x/u_z \approx 0.43$), highlighting the stronger vertical stiffness component of the VTI medium. Thus, CASE C not only slows and strengthens the wavefield compared to CASE A and B but also redistributes deformation between nodes, leading to more persistent and vertically controlled ground motions.

Taken together, anisotropy redistributes energy and delays arrivals, yielding higher amplitudes but reduced apparent speeds, with clear S-wave polarization, a combination that elevates horizontal ground-motion demands and has direct implications for PGV/MMI mapping and design assessments in layered, depleted reservoirs.

5.3 Potential Ground Shaking Intensity

To assess the potential ground shaking intensity arising from the wave propagation, it is essential to establish the reliability of the wavefield within the numerical domain. This is because wave propagation in saturated porous medium is highly sensitive to boundary interactions. This could give rise to spurious reflections that could distort seismic response and lead to misleading shaking estimates. To address this, the reflectivity of the wave was evaluated using equations (3.97(a) – (d)) for the anisotropic categories CASE (B and C). This is because, the contrast in material properties across the layers, could introduce impedance mismatches at the interfaces, rendering the medium more susceptible to boundary-induced wave reflections, unlike the isotropic case.

5.3.1 Reflectivity of body waves (P- waves and S- waves)

The detailed step-by-step calculations presented in Appendix C, yield the reflection and mode conversion coefficients for the following waves:

- Rpp: P-P reflection coefficient (incident P-wave producing a reflected P-wave),
- Rps: P-S reflection coefficient (incident P-wave produces reflected S-wave),
- Rsp: S-P reflection coefficient (incident S-wave produces reflected P-wave),
- Rss: S-S reflection coefficient (incident S-wave produces reflected S-wave)

The results summarized in Table 5.6, demonstrate that only a very minimal portion of the incident energy is reflected at the material boundary. This finding indicates that the chosen domain size is sufficiently large to suppress spurious reflections caused by contrasts in material properties. As a result, confidence can be placed in the interpretation of the simulated wavefield since the computed wave profiles can be considered reliable.

Table 5.6 Body wave reflection coefficient due to layered anisotropy for angle of incidence

(θ =0.0° and θ =30°)

Body wave	Reflection and conversion coefficient	
Rpp	0.07 for θ = 0.0°	0.057 for θ = 30°
Rps	0.00 for θ = 0.0°	0.025 for θ = 30°
Rsp	0.00 for θ = 0.0°	0.0016 for θ = 30°
Rss	0.0706 for θ = 0.0°	0.0413 for θ = 30°

5.3.2 Modified Mercalli intensity (MMI) vs peak ground velocity (PGV) for ground shaking analysis

The dynamic response at the ground surface is evaluated, with emphasis on the peak ground velocity at the top of the domain. This step is critical, as peak ground velocity at the surface is directly related to MMI through equation (3.98). This tells us the extent to which the fault slip may translate to felt ground motion at the surface. The peak ground velocity and intensity, computed from velocity magnitudes extracted from the dynamic multi-field analysis, are shown for the isotropic and anisotropic simulations.

A.) Isotropic case study

The registered spatiotemporal wave profile plot (Figure 5.41(a)) revealed the propagation of seismic energy along the surface , with distinct phase arrivals and localized zones of amplitude

culminating to peak ground velocity of 0.243cm/s, at approximately time, t=0.03s and node number 25039, owing to the start of S-wave propagation. The corresponding temporal plot (Figure 5.41(b)) represents these results as a single curve representing the maximum velocity across selected monitored nodes (i.e. 60 nodes on surface) at each time step.

The computed peak ground velocity of 0.243cm/s, when interpreted using the Modified Mercalli Intensity (MMI) scale ([255]; see Appendix B), corresponds to weak perceived shaking, no expected surface damage, and an instrumental intensity level of II-III.

(a)

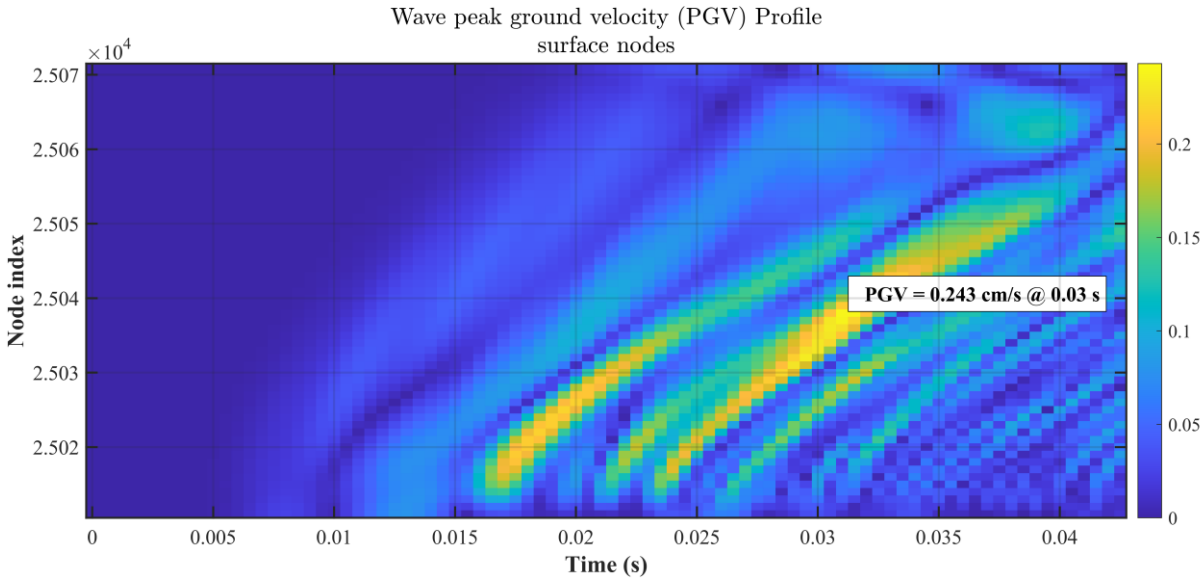

(b)

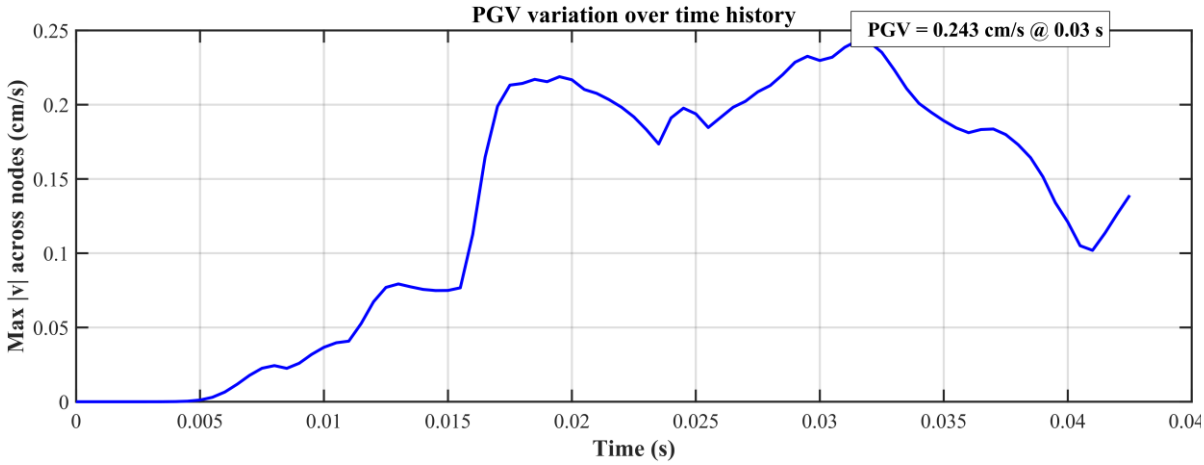

Figure 5.41: Isotropic case: peak ground velocity (PGV) for 60 monitored nodes in surface of domain. (a) spatiotemporal variation vs time; (b) PGV temporal variation for 60 monitored surface nodes

B.) Layered anisotropic case study (Case-B)

In the anisotropic scenario, the spatiotemporal wave profile plot (Figure 5.42(a)) revealed that the propagation of seismic energy along the surface, registered a peak ground velocity of 0.362cm/s, at approximately time, t ~ 0.024s and node number 25019. The early registration of PGV in the anisotropic case, is attributed to shear polarization, as the fast wave quickly is noticed at this point. The corresponding temporal plot (Figure 5.42b)) presents the results as a single curve for the selected monitored nodes (i.e. 60 nodes on surface) at each time step.

The simulated anisotropic case yields a peak ground velocity of 0.362 cm/s, which is higher than the isotropic result of 0.243 cm/s. Despite this relative increase, comparison with the Modified Mercalli Intensity (MMI) scale indicates that both values fall within the range of weak or imperceptible shaking, with no expected surface damage and an instrumental intensity level of II–III

(a)

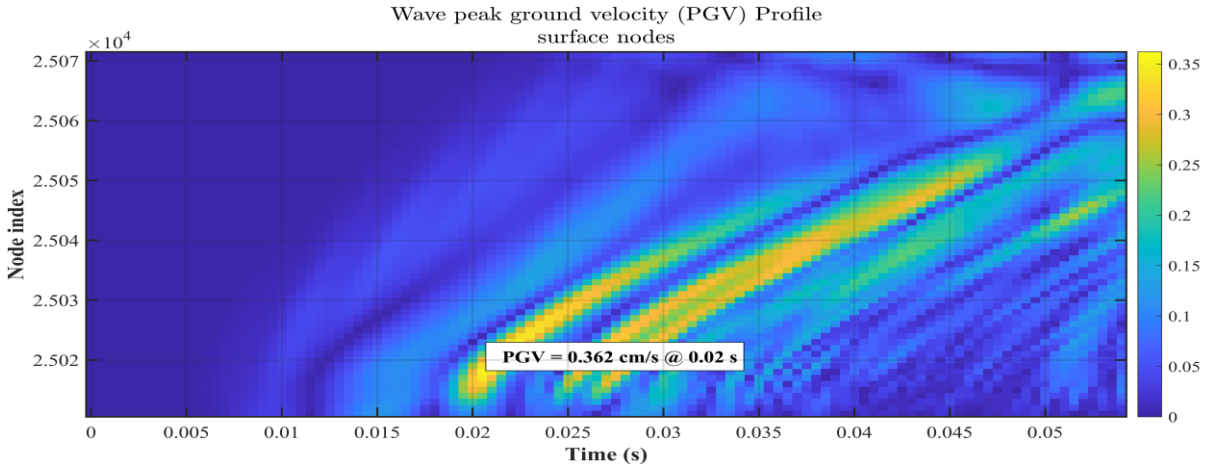

(b)

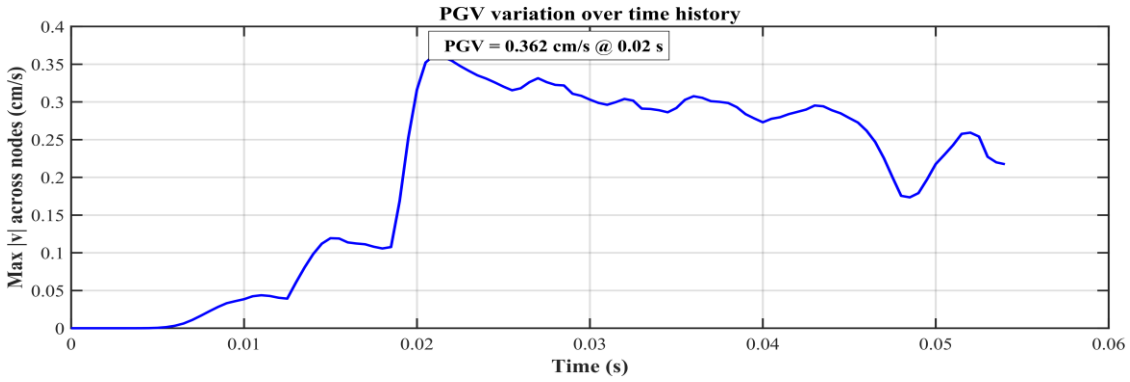

Figure 5.42: Layered anisotropic case: peak ground velocity (PGV) for 60 monitored nodes in surface of domain. (a) spatiotemporal variation vs time; (b) PGV temporal variation for 60 monitored surface nodes

C.) Transverse vertical isotropy (Case-C)

In the TVI case, the spatiotemporal wave profile plot (Figure 5.43(a)) shows that the seismic energy propagation along the surface reaches a peak ground velocity of 0.398cm/s, at approximately time, t ~ 0.04s and node index 25034. This value is both higher in amplitude and later in occurrence compared to the anisotropic layered category, where PGV peaked earlier (~0.024 s) due to the faster S-wave polarization. The delayed registration in the TVI medium reflects the slower propagation speed caused by the imposed condition of vertical stiffness and anisotropy-driven energy redistribution. The corresponding temporal plot Figure 5.43 (b) confirms this behaviour, with the 60 monitored surface nodes showing a gradual build-up of PGV before the maximum of 0.0398cm/s is reached at ~0.04 s. When compared to the isotropic case (0.243 cm/s) and the layered anisotropy case (0.362 cm/s), the TVI scenario produces the highest PGV amplitude but also the slowest surface arrival.

The simulated results when compared against the Modified Mercalli Intensity (MMI) scale, the recorded PGV still falls within the weak to imperceptible shaking range (II–III)**,** indicating no expected surface damage, but the elevated amplitude in the TVI case suggests stronger ground-motion demands relative to the other two scenarios.

(a)

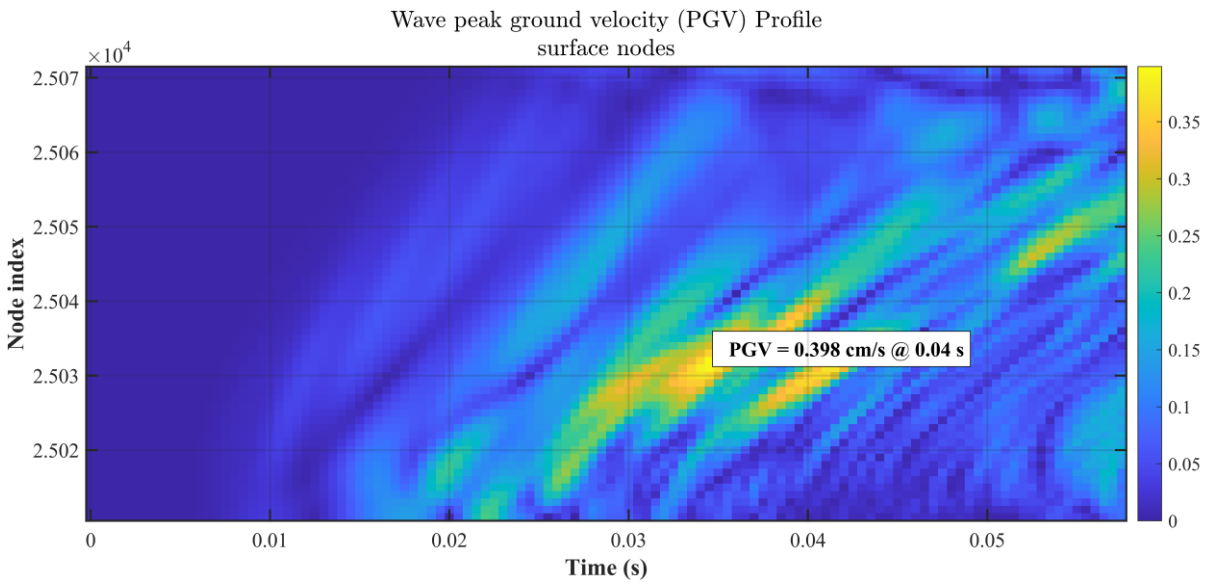

(b)

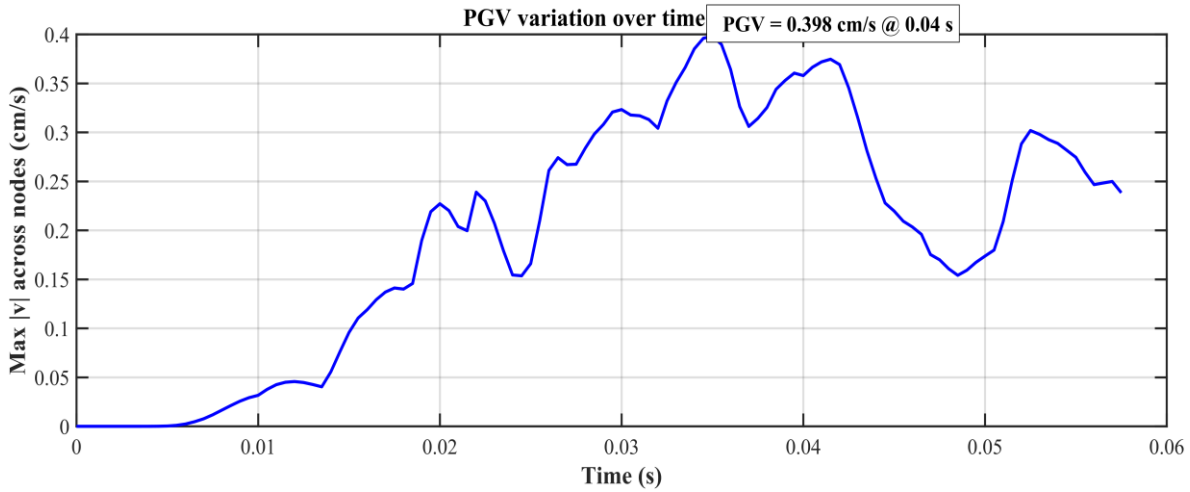

Figure 5.43: Transverse vertical isotropy case: peak ground velocity (PGV) for 60 monitored nodes in surface of domain. (a) spatiotemporal variation vs time; (b) PGV temporal variation for 60 monitored surface nodes.

5.4 Summary of potential ground shaking intensity

The ground surface response was investigated through the peak ground velocity (PGV), which serves as an indicator for shaking intensity and links numerical simulations to empirical measures such as the Modified Mercalli Intensity (MMI) scale.

In the isotropic case, the spatiotemporal wave profile revealed the arrival of seismic energy with localized amplification leading to a PGV of 0.243 cm/s at approximately t = 0.03 s and node 25039, corresponding to the onset of S-wave propagation. The computed PGV corresponds to weak perceived shaking, no anticipated surface damage, and an instrumental intensity of II–III.

The anisotropic case exhibited a notably different response, with the spatiotemporal profile indicating an earlier PGV at t ≈ 0.024 s and node 25019, with the crest at 0.362 cm/s. The earlier onset is attributed to shear-wave polarization, whereby the fast shear-wave component dominates the observed motion.

In the transvers vertical isotropy (TVI) scenario, the surface response is more pronounced, with a PGV of 0.398 cm/s at approximately 0.04s and node 25024. Unlike the earlier arrival observed in the layered anisotropy (Case-B), the TVI model produces a delayed but stronger PGV, reflecting the slower wavefront propagation due to vertical stiffness coupled with enhanced amplification of surface displacement.

Although the PGV from TVI is larger than the layered anisotropy and the isotropic categories, all results fall within the range of weak or imperceptible shaking and imply no risk of structural damage. These findings demonstrate that anisotropy can influence both the timing and amplitude of peak surface motion, yet under the present model conditions, the predicted shaking intensity remains below thresholds, ensuring the safe deployment of GCS activity.

Chapter 6: Conclusion

The aim of this study was to develop and test an extensive integrated two-stage framework that connects injection-induced hydromechanical processes, with a fully coupled dynamic 3D wave propagation formulation analysis to advance the understanding of geomechanical and seismic risks associated with geological carbon sequestration (GCS).

This was done through four interconnected objectives. The first was to undertake a hydromechanical investigation to quantify pore-pressure buildup and fault slip in isotropic, layered anisotropic depleted oil and gas reservoir, and reservoir where transverse vertical isotropy is imposed in each layer of the reservoir media. Thereafter, evaluate the effects of injection-induced pore pressure buildup and fault slip on measurable micro-seismic events. The third objective focused on quantifying seismic source parameters, including seismic moment (M_o), moment magnitude (M_w), energy magnitude (M_e), and radiated seismic energy (E_r), to capture both the size of induced events and the energy released. Finally, implement a fully coupled dynamic 3D wave propagation (u-v-p) analysis to simulate P-waves, S-waves, and Rayleigh-wave behaviour, with the goal of assessing ground-shaking intensity and its implications for seismic hazard during carbon dioxide (CO_2) storage.

To achieve these objectives, the first stage of the framework integrated a multiphase flow model in MATLAB Reservoir Simulation Toolbox (MRST) using finite volume method, with geomechanical analysis in GeoMatFEM using the finite element method. This was coupled using an explicit coupling scheme (i.e. one way coupling), enabling the monitoring of pore pressure evolution, fault reactivation and obtaining seismic source parameters. The resulting seismic source parameters were then introduced into a fully coupled three-dimensional poroelastic wave-propagation model, which resolved body and surface wave evolution.

The application of this framework to an isotropic, layered anisotropy and transverse vertical isotropy, in depleted oil and gas reservoir, yielded several key findings, which are outlined as follows:

- CO_2 injection generated significant pressure build-up in both all cases. However, for the layered-anisotropic and TVI case, a significantly amplified pressure build-up was observed, as the low permeability of the surrounding layers confined the pressure within the reservoir layer, increasing the likelihood of fault slip.
- This amplified pressure resulted into greater fault displacement in the TVI case compared with the layered anisotropy and isotropic scenarios. Following the injection period, the isotropic model produced a vertical displacement of approximately 3.5 mm

and a horizontal displacement of less than 1mm. In contrast, the layered-anisotropy scenario registered displacements of up to 17 mm vertically and 10 mm horizontally, whereas the TVI exhibited the largest values, with 25mm in the vertical direction and 16mm horizontally. These results confirm that TVI can substantially enhance fault reactivation under the given circumstances.

- These fault displacements were further analysed using seismic source characteristics. Both models generated micro-seismic events with energy magnitudes and moment magnitudes below 3; however, the TVI configurations released greater seismic energy, when compared to the layered anisotropy and isotropic case studies.
- Using the seismic source results, the wave propagation analysis further revealed the contrast among the three categories. In the isotropic medium (i.e. where all material and petrophysical properties are similar in all layers), the body waves produced low displacement and velocity amplitudes in both the horizontal and vertical directions. Conversely, the anisotropic layering effects caused directional wave amplification, shear wave splitting, altered arrival times, resulting in higher peaks in displacement and velocities in both horizontal and vertical directions. Under TVI condition, these effects were further accentuated, with more pronounced shear-wave splitting and additional delays in wave propagation arrivals. Collectively, these findings indicate that TVI not only enhances fault slip but also governs the transmission.
- Finally, by using the velocity magnitudes to evaluate the peak ground velocities against the Mercalli Modified intensity scale (MMI), it was observed that the shaking intensities in all cases remained weak, with no expected surface damage, and an instrumental intensity level between II-III on the MMI scale.

This study makes important contributions to the field of geological carbon sequestration (GCS) for the safe long-term storage of carbon dioxide CO_2. The first being: (i) a demonstration of an extensive integrated framework that first analyse pore-pressure build-up and fault slip through a displacement–pressure (u–p) study, and then employs mixture theory for a displacement–velocity–pressure (u–v–p) study to evaluate ground-shaking potential during CO_2 storage, (ii) advanced the effects of layered-anisotropy during CO_2 storage and seismic wave propagation, (iii) This study demonstrates that CO_2 injection remains within the bounds of micro-seismicity, producing weak ground shaking. (iv) Finally, this study provides regulators with seismic datasets such as wavefield characteristics, and ground-shaking profiles which offer a more comprehensive understanding of reservoir behaviour. Such data insights strengthen the

evidential basis for regulatory frameworks, enabling more informed decisions, mitigating risks for the safe deployment of CO_2 storage.

Although the presented model has shown good capabilities in predicting seismic behaviour in depleted oil reservoir, the following limitations are recognized:

- Thermal and chemical processes (THM/THMC) couplings were excluded from the model,
- The boundaries of domain were void of advanced artificial boundary techniques that minimize reflections of the wave.
- Computational resource constraints necessitated domain downsizing for the u-v-p wave propagation simulation, and

Therefore, as further work, extending the model to include the thermal and chemical coupling properties, and include artificial boundaries to avoid any reflections as the waves propagate through the domain to analyse the seismic propagation characteristics. This would improve accuracy of seismic wave prediction during geological carbon sequestration (GCS).

Bibliography

[1] S. Bachu, ‘Review of CO2 storage efficiency in deep saline aquifers’, *International Journal of Greenhouse Gas Control*, vol. 40, pp. 188–202, Oct. 2015, doi: 10.1016/j.ijggc.2015.01.007.

[2] M. Hadi Mosleh, M. Sedighi, M. Babaei, and M. Turner, ‘Geological sequestration of carbon dioxide’, in *Managing Global Warming: An Interface of Technology and Human Issues*, Elsevier, 2018, pp. 487–500. doi: 10.1016/B978-0-12-814104-5.00016-8.

[3] ‘UNFCCC REPORT’, 2015.

[4] I. International Energy Agency, ‘CO2 emissions from fuel combustion 2019 - Highlights’, 2019. [Online]. Available: www.iea.org/t&c/

[5] M. H. Dorfman, H. B. (Burt, and) Harkins, ‘SPE10954. . 4 PETROLEUM ENGINEERING MANPOWER SUPPLY’, New Orleans, Sep. 1982.

[6] J. Ma *et al.*, ‘Carbon Capture and Storage: History and the Road Ahead’, Jul. 01, 2022, *Elsevier Ltd*. doi: 10.1016/j.eng.2021.11.024.

[7] C. Marchetti, ‘ON GEOENGINEERING AND THE CO2 PROBLEM’, 1977.

[8] Z. Lin, Y. Kuang, W. Li, and Y. Zheng, ‘Research status and prospects of CO2 geological sequestration technology from onshore to offshore: A review’, Nov. 01, 2024, *Elsevier B.V.* doi: 10.1016/j.earscirev.2024.104928.

[9] E. E. Adams and K. Caldeira, ‘Ocean storage of CO2’, *Elements*, vol. 4, no. 5, pp. 319–324, 2008, doi: 10.2113/gselements.4.5.319.

[10] Global CCS Institute, ‘GLOBAL STATUS OF CCS 2023 SCALING UP THROUGH 2030’, 2023. Accessed: Oct. 29, 2024. [Online]. Available: https://status23.globalccsinstitute.com/

[11] T. A. Torp and J. Gale, ‘Demonstrating storage of CO2 in geological reservoirs: The Sleipner and SACS projects’, *Energy*, vol. 29, no. 9–10, pp. 1361–1369, 2004, doi: 10.1016/j.energy.2004.03.104.

[12] M. A. Celia, ‘Geological storage of captured carbon dioxide as a large-scale carbon mitigation option’, May 01, 2017, *Blackwell Publishing Ltd*. doi: 10.1002/2017WR020841.

[13] O. Babarinde *et al.*, ‘An overview of geological carbon sequestration and its geomechanical aspects’, *Geological Society, London, Special Publications*, vol. 528, no. 1, pp. 61–72, Aug. 2023, doi: 10.1144/sp528-2022-51.

[14] J. Rutqvist, ‘The geomechanics of CO 2 storage in deep sedimentary formations’, *Geotechnical and Geological Engineering*, vol. 30, no. 3, pp. 525–551, Jun. 2012, doi: 10.1007/s10706-011-9491-0.

[15] J. Rutqvist, ‘Fractured rock stress-permeability relationships from in situ data and effects of temperature and chemical-mechanical couplings’, *Geofluids*, vol. 15, no. 1–2, pp. 48–66, Feb. 2015, doi: 10.1111/gfl.12089.

[16] X. Li, Q. Li, B. Bai, N. Wei, and W. Yuan, ‘The geomechanics of Shenhua carbon dioxide capture and storage (CCS) demonstration project in Ordos Basin, China’, Dec. 01, 2016, *Chinese Academy of Sciences*. doi: 10.1016/j.jrmge.2016.07.002.

[17] J. M. Carcione, C. Morency, and J. E. Santos, ‘Computational poroelasticity - A review’, 2010, *Society of Exploration Geophysicists*. doi: 10.1190/1.3474602.

[18] M. A. Biot, ‘General theory of three-dimensional consolidation’, *J Appl Phys*, vol. 12, no. 2, pp. 155–164, 1941, doi: 10.1063/1.1712886.

[19] N. De Marchi, W. Sun, and V. Salomoni, ‘Shear wave splitting and polarization in anisotropic fluid-infiltrating porous media: A numerical study’, *Materials*, vol. 13, no. 21, pp. 1–27, Nov. 2020, doi: 10.3390/ma13214988.

[20] L. George, ‘Seismic Waves and their Role in Mapping Earth’s Interior’, 2024, doi: 10.4172/JPRA.1000128.

[21] S. Mahmoodpour, M. Singh, A. Turan, K. Bär, and I. Sass, ‘Simulations and global sensitivity analysis of the thermo-hydraulic-mechanical processes in a fractured geothermal reservoir’, *Energy*, vol. 247, May 2022, doi: 10.1016/j.energy.2022.123511.

[22] J. Tao, Y. Wu, D. Elsworth, P. Li, and Y. Hao, ‘Coupled Thermo-Hydro-Mechanical-Chemical Modeling of Permeability Evolution in a CO2-Circulated Geothermal Reservoir’, *Geofluids*, vol. 2019, 2019, doi: 10.1155/2019/5210730.

[23] C. Fan, D. Elsworth, S. Li, L. Zhou, Z. Yang, and Y. Song, ‘Thermo-hydro-mechanical-chemical couplings controlling CH4 production and CO2 sequestration in enhanced coalbed methane recovery’, *Energy*, vol. 173, pp. 1054–1077, Apr. 2019, doi: 10.1016/j.energy.2019.02.126.

[24] F. Doster, J. M. Nordbotten, and M. A. Celia, ‘Impact of capillary hysteresis and trapping on vertically integrated models for CO2 storage’, *Adv Water Resour*, vol. 62, pp. 465–474, Dec. 2013, doi: 10.1016/j.advwatres.2013.09.005.

[25] A. Bashir *et al.*, ‘Comprehensive review of CO2 geological storage: Exploring principles, mechanisms, and prospects’, Feb. 01, 2024, *Elsevier B.V.* doi: 10.1016/j.earscirev.2023.104672.

[26] T. Ajayi, J. S. Gomes, and A. Bera, ‘A review of CO2 storage in geological formations emphasizing modeling, monitoring and capacity estimation approaches’, Oct. 01, 2019, *China University of Petroleum Beijing*. doi: 10.1007/s12182-019-0340-8.

[27] M. A. Celia, S. Bachu, J. M. Nordbotten, and K. W. Bandilla, ‘Status of CO2 storage in deep saline aquifers with emphasis on modeling approaches and practical simulations’, Sep. 01, 2015, *Blackwell Publishing Ltd*. doi: 10.1002/2015WR017609.

[28] J. Al-Darweesh, M. S. Aljawad, M. S. Kamal, M. Mahmoud, Z. Al-Yousef, and D. Al-Shehri, ‘Water chemistry role in the stability of CO2 foam for carbon sequestration in water aquifers’, *Gas Science and Engineering*, vol. 118, Oct. 2023, doi: 10.1016/j.jgsce.2023.205090.

[29] G. P. D. De Silva, P. G. Ranjith, and M. S. A. Perera, ‘Geochemical aspects of CO2 sequestration in deep saline aquifers: A review’, Sep. 01, 2015, *Elsevier Ltd*. doi: 10.1016/j.fuel.2015.03.045.

[30] E. A. Al-Khdheeawi, S. Vialle, A. Barifcani, M. Sarmadivaleh, and S. Iglauer, ‘Effect of wettability heterogeneity and reservoir temperature on CO2 storage efficiency in deep saline aquifers’, *International Journal of Greenhouse Gas Control*, vol. 68, pp. 216–229, Jan. 2018, doi: 10.1016/j.ijggc.2017.11.016.

[31] X. Qiao, G. Li, M. Li, and Z. Wang, ‘CO2 storage capacity assessment of deep saline aquifers in the Subei Basin, East China’, *International Journal of Greenhouse Gas Control*, vol. 11, pp. 52–63, 2012, doi: 10.1016/j.ijggc.2012.07.020.

[32] K. Michael *et al.*, ‘CO2 storage in saline aquifers I-Current state of scientific knowledge’, in *Energy Procedia*, Feb. 2009, pp. 3197–3204. doi: 10.1016/j.egypro.2009.02.103.

[33] M. H. Rasool, M. Ahmad, and M. Ayoub, ‘Selecting Geological Formations for CO2 Storage: A Comparative Rating System’, Apr. 01, 2023, *MDPI*. doi: 10.3390/su15086599.

[34] M. D. Aminu, S. A. Nabavi, C. A. Rochelle, and V. Manovic, ‘A review of developments in carbon dioxide storage’, Dec. 15, 2017, *Elsevier Ltd*. doi: 10.1016/j.apenergy.2017.09.015.

[35] A. Talapatra, ‘A study on the carbon dioxide injection into coal seam aiming at enhancing coal bed methane (ECBM) recovery’, *J Pet Explor Prod Technol*, vol. 10, no. 5, pp. 1965–1981, Jun. 2020, doi: 10.1007/s13202-020-00847-y.

[36] Gilles. Pijaudier-Cabot and J.-Michel. Pereira, *Geomechanics in CO_2 storage facilities*. ISTE, 2013.

[37] V. Vishal, T. N. Singh, and P. G. Ranjith, ‘Influence of sorption time in CO2-ECBM process in Indian coals using coupled numerical simulation’, *Fuel*, vol. 139, pp. 51–58, Jan. 2015, doi: 10.1016/j.fuel.2014.08.009.

[38] H. Xu, S. Sang, J. Yang, and H. Liu, ‘CO2 storage capacity of anthracite coal in deep burial depth conditions and its potential uncertainty analysis: a case study of the No. 3 coal seam in the Zhengzhuang Block in Qinshui Basin, China’, *Geosciences Journal*, vol. 25, no. 5, pp. 715–729, Oct. 2021, doi: 10.1007/s12303-020-0058-z.

[39] J. Q. Shi and S. Durucan, ‘CO 2 Storage in Deep Unminable Coal Seams’, 2005.

[40] M. Mazzotti, R. Pini, G. Storti, and L. Burlini, ‘Carbon dioxide (CO2) sequestration in unmineable coal seams and use for enhanced coalbed methane recovery (ECBM)’, in *Developments and Innovation in Carbon Dioxide (Co*, vol. 2, Elsevier Ltd, 2010, pp. 127–165. doi: 10.1533/9781845699581.1.127.

[41] E. Agartan, M. Gaddipati, Y. Yip, B. Savage, and C. Ozgen, ‘CO2 storage in depleted oil and gas fields in the Gulf of Mexico’, *International Journal of Greenhouse Gas Control*, vol. 72, pp. 38–48, May 2018, doi: 10.1016/j.ijggc.2018.02.022.

[42] S. Hannis *et al.*, ‘CO2 Storage in Depleted or Depleting Oil and Gas Fields: What can We Learn from Existing Projects?’, in *Energy Procedia*, Elsevier Ltd, 2017, pp. 5680–5690. doi: 10.1016/j.egypro.2017.03.1707.

[43] N. Gaurina-Međimurec and K. Novak Mavar, ‘Carbon Capture and Storage (CCS): Geological Sequestration of CO 2’, 2019. [Online]. Available: www.intechopen.com

[44] M. Albertz, S. A. Stewart, and R. Goteti, ‘Perspectives on geologic carbon storage’, Apr. 17, 2023, *Frontiers Media S.A.* doi: 10.3389/fenrg.2022.1071735.

[45] B. Wei, B. Wang, X. Li, M. Aishan, and Y. Ju, ‘CO2 storage in depleted oil and gas reservoirs: A review’, Aug. 01, 2023, *Yandy Scientific Press*. doi: 10.46690/ager.2023.08.02.

[46] B. Metz, H. Coninck, M. Loos, L. Meyer, and D. Ogunlade, ‘IPCC Special Report on Carbon dioxide Capture and Storage’, 2005. [Online]. Available: https://www.researchgate.net/publication/239877190

[47] O. Møyner and H. M. Nilsen, ‘Multiresolution coupled vertical equilibrium model for fast flexible simulation of CO2 storage’, *Comput Geosci*, vol. 23, no. 1, pp. 1–20, Feb. 2019, doi: 10.1007/s10596-018-9775-z.

[48] F. Al Hameli, H. Belhaj, and M. Al Dhuhoori, ‘CO2 Sequestration Overview in Geological Formations: Trapping Mechanisms Matrix Assessment’, Oct. 01, 2022, *MDPI*. doi: 10.3390/en15207805.

[49] E. Saadatpoor, S. L. Bryant, and K. Sepehrnoori, ‘New trapping mechanism in carbon sequestration’, *Transp Porous Media*, vol. 82, no. 1, pp. 3–17, Feb. 2010, doi: 10.1007/s11242-009-9446-6.

[50] N. M. Burnside and M. Naylor, ‘Review and implications of relative permeability of CO2/brine systems and residual trapping of CO2’, *International Journal of Greenhouse Gas Control*, vol. 23, pp. 1–11, 2014, doi: 10.1016/j.ijggc.2014.01.013.

[51] M. Azran, A. Jalil, R. Masoudi, N. H. Darman, and M. Othman, ‘Study the CO2 Injection and Sequestration in Depleted M4 Carbonate Gas Condensate Reservoir, Malaysia’, 2012.

[52] P. Chidambaram, P. A. Patil, P. K. Tiwari, D. P. Das, and R. D. Tewari, ‘Injector Design Plays an Important Role In Maximisation of CO2 Trapping in Geological Formations’, in *Offshore Technology Conference Asia, OTCA 2022*, Offshore Technology Conference, 2022. doi: 10.4043/31425-MS.

[53] J. Ennis-King, L. Paterson, and C. Petroleum, ‘Role of Convective Mixing in the Long-Term Storage of Carbon Dioxide in Deep Saline Formations’, 2005.

[54] K. Shogenov, A. Shogenova, O. Vizika-Kavvadias, and J. F. Nauroy, ‘Experimental modeling of CO2-fluid-rock interaction: The evolution of the composition and properties

of host rocks in the Baltic Region', *Earth and Space Science*, vol. 2, no. 7, pp. 262–284, 2015, doi: 10.1002/2015EA000105.

[55] Y. Verma, V. Vishal, and P. G. Ranjith, 'Sensitivity Analysis of Geomechanical Constraints in CO2 Storage to Screen Potential Sites in Deep Saline Aquifers', *Frontiers in Climate*, vol. 3, Oct. 2021, doi: 10.3389/fclim.2021.720959.

[56] Intergovernmental Panel on Climate Change, *Climate change 2014 : synthesis report : longer report.* 2014.

[57] N. Budisa and D. Schulze-Makuch, 'Supercritical carbon dioxide and its potential as a life-sustaining solvent in a planetary environment', *Life*, vol. 4, no. 3, pp. 331–340, Aug. 2014, doi: 10.3390/life4030331.

[58] S. M. Hitchen and J. R. Dean, 'Properties of supercritical Fluids', 1993.

[59] J. Wang and R. Weijermars, 'Production-induced pressure-depletion and stress anisotropy changes near hydraulically fractured wells: Implications for intra-well fracture interference and fracturing treatment efficacy', *Geoenergy Science and Engineering*, vol. 222, Mar. 2023, doi: 10.1016/j.geoen.2023.211450.

[60] Y. Song, S. Jun, Y. Na, K. Kim, Y. Jang, and J. Wang, 'Geomechanical challenges during geological CO2 storage: A review', Jan. 15, 2023, *Elsevier B.V.* doi: 10.1016/j.cej.2022.140968.

[61] K.-Andreas. Lie, *An Introduction to Reservoir Simulation Using MATLAB/GNU Octave : User Guide for the MATLAB Reservoir Simulation Toolbox (MRST)*. Cambridge University Press, 2019.

[62] F. Cappa and J. Rutqvist, 'Modeling of coupled deformation and permeability evolution during fault reactivation induced by deep underground injection of CO2', *International Journal of Greenhouse Gas Control*, vol. 5, no. 2, pp. 336–346, 2011, doi: 10.1016/j.ijggc.2010.08.005.

[63] J. E. Aarnes, T. Gimse, and L. Knut–Andreas, 'Modelling of Multiscale Structures in Flow Simulations for Petroleum Reservoirs', in *Geometrical Modeling, Numerical Simulation and Optimization: Industrial Mathematics at SINTEF.*, Springer Verlag, 2007.

[64] O. Coussy, *Mechanics of porous continua*. Chichester: Wiley, 1995.

[65] SINTEF GROUP, *Advanced Modeling with the MATLAB Reservoir Simulation Toolbox*. Cambridge University Press, 2021. doi: 10.1017/9781009019781.

[66] R. H. Brooks and A. T. Corey, 'HYDRAULIC PROPERTIES OF POROUS MEDIA', 1964.

[67] M. T. Van Genuchten, 'A Closed-form Equation for Predicting the Hydraulic Conductivity of Unsaturated Soils 1', 1980.

[68] S. MO and I. Akervoll, 'Modeling Long-Term CO2 Storage in Aquifer with a Black-Oil Reservoir Simulator', 2005. doi: 10.2118/93951-MS.

[69] H. Hassanzadeh, M. Pooladi-Darvish, A. M. Elsharkawy, D. W. Keith, and Y. Leonenko, 'Predicting PVT data for CO2-brine mixtures for black-oil simulation of CO2 geological storage', *International Journal of Greenhouse Gas Control*, vol. 2, no. 1, pp. 65–77, 2008, doi: 10.1016/S1750-5836(07)00010-2.

[70] I. Ismail, S. P. Fotias, D. Avgoulas, and V. Gaganis, 'Integrated Black Oil Modeling for Efficient Simulation and Optimization of Carbon Storage in Saline Aquifers', *Energies (Basel)*, vol. 17, no. 8, Apr. 2024, doi: 10.3390/en17081914.

[71] B. Rostami, W. F. Al-Masri, and N. Andrianov, 'Evaluating the Benefits and Limitations of Black-Oil Models for Simulating CO2 Storage in Saline Aquifers', in *Fifth EAGE Global Energy Transition Conference & Exhibition (GET 2024)*, European Association of Geoscientists & Engineers, Nov. 2024, pp. 1–5. doi: 10.3997/2214-4609.202421052.

[72] A. Hashemi Fath and A. R. Pouranfard, 'Evaluation of miscible and immiscible CO2 injection in one of the Iranian oil fields', *Egyptian Journal of Petroleum*, vol. 23, no. 3, pp. 255–270, Sep. 2014, doi: 10.1016/j.ejpe.2014.08.002.

[73] C. Di *et al.*, 'A parallel compositional reservoir simulator for large-scale CO2 geological storage modeling and assessment', *Science of the Total Environment*, vol. 955, Dec. 2024, doi: 10.1016/j.scitotenv.2024.177065.

[74] A. Kamashev and Y. Amanbek, 'Reservoir simulation of co2 storage using compositional flow model for geological formations in frio field and precaspian basin', *Energies (Basel)*, vol. 14, no. 23, Dec. 2021, doi: 10.3390/en14238023.

[75] J. Rutqvist, J. Birkholzer, F. Cappa, and C. F. Tsang, 'Estimating maximum sustainable injection pressure during geological sequestration of CO2 using coupled fluid flow and

geomechanical fault-slip analysis', *Energy Convers Manag*, vol. 48, no. 6, pp. 1798–1807, Jun. 2007, doi: 10.1016/j.enconman.2007.01.021.

[76] S. Kim and S. Hosseini, 'Above-zone pressure monitoring and geomechanical analyses for a field-scale CO2 injection project in Cranfield, MS', *Greenhouse Gases: Science and Technology*, vol. 2, no. 5, pp. 352–368, 2012, doi: 10.1002/ghg.

[77] J. A. Torres, I. Bogdanov, and M. Boisson, 'Hydromechanical Model of Geological Carbon Sequestration in Saline Aquifers', 2019.

[78] M. Cao *et al.*, 'Hydromechanical Modeling of Fault Rupture in Geologic CO2 Sequestration: A Comparison of Two Failure Criteria', *Geophys Res Lett*, vol. 52, no. 10, May 2025, doi: 10.1029/2025GL115250.

[79] X. Ju, P. Fu, R. R. Settegast, and J. P. Morris, 'A coupled thermo-hydro-mechanical model for simulating leakoff-dominated hydraulic fracturing with application to geologic carbon storage', *International Journal of Greenhouse Gas Control*, vol. 109, Jul. 2021, doi: 10.1016/j.ijggc.2021.103379.

[80] K. W. Bandilla, M. A. Celia, J. T. Birkholzer, A. Cihan, and E. C. Leister, 'Multiphase modeling of geologic carbon sequestration in saline aquifers', *Groundwater*, vol. 53, no. 3, pp. 362–377, May 2015, doi: 10.1111/gwat.12315.

[81] M. J. A. Moein *et al.*, 'The physical mechanisms of induced earthquakes', Dec. 01, 2023, *Springer Nature*. doi: 10.1038/s43017-023-00497-8.

[82] K. Terzaghi, *Theoretical Soil Mechanics*. 1943. doi: https://doi.org/10.1002/9780470172766open_in_newISBN9780470172766.

[83] J. Rutqvist, D. W. Vasco, and L. Myer, 'Coupled reservoir-geomechanical analysis of CO2 injection at In Salah, Algeria', in *Energy Procedia*, Feb. 2009, pp. 1847–1854. doi: 10.1016/j.egypro.2009.01.241.

[84] J. Rutqvist and C.-F. Tsang, 'Coupled Hydromechanical Effects In CO2 Injection', 2005.

[85] J. P. Verdon, A. L. Stork, R. C. Bissell, C. E. Bond, and M. J. Werner, 'Simulation of seismic events induced by CO2 injection at In Salah, Algeria', *Earth Planet Sci Lett*, vol. 426, pp. 118–129, Sep. 2015, doi: 10.1016/j.epsl.2015.06.029.

[86] J. P. Verdon, J. M. Kendall, D. J. White, and D. A. Angus, 'Linking microseismic event observations with geomechanical models to minimise the risks of storing CO2 in

geological formations', *Earth Planet Sci Lett*, vol. 305, no. 1–2, pp. 143–152, May 2011, doi: 10.1016/j.epsl.2011.02.048.

[87] N. Bondarenko, Y. Podladchikov, S. Williams-Stroud, and R. Makhnenko, 'Stratigraphy-Induced Localization of Microseismicity During CO2 Injection in Illinois Basin', *J Geophys Res Solid Earth*, vol. 130, no. 3, Mar. 2025, doi: 10.1029/2024JB029526.

[88] P. Braun, S. Ghabezloo, P. Delage, J. Sulem, and N. Conil, 'Transversely Isotropic Poroelastic Behaviour of the Callovo-Oxfordian Claystone: A Set of Stress-Dependent Parameters', *Rock Mech Rock Eng*, vol. 54, no. 1, pp. 377–396, Jan. 2020, doi: 10.1007/s00603-020-02268-z.

[89] N. T. Singh and B. Singh, 'Settlement Profile and Pile Load Distribution Under Vertical Load of Piled Raft Foundation in Clay', *Geotechnical and Geological Engineering*, vol. 38, no. 5, pp. 5229–5244, Oct. 2020, doi: 10.1007/s10706-020-01359-6.

[90] D. Rakic and M. Zivkovic, 'Stress integration of the Drucker-Prager material model with kinematic hardening', *Theoretical and Applied Mechanics*, vol. 42, no. 3, pp. 201–209, 2015, doi: 10.2298/tam1503201r.

[91] M. Beck, G. Seitz, and H. Class, 'Volume-Based Modelling of Fault Reactivation in Porous Media Using a Visco-Elastic Proxy Model', *Transp Porous Media*, vol. 114, no. 2, pp. 505–524, Sep. 2016, doi: 10.1007/s11242-016-0663-5.

[92] E. Ekpo Johnson, M. Scherwath, K. Moran, S. E. Dosso, and K. M. Rohr, 'Fault Slip Tendency Analysis for a Deep-Sea Basalt CO2 Injection in the Cascadia Basin', *GeoHazards*, vol. 4, no. 2, pp. 121–135, Apr. 2023, doi: 10.3390/geohazards4020008.

[93] B. Figueiredo, C. F. Tsang, J. Rutqvist, J. Bensabat, and A. Niemi, 'Coupled hydro-mechanical processes and fault reactivation induced by Co2 Injection in a three-layer storage formation', *International Journal of Greenhouse Gas Control*, vol. 39, pp. 432–448, Aug. 2015, doi: 10.1016/j.ijggc.2015.06.008.

[94] A. Mazzoldi, A. P. Rinaldi, A. Borgia, and J. Rutqvist, 'Induced seismicity within geological carbon sequestration projects: Maximum earthquake magnitude and leakage potential from undetected faults', *International Journal of Greenhouse Gas Control*, vol. 10, pp. 434–442, 2012, doi: 10.1016/j.ijggc.2012.07.012.

[95] P. Olden *et al.*, ‘Use of rock mechanics laboratory data in geomechanical modelling to increase confidence in CO2 geological storage’, *International Journal of Greenhouse Gas Control*, vol. 11, pp. 304–315, 2012, doi: 10.1016/j.ijggc.2012.09.011.

[96] J. Rohmer and D. M. Seyedi, ‘Analyse hydromècanique á grande èchelle pour l’èvaluation du risque de fracturation de la couverture de stockage du CO2 dans les aquifères profonds’, *Oil and Gas Science and Technology*, vol. 65, no. 3, pp. 503–517, May 2010, doi: 10.2516/ogst/2009049.

[97] J. Rutqvist, J. T. Birkholzer, and C.-F. Tsang, ‘Coupled Reservoir-Geomechanical Analysis of the Potential for Tensile and Shear Failure Associated with CO 2 Injection in Multilayered Reservoir-Caprock Systems’, 2009.

[98] R. H. Sibson, ‘Brittle-failure controls on maximum sustainable overpressure in different tectonic regimes’, *American Association of Petroleum Geologists Bulletin*, vol. 87, no. 6, pp. 901–908, 2003, doi: 10.1306/01290300181.

[99] J. E. Streit and R. R. Hillis, ‘Estimating fault stability and sustainable fluid pressures for underground storage of CO2 in porous rock’, *Energy*, vol. 29, no. 9–10, pp. 1445–1456, 2004, doi: 10.1016/j.energy.2004.03.078.

[100] J. Huang *et al.*, ‘Simulation of Multiphase Flow and Poromechanical Effects Around Injection Wells in CO2 Storage Sites’, *Rock Mech Rock Eng*, 2024, doi: 10.1007/s00603-024-04051-w.

[101] J.-Q. Shi, W. Cao, S. Durucan, and A. Korre, ‘Assessment of CO 2 injection induced fault reactivation and reservoir performance conformance at the In Salah CO 2 storage site’, 2024. [Online]. Available: https://ssrn.com/abstract=5068664

[102] M. L. McLean and D. N. Espinoza, ‘An open source FEM code for solving coupled thermo-poroelastoplastic processes’, *Open Geomechanics*, vol. 5, pp. 1–19, Feb. 2024, doi: 10.5802/ogeo.17.

[103] M. Sanei, P. R. B. Devloo, T. L. D. Forti, O. Durán, and E. S. R. Santos, ‘An Innovative Scheme to Make an Initial Guess for Iterative Optimization Methods to Calibrate Material Parameters of Strain-Hardening Elastoplastic Models’, *Rock Mech Rock Eng*, vol. 55, no. 1, pp. 399–421, Jan. 2022, doi: 10.1007/s00603-021-02665-y.

[104] T. D. Rathnaweera, W. Wu, Y. Ji, and R. P. Gamage, ‘Understanding injection-induced seismicity in enhanced geothermal systems: From the coupled thermo-hydro-

mechanical-chemical process to anthropogenic earthquake prediction', Jun. 01, 2020, *Elsevier B.V.* doi: 10.1016/j.earscirev.2020.103182.

[105] F. Cappa and J. Rutqvist, 'Impact of CO2 geological sequestration on the nucleation of earthquakes', *Geophys Res Lett*, vol. 38, no. 17, Sep. 2011, doi: 10.1029/2011GL048487.

[106] F. Cappa, J. ; F. Rutqvist, and J. Rutqvist, 'Impact of CO2 geological sequestration on the nucleation of earthquakes', *Geophys Res Lett*, vol. 38, p. 17313, 2011, doi: 10.1029/2011GL048487ï.

[107] J. Rutqvist *et al.*, 'Fault activation and induced seismicity in geological carbon storage – Lessons learned from recent modeling studies', *Journal of Rock Mechanics and Geotechnical Engineering*, vol. 8, no. 6, pp. 789–804, Dec. 2016, doi: 10.1016/j.jrmge.2016.09.001.

[108] M. O. Häring, U. Schanz, F. Ladner, and B. C. Dyer, 'Characterisation of the Basel 1 enhanced geothermal system', *Geothermics*, vol. 37, no. 5, pp. 469–495, Oct. 2008, doi: 10.1016/j.geothermics.2008.06.002.

[109] Y. Mukuhira, H. Asanuma, H. Niitsuma, and M. O. Häring, 'Characteristics of large-magnitude microseismic events recorded during and after stimulation of a geothermal reservoir at Basel, Switzerland', *Geothermics*, vol. 45, pp. 1–17, Jan. 2013, doi: 10.1016/j.geothermics.2012.07.005.

[110] K. M. Bowert and G. Zyvoloski~, 'A Numerical Model for Thermo-Hydro-Mechanical Coupling in Fractured Rock', 1997.

[111] I. Stefansson, I. Berre, and E. Keilegavlen, 'A fully coupled numerical model of thermo-hydro-mechanical processes and fracture contact mechanics in porous media', *Comput Methods Appl Mech Eng*, vol. 386, Dec. 2021, doi: 10.1016/j.cma.2021.114122.

[112] M. Cacace and A. B. Jacquey, 'Flexible parallel implicit modelling of coupled thermal-hydraulic-mechanical processes in fractured rocks', *Solid Earth*, vol. 8, no. 5, pp. 921–941, Sep. 2017, doi: 10.5194/se-8-921-2017.

[113] F. Tong, L. Jing, and R. W. Zimmerman, 'A fully coupled thermo-hydro-mechanical model for simulating multiphase flow, deformation and heat transfer in buffer material and rock masses', *International Journal of Rock Mechanics and Mining Sciences*, vol. 47, no. 2, pp. 205–217, 2010, doi: 10.1016/j.ijrmms.2009.11.002.

[114] O. Coussy, *Poromechanics*. 2004.

[115] A. P. Rinaldi, J. Rutqvist, and F. Cappa, ‘Geomechanical effects on CO2 leakage through fault zones during large-scale underground injection’, *International Journal of Greenhouse Gas Control*, vol. 20, pp. 117–131, 2014, doi: 10.1016/j.ijggc.2013.11.001.

[116] A. Settari and D. A. Walters, ‘Advances in coupled geomechanical and reservoir modeling with applications to reservoir compaction’, *SPE Journal*, vol. 6, no. 3, pp. 334–342, 2001, doi: 10.2118/74142-PA.

[117] R. H. Dean, S. Systems, ; X Gai, and S. E. Minkoff, ‘A Comparison of Techniques for Coupling Porous Flow and Geomechanics’, 2006.

[118] S. E. Minkoff, C. M. Stone, S. Bryant, M. Peszynska, and M. F. Wheeler, ‘Coupled fluid flow and geomechanical deformation modeling’, *J Pet Sci Eng*, vol. 38, no. 1–2, pp. 37–56, 2003, doi: 10.1016/S0920-4105(03)00021-4.

[119] B. Jha and R. Juanes, ‘Coupled multiphase flow and poromechanics: A computational model of pore pressure effects on fault slip and earthquake triggering’, *Water Resour Res*, vol. 50, no. 5, pp. 3776–3808, 2014, doi: 10.1002/2013WR015175.

[120] Y. Liu, L. Liu, J. Y. Leung, and G. J. Moridis, ‘Sequentially coupled flow and geomechanical simulation with a discrete fracture model for analyzing fracturing fluid recovery and distribution in fractured ultra-low permeability gas reservoirs’, *J Pet Sci Eng*, vol. 189, Jun. 2020, doi: 10.1016/j.petrol.2020.107042.

[121] R. Quevedo and D. Roehl, ‘A novel and efficient sequential-explicit technique for poroelasticity problems’, *Comput Geotech*, vol. 138, Oct. 2021, doi: 10.1016/j.compgeo.2021.104334.

[122] J. Kim, H. A. Tchelepi, and R. Juanes, ‘Stability and convergence of sequential methods for coupled flow and geomechanics: Fixed-stress and fixed-strain splits’, *Comput Methods Appl Mech Eng*, vol. 200, no. 13–16, pp. 1591–1606, Mar. 2011, doi: 10.1016/j.cma.2010.12.022.

[123] M. Beck, A. P. Rinaldi, B. Flemisch, and H. Class, ‘Accuracy of fully coupled and sequential approaches for modeling hydro- and geomechanical processes’, *Comput Geosci*, vol. 24, no. 4, pp. 1707–1723, Aug. 2020, doi: 10.1007/s10596-020-09987-w.

[124] M. Ferronato, N. Castelletto, and G. Gambolati, ‘A fully coupled 3-D mixed finite element model of Biot consolidation’, *J Comput Phys*, vol. 229, no. 12, pp. 4813–4830, 2010, doi: 10.1016/j.jcp.2010.03.018.

[125] R. W. Lewis, A. Makurat, and W. K. S. Pao, ‘Fully coupled modeling of seabed subsidence and reservoir compaction of North Sea oil fields’, *Hydrogeol J*, vol. 11, no. 1, pp. 142–161, 2003, doi: 10.1007/s10040-002-0239-z.

[126] X. Li, Z. Liu, and R. W. Lewis, ‘Mixed finite element method for coupled thermo-hydro-mechanical process in poro-elasto-plastic media at large strains’, *Int J Numer Methods Eng*, vol. 64, no. 5, pp. 667–708, Oct. 2005, doi: 10.1002/nme.1469.

[127] B. Nasrollahzadeh, H. A. Akhlaghi Amiri, and S. Ghabezloo, ‘Field-scale fully coupled simulation of fluid flow and geomechanics: Gas storage/recovery process in a depleted sandstone reservoir’, *J Pet Sci Eng*, vol. 200, May 2021, doi: 10.1016/j.petrol.2021.108423.

[128] J. T. Birkholzer *et al.*, ‘DECOVALEX-2023: An international collaboration for advancing the understanding and modeling of coupled thermo-hydro-mechanical-chemical (THMC) processes in geological systems’, *Geomechanics for Energy and the Environment*, p. 100685, May 2025, doi: 10.1016/j.gete.2025.100685.

[129] L. Jing, ‘A review of techniques, advances and outstanding issues in numerical modelling for rock mechanics and rock engineering’, 2004, *Elsevier BV*. doi: 10.1016/S1365-1609(03)00013-3.

[130] P. Pan, Z. Wu, X. Feng, and F. Yan, ‘Geomechanical modeling of CO2 geological storage: A review’, Dec. 01, 2016, *Chinese Academy of Sciences*. doi: 10.1016/j.jrmge.2016.10.002.

[131] O. Mahian *et al.*, ‘Recent advances in modeling and simulation of nanofluid flows—Part II: Applications’, Feb. 13, 2019, *Elsevier B.V.* doi: 10.1016/j.physrep.2018.11.003.

[132] D. Kuzmin, ‘A Guide to Numerical Methods for Transport Equations’, 2010.

[133] E. Oñate, ‘Structural Analysis with the Finite Element Method. Linear Statics: Volume 1: Basis and Solids (Lecture Notes on Numerical Methods in Engineering and Sciences)’, 2009.

[134] L. Beirão Da Veiga, F. Brezzi, A. Cangiani, G. Manzini, L. D. Marini, and A. Russo, ‘Basic principles of virtual element methods’, *Mathematical Models and Methods in Applied Sciences*, vol. 23, no. 1, pp. 199–214, Jan. 2013, doi: 10.1142/S0218202512500492.

[135] L. B. Da Veiga, F. Brezzi, L. D. Marini, and A. Russo, 'The Hitchhiker's guide to the virtual element method', *Mathematical Models and Methods in Applied Sciences*, vol. 24, no. 8, pp. 1541–1573, Jul. 2014, doi: 10.1142/S021820251440003X.

[136] O. Andersen, H. M. Nilsen, and X. Raynaud, 'Virtual element method for geomechanical simulations of reservoir models', *Comput Geosci*, vol. 21, no. 5–6, pp. 877–893, Dec. 2017, doi: 10.1007/s10596-017-9636-1.

[137] T. P. Fries and T. Belytschko, 'The extended/generalized finite element method: An overview of the method and its applications', *Int J Numer Methods Eng*, vol. 84, no. 3, pp. 253–304, Oct. 2010, doi: 10.1002/nme.2914.

[138] L. Gutierrez-Sosa, S. Geiger, and F. Doster, 'Poro-Mechanical Coupling for Flow Diagnostics', *Transp Porous Media*, vol. 145, no. 2, pp. 389–411, Nov. 2022, doi: 10.1007/s11242-022-01857-6.

[139] J. S. Azevedo and J. A. Fernandes, 'The parameter inversion in coupled geomechanics and flow simulations using Bayesian inference', *Journal of Computational Mathematics and Data Science*, vol. 9, Dec. 2023, doi: 10.1016/j.jcmds.2023.100083.

[140] O. Andersen, H. M. Nilsen, and X. Raynaud, 'Virtual Element Method for geomechanics on reservoir grids', Jun. 2016, [Online]. Available: http://arxiv.org/abs/1606.09508

[141] S. S. Ali *et al.*, 'Leveraging Two-Way Coupled Geomechanics-Dynamic Modelling Workflow in Evaluating Highly Porous and Depleted Carbonate Field for CO2 Injection Site', in *56th U.S. Rock Mechanics/Geomechanics Symposium*, American Rock Mechanics Association (ARMA), 2022. doi: 10.56952/arma-2022-0804.

[142] M. A. Mustafa, S. S. M. Ali, M. H. Yakup, and C. P. Tan, 'Integrated 2-Way Fully Coupled Reservoir Dynamic-Geomechanical Modelling Approach for CO2 Storage Risk Assessment in a Malaysian Carbonate Field', in *International Petroleum Technology Conference, IPTC 2022*, International Petroleum Technology Conference (IPTC), 2022. doi: 10.2523/IPTC-22685-MS.

[143] S. Khan, Y. A. Khulief, and A. A. Al-Shuhail, 'Effects of reservoir size and boundary conditions on pore-pressure buildup and fault reactivation during CO2 injection in deep geological reservoirs', *Environ Earth Sci*, vol. 79, no. 12, Jun. 2020, doi: 10.1007/s12665-020-09040-0.

[144] S. Khan, Y. Khulief, R. Juanes, S. Bashmal, M. Usman, and A. Al-Shuhail, ‘Geomechanical modeling of CO2 sequestration: A review focused on CO2 injection and monitoring’, Jun. 01, 2024, *Elsevier Ltd*. doi: 10.1016/j.jece.2024.112847.

[145] J. Rutqvist, A. P. Rinaldi, V. Vilarrasa, and F. Cappa, ‘Numerical geomechanics studies of geological carbon storage (GCS)’, in *Science of Carbon Storage in Deep Saline Formations: Process Coupling across Time and Spatial Scales*, Elsevier, 2018, pp. 237–252. doi: 10.1016/B978-0-12-812752-0.00010-1.

[146] C. M. Aruffo, A. Rodriguez-herrera, E. Tenthorey, F. Krzikalla, J. Minton, and A. Henk, ‘Geomechanical modelling to assess fault integrity at the CO2CRC Otway Project, Australia’, *Australian Journal of Earth Sciences*, vol. 61, no. 7, pp. 987–1001, Oct. 2014, doi: 10.1080/08120099.2014.958876.

[147] J. T. Birkholzer and Q. Zhou, ‘Basin-scale hydrogeologic impacts of CO2 storage: Capacity and regulatory implications’, *International Journal of Greenhouse Gas Control*, vol. 3, no. 6, pp. 745–756, 2009, doi: 10.1016/j.ijggc.2009.07.002.

[148] T. Treffeisen and A. Henk, ‘Representation of faults in reservoir-scale geomechanical finite element models – A comparison of different modelling approaches’, *J Struct Geol*, vol. 131, Feb. 2020, doi: 10.1016/j.jsg.2019.103931.

[149] S. Ye *et al.*, ‘A Novel Approach to Model Earth Fissure Caused by Extensive Aquifer Exploitation and its Application to the Wuxi Case, China’, *Water Resour Res*, vol. 54, no. 3, pp. 2249–2269, Mar. 2018, doi: 10.1002/2017WR021872.

[150] K. Fischer and A. Henk, ‘A workflow for building and calibrating 3-D geomechanical models-A case study for a gas reservoir in the North German Basin’, *Solid Earth*, vol. 4, no. 2, pp. 347–355, Oct. 2013, doi: 10.5194/se-4-347-2013.

[151] A. Franceschini, M. Ferronato, C. Janna, and P. Teatini, ‘A novel Lagrangian approach for the stable numerical simulation of fault and fracture mechanics’, *J Comput Phys*, vol. 314, pp. 503–521, Jun. 2016, doi: 10.1016/j.jcp.2016.03.032.

[152] T. Hergert, O. Heidbach, A. Bécel, and M. Laigle, ‘Geomechanical model of the Marmara Sea region-I. 3-D contemporary kinematics’, *Geophys J Int*, vol. 185, no. 3, pp. 1073–1089, Jun. 2011, doi: 10.1111/j.1365-246X.2011.04991.x.

[153] I. Berre, F. Doster, and E. Keilegavlen, ‘Flow in Fractured Porous Media: A Review of Conceptual Models and Discretization Approaches’, *Transp Porous Media*, vol. 130, no. 1, pp. 215–236, Oct. 2019, doi: 10.1007/s11242-018-1171-6.

[154] C. Soulaine, ‘Micro-Continuum Modeling: An Hybrid-Scale Approach for Solving Coupled Processes in Porous Media’, Feb. 01, 2024, *John Wiley and Sons Inc*. doi: 10.1029/2023WR035908.

[155] G. S. Seabra, M. V. Barbosa Machado, M. Delshad, K. Sepehrnoori, D. Voskov, and F. C. Vossepoel, ‘Unveiling Valuable Geomechanical Monitoring Insights: Exploring Ground Deformation in Geological Carbon Storage’, *Applied Sciences (Switzerland)*, vol. 14, no. 10, May 2024, doi: 10.3390/app14104069.

[156] B. Orlic, ‘Geomechanical effects of CO2 storage in depleted gas reservoirs in the Netherlands: Inferences from feasibility studies and comparison with aquifer storage’, *Journal of Rock Mechanics and Geotechnical Engineering*, vol. 8, no. 6, pp. 846–859, Dec. 2016, doi: 10.1016/j.jrmge.2016.07.003.

[157] J. Rutqvist and C. F. Tsang, ‘A study of caprock hydromechanical changes associated with CO2-injection into a brine formation’, *Environmental Geology*, vol. 42, no. 2–3, pp. 296–305, Jun. 2002, doi: 10.1007/s00254-001-0499-2.

[158] Z. Wei, K. Gao, and S. Li, ‘Integrated Thermo-Hydro-Mechanical Workflow for Modeling CO2 Storage with Fault Activation Risk’, *SPE Journal*, vol. 30, no. 05, pp. 2975–2995, May 2025, doi: 10.2118/225428-PA.

[159] T. Roubicek and U. Stefanelli, ‘Thermodynamics of elastoplastic porous rocks at large strains towards earthquake modeling’, *SIAM J Appl Math*, vol. 78, no. 5, pp. 2597–2625, 2018, doi: 10.1137/17M1137656.

[160] Z. Hou, Y. Gou, J. Taron, U. J. Gorke, and O. Kolditz, ‘Thermo-hydro-mechanical modeling of carbon dioxide injection for enhanced gas-recovery (CO 2-EGR): A benchmarking study for code comparison’, *Environ Earth Sci*, vol. 67, no. 2, pp. 549–561, Sep. 2012, doi: 10.1007/s12665-012-1703-2.

[161] L. Dal Zilio, B. Hegyi, W. Behr, and T. Gerya, ‘Hydro-mechanical earthquake cycles in a poro-visco-elasto-plastic fluid-bearing fault structure’, *Tectonophysics*, vol. 838, Sep. 2022, doi: 10.1016/j.tecto.2022.229516.

[162] M. Zoblack, ‘The Potential for Triggered Seismicity Associated With Geologic Sequestration of CO2 in Saline Aquifers’, *National Academy of Sciences*, 2010.

[163] H. Kanamori and D. L. Anderson, ‘THEORETICAL BASIS OF SOME EMPIRICAL RELATIONS IN SEISMOLOGY’, 1975. [Online]. Available: http://pubs.geoscienceworld.org/ssa/bssa/article-pdf/65/5/1073/5320189/bssa0650051073.pdf

[164] H. Kanamori, ‘The energy release in great earthquakes’, *J Geophys Res*, vol. 82, no. 20, pp. 2981–2987, Jul. 1977, doi: 10.1029/jb082i020p02981.

[165] B. Gutenberg, ‘AMPLITUDES OF SURFACE WAVES AND MAGNITUDES OF SHALLOW EARTHQUAKES’, 1945. [Online]. Available: http://pubs.geoscienceworld.org/ssa/bssa/article-pdf/35/1/3/5300912/bssa0350010003.pdfbyPadovaGeoscienzeuser

[166] H. Kanamori, ‘MAGNITUDE SCALE AND QUANTIFICATION OF EARTHQUAKES’, 1983.

[167] P. Bormann and D. Giacomo, ‘The moment magnitude and the energy magnitude : common roots and differences’, *J Seismol*, vol. 15, no. 2, 2010, doi: 10.1007/s10950-010-9219-2ï.

[168] D. Di Giacomo *et al.*, ‘Suitability of rapid energy magnitude determinations for emergency response purposes’, *Geophys J Int*, vol. 180, no. 1, pp. 361–374, Jan. 2010, doi: 10.1111/j.1365-246X.2009.04416.x.

[169] Y. Cheng *et al.*, ‘Seismicity induced by geological CO2 storage: A review’, Apr. 01, 2023, *Elsevier B.V.* doi: 10.1016/j.earscirev.2023.104369.

[170] J. Rutledge, ‘Southwest Regional Partnership on Carbon Sequestration Phase II Geologic Demonstration at the Aneth Oil Field, Paradox Basin, Utah’, 2011.

[171] J. A. White and W. Foxall, ‘Assessing induced seismicity risk at CO2 storage projects: Recent progress and remaining challenges’, *International Journal of Greenhouse Gas Control*, vol. 49, pp. 413–424, Jun. 2016, doi: 10.1016/j.ijggc.2016.03.021.

[172] S. Whittakera *et al.*, ‘A decade of CO2 injection into depleting oil fields: Monitoring and research activities of the IEA GHG Weyburn-Midale CO2 monitoring and storage project’, in *Energy Procedia*, Elsevier Ltd, 2011, pp. 6069–6076. doi: 10.1016/j.egypro.2011.02.612.

[173] A. Mathieson, J. Midgely, I. Wright, N. Saoula, and P. Ringrose, 'In Salah CO2 storage JIP: CO2 sequestration monitoring and verification technologies applied at Krechba, Algeria', in *Energy Procedia*, Elsevier Ltd, 2011, pp. 3596–3603. doi: 10.1016/j.egypro.2011.02.289.

[174] T. Onuma and S. Ohkawa, 'Detection of surface deformation related with CO2 injection by DInSAR at In Salah, Algeria', in *Energy Procedia*, Feb. 2009, pp. 2177–2184. doi: 10.1016/j.egypro.2009.01.283.

[175] J. P. Verdon and A. L. Stork, 'Carbon capture and storage, geomechanics and induced seismic activity', *Journal of Rock Mechanics and Geotechnical Engineering*, vol. 8, no. 6, pp. 928–935, Dec. 2016, doi: 10.1016/j.jrmge.2016.06.004.

[176] V. Vilarrasa, J. Carrera, S. Olivella, J. Rutqvist, and L. Laloui, 'Induced seismicity in geologic carbon storage', *Solid Earth*, vol. 10, no. 3, pp. 871–892, Jun. 2019, doi: 10.5194/se-10-871-2019.

[177] G. L. Choy and J. L. Boatwright, 'Global patterns of radiated seismic energy and apparent stress', *J Geophys Res*, vol. 100, no. B9, 1995, doi: 10.1029/95jb01969.

[178] M. A. Biot, 'Mechanics of deformation and acoustic propagation in porous media', *J Appl Phys*, vol. 33, no. 4, pp. 1482–1498, 1962, doi: 10.1063/1.1728759.

[179] M. A. Biot, 'Theory of Propagation of Elastic Waves in a Fluid-Saturated Porous Solid. I. Low-Frequency Range', *J Acoust Soc Am*, vol. 28, no. 2, pp. 168–178, Mar. 1956, doi: 10.1121/1.1908239.

[180] M. A. Biot, 'Theory of Propagation of Elastic Waves in a Fluid-Saturated Porous Solid. II. Higher Frequency Range', *J Acoust Soc Am*, vol. 28, no. 2, pp. 179–191, Mar. 1956, doi: 10.1121/1.1908241.

[181] J. G. Berryman, 'Elastic wave propagation in fluid-saturated porous media', *J Acoust Soc Am*, vol. 69, no. 2, pp. 416–424, Feb. 1981, doi: 10.1121/1.385457.

[182] M. D. Sharma, 'Propagation of seismic waves in patchy-saturated porous media: double-porosity representation', *Geophys Prospect*, vol. 67, no. 8, pp. 2147–2160, Oct. 2019, doi: 10.1111/1365-2478.12806.

[183] J. Ritsema and V. Lekic, 'Heterogeneity of Seismic Wave Velocity in Earth's Mantle', vol. 16, 2020, doi: 10.1146/annurev-earth-082119.

[184] N. Rawlinson, S. Pozgay, and S. Fishwick, ‘Seismic tomography: A window into deep Earth’, Feb. 2010. doi: 10.1016/j.pepi.2009.10.002.

[185] T. M. Müller, B. Gurevich, and M. Lebedev, ‘Seismic wave attenuation and dispersion resulting from wave-induced flow in porous rocks - A review’, 2010, *Society of Exploration Geophysicists*. doi: 10.1190/1.3463417.

[186] G. Mavko and A. Nur, ‘Melt squirt in the asthenosphere’, *J Geophys Res*, vol. 80, no. 11, pp. 1444–1448, Apr. 1975, doi: 10.1029/jb080i011p01444.

[187] I. D. Palmer and M. L. Traviolia, ‘Attenuation by squirt flow in undersaturated gas sands.’, *Geophysics*, vol. 45, no. 12, pp. 1780–1792, 1980, doi: 10.1190/1.1441065.

[188] S. A. Shapiro, ‘Elastic piezosensitivity of porous and fractured rocks’, *Geophysics*, vol. 68, no. 2, pp. 482–486, 2003, doi: 10.1190/1.1567215.

[189] S. R. Pride, J. G. Berryman, and J. M. Harris, ‘Seismic attenuation due to wave-induced flow’, *J Geophys Res Solid Earth*, vol. 109, no. B1, Jan. 2004, doi: 10.1029/2003jb002639.

[190] X. Zhu and G. A. McMechan, ‘Numerical simulation of seismic responses of poroelastic reservoirs using Biot theory’, *Geophysics*, vol. 56, no. 3, pp. 328–339, 1991, doi: 10.1190/1.1443047.

[191] N. De Marchi, G. Xotta, M. Ferronato, and V. Salomoni, ‘An efficient multi-field dynamic model for 3D wave propagation in saturated anisotropic porous media’, *J Comput Phys*, vol. 510, Aug. 2024, doi: 10.1016/j.jcp.2024.113082.

[192] R. M. Bowen, ‘COMPRESSIBLE POROUS MEDIA MODELS BY USE OF THE THEORY OF MIXTURES’, 1982.

[193] M. M. Carroll, ‘An effective stress law for anisotropic elastic deformation.’, *J Geophys Res*, vol. 84, no. B13, pp. 7510–7512, 1979, doi: 10.1029/JB084iB13p07510.

[194] B. Lombard and J. Piraux, ‘Numerical treatment of two-dimensional interfaces for acoustic and elastic waves’, *J Comput Phys*, vol. 195, no. 1, pp. 90–116, Mar. 2004, doi: 10.1016/j.jcp.2003.09.024.

[195] B. L. N. Kennett and T. Furumura, ‘The Influence of 3-D Structure on the Propagation of Seismic Waves Away from Earthquakes’, 2002.

[196] W. Zhang, Y. Zhuang, and L. Zhang, ‘A new high-order finite volume method for 3D elastic wave simulation on unstructured meshes’, *J Comput Phys*, vol. 340, pp. 534–555, Jul. 2017, doi: 10.1016/j.jcp.2017.03.050.

[197] J. F. Semblat, ‘Modeling Seismic Wave Propagation in 1D/2D/3D Linear and Nonlinear Media’, 2008.

[198] A. Bermã Udez, R. Rodrã Guez B;, and D. Santamarina, ‘Finite element approximation of a displacement formulation for time-domain elastoacoustic vibrations’, 2003. [Online]. Available: www.elsevier.com/locate/cam

[199] S. Ham and K. J. Bathe, ‘A finite element method enriched for wave propagation problems’, *Comput Struct*, vol. 94–95, pp. 1–12, Mar. 2012, doi: 10.1016/j.compstruc.2012.01.001.

[200] E. T. Chung, Y. Efendiev, R. L. Gibson, and M. Vasilyeva, ‘A generalized multiscale finite element method for elastic wave propagation in fractured media’, *GEM*, vol. 7, no. 2, pp. 163–182, Nov. 2016, doi: 10.1007/s13137-016-0081-4.

[201] N. Castelletto, J. A. White, and M. Ferronato, ‘Scalable algorithms for three-field mixed finite element coupled poromechanics’, *J Comput Phys*, vol. 327, pp. 894–918, Dec. 2016, doi: 10.1016/j.jcp.2016.09.063.

[202] C. Morency and J. Tromp, ‘Spectral-element simulations of wave propagation in porous media’, *Geophys J Int*, vol. 175, no. 1, pp. 301–345, 2008, doi: 10.1111/j.1365-246X.2008.03907.x.

[203] R. Sidler, J. M. Carcione, and K. Holliger, ‘Simulation of surface waves in porous media’, *Geophys J Int*, vol. 183, no. 2, pp. 820–832, Nov. 2010, doi: 10.1111/j.1365-246X.2010.04725.x.

[204] I. Ambartsumyan, E. Khattatov, I. Yotov, and P. Zunino, ‘A Lagrange multiplier method for a Stokes-Biot fluid-poroelastic structure interaction model’, 2018.

[205] R. T. Rockafellar, ‘lagrange paper’, 1993.

[206] B. Flemisch, M. Kaltenbacher, and B. I. Wohlmuth, ‘Elasto-acoustic and acoustic-acoustic coupling on non-matching grids’, *Int J Numer Methods Eng*, vol. 67, no. 13, pp. 1791–1810, Sep. 2006, doi: 10.1002/nme.1669.

[207] Y. Chen, X. Liu, W. Zhang, and Y. Nie, ‘Mixed virtual element methods for the poro-elastodynamics model on polygonal grids’, *Computers and Mathematics with Applications*, vol. 174, pp. 431–448, Nov. 2024, doi: 10.1016/j.camwa.2024.09.025.

[208] S. K. Garg, A. H. Nayfeh, and A. J. Good, ‘Compressional waves in fluid-saturated elastic porous media’, *J Appl Phys*, vol. 45, no. 5, pp. 1968–1974, 1974, doi: 10.1063/1.1663532.

[209] O. O’Reilly, T. Lundqvist, J. Nordstrom, and E. Drunham, ‘Energy stable and high-order-accurate fi

nite difference methods on staggered grids', 2016.

[210] J. Vamaraju and M. K. Sen, 'Finite Difference Based Wave Simulation in Fractured Porous Rocks', 2019.

[211] S. Moradi and D. C. Lawton, 'Velocity-stress finite-difference modeling of poroelastic wave propagation', 2013.

[212] G. Chiavassa and B. Lombard, 'Wave propagation across acoustic/Biot's media: A finite-difference method', *Commun Comput Phys*, vol. 13, no. 4, pp. 985–1012, 2013, doi: 10.4208/cicp.140911.050412a.

[213] A. Franczyk, D. Gwizdz, and A. Leśniak, 'Performance of 3d wave field modeling using the staggered grid finite difference method with general-purpose processors', *Energies (Basel)*, vol. 13, no. 17, Sep. 2020, doi: 10.3390/en13174573.

[214] O. O'reilly *et al.*, 'A High-Order Finite-Difference Method on Staggered Curvilinear Grids for Seismic Wave Propagation Applications with Topography', *Bulletin of the Seismological Society of America*, vol. 112, no. 1, pp. 3–22, Feb. 2022, doi: 10.1785/0120210096.

[215] R. W. Graves, 'Simulating Seismic Wave Propagation in 3D Elastic Media Using Staggered-Grid Finite Differences', 1996. [Online]. Available: http://pubs.geoscienceworld.org/ssa/bssa/article-pdf/86/4/1091/5932022/bssa0860041091.pdf

[216] C. K. Saikia, 'Modified frequency-wavenumber algorithm for regional seismograms using Filon's quadrature: modelling of Lg waves in eastern North America', 1994. [Online]. Available: https://academic.oup.com/gji/article/118/1/142/582937

[217] G. Yao, D. Wu, and H. A. Debens, 'Adaptive finite difference for seismic wavefield modelling in acoustic media', *Sci Rep*, vol. 6, Aug. 2016, doi: 10.1038/srep30302.

[218] A. T. Patera, 'A Spectral Element Method for Fluid Dynamics: Laminar Flow in a Channel Expansion', 1984.

[219] Y. Maday and E. M. Rønquist, 'OPTIMAL ERROR ANALYSIS OF SPECTRAL METHODS WITH EMPHASIS ON NON-CONSTANT COEFFICIENTS AND DEFORMED GEOMETRIES', 1990.

[220] K. C. Meza-Fajardo and A. S. Papageorgiou, ‘THE SPECTRAL ELEMENT METHOD (SEM): FORMULATION AND IMPLEMENTATION OF THE METHOD FOR ENGINEERING SEISMOLOGY PROBLEMS’, 2008.

[221] D. Komatitsch, S. Tsuboi, and J. Tromp, ‘The Spectral-Element Method in Seismology’, in *Seismic Earth: Array Analysis of Broadband Seismograms*, A. Levander, Ed., American Geophysical Union, 2005.

[222] F. Li, Y. Su, and X. Sun, ‘Extended spectral element formulation for modeling the propagation of nonlinear ultrasonic waves produced by multiple cracks in solid media’, *Comput Struct*, vol. 307, Jan. 2025, doi: 10.1016/j.compstruc.2024.107639.

[223] Y. Qu, J. Zhang, S. Eisenträger, and C. Song, ‘A time-domain approach for the simulation of three-dimensional seismic wave propagation using the scaled boundary finite element method’, *Soil Dynamics and Earthquake Engineering*, vol. 152, Jan. 2022, doi: 10.1016/j.soildyn.2021.107011.

[224] S. Jayalakshmi, J. Dhanya, S. T. G. Raghukanth, and P. Martin Mai, ‘3D seismic wave amplification in the Indo-Gangetic basin from spectral element simulations’, *Soil Dynamics and Earthquake Engineering*, vol. 129, Feb. 2020, doi: 10.1016/j.soildyn.2019.105923.

[225] Y. Li, R. Brossier, and L. Métivier, ‘3D frequency-domain elastic wave modeling with the spectral element method using a massively parallel direct solver’, *Geophysics*, vol. 85, no. 2, pp. T71–T88, Mar. 2020, doi: 10.1190/GEO2019-0172.1.

[226] L. Shi, M. Zhuang, Y. Zhou, N. Liu, and Q. Liu, ‘Domain decomposition based on the spectral element method for frequency-domain computational elastodynamics’, *Sci China Earth Sci*, vol. 64, no. 3, pp. 388–403, Mar. 2021, doi: 10.1007/s11430-020-9696-4.

[227] S. Beller, S. Operto, S. Beller, and S. Operto, ‘A Frequency-Domain Spectral-Element Solver for Fluid-Solid Media A Frequency-Domain Spectral-Element Solver for Fluid A frequency-domain spectral-element solver for fluid-solid media Introduction’, pp. 1–6, 2024, doi: 10.3997/2214.

[228] H. N. Gharti, V. Oye, M. Roth, and D. Kuehn, ‘Wave propagation modelling in various microearthquake environments using a spectral-element method’, Jun. 2017, [Online]. Available: http://arxiv.org/abs/1706.05217

[229] M. Palacz, ‘Spectral methods for modelling ofwave propagation in structures in terms of damage detection-A review’, *Applied Sciences (Switzerland)*, vol. 8, no. 7, Jul. 2018, doi: 10.3390/app8071124.

[230] T. Liu and C. Zhao, ‘Finite element modeling of wave propagation problems in multilayered soils resting on a rigid base’, *Comput Geotech*, vol. 37, no. 3, pp. 248–257, Apr. 2010, doi: 10.1016/j.compgeo.2009.09.005.

[231] D. Givoli, T. Hagstrom, and I. Patlashenko, ‘Finite element formulation with high-order absorbing boundary conditions for time-dependent waves’, *Comput Methods Appl Mech Eng*, vol. 195, no. 29–32, pp. 3666–3690, Jun. 2006, doi: 10.1016/j.cma.2005.01.021.

[232] F. Mahmoudian and G. F. Margrave, ‘Review of the finite-element method CREWES’, 2003. [Online]. Available: https://www.researchgate.net/publication/254872078

[233] X. M. Shao and Z. L. Lan, ‘Finite element methods for the equations of waves in fluid-saturated porous media’, *Acta Geophysica Sinica*, vol. 43, no. 2, pp. 264–278, 2000, doi: 10.1002/cjg2.37.

[234] R. Kolman, M. Okrouhlík, and A. Kruisová, ‘A review of temporal and spatial dispersions of linear and quadratic finite elements in linear elastic wave propagation problems’, *Proceedings of the Estonian Academy of Sciences*, vol. 73, no. 3, p. 279, 2024, doi: 10.3176/proc.2024.3.11.

[235] C. Duc Toan, Y. Wang, and L. Sanavia, *Mixed finite element formulation for non-isothermal porous media in dynamics*. 2015. [Online]. Available: https://www.researchgate.net/publication/282642476

[236] B. Campos and R. Gracie, ‘A Dynamic Three-Field Finite Element Model for Wave Propagation in Linear Elastic Porous Media’, *Int J Numer Anal Methods Geomech*, Mar. 2024, doi: 10.1002/nag.3916.

[237] K. A. Lie, J. E. Aarnes, and T. Gimse, ‘An introduction to the numerics of flow in porous media using matlab’, in *Geometric Modelling, Numerical Simulation, and Optimization: Applied Mathematics at SINTEF*, Springer Berlin Heidelberg, 2007, pp. 265–306. doi: 10.1007/978-3-540-68783-2_9.

[238] R. W. Lewis and B. A. Schrefler, ‘The Finite Element Method in the Static and Dynamic Deformation and Consolidation in Porous Media’, 1998. [Online]. Available: https://www.researchgate.net/publication/275406595

[239] Ö. Aydan, ‘Rock Mechanics and Rock Engineering; Volume 2: Applications of Rock Mechanics – Rock Engineering’, 2019.

[240] E. A. de Souza. Neto, Djordje. Perić, and D. R. J. . Owen, *Computational methods for plasticity : theory and applications*. Wiley, 2008.

[241] M. Aubertin and L. Li, ‘A porosity-dependent inelastic criterion for engineering materials’, *Int J Plast*, vol. 20, no. 12, pp. 2179–2208, Dec. 2004, doi: 10.1016/j.ijplas.2004.05.004.

[242] O. Coussy, R. Eymard, and T. Lassabatere, ‘CONSTITUTIVE MODELING OF UNSATURATED DRYING DEFORMABLE MATERIALS’, 1998.

[243] J. Kim, H. A. Tchelepi, and R. Juanes, ‘Stability, accuracy and efficiency of sequential methods for coupled flow and geomechanics’, in *SPE Reservoir Simulation Symposium Proceedings*, Society of Petroleum Engineers, 2009, pp. 802–821. doi: 10.2118/119084-ms.

[244] K.-A. Lie and O. Møyner, *Advanced Modeling with the MATLAB Reservoir Simulation Toolbox*. Cambridge University Press, 2021. doi: 10.1017/9781009019781.

[245] O. Zienkiewicz and R. L. Taylor, ‘The Finite Element Method Fifth edition Volume 1: The Basis’, 2000.

[246] Y. Hiramatsu, H. Yamanaka, K. Tadokoro, K. Nishigami, and S. Ohmi, ‘Scaling law between corner frequency and seismic moment of microearthquakes: Is the breakdown of the cube law a nature of earthquakes?’, *Geophys Res Lett*, vol. 29, no. 8, Apr. 2002, doi: 10.1029/2001GL013894.

[247] E. Orowan, *Mechanism of Seismic Faulting*. 1960.

[248] S. C. Cowin and S. B. Doty, ‘Tissue Mechanics’, 2007.

[249] B. Markert, Y. Heider, and W. Ehlers, ‘Comparison of monolithic and splitting solution schemes for dynamic porous media problems’, *Int J Numer Methods Eng*, vol. 82, no. 11, pp. 1341–1383, Jun. 2010, doi: 10.1002/nme.2789.

[250] Z. Lotfian and M. V. Sivaselvan, ‘Mixed finite element formulation for dynamics of porous media’, *Int J Numer Methods Eng*, vol. 115, no. 2, pp. 141–171, Jul. 2018, doi: 10.1002/nme.5799.

[251] J. N. Reddy, *Introduction-to-the-Finite-Element-Method-Reddy*. McGraw-Hill Education, 2019.

[252] H. A. VAN DER VORST, 'BI-CGSTAB: A FAST AND SMOOTHLY CONVERGING VARIANT OF BI-CG FOR THE SOLUTION OF NONSYMMETRIC LINEAR', 1992. [Online]. Available: http://www.siam.org/journals/ojsa.php

[253] G. Muller, 'The reflectivity method: a tutorial', 1985.

[254] K. Du, B. Ding, H. Luo, and J. Sun, 'Relationship between peak ground acceleration, peak ground velocity, and macroseismic intensity in Western China', *Bulletin of the Seismological Society of America*, vol. 109, no. 1, pp. 284–297, Feb. 2019, doi: 10.1785/0120180216.

[255] D. Wald, V. Quitoriano, T. Heaton, and H. Kanamori, 'Relationships between Peak Ground Acceleration, Peak Ground Velocity, and Modified Mercalli Intensity in California', 1999.

[256] N. Spiezia and V. A. L. Salomoni, 'A unified general framework for small and finite strain two-invariants elastoplasticity', *Engineering Computations (Swansea, Wales)*, vol. 39, no. 9, pp. 3181–3210, Nov. 2022, doi: 10.1108/EC-08-2021-0482.

[257] X. Zhang, X. Li, Z. Zhou, G. Chen, X. Peng, and M. Lu, 'Three-dimensional numerical modeling of seismic wave propagation in Wudu Basin, China', in *COMPDYN 2017 - Proceedings of the 6th International Conference on Computational Methods in Structural Dynamics and Earthquake Engineering*, National Technical University of Athens, 2017, pp. 4821–4836. doi: 10.7712/120117.5764.18321.

[258] Open Geospatial Consortium, 'Open Geospatial Consortium', 2023. [Online]. Available: http://www.opengeospatial.org/legal/.

[259] F. Cappa and J. Rutqvist, 'Seismic rupture and ground accelerations induced by CO 2 injection in the shallow crust', *Geophys J Int*, vol. 190, no. 3, pp. 1784–1789, Sep. 2012, doi: 10.1111/j.1365-246X.2012.05606.x.

[260] A. Rinaldi, J. Rutqvist, and V. Vilarrasa, 'Deep Fracture Zone Reactivation During CO2 Storage at In Salah (Algeria) – A Review of Recent Modeling Studies', in *Energy Geotechnics*, Springer, 2018, pp. 394–402. [Online]. Available: http://www.springer.com/series/8069

[261] E. H. P. U.S. Geological Survey, ‘Earthquake Magnitude, Energy Release, and Shaking Intensity’.

[262] L. Moratto *et al.*, ‘Source parameter analysis of microearthquakes recorded around the underground gas storage in the Montello-Collalto Area (Southeastern Alps, Italy)’, *Tectonophysics*, vol. 762, pp. 159–168, Jul. 2019, doi: 10.1016/j.tecto.2019.04.030.

[263] L. Urpi, A. P. Rinaldi, J. Rutqvist, F. Cappa, and C. J. Spiers, ‘Dynamic simulation of CO2-injection-induced fault rupture with slip-rate dependent friction coefficient’, *Geomechanics for Energy and the Environment*, vol. 7, pp. 47–65, Sep. 2016, doi: 10.1016/j.gete.2016.04.003.

[264] H. Mittal, B. M. Yang, T. L. Tseng, and Y. M. Wu, ‘Importance of real-time PGV in terms of lead-time and shakemaps: Results using 2018 ML 6.2 & 2019 ML 6.3 Hualien, Taiwan earthquakes’, *J Asian Earth Sci*, vol. 220, Oct. 2021, doi: 10.1016/j.jseaes.2021.104936.

[265] S. Takemura, M. Kobayashi, and K. Yoshimoto, ‘Prediction of maximum P- and S-wave amplitude distributions incorporating frequency- and distance-dependent characteristics of the observed apparent radiation patterns 4. Seismology’, *Earth, Planets and Space*, vol. 68, no. 1, Dec. 2016, doi: 10.1186/s40623-016-0544-8.

[266] T. Tanimoto and L. Rivera, ‘Prograde Rayleigh wave particle motion’, Aug. 2005. doi: 10.1111/j.1365-246X.2005.02481.x.

Appendices

Appendix A: Seismic Moment, Mo, vs Corner Frequency, fc, Relationship.

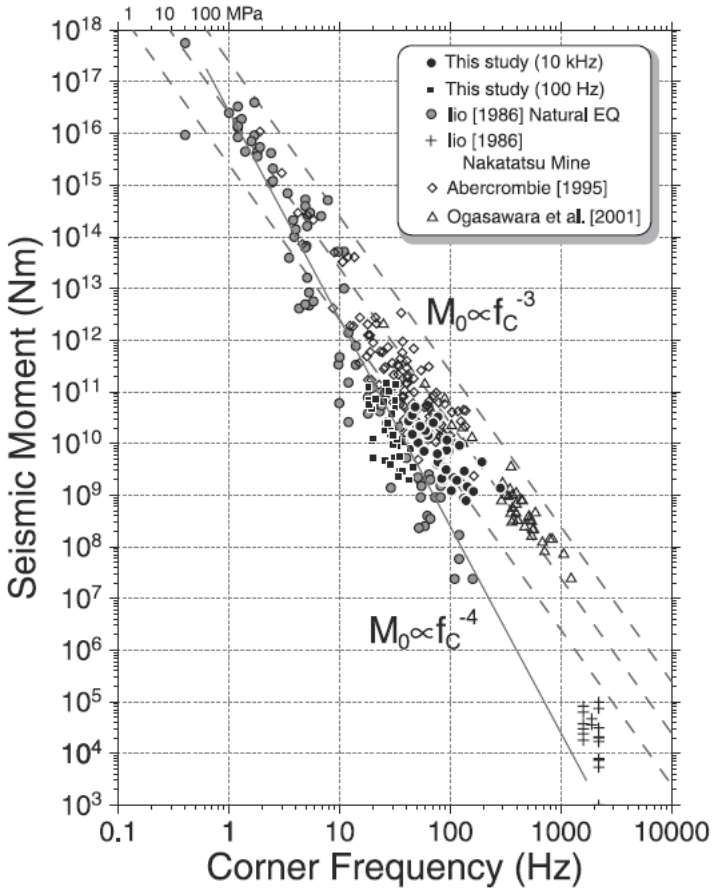

Appendix B: A Modified Mercalli Intensity (MMI) vs Peak Ground Velocity (PGV) Relationships in California.

PERCEIVED SHAKING	Not felt	Weak	Light	Moderate	Strong	Very strong	Severe	Violent	Extreme
POTENTIAL DAMAGE	none	none	none	Very light	Light	Moderate	Mod./Heavy	Heavy	Very Heavy
PEAK ACC.(%g)	*<0.1*	*0.5*	*2.4*	*6.7*	*13*	24	44	83	>156
PEAK VEL.(cm/s)	<0.07	0.4	1.9	5.8	*11*	*22*	*43*	*83*	*>160*
INSTRUMENTAL INTENSITY	I	II–III	IV	V	VI	VII	VIII	IX	X+

Appendix C: Interface Reflectivity Coefficients

This appendix reports step-by-step calculations for wave reflection and conversion at interface of the anisotropic medium, using slowness-form expressions consistent with reflectivity formulations [253]. We derive R_{pp}, R_{ps}, R_{ss}, R_{sp} when incident angle θ =0.0°, and θ =30°.

Properties for calculation are defined in Table 4.6. and variables used are defined in section 3.8.1.

α_1 = 1040.0 m/s, α_2 = 1246.3 m/s; β_1 = 556.0 m/s, β_2 = 666.2 m/s; ρ_1 = 2600.0 kg/m³, ρ_2 = 2500.0 kg/m³.

Shear moduli: $\mu_1 = \rho_1 \beta_1^2$ = 8.038e+08 Pa; $\mu_2 = \rho_2 \beta_2^2$ = 1.110e+09 Pa;

$C = 2(\mu_1 - \mu_2)$ = -6.116e+08 Pa.

Definitions

Horizontal slowness: $u = \sin(\theta) / c\_h$, where c_h is the horizontal-phase velocity of the incident wave (α_1 for incident P from above; β_2 for upgoing SV from below).

Vertical slowness: $a_i = \sqrt{(1/\alpha_i^2 - u^2)}$; $b_i = \sqrt{(1/\beta_i^2 - u^2)}$.

Auxiliary quantity: $C = 2(\mu_1 - \mu_2)$, with $\mu_i = \rho_i \beta_i^2$.

Shared denominators for P–SV coupling (functions of u):

$D_1^u = (C u^2 - \rho_1 + \rho_2)^2 u^2 + (C u^2 - \rho_1)^2 a_2 b_2 + \rho_1 \rho_2 a_2 b_1$.

$D_2^u = C^2 u^2 a_1 a_2 b_1 b_2 + (C u^2 + \rho_2)^2 a_1 b_1 + \rho_1 \rho_2 a_1 b_2$.

Coefficients:

• Case I (incident P-wave): $R_{pp} = (D_2^u - D_1^u) / (D_1^u + D_2^u)$.

• Case I (incident P-wave) : $R_{ps} = [\ 2 u a_1 \{(C u^2 - \rho_1 + \rho_2)(C u^2 + \rho_2) + C(C u^2 - \rho_1) a_2 b_2 \}\ ] / (D_1^u + D_2^u)$.

• Case II (upgoing S-wave): $R_{ss}^u = (D_2^u - D_1^u - 2 \rho_1 \rho_2 (a_2 b_1 - a_1 b_2)\ ) / (D_1^u + D_2^u)$.

• Case II (upgoing S-wave): $R_{sp}^u = -[\ 2 u b_2 \{(C u^2 - \rho_1 + \rho_2)(C u^2 - \rho_1) + C (C u^2 + \rho_2) a_1 b_1\}\ ] / (D_1^u + D_2^u)$.

θ = 0.0°

C1) Case I: Incident P from medium 1 (R_{pp}, R_{sp}^u) at θ = 0.0°

Horizontal slowness: $u = \sin(\theta)/\alpha_1 = \sin(0.0°)/1040.0 = 0.0000000000$ s/m.

Vertical slowness:

$a_1 = \sqrt{(1/\alpha_1^2 - u^2)} = 0.0009615385$ s/m; $a_2 = \sqrt{(1/\alpha_2^2 - u^2)} = 0.0008023750$ s/m.

$b_1 = \sqrt{(1/\beta_1^2 - u^2)} = 0.0017985612$ s/m; $b_2 = \sqrt{(1/\beta_2^2 - u^2)} = 0.0015010507$ s/m.

$C\,u^2 = -0.0000000000$.

Denominators:

$D_1^u = (C\,u^2 - \rho_1 + \rho_2)^2\,u^2 + (C\,u^2 - \rho_1)^2\,a_2\,b_2 + \rho_1\,\rho_2\,a_2\,b_1 = 17.5220656777$.

$D_2^u = C^2\,u^2\,a_1\,a_2\,b_1\,b_2 + (C\,u^2 + \rho_2)^2\,a_1\,b_1 + \rho_1\,\rho_2\,a_1\,b_2 = 20.1902278607$.

Final: R_{pp} = 0.07075046 when θ = 0.0°

Final: R_{ps} = 0.00000000 when θ = 0.0°

C2) Case II: Upgoing S-wave from medium 2 (R_{ss}^u, R_{sp}^u) at θ = 0.0°

Horizontal slowness: $u = \sin(\theta)/\beta_2 = \sin(0.0°)/666.2 = 0.0000000000$ s/m.

Vertical slownesses:

$a_1 = \sqrt{(1/\alpha_1^2 - u^2)} = 0.0009615385$ s/m; $a_2 = \sqrt{(1/\alpha_2^2 - u^2)} = 0.0008023750$ s/m.

$b_1 = \sqrt{(1/\beta_1^2 - u^2)} = 0.0017985612$ s/m; $b_2 = \sqrt{(1/\beta_2^2 - u^2)} = 0.0015010507$ s/m.

$C\,u^2 = -0.0000000000$.

Denominators:

$D_1^u = (C\,u^2 - \rho_1 + \rho_2)^2\,u^2 + (C\,u^2 + \rho_2)^2\,a_1\,b_1 + \rho_1\,\rho_2\,a_1\,b_2 = 20.1902278607$.

$D_2^u = C^2\,u^2\,a_1\,a_2\,b_1\,b_2 + (C\,u^2 - \rho_1)^2\,a_2\,b_2 + \rho_1\,\rho_2\,a_2\,b_1 = 17.5220656777$.

Final: R_ss^u = -0.07068240 when θ = 0.0°

Final: R_sp^u = 0.00000000 when θ = 0.0°

θ = 30.0°

C3) Case I: Incident P from medium 1 (R_{pp}, R_{ps}) at θ = 30°

Horizontal slowness: $u = \sin(\theta)/\alpha_1 = \sin(30.0°)/1040.0 = 0.0004807692$ s/m.

Vertical slownesses:

$a_1 = \sqrt{(1/\alpha_1^2 - u^2)} = 0.0008327167$ s/m; $a_2 = \sqrt{(1/\alpha_2^2 - u^2)} = 0.0006423913$ s/m.

$b_1 = \sqrt{(1/\beta_1^2 - u^2)} = 0.0017331137$ s/m; $b_2 = \sqrt{(1/\beta_2^2 - u^2)} = 0.0014219755$ s/m.

$C\,u^2 = -141.3658006657$.

Denominators:

$D_1^u = (C\,u^2 - \rho_1 + \rho_2)^2\,u^2 + (C\,u^2 - \rho_1)^2\,a_2\,b_2 + \rho_1\,\rho_2\,a_2\,b_1 = 14.1149241246$.

$D_2^u = C^2\,u^2\,a_1\,a_2\,b_1\,b_2 + (C\,u^2 + \rho_2)^2\,a_1\,b_1 + \rho_1\,\rho_2\,a_1\,b_2 = 15.8393544268$.

Final: $R_{pp} = 0.05756875$ at $\theta = 30°$

Final: $R_{ps} = 0.02572135$ at $\theta = 30°$

C4) Case II: (Rss^u, Rsp^u) at $\theta = 30°$

Horizontal slowness: $u = \sin(\theta)/\beta_2 = \sin(30.0°)/666.2 = 0.0007505254$ s/m.

Vertical slownesses:

$a_1 = \sqrt{(1/\alpha_1^2 - u^2)} = 0.0006010556$ s/m; $a_2 = \sqrt{(1/\alpha_2^2 - u^2)} = 0.0002837558$ s/m.

$b_1 = \sqrt{(1/\beta_1^2 - u^2)} = 0.0016344828$ s/m; $b_2 = \sqrt{(1/\beta_2^2 - u^2)} = 0.0012999481$ s/m.

$C\,u^2 = -344.5099576308$.

Denominators:

$D_1^u = (C\,u^2 - \rho_1 + \rho_2)^2\,u^2 + (C\,u^2 + \rho_2)^2\,a_1\,b_1 + \rho_1\,\rho_2\,a_1\,b_2 = 9.7544523178$.

$D_2^u = C^2\,u^2\,a_1\,a_2\,b_1\,b_2 + (C\,u^2 - \rho_1)^2\,a_2\,b_2 + \rho_1\,\rho_2\,a_2\,b_1 = 6.2891513284$.

Final: $R_{ss^u} = 0.04131315$ at $\theta = 30°$

Final: $R_{sp^u} = -0.00167085$ at $\theta = 30°$

Appendix D: Algorithm of the Multi-Physics Approach

For full details of this algorithm, refer to the article by [191]

Algorithm 1: Construction of Preconditioner$\left[\tilde{A}_{vv}, \tilde{B}_{ww}, \tilde{C}_{pp}, \tilde{B}_{pw}, \tilde{B}_{wp}\right] = \text{cpt_prc}(\mathbf{A})$

1: $\tilde{A}_{vv} = \mathbb{LU}(A_{vv})$;

2: $\tilde{B}_{ww} = \text{lump}[A_{ww} - \text{FS}(A_{wv}A_{vv}^{-1}A_{wv})]$

3: $\tilde{B}_{pw} = A_{pw} - \text{FS}\left(A_{pv}A_{vv}^{-1}A_{vw}\right)$

4: $\tilde{B}_{wp} = A_{wp} - \text{FS}\left(A_{wv}A_{vv}^{-1}A_{vp}\right)$

5: $\tilde{C}_{pp} = I\mathbb{LU}\left(A_{pp} - \text{FS}\left(A_{pv}A_{vv}^{-1}A_{vp}\right) - \tilde{B}_{pw}\tilde{B}_{ww}^{-1}\tilde{B}_{wp}\right)$

Algorithm 2: Application of Pre-conditioner

$\left[\mathbf{g}_v, \mathbf{g}_w, \mathbf{g}_p\right] =$ app_prc(A, $\tilde{A}_{vv}, \tilde{B}_{ww}, \tilde{C}_{pp}, \tilde{B}_{pw}, \tilde{B}_{wp}, \mathbf{r}_v, \mathbf{r}_w, \mathbf{r}_p\right)$

1: $\mathbf{x}_v = \tilde{A}_{vv}^{-1}\mathbf{r}_v$

2: $\mathbf{s}_w = \mathbf{r}_w - A_{wv}\mathbf{x}_v$,

3: $\mathbf{t}_w = B_{ww}^{-1}\mathbf{s}_w$,

4: $\mathbf{t}_p = \mathbf{r}_p - A_{pv}\mathbf{x}_v - B_{pw}\mathbf{t}_w$

5: $\mathbf{g}_p = \tilde{C}_{pp}^{-1}\mathbf{t}_p$

6: $\mathbf{y}_w = \tilde{B}_{wp}\mathbf{g}_p$

7: $\mathbf{x}_w = \tilde{B}_{ww}^{-1}\mathbf{y}_w$

8: $\mathbf{g}_w = \mathbf{t}_w - \mathbf{x}_w$

9: $\mathbf{s}_v = A_{vw}\mathbf{g}_w + A_{vp}\mathbf{g}_p$

10: $\mathbf{t}_v = \tilde{A}_{vv}^{-1}\mathbf{s}_v$

11: $\mathbf{g}_v = \mathbf{x}_v - \mathbf{t}_v$

Algorithm 3: Left preconditioner BI-CGSTAB

$[\mathbf{x}_v, \mathbf{x}_w, \mathbf{x}_p] =$ block_Bi-CGStab(A, $\mathbf{b}_v, \mathbf{b}_w, \mathbf{b}_p, \varepsilon, k_{max}$)

1: $[\mathbf{x}_v; \mathbf{x}_w; \mathbf{x}_p] = \mathbf{0}$

2: $[\tilde{A}_{vv}, \tilde{B}_{ww}, \tilde{C}_{pp}, \tilde{B}_{pw}, \tilde{B}_{wp}] =$ cpt_prc($\mathbf{A}$)

3: $[\mathbf{r}_v, \mathbf{r}_w, \mathbf{r}_p] =$ app_prc$(\mathbf{A}, \tilde{A}_{ww}, \tilde{B}_{vv}, \tilde{C}_{pp}, \tilde{B}_{pv}, \tilde{B}_{vp}, \mathbf{b}_v, \mathbf{b}_w, \mathbf{b}_p)$

4: $\mathbf{r} = [\mathbf{r}_v; \mathbf{r}_w; \mathbf{r}_p]$;

5: $\mathbf{r}^* = \mathbf{r}$

6: $\mathbf{p} = \mathbf{r}$;

7: $k = 0$

8: $r_0 = \|\mathbf{r}\|_2$

9: $r_k = \|\mathbf{r}\|_2 / r_0$

10: $\rho_k = \mathbf{r}^T \mathbf{r}^*$

11: **while** $r_k > \varepsilon \& k < k_{max}$ **do**

12: $k \leftarrow \hat{k} + 1$

13: $[\mathbf{v}_v^*; \mathbf{v}_w^*; \mathbf{v}_p^*] = \mathbf{Ap}$

14: $[\mathbf{v}_v, \mathbf{v}_w, \mathbf{v}_p] =$ app_prc $(\mathbf{A}, \tilde{A}_{vv}, \tilde{B}_{ww}, \tilde{C}_{pp}, \tilde{B}_{pw}, \tilde{B}_{wp}, \mathbf{v}_v^*, \mathbf{v}_w^*, \mathbf{v}_p^*)$

15: $\mathbf{v} = [\mathbf{v}_v; \mathbf{v}_w; \mathbf{v}_p]$;

16: $\alpha = \rho_k / (\mathbf{v}^T \mathbf{r}^*)$

17: $\mathbf{s} = \mathbf{r} - \alpha \mathbf{v}$

18: $\mathbf{u}^* = \mathbf{As}$

19: $[\mathbf{u}_v, \mathbf{u}_w, \mathbf{u}_p] =$ app_prc$(\mathbf{A}, \tilde{A}_{vv}, \tilde{B}_{ww}, \tilde{C}_{pp}, \tilde{B}_{pw}, \tilde{B}_{wp}, \mathbf{u}_v^*, \mathbf{u}_w^*, \mathbf{u}_p^*)$

20: $\mathbf{u} = [\mathbf{u}_v; \mathbf{u}_w; \mathbf{u}_p]$

21: $\omega = \mathbf{s}^T \mathbf{u} / (\mathbf{u}^T \mathbf{u})$

22: $[\mathbf{x}_v; \mathbf{x}_w; \mathbf{x}_p] \leftarrow [\mathbf{x}_v; \mathbf{x}_w; \mathbf{x}_p] + \alpha \mathbf{p} + \omega \mathbf{s}$

23: $\mathbf{r} = \mathbf{s} - \omega \mathbf{u}$

24: $r_k = \|\mathbf{r}\|_2 / r_0$

25: $\rho_{k+1} = \mathbf{r}^T \mathbf{r}^*$

26: $\beta = \rho_{k+1} \alpha / (\rho_k \omega)$

27: $\mathbf{p} \leftarrow \mathbf{r} + \beta\mathbf{p} - \omega\beta\mathbf{v}$

28: **end while**

Appendix E: Appropriate Grid Size Determination and Wave propagation calculations for u-v-p Analysis

E1: Grid size determination (justifying grid size chosen for model)

To adequately resolve the smallest wavelength in the model, the grid spacing (Δx) must satisfy:

$\Delta x \leq \frac{V_{min}}{f \cdot n}$

Where:

- Vmin = minimum propagation velocity within the layers, (m/s)
- f = characteristic frequency at which simulation is done.
- n = desired number of grid points per wavelength

For both case studies f = 100 Hz and n = 10

1.) Isotropic case

Inputs: Vmin = 666.2 m/s, f = 100, n = 10

Calculation:

Δx ≤ 666.2 / (100 × 10) = 0.6662

Result (constraint): Δx ≤ 0.6662

Design choice (highlight): For the isotropic case we use Δx = 0.5 (more conservative than the limit to ensure spectral resolution and mitigate dispersion).

2.) Layered anisotropic case.

Inputs: Vmin = 556 m/s, f = 100Hz, n = 10

Calculation:

Δx ≤ 556 / (100 × 10) = 0.556

Result (constraint): Δx ≤ 0.556

3.) Transverse vertical isotropy imposed in anisotropic case.

Inputs: Vmin = 537.1 m/s, f = 100Hz, n = 10

Calculation:
$\Delta x \leq 537.1 / (100 \times 10) = 0.5371$

Result (constraint): $\Delta x \leq 0.5371$

Notes: Choosing $\Delta x \leq 0.5$ suits all case configurations as it reduces numerical dispersion and ensures the wave profile is accurately captured during propagation.

Reason the initial model was downsized by 10^3 for u-v-p analysis. This is because discretizing u-p domain (30000 by 20000 by 5000)m with this grid size would require approximately 60000 elements in the x-direction: 40000 elements in the y-direction and 10000 in the z-direction, amounting to approximately 2.4 10^{13} elements. Which the processor described in Table 4.1 cannot handle.

By downsizing the original model by 10^3 we ensure that the wavelength for the fastest P-wave between layers can be captured as propagation occurs. This was done as follows:

3. Domain size selection for u-v-p analysis

To ensure the model domain captures at least one full wavelength of the fastest wave, choose the spatial domain length (L) such that:

$L \geq \lambda\_fastest$, where $\lambda\_fastest = Vp\_fastest / f$

Inputs used for both isotropic and anisotropic cases:

- Fastest wave in all layers for studies is Vp_fastest = 1246.3 m/s
- f = 100 Hz

$\lambda\_fastest = 1246.3 / 100 = 12.463$ m

Therefore, the domain length must satisfy: $L \geq 12.463$ m.

Notes:

However, to limit boundary interference and allow wave spreading, it is advised to extend L by 2–3× L. In u-v-p final domain selected is (30 by 20 by 5) suggesting domain was extended by 2.4× L.

E2: Wave propagation calculations

This appendix computes: (1) travel time over a given distance, (2) a frequency-resolving time step, and (3) the number of time steps required. The isotropic case is considered first.

i.) Isotropic case

With impulse applied in x-direction, we consider propagation distance in x-direction.

- Propagation distance: x = 30 m
- Frequency: f = 100 Hz
- Samples per period: n = 20
- Compressional speed (V_p): 1246.3 m/s
- Shear wave speed (V_s): 666.2 m/s.
- $travel\ time, t = \frac{x}{V_{p,s}}$

This implies: Vp path: t_p = 30 / 1246.3 = 0.0241 s and Vs path: t_s = 30 / 666.2 = 0.04503s

To obtain time step from frequency resolution:

- Period of the 100 Hz signal: T = 1 / f = 0.01 s
- Using n = 20 samples per period: Δt = T / n = 0.01 / 20 = 0.0005 s

To determine the number of time steps required:

- Formula: N = t / Δt
- Vp path: N_p = 0.024071 / 0.000500 = 48 steps
- Vs path: N_s = 0.045032 / 0.000500 = 90 steps

ii.) Layered anisotropic case.

- Propagation distance: x = 30 m
- Frequency: f = 100 Hz
- Samples per period: n = 20
- Compressional speed (V_p): 1040 m/s
- Shear wave speed (V_s): 556
- $travel\ time, t = \frac{x}{V_{p,s}}$

This implies: Vp path: t_p = 30 / 1040 = 0.0288 s and Vs path: t_s = 30 / 556= 0.0539s

To obtain time step from frequency resolution:

- Period of the 100 Hz signal: T = 1 / f = 0.01 s
- Using n = 20 samples per period: Δt = T / n = 0.01 / 20 = 0.0005s

To determine the number of time steps required:

- Formula: $N = t / \Delta t$
- Vp path: $N_p = 0.0288 / 0.0005 = 58$ steps
- Vs path: $N_s = 0.0539 / 0.0005 = 108$ steps

iii.) Transverse vertical isotropy imposed in anisotropic case.

- Propagation distance: x = 30 m
- Frequency: f = 100 Hz
- Samples per period: n = 20
- Compressional speed (V_p): 938.7 m/s
- Shear wave speed (V_s): 537.1 m/s
- $travel\ time, t = \frac{x}{V_{p,s}}$

This implies: Vp path: $t_p = 30 / 938.7 = 0.032$s and Vs path: $t_s = 30 / 537.1 = 0.0565$s

To obtain time step from frequency resolution:

- Period of the 100 Hz signal: $T = 1 / f = 0.01$ s
- Using n = 20 samples per period: $\Delta t = T / n = 0.01 / 20 = 0.0005$s

To determine the number of time steps required:

- Formula: $N = t / \Delta t$
- Vp path: $N_p = 0.032 / 0.0005 = 64$ steps
- Vs path: $N_s = 0.0565 / 0.0005 = 112$ steps